Studies on Temperature Dependence of Intermolecular Vibrational Dynamics in Ionic Liquids by Femtosecond Raman-Induced Kerr Effect Spectroscopy

January 2019

Shohei Kakinuma

Department of Nanomaterial Science
Division of Nanoscience
Graduate School of Advanced Integration Science

CHIBA UNIVERSITY

（千葉大学審査学位論文）

Studies on Temperature Dependence of Intermolecular Vibrational Dynamics in Ionic Liquids by Femtosecond Raman-Induced Kerr Effect Spectroscopy

January 2019

Shohei Kakinuma

Department of Nanomaterial Science
Division of Nanoscience
Graduate School of Advanced Integration Science

CHIBA UNIVERSITY

Contents

Chapter 1 General Introduction 1
1.1. Ultrafast Dynamics of Liquids and Solutions 2
1.2 Ionic Liquids 4
1.3. Intermolecular Dynamics of Ionic Liquids 5
1.4. Purpose of This Study 10
Chapter 2 Experimental Section 11
2.1 Femtosecond Raman-Induced Kerr Effect Spectroscopy 12
2.2. Sample Preparation 18
2.3 Measurements of Physical Properties 18
Chapter 3 Temperature Dependence of Low-Frequency Spectra in Imidazolium-Based Ionic Liquids 21
3.1. Introduction 22
3.2. Experimental and Computational Methods 23
3.3. Results 24
3.4. Discussion 33
3.5 Conclusions 44
Chapter 4 Effects of Cations Species on Temperature-Dependent Low-Frequency Spectra: Imidazolium, Pyridinium, Pyrrolidinium, Ammonium, and Phosphonium Cations 45
4.1. Introduction 46
4.2. Experimental Section 47
4.3. Results and Discussion 48
4.4 Conclusions 64
Chapter 5 Temperature Dependence of Low-Frequency Spectra in Pyrrolidinium-Based Ionic Liquids: Effects of Anion Species 67
5.1. Introduction 68
5.2. Experimental Methods 69
5.3. Results 70
5.4. Discussion 79
5.5. Conclusions 96
Chapter 6 Comparison of Temperature-Dependent Low-Frequency Spectra between Dicationic and Monocationic Ionic Liquids 97

6.1. Introduction 98
6.2. Experimental Methods 99
6.3. Results and Discussion 99
6.4. Conclusion 110
Chapter 7 Effects of Aromaticity in Cations and Their Functional Groups on Temperature Dependence of Low-Frequency Spectra of Ionic Liquids 113
7.1. Introduction 114
7.2. Experiments 115
7.3. Results and Discussion 115
7.4. Conclusions 126
Chapter 8 Effects of Conjugations on Intermolecular Vibrational Dynamics for Six-Membered-Ring Molecular Liquids 129
8.1. Introduction 130
8.2. Experimental Section 131
8.3. Results 132
8.4. Discussion 142
8.5 Conclusions 149
Chapter 9 Summary 151
References 154
Appendix 165
Acknowledgments 265
Publication List 266

Chapter 1

General Introduction

1.1. Ultrafast Dynamics of Liquids and Solutions

Molecular dynamics of liquids and solutions include inter- and intramolecular vibrations, collision, optical and vibrational dephasing, solvent relaxation, vibrational relaxation, molecular rotation, and electronic relaxation, which have the time scale of 10^{-14} to 10^{-8} s.[1-2] These motions have gained attention because they influence the rates of chemical reactions in solutions. One example is a reaction rate of electron transfer in solutions. According to the Marcus theory of electron transfer, in the nonadiabatic limit, the rate constant k_{NA} is expressed as[3]

$$k_{\mathrm{NA}} = \frac{2\pi}{\hbar}\frac{V_{\mathrm{el}}^2}{\sqrt{4\pi\lambda_{\mathrm{S}}k_{\mathrm{B}}T}}\exp\left(-\frac{\Delta G^*}{k_{\mathrm{B}}T}\right) \tag{1.1}$$

where V_{el} is the coupling of electronic states between reactant and product, λ_{S} is the solvent reorganization energy, ΔG^* is the free energy of activation, and $k_{\mathrm{B}}T$ is the thermal energy. On the other hand, in the adiabatic limit, the rate constant k_{A} is expressed as[3]

$$k_{\mathrm{A}} = \frac{1}{\tau_{\mathrm{S}}}\sqrt{\frac{\lambda_{\mathrm{S}}}{16\pi k_{\mathrm{B}}T}}\exp\left(-\frac{\Delta G^*}{k_{\mathrm{B}}T}\right) \tag{1.2}$$

where τ_{S} is the solvent relaxation time. The term in the square root is usually equal to or less than one at room temperature, and thus τ_{S} gives the maximum limit of electron transfer reactions. This shows the importance of the solvation dynamics in the electron transfer reaction rates, although the nonadiabatic and adiabatic regimes are limiting cases and other factors affect the reaction rates.

In order to gain information of femtosecond and picosecond dynamics (which corresponds to sub-THz to tens of THz or one to several hundred cm^{-1} region) of liquids and solutions, several ultrafast spectroscopic techniques that use femtosecond lasers,[4] such as time-resolved fluorescence Stokes shift measurements,[5-6] dielectric response measurements,[7] and femtosecond Raman-induced Kerr effect spectroscopy (fs-RIKES),[8-11] have been employed. Time-resolved fluorescence Stokes shift experiment monitors the dynamics fluorescence Stokes shift, namely, the time evolution of the fluorescence spectral frequency of a probe molecule. When a probe dye molecule, such as coumarin, dissolved in a liquid is photo-excited, the dipole moment of the probe molecule changes instantaneously. Subsequently, the solvent molecules reorganize to stabilize the energy of the system responding to the change of the dipole moment. As a result, the frequency of the fluorescence of the probe molecules redshifts with time, which reflects the solvation dynamics. Dielectric response measurements observe the

fluctuations of the dipole moment of the sample. Using femtosecond lasers enables the time-resolved measurements, that is, terahertz time-domain spectroscopy (THz-TDS). THz-TDS can obtain the dielectric spectra in the THz region. These spectra are related to the solvation dynamics through the dipole moments, although a dielectric response is of pure solvents while solvation dynamics is connected to solute-solvent interactions. fs-RIKES detects the fluctuations of the polarizability anisotropy. In fact, fs-RIKES and THz-TDS are complementary methods to each other, which is the same as the relation between Raman and infrared spectroscopies. fs-RIKES can measure the dynamics of the fluids in tens of fs to tens of ps, which can be converted to the low-frequency spectra in the range of 1–300 cm^{-1} by Fourier transform analysis.[9]

In the above spectroscopic techniques, fs-RIKES, which is the main research method in this thesis, has been used intently to investigate the intermolecular dynamics of condensed phases. Intermolecular dynamics of typical liquids and solutions, except for hydrogen-bonding liquids such as water, appear in the frequency region below ca. 200 cm^{-1}. Thus, fs-RIKES can obtain the spectra that include the whole range of intermolecular dynamics of a fluid with a high signal-to-noise ratio. Until now, intermolecular vibrational dynamics of various molecular liquids, such as CS_2,[12] acetonitrile,[9] benzene derivatives,[13-15] water,[16] alcohol, and so on, have been investigated by fs-RIKES. Shirota and coworkers have systematically investigated the intermolecular dynamics for as many as 40 aprotic molecular liquids.[17] As general features of the low-frequency spectra, aromatic molecular liquids showed trapezoidal or bimodal spectral shapes, while those of nonaromatic molecular liquids depend on the samples. This feature for aromatic liquids was attributed to the librational motions of aromatic rings. This is supported by the report of Ryu and Stratt.[18] They showed the analysis of the low-frequency spectra for benzene and CS_2 by molecular dynamics (MD) simulation with the instantaneous normal mode analysis. In that report, the contributions of molecular motions were divided into translational and rotational contributions. The rotational contribution of benzene, that is, the librational motion had a peak at approximately 100 cm^{-1}, which is consistent with the trapezoidal spectral line shape of benzene.[18]

The applications of fs-RIKES have been broadened to complex systems,[19] such as microemulsions,[20-21] liquid crystals,[22] polymer solutions,[23] confined fluids,[24] hydrogen-bonding systems[25] such as DNA and its model molecules,[26-27] and ionic liquids (ILs), which is the main subject of this thesis.

1.2 Ionic Liquids

ILs are salts which remain in liquid state near room temperature. The term "IL" is conventionally defined as a salt whose melting point is under 373 K.[28-30] The first reported IL is said to be ethylammonium nitrate whose melting point was 285 K, reported by Walden in 1914.[31] However, it was in the 1990s that the detailed studies of ILs started; the air- and water-stable ILs have been reported by Wilkes and Zaworotko in 1992.[32] Since then, ILs have attracted much interest of many researchers and the number of the papers on ILs increased exponentially because of their fascinating features. For example, ILs show negligibly small volatilities at ambient conditions because strong Coulomb interactions attract the ions. This feature gives the potential of ILs as green and safe solvents that substitute for conventional volatile solvents. Other features of ILs, such as high electrical conductivity and ability to dissolve various compounds, also broaden the field of applications including electrochemistry, analytical chemistry, and so on.[29,33]

ILs are typically composed of organic cations having asymmetric and rather bulky structures, and both inorganic and organic anions, as shown in Figure 1.1. The representative basic structures of cations are imidazolium, pyridinium, pyrrolidinium, ammonium, phosphonium, and so forth. Bulky and asymmetric structures of cations act as preventing the systematic packing, which lowers their melting points. On the other hand, the anions that are commonly used for ILs typically have electron withdrawing groups, such as fluorine atom, trifluoromethylsulfonyl group, and cyano group, which disperses charges of anions and contributes to lowering melting points by weakening Coulomb interaction. The physical and chemical properties, such as density, viscosity, hydrophilicity/hydrophobicity, and so on, of ILs significantly depend on the combinations of ions, which leads to the possibility of controlling the properties of ILs. The cation structures especially can be easily modified by introducing the various functional groups in cations' side groups, which is the reason why ILs are sometimes called as "designer solvents". Therefore, it is of importance to get a molecular-level understanding of the properties of ILs in order to utilize the ILs.

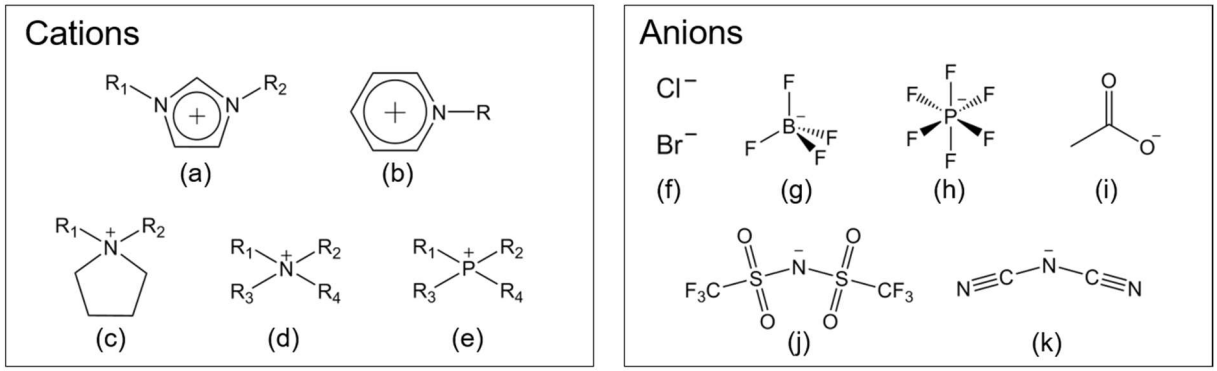

Figure 1.1. Typical cations and anions for ILs. (a) Imidazolium, (b) pyridinium. (c) pyrrolidinium, (d) ammonium, (e) phosphonium, (f) halides, (g) tetrafluoroborate, (h) hexafluorophosphate, (i) acetate, (j) bis(trifluoromethylsulfonyl)amide, and (k) dicyanamide. R_n (n: 1–4) denotes alkyl groups.

From physicochemical point of view, one of the most interesting features of ILs may be their mesoscopic structures. ILs have both ionic parts (head groups of cations and anions) and nonionic parts (alkyl chain groups), as shown in Figure 1.1. These parts segregate in nano-scale and form polar and nonpolar domains. This heterogeneous structure was suggested by both theoretical[34] and experimental studies.[35-36] X-ray scattering studies of 1-alkyl-3-methylimidazolium-based ILs showed the characteristic peaks in low-Q region.[35] This peak shifted to lower-Q region with increasing alkyl chain length. The peak is claimed to represent the size of domain structure.

1.3. Intermolecular Dynamics of Ionic Liquids

Ultrafast dynamics as well as the static structures of ILs have been investigated by various spectroscopic techniques. Intermolecular dynamics especially is important because the characteristic features of ILs are thought to be derived from their intermolecular interactions, which are directly related to intermolecular dynamics.

Solvation dynamics of ILs have been studied comprehensively.[37-38] Maroncelli and coworkers have investigated the dynamics Stokes shifts of 21 ILs in the range of 100 fs to 20 ns by combining broadband fluorescence upconversion and time-correlated single photon counting spectroscopies.[39] The solvation response functions were bimodal with sub-ps component and slower ns components. These responses were well fitted a combination of a rapid Gaussian and a slow stretched exponential functions. The Gaussian frequencies were correlated with the inverse of reduced mass of cation and anion. On the other hand, the integral

times of the stretched exponential functions were correlated with viscosities of ILs. These results imply that the fast component is related to the inertial dynamics, while the slow component is related to the diffusive structural relaxation.

Dielectric spectra in THz region also have been investigated.[40] Yamamoto and coworkers reported the THz spectra of imidazolium-based ILs by THz-TDS.[40] They attributed the THz bands to interionic vibrations of ILs. Buchner and coworkers reported the dielectric spectra in the range of ~10 MHz to ~20THz by a combination of a waveguide interferometer, a vector network analyzer, and THz-TDS, and compared the dielectric and optical Kerr effect (which is equivalent to RIKES) spectra for several ILs.[41-43] Both spectra were generally composed of the relaxational component around 1 GHz, an intermediate constant-loss region, and the librational motions at a few THz region.

The first study of ILs with fs-RIKES have been reported by Quitevis and coworkers in 2002.[44] They reported a series of the low-frequency spectra of 1-alkyl-3-methylimidazolium bis(trifluoromethylsulfonyl)amide ([C$_n$MIm][NTf$_2$]; *n* denotes the number of carbons of alkyl groups) having several different alkyl chain length. They showed that these ILs exhibited bimodal low-frequency spectra with a low-frequency component at ca. 22 cm^{-1} and a high-frequency component at 84 cm^{-1}, and the relative contributions of the high-frequency component to the low-frequency spectral band increased from ethyl(C_2) to pentyl (C_5) but keep constant for pentyl (C_5), hexyl (C_6), and octyl (C_8). They further investigated the IL-IL mixtures[45] and IL-molecular liquids mixtures.[46-47] Wynne and coworkers have studied the effects of cation and anion substitution on low-frequency spectra of ILs. They compared the [C$_4$MIm]$^+$-based ILs with [NTf$_2$]$^-$, hexafluorophosphate ([PF$_6$]$^-$), and trifluoromethanesulfonate ([OTf]$^-$), and [NTf$_2$]$^-$ salts of [C$_4$MIm]$^+$, [C$_8$MIm]$^+$, and 1-butyl-2,3-dimethylimidazolium cations.[48] They showed that the anions as well as cations play a key role in determining the spectral shapes. Fayer and coworkers have focused on the orientational dynamics of ILs rather than intermolecular vibrational dynamics.[49-50] They showed that ILs have complex dynamics that span hundreds fs to tens of ns. Shirota and coworkers have studied the intermolecular dynamics of various ILs including both aromatic and nonaromatic ILs.[51-52] They clarified the difference of the low-frequency spectral features between aromatic and nonaromatic ILs; aromatic ILs showed bimodal or trapezoidal spectral shapes, while nonaromatic ILs showed triangular shapes.[53] This was due to the high-frequency components at approximately 100 cm^{-1} that appeared in the case of aromatic ILs, which were attributed to the librational motions of aromatic rings of cations. In addition, the relationship between the

first moments of the low-frequency spectra and the bulk properties, which has been found in the case of aprotic molecular liquids,[17] was different between aromatic and nonaromatic ILs.[53] They attributed this feature to the difference of nanosegregation structures between aromatic and nonaromatic ILs. Further, they have systematically investigated the intermolecular vibrational dynamics of as many as 40 aromatic, namely, imidazolium- and pyridinium-based ILs, and discussed the effects of anions, alkyl chain length in cations, methylation in cations, and the difference between imidazolium and pyridinium cations.[54] Other notable work is the comparison between IL and its isoelectric neutral analogue: *N*-methoxyethylpyridinium dicyanamide and methoxyethylbenzene/dicyanomethane.[55] The low-frequency spectra of IL were broader, and the first moment of the spectra was higher than those of neutral analogue, which implies the stronger interactions in ILs. On the other hand, when comparing the first moments of the low-frequency spectra between nonaromatic ILs and concentrated electrolyte solutions, that is, $Li[NTf_2]$ solution in propylene carbonate and poly(ethylene glycol), ILs show smaller values than electrolyte solutions. This result implies the weaker interactions in ILs than "normal" salts.[56]

In addition to the experimental studies, MD simulation is also used to elucidate the ultrafast dynamics of ILs in molecular-level.[57-60] MD simulation has the advantage of being able to gain information which the experimental procedures cannot obtain, for example, decomposition of the spectra into the contributions of cations and anions. Since ILs are essentially multicomponent systems, namely, cations and anions, simulation studies are suitable for investigating IL dynamics. By comparing the experimental results of ultrafast dynamics of ILs with MD simulation works, deeper information of IL dynamics has been obtained.[47,61-62]

Temperature Dependence of Intermolecular Dynamics

Investigating the temperature dependence of the intermolecular dynamics is of great importance in order to extract more information from the low-frequency spectra and to elucidate complex intermolecular dynamics. There are several papers on the temperature-dependent low-frequency spectra for molecular liquids.[14-15,63-65] Generally, the low-frequency spectra shift to lower-frequency side with increasing temperature. This can be understood as following: with increasing temperature, the density of liquid decreases and free volume of liquid increases. As a result, the curvature of intermolecular potential decreases, which causes the redshift the spectra. Bender et al. reported the MD simulation study that isolated the effects of temperature and density on the shift in the high-frequency portion of the low-frequency spectrum of benzene

and concluded that density has larger effects than temperature.

In the case of ILs, there are few reports of the temperature dependence of the low-frequency spectra. Quitevis and coworkers reported the temperature dependence of the low-frequency spectra of 1-methyl-3-pentylimidazolium ($[C_5MIm]^+$) based ILs with bis(trifluoromethylsulfonyl)amide ($[NTf_2]^-$) in 2004[66] and hexafluorophosphate ($[PF_6]^-$) and Br^- in 2007.[67] Figure 1.2 shows the temperature dependence of the low-frequency spectra below 200 cm^{-1} of $[C_5MIm][NTf_2]$, $[C_5MIm][PF_6]$, and $[C_5MIm]Br$. Note that these spectra were renormalized at the peak intensities in the low-frequency bands. In the case of $[C_5MIm][NTf_2]$, the low-frequency spectra shifted to lower frequency region with increasing temperature. On the other hand, the low-frequency spectra of $[C_5MIm][PF_6]$ and $[C_5MIm]Br$ are temperature independent within the experimental error. This is rather surprising as the densities of ILs depend on temperature. They interpreted these results as follows: The ionic networks in $[C_5MIm][PF_6]$ and $[C_5MIm]Br$ are more closely packed than in $[C_5MIm][NTf_2]$, that is, $[C_5MIm][PF_6]$ and $[C_5MIm]Br$ have domains of "solid-like" structures, whereas $[C_5MIm][NTf_2]$ has "liquid-like" ones. There likely exist defects between domains in solid-like structures, which enable them to thermally expand without changing the local structures. Low-frequency spectra obtained by fs-RIKES mainly reflects the information of polar regions of ILs, rather than nonpolar regions. Thus, such ILs having solid-like structures show temperature-independent low-frequency spectra because of remaining the local structures in their ionic networks. Although this hypothesis is interesting in that it reflects the uniqueness of ILs, the further experimental results that corroborate this hypothesis have not been reported yet.

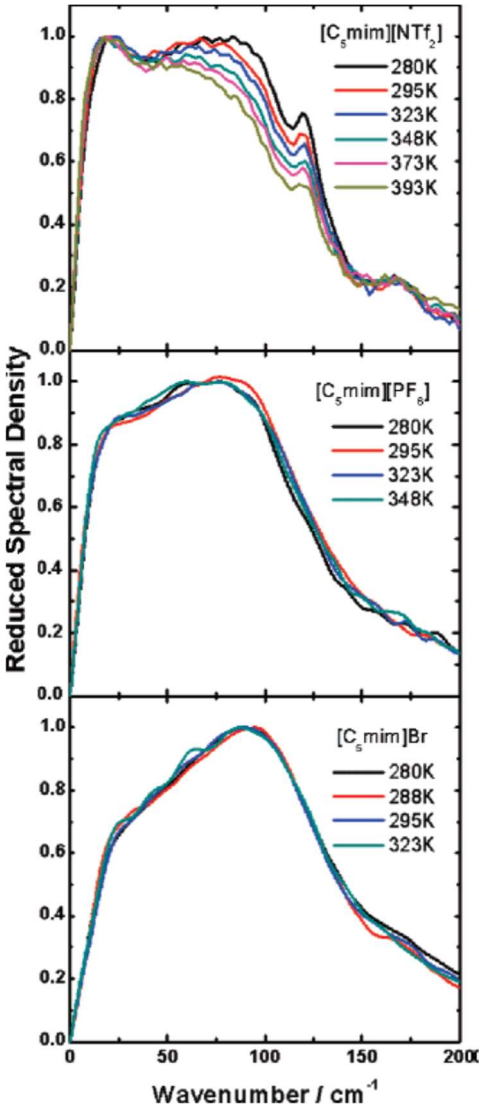

Figure 1.2. Adapted from ref 67. Temperature-dependent renormalized Kerr spectra of $[C_5MIm][NTf_2]$, $[C_5MIm][PF_6]$, and $[C_5MIm]Br$.

Wynne and coworkers compared the temperature-dependent THz spectra for ethylammonium and propylammonium nitrates obtained by fs-RIKES and THz-TDS.[42-43] Nitrate ($[NO_3]^-$) has no dipole moment, which means that the THz-TDS signals mainly reflect the cation motions. In contrast, fs-RIKES signals are dominated by the anions due to their highly polarizable nature. They reported that the α-relaxational components that located in a few GHz region largely depend on temperature, although their relaxation times do not show Stokes–Einstein–Debye behavior, which implies the strong interionic interactions between cation and anion through hydrogen-bonding. In contrast, the intermolecular vibrational parts above tens of THz, which include the librational motions of cation and anion, and the interionic hydrogen-bond vibrations, are insensitive to temperature.

1.4. Purpose of This Study

Temperature independence of the low-frequency spectra of ILs is reported for only some ILs at this moment and considered to be unusual features for liquids. Thus, it is worth investigating the reason of temperature independence to clarify the peculiarity of ILs. Nonetheless, there are few papers of the temperature dependence of the low-frequency spectra of ILs. In this thesis, the temperature-dependent features of low-frequency spectra for various ILs are systematically investigated by fs-RIKES. As typical cations for ILs, five cation structures, namely imidazolium, pyridinium, pyrrolidinium, ammonium, and phosphonium (shown in Figure 1.1) are focused on. Anions are chosen on the basis of their structures such as spherical top, less symmetric, and anions having two stable conformers. In addition, six cations having aromatic or aliphatic moieties in their ionic parts and functional groups, which are designed to study the effects of aromaticity in cations are compared. Dicationic ILs, which are composed of one dication and two monoanions, are also investigated and compared to standard monocationic ILs. Furthermore, the effects of conjugations on the low-frequency spectra are discussed by investigating the intermolecular dynamics of five six-membered-ring molecular liquids whose double-bonds differ in number and position.

This thesis consists of the following chapters. In Chapter 2, the principle and the setup of fs-RIKES are explained. Measurements of the physical properties such as viscosities, thermal properties are also described. In Chapter 3, the imidazolium-based ILs with 10 different anions are focused on. In Chapter 4, how the cation structures of ILs affect the temperature dependence of the low-frequency spectra is studied. In Chapter 5, the pyrrolidinium-based ILs with 10 different anions are investigated. The effects of anions particularly discussed in this chapter. Combining the obtained results of Chapter 3, 4, and 5 gives the overview of the temperature dependence of low-frequency spectra for ILs. In Chapter 6, the temperature dependence of the low-frequency spectra for dicationic ILs is compared to that of monocationic ILs. In Chapter 7, the effects of aromaticity in cations and their functional groups on the temperature-dependent features of ILs are investigated. In Chapter 8, the effects of aromaticity and conjugations on the low-frequency spectra are investigated for five six-membered-ring molecular liquids. In Chapter 9, I will summarize the temperature-dependent features of the low-frequency spectra for ILs.

Chapter 2

Experimental Section

2.1 Femtosecond Raman-Induced Kerr Effect Spectroscopy

Principal of fs-RIKES

At first, the principle of fs-RIKES is described. fs-RIKES is one of third-order nonlinear spectroscopy. Figure 2.1 shows a schematic energy diagram for fs-RIKES. A femtosecond laser pulse is used as a light source in fs-RIKES. A very short pulse has strong peak power instantaneously, which cause nonlinear processes easily. Once a femtosecond pulse enters a sample as a pump pulse, the vibrational coherence of Raman-active vibrational modes is induced instantaneously. A following pulse (a probe pulse) that enters the sample after τ second detects a Raman scattering that is derived from the coherent vibrations at time τ. The signal intensity is monitored as a function of time, and the dephasing of vibrations is measured. A femtosecond pulse has a very wide spectral width owing to the uncertainty principle, so various Raman-active vibrational modes within the width of the femtosecond pulse can be induced.

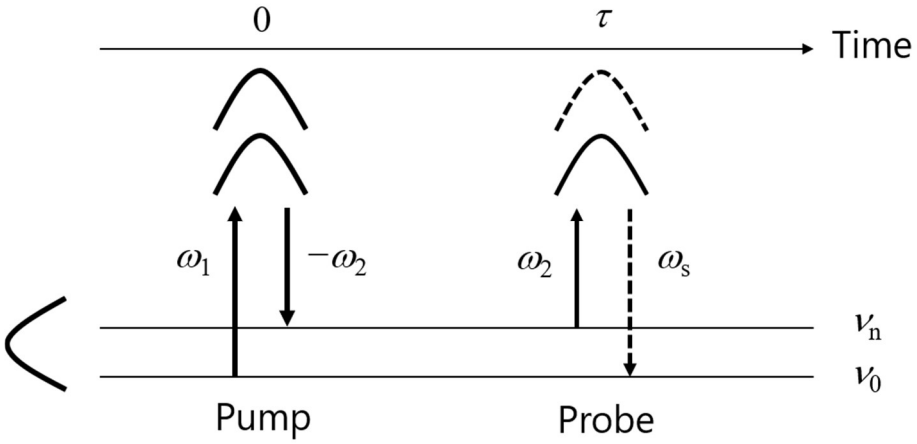

Figure 2.1. An energy diagram for fs-RIKES.

Setup of fs-RIKES used in this thesis

The setup of the fs-RIKES used in this study are shown in Figure 2.2.[68-69] This setup is based on the standard design established by McMorrow, Lotshaw, and coworkers.[12] The light source is a titanium sapphire laser (KMLabs, Griffin) pumped by a Nd:YVO_4 diode laser (Spectra Physics, Millennia Pro 5sJ). The output power of the laser was approximately 400 mW. The laser was first introduced to an optical line including a pair of fused silica Brewster prisms in order to compensate group velocity dispersion. Then the light was collimated by two concave mirrors with the focusing points of 200 and 50 mm. After the light polarization was rotated to

vertical by a half-wave plate, the light separated in to pump and probe beams with an intensity ratio of 95:5 by an uncoated fused silica interferometric wedge. The pump beam was modulated by a mechanical chopper at 1 kHz (Stanford Research System). Then the pump beam was routed through a half-wave plate and a Glan-Thompson polarizer. The probe beam was routed through a variable optical delay line (Sigma Tech, FS-1050, 0.2 μm accuracy). Then the probe beam was routed through a Glan-Thomson polarized to set the polarization of +45° and a quarter-wave plate. The pump and probe beams were focused on the sample with a 150 mm focal length achromatic lens and recollimated by an identical lens. The pump beam was blocked, and the probe beam was routed through a Glan-Thomson polarizer that was set at the polarization of −45°, then routed to a spatial filter consisting of two lenses on both sides of a 250 μm pinhole. The signal was detected by a large are amplified PIN photodiode (New Focus, 2032) and recorded by a lock-in amplifier (Stanford Research System, SR 830). The temporal response of this setup was estimated by measuring the cross-correlation using a 200-μm KDP crystal as 38±2 fs (full-width at half-maximum, FWHM). The temperature was controlled by a laboratory-built temperature controller based on a Peltier temperature controller set (VICS, VPE35-5-20TS).

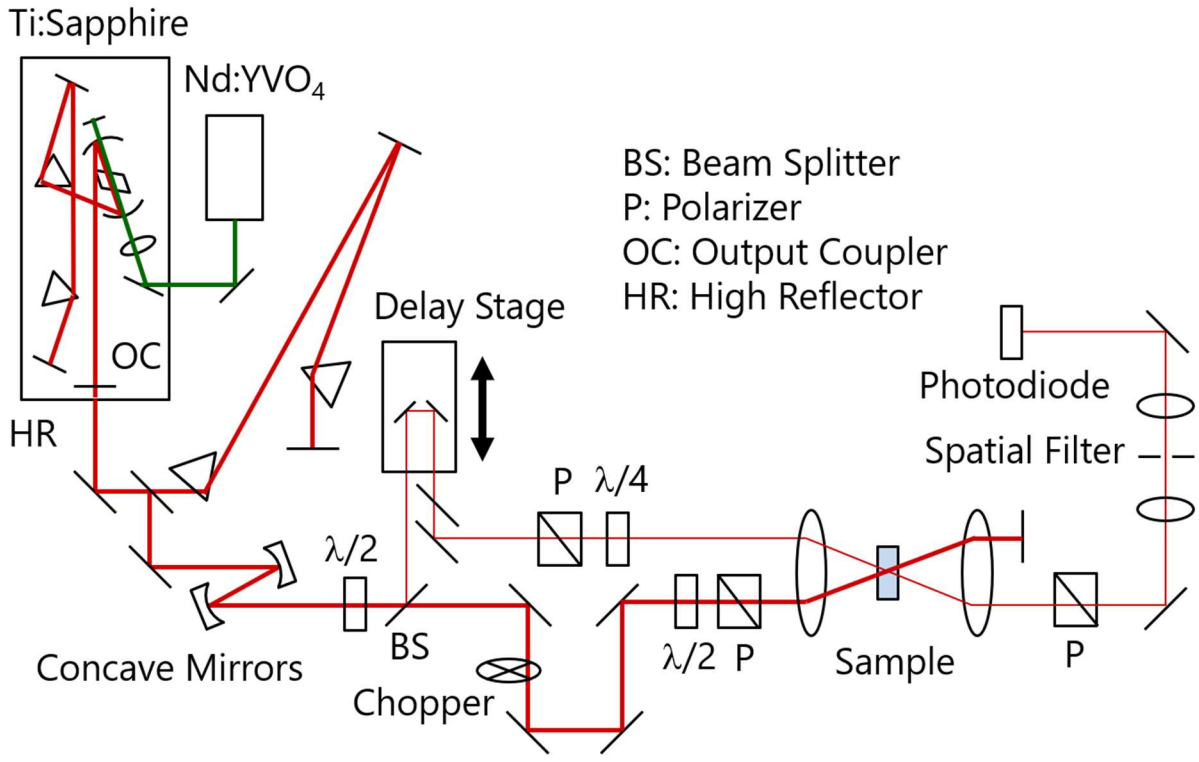

Figure 2.2. The setup of fs-RIKES in this study.

A homodyne signal is detected as the pump pulse induces a birefringence of a sample and the signal field E_s transmits through the polarizer for the detector. This signal is generally very weak. Heterodyne detection is achieved by introducing a local oscillator E_{LO} generated by rotating the input polarizer by ~1.5°. The total signal intensity is

$$\begin{aligned} I_{s,hetero} &\propto |E_s(t) \pm E_{\mathrm{LO}}(t)|^2 \\ &= |E_s(t)|^2 \pm \{E_s(t) \cdot E_{\mathrm{LO}}^*(t) + E_s^*(t) \cdot E_{\mathrm{LO}}(t)\} + |E_{\mathrm{LO}}(t)|^2 \\ &= I_{s,homo} \pm 2\mathrm{Re}\{E_s(t) \cdot E_{\mathrm{LO}}^*(t)\} + I_{\mathrm{LO}}(t) \end{aligned} \tag{2.1}$$

I_{LO} is eliminated if the output is measured by a lock-in amplifier referenced to the modulation frequency of the pump beam. Pure heterodyne signals were obtained by recording scans for both plus and minus ~1.5° rotations of the input polarizer and combining both data to eliminate the residual homodyne signal. As a result, the signal that is strong and linear to E_s is obtained.

The scans were performed with a high time resolution of 4096 (Chapter 3–7), or 3072 (Chapter 8) points at 0.5 μm/step. In Chapter 8, long-time-window data were recorded at 5.0 μm/step. Three and five scans for each polarization were averaged for the short- and long-time-window data, respectively. The sample liquids were injected into a 3 mm optical-path-length quartz cell (Tosoh Quartz) using a 0.2 or 0.02 μm pore size Anotop filter (Whatman) depending on the viscosities of the samples in order to remove the particles that cause the light scattering.

Data analysis

Figure 2.3 shows the Kerr transient of liquid benzene as an example of typical time domain data. The transient is normalized by the intensity at $t = 0$. The strong peak is observed at $t = 0$, which is attributed to the instantaneous electronic response. After this, the contributions of inter- and intramolecular vibrational dynamics appear as fast and slow dephasing components, respectively. Finally, a picosecond time-scale relaxation is observed, which is often represented by multiexponential functions. In the case of benzene, a biexponential function can fit the relaxational component sufficiently, as depicted by a blue line in Figure 2.3. The slower component is attributed to the collective reorientational dynamics. On the other hand, the faster component is thought to contain a part of intermolecular vibrational contributions because the time constant of the faster component is not more than a few picoseconds, which is near those for intermolecular vibrations.

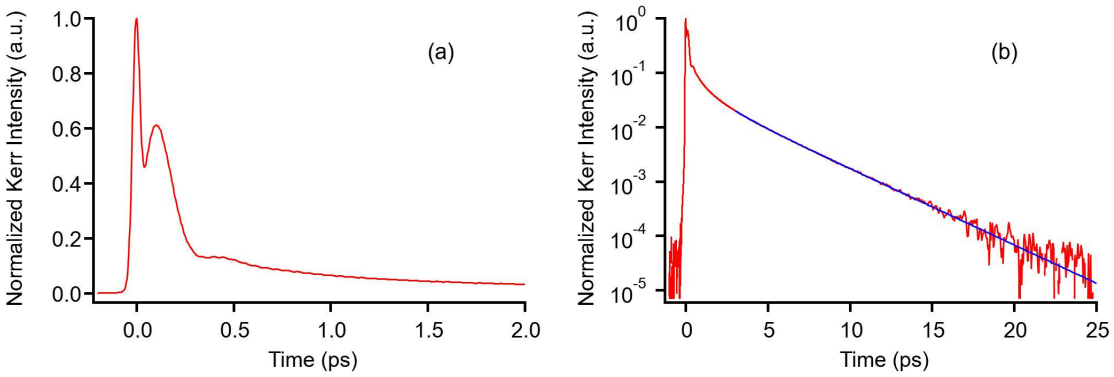

Figure 2.3. (a) Linear plot of Kerr transient for liquid benzene with the time window from −0.2 to 2 ps. (b) Semi-logarithmic plot of the Kerr transient of liquid benzene with the time window from −1 to 25 ps. Blue line denotes the biexponential fit curve.

The Kerr response $R(t)$ contains both the electronic and nuclear contributions:

$$R(t) = \sigma(t) + \sum_i r_i(t) \tag{2.2}$$

where $\sigma(t)$ is the instantaneous electronic hyperpolarizability and $r_i(t)$ is the nuclear contribution. Due to femtosecond laser pulses that are not instantaneous, the measured signal $T(t)$ is a convolution of the molecular nonlinear response $R(t)$ with second-order autocorrelation function of the laser pulse $G_2(t)$:

$$T(t) = \int_{-\infty}^{\infty} dt R(t-\tau) G_2(t) \tag{2.3}$$

The pure nuclear contribution can be obtained by Fourier transform deconvolution analysis, which was established by Lotshaw and McMorrow.[9] The nuclear contributions in the frequency domain are separated by the imaginary part of the Fourier transform:

$$\mathrm{Im}[R(\omega)] = \frac{F[T(\tau)]}{F[G_2(\tau)]} \tag{2.4}$$

The contribution of electronic responses is removed by this Fourier transform procedure. The obtained Kerr spectrum is shown in Figure 2.4. The current fs-RIKES setup used in this thesis can yield the low-frequency spectra up to approximately 700 cm^{-1}. The contribution of the relaxational dynamics appears near zero frequency with a sharp peak. The broad band that locates below 200 cm^{-1} is attributed to the intermolecular vibration. The sharp band at ca. 607

cm^{-1} is due to the intramolecular vibrational contribution: in the case of benzene, the degenerated in-plane ring deformations. In order to focus on the inter- (and intra-) molecular vibrational dynamics, the spectra without the picosecond relaxational contributions are used to discuss the spectral features.

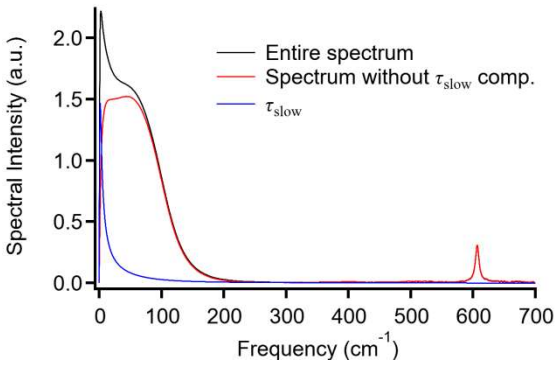

Figure 2.4. Fourier transform Kerr spectra for liquid benzene in the range of 0–700 cm^{-1}. Black line denotes the entire spectrum. Blue line denotes the picosecond relaxational components. Red line denotes the spectrum from which the picosecond relaxational components are subtracted.

The obtained Kerr spectra are analyzed by line shape analyses. One of the purposes of line shape analysis is to reproduce the spectra numerically, which allow us to discuss the features of the low-frequency spectra semi-quantitatively. As the model functions, a sum of Bucaro-Litovitz functions I_{BL} and antisymmetrized Gaussian functions I_{G} are often used. Bucaro-Litovitz functions have been originally an empirical function used to represent a depolarized Rayleigh scattering spectrum of atomic and simple molecular liquids by Bucaro and Litovitz,[70] and represented as

$$I_{BL}(\omega) = a_{\mathrm{BL}}\omega^{\alpha}\exp(-\omega/\omega_{\mathrm{BL}}) \qquad (2.5)$$

where a_{BL} is the amplitude parameter and ω is the characteristic frequency parameter. If the index α in eq 2.5 is unity, eq 2.5 is called as Ohmic function and used to fit the low-frequency spectrum because of smaller numbers of the variables. This function is included in the fits as assuming a translational vibrational motion. Antisymmetrized Gaussian function[16] is represented as

$$I_{\mathrm{G}}(\omega) = a_{\mathrm{G}}\left[\exp\left(\frac{-2(\omega-\omega_G)^2}{\Delta\omega_G^2}\right) - \exp\left(\frac{-2(\omega+\omega_G)^2}{\Delta\omega_G^2}\right)\right] \tag{2.6}$$

where a_{G} is the amplitude parameter, ω_{G} is the characteristic frequency parameter, and $\Delta\omega_{\mathrm{G}}$ is the width parameter. If clear intramolecular vibrational bands appear in the low-frequency region, Lorentzian functions are used to fit them, represented as

$$I_{\mathrm{L}}(\omega) = a_{\mathrm{L}}/[(\omega-\omega_{\mathrm{L}})^2 + \Delta\omega_{\mathrm{L}}^2] \tag{2.7}$$

where a_{L} is the amplitude parameter, ω_{L} is the characteristic frequency parameter, and $\Delta\omega_{\mathrm{L}}$ is the width parameter. On the basis of the above analysis, the first moments M_1, which are the characteristic frequencies of the intermolecular vibrational bands, defined as

$$M_1 = \int \omega I(\omega)d\omega \Big/ \int I(\omega)d\omega \tag{2.8}$$

where $I(\omega)$ is the frequency-dependent intensity of a spectrum that does not contain the contributions of picosecond overdamped relaxation and clear intramolecular vibrations, was estimated.

The slowest relaxational components of the Kerr signals of ILs show the time scale of sub-ns to ns.[49] It is desirable to capture the full dynamics that spans from femtosecond to nanosecond. However, the fs-RIKES setup used in this thesis can measure the Kerr transients only up to 300 ps due to the limitation of the time delay, and because the Kerr signal over tens or hundreds picosecond is too weak to observe. In addition, too many sets of experimental data are required to discuss the temperature-dependent features compared to other single-temperature experiments. Thus, in the researches on the temperature dependence of the low-frequency spectra of ILs in this thesis, only the short-time-window data of the Kerr transients were measured. The adequacy of a discussion on the temperature dependence of the low-frequency spectra without long-time-window data is confirmed by comparing the low-frequency spectra which are derived from the Kerr transients with and without long-time-window data. The detailed discussion is described in Appendix B. When focusing on intermolecular vibrational dynamics, the difference of the low-frequency spectra obtained from two data sets is only 1–2% in their intensities. Thus, the discussion without log-time-window data is considered to be adequate.

2.2. Sample Preparation

A part of sample ILs were synthesized according to the standard procedures. Briefly, amines, such as imidazole, pyridine, pyrrolidine, amine, and alkyl chlorides or bromides having desired alkyl chain length were mixed typically in acetonitrile at the range of 293 to 353 K, which formed ILs having target cations with chloride or bromide. Then, ILs with chloride or bromide and the salts of alkali metals (lithium, sodium, and potassium) and desired anions were mixed in water at room temperature. If obtained ILs were hydrophobic, the IL layer was separated from the water layer. After the water layer was removed, the IL layer was washed with water several times in order to remove alkali metal halides, which were byproducts. If obtained ILs were hydrophilic, ILs were dissolved in methylene chloride and washed with water. After that, if the obtained ILs were colored, the ILs were mixed with activated charcoal in acetonitrile overnight. Then ILs were dried in vacuo, and the target ILs were obtained. The purity of the synthesized ILs were checked by ^{1}H NMR and elementary analysis. It was confirmed that any peaks due to impurities were not detected except for those of solvents. It was also confirmed that the experimental values of weight percent for C, H, and N agreed with the calculated values in ±0.4%. Other ILs were purchased from the suppliers. Details are described in each chapter.

Molecular liquids used in this thesis were purchased from suppliers and used without further purification or purified by distillation.

2.3 Measurements of Physical Properties

The values of viscosities (η) of the sample liquids were measured using a reciprocating electromagnetic piston viscometer (Cambridge Viscosity, ViscoLab 4100). The temperature for η measurements was controlled by a circulating water bath (Yamato, BB300) to be 278–353 K at 5 K interval.

The glass transition temperatures (T_g) and the melting points (T_m) of ILs were estimated using a differential scanning calorimetry (DSC) apparatus (TA Instruments, DSC 2920 for Chapter 3; Shimadzu, DSC-60 Plus for Chapter 5). The sample ILs of 5–18 mg were hermetically sealed in aluminum pans. They were cooled to 143–153 K and then heated to 323 or 373 K depending on the T_m values of the samples in order to erase the thermal histories of the samples. They were again cooled to 143–153 K and heated to 323 or 373 K at a scan rate of 5 K/min. The values of T_g and T_m were estimated from the second heating cycles.

The water contents of ILs were measured using a Karl Fischer titration coulometer

(Hiranuma, AQ-300) to be less than 100 ppm.

For the molecular liquids investigated in Chapter 8, the values of densities (d) and surface tensions (γ) were obtained in addition to the values of η. The d values of the sample liquids were measured using a 2 mL volumetric flask at 293.0 ± 0.3 K. The γ values of the samples were measured using a du Noüy tensiometer (Yoshida Seisakusho) at 293.0 ± 0.3 K.

Chapter 3

Temperature Dependence of Low-Frequency Spectra in Imidazolium-Based Ionic Liquids

J. Phys. Chem. B, **2017**, *121*, 250–264.

3.1. Introduction

In this chapter, the temperature dependence of the low-frequency spectra of imidazolium-based ILs is focused on. As stated in Chapter 1, the reports of Quitevis and coworkers suggest that some of imidazolium-based ILs may show temperature-independent spectral features. Therefore, it is important to clarify what factors cause this unusual temperature-dependent features. To this end, the effects of anions species on the temperature dependence of the low-frequency spectra of imidazolium-based ILs were investigated. The anions were selected on the basis of their molecular structures and categorized into the following three types: (i) spherical top anions: hexafluorophosphate ($[PF_6]^-$), tetrafluoroborate ($[BF_4]^-$), and iodide (I^-), (ii) less symmetric anions: trifluoromethanesulfonate ($[OTf]^-$), thiocyanate ($[SCN]^-$), dicyanamide ($[DCA]^-$), and cyclohexafluoropropane-1,3-bis(sulfonyl)amide ($[NCyF]^-$), and (iii) anions having two stable conformers: bis(fluorosulfonyl)amide ($[NF_2]^-$), bis(trifluoromethylsulfonyl)amide ($[NTf_2]^-$), and bis(pentafluoroethylsulfonyl)amide ($[NPf_2]^-$). As the counter cation, 1-butyl-3-methylimidazolium ($[C_4MIm]^+$), which is one of the most popular IL cations, was used. In addition, the effects of alkyl group length on the temperature dependence of the low-frequency spectra were elucidated by comparing the results obtained with a common anion, $[PF_6]^-$, for 1-hexyl-3-methylimidazolium ($[C_6MIm]^+$) and 1-heptyl-3-methylimidazolium ($[C_7MIm]^+$) to that of $[C_4MIm]^+$. The chemical formulas of the cations and anions of ILs in this study are shown in Figure 3.1. Furthermore, the temperature-dependent low-frequency spectra of some molecular liquids that are analogous to the cations or anions of ILs, namely, 1-methylimidazole, propionitrile, and CCl_4, were investigated to see how the nature of ILs (consisting only of ions) affects the temperature dependence of their spectra. To understand the temperature-dependent behavior of ILs and , the temperature dependence of the density of states (DOS) for intermolecular vibrations of $[C_4MIm][PF_6]$ was examined by MD simulations. In addition to the low-frequency spectra, the temperature-dependent viscosities, glass transition temperatures, and melting points of the samples in this study were estimated to clarify the relation between intermolecular vibrational dynamics and the bulk properties.

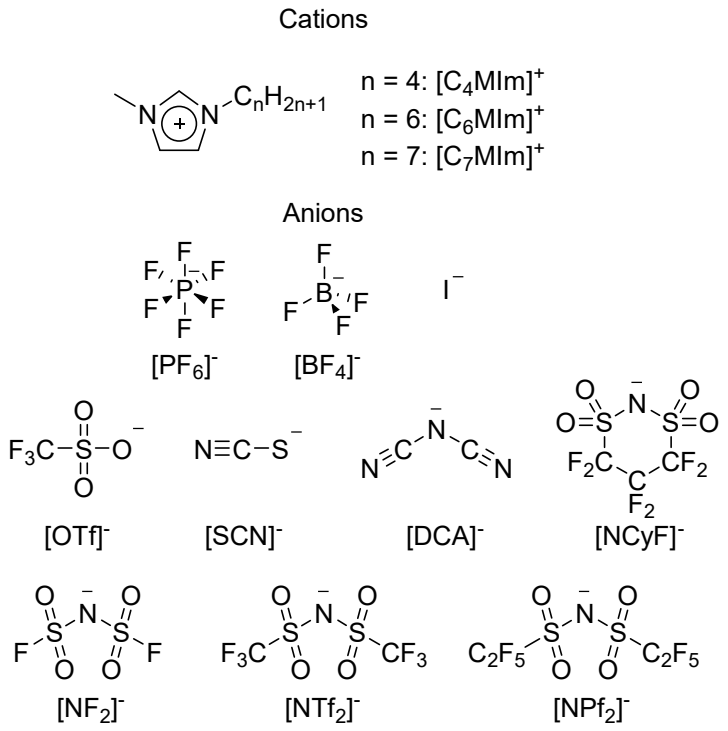

Figure 3.1. Chemical formulas of cations and anions of ILs used in this study.

3.2. Experimental and Computational Methods

3.2.1. Materials

[C_4MIm][PF_6] (Fluka), [C_4MIm]I (Kanto), [C_4MIm][OTf] (Iolitec), [C_4MIm][DCA] (Merck), [C_4MIm][NF_2] (Kanto), [C_4MIm][NTf_2] (Kanto), 1-methylimidazole (Aldrich), propionitrile (TCI), and CCl_4 (Wako) were used as received. [C_4MIm][SCN] was received from Aldrich and subsequently purified by column chromatography (aluminum oxide, chloroform/ethanol, 20:1 v/v) after the standard activated charcoal decolorization treatment.[71] [C_4MIm][BF_4], [C_4MIm][NPf_2], and [C_6MIm][PF_6] were previously synthesized,[54] and the preparation details were already reported. [C_4MIm][NCyF] and [C_7MIm][PF_6] in this study were prepared in our laboratory according to previously reported preparation procedures for imidazolium-based ILs.[72] Detailed synthetic procedures and assignments for these ILs are described in Appendix A. The sample ILs were dried in vacuo for more than 36 hours before measurements. Because the liquid property values of the ILs estimated in this study are in good agreement with the reported values (see below), these values were not influenced much by the water content.

3.2.2. Computational Details

MD simulations were carried out with the GROMACS 5.0.6 simulation package.[73] All of the simulations utilized the force field parameters[74-75] for the cation and anion. In the [C_4MIm][PF_6] IL system at different temperatures (293, 323, and 353 K), 256 ion pairs (8192 atoms) were set in a cubic box, and the periodic boundary condition was applied. The Lennard-Jones interactions were calculated using a cutoff of 12 Å. The particle-mesh Ewald method[76] was applied to compute Coulombic interactions using an electrostatic cutoff of 12 Å, a Fourier grid spacing of 2.0 Å, and a time step of 1.0 fs. Initially, each system was equilibrated under NPT conditions for 5 ns at each temperature with a target pressure of 1 atm. The temperature was kept constant using a Nosé-Hoover thermostat,[77-78] whereas the pressure was controlled using a Parrinello-Rahman barostat.[79] The time constants of temperature and pressure were set to be 0.8 and 1.0 ps, respectively. On the basis of the NPT simulation results, the length of the cubic box size was set to be 43.854, 44.028, and 44.299 Å for 293, 323, and 353K, respectively. Thereafter, we carried out NVT simulations for a 5 ns equilibration run, followed by a 20 ns production run at each temperature. Simulation data were collected at 50 fs intervals during production runs.

It is considered that the interionic vibrational spectrum of ILs includes the contribution from the interionic interaction among ionic species and that important information on the motion of cation and anion in ILs can be provided by the DOS profile. Therefore, with MD simulation results, we computed velocity autocorrelation functions (VACFs), $\langle \boldsymbol{v}_i(0)\cdot\boldsymbol{v}_i(t)\rangle$, where $\boldsymbol{v}_i(t)$ is the velocity of the center of the mass of the ith ionic species, and obtained the vibrational density of states with the Fourier transformation of VACFs.[60-61,80] In this study, we performed a calculation of the time correlation of the total velocity, which includes the velocities of all atoms (cation and anion) at the different temperatures, and also, the time correlation functions were calculated for the cation and anion species at the different temperatures.

3.3. Results

3.3.1. Temperature-Dependent Viscosities and Glass Transition Temperatures.

Before describing the results of fs-RIKES, temperature-dependent viscosities of ILs are presented. These data are used to estimate the fragilities of ILs, which are discussed in Section 3.4.1. Figure 3.2 shows the temperature dependence of η of [C_4MIm][PF_6], [C_4MIm][DCA], and [C_4MIm][NTf_2], as examples. Most viscosities at various temperatures for the ILs studied here have been reported by other groups,[81-85] being in good agreement with these reported

values within experimental error. Note that the η data of [C4MIm][NCyF] are reported in this study for the first time. The temperature dependence of η shows non-Arrhenius behavior for each IL. The Vogel-Tammann-Fulcher (VTF) equation[86-89] is commonly used to fit the temperature dependence of η of ILs[90] and is given by

$$\eta(T) = \eta_0 \exp\left[\frac{DT_0}{T - T_0}\right] \tag{3.1}$$

where T is the absolute temperature, η_0 is the reference viscosity at which the exponential term approaches unity, D is a fragility-related parameter, and T_0 is the characteristic temperature at which η diverges. The collected data were fitted using the logarithmic form of eq 3.1, $\ln[\eta(T)] = \ln(\eta_0) + [DT_0/(T - T_0)]$, to properly treat the η data, spanning several orders of magnitude. Each data set included a value of 1×10^{13} cP at the liquid's T_g, according to the report by Angell and coworkers.[90] Note that the $\eta(T)$ fits of [C4MIm][OTf] and [C4MIm][NCyF] were obtained without the data at T_g because these ILs did not show glass transitions (described below). The corresponding fit parameters for $\eta(T)$ of the studied ILs are summarized in Table 3.1.

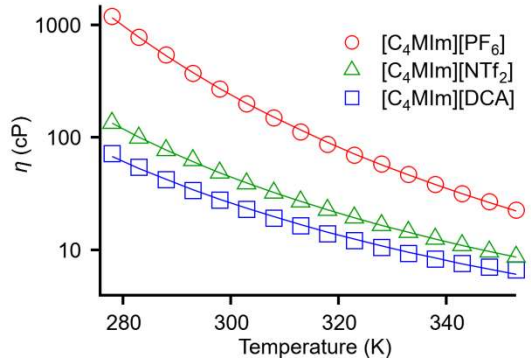

Figure 3.2. Temperature-dependent shear viscosities for [C4MIm][PF6] (red circles), [C4MIm][DCA] (blue squares), and [C4MIm][NTf2] (green triangles). The solid lines denote the VTF fits to eq 3.1 for each IL.

Table 3.1. Melting Points (T_m), Glass Transition Temperatures (T_g), and VTF Fit Parameters for ILs

IL	T_m (K)	T_g (K)	η_0 (cP)	D	T_0 (K)
$[C_4MIm][PF_6]$	283	192	0.0289	8.766	152.2
$[C_4MIm][BF_4]$	n.o.[b]	179	0.0205	9.823	138.7
$[C_4MIm]I$	n.o.[b]	197	0.0030	14.60	139.9
$[C_4MIm][OTf]$[a]	285	n.o.[b]	(0.0838)	(6.154)	(158.0)
$[C_4MIm][SCN]$	n.o.[b]	181	0.0351	7.925	146.2
$[C_4MIm][DCA]$	n.o.[b]	174	0.0902	5.874	147.3
$[C_4MIm][NCyF]$[a]	301	n.o.[b]	(0.0981)	(5.547)	(171.3)
$[C_4MIm][NF_2]$	n.o.[b]	172	0.1216	5.818	145.6
$[C_4MIm][NTf_2]$	269	183	0.0986	5.665	155.7
$[C_4MIm][NPf_2]$	n.o.[b]	186	0.0456	7.487	151.6
$[C_6MIm][PF_6]$	n.o.[b]	198	0.0200	9.351	155.1
$[C_7MIm][PF_6]$	n.o.[b]	197	0.0146	10.37	151.1

[a]VTF fit parameters were obtained without T_g data. [b]n.o. denotes not observed.

The T_g values for the studied ILs estimated in this study ranged from approximately 170 to 200 K. $[C_4MIm][OTf]$ and $[C_4MIm][NCyF]$ crystallized during the first cooling cycle. To prevent these ILs from crystallizing, the fast cooling was performed at a scan rate of 10 K/min. However, these ILs crystallized again during the first cooling cycle, preventing the determination of their T_g values. Because the T_m of $[C_4MIm][NCyF]$ is 301 K, this IL existed in a supercooled state at room temperature in this study. The values of T_m and T_g for the studied ILs are summarized in Table 3.1. The determined $\eta(T)$ and T_g for the ILs enable the estimation of IL fragilities, which is discussed in Section 3.4.1.

3.3.2 Temperature-Dependent Low-Frequency Spectra Obtained by fs-RIKES

Figure 3.3 displays the Kerr transients of $[C_4MIm][PF_6]$ at 293, 308, 323, 338, and 353 K. The Kerr transients show instantaneous responses due to electronic responses at $t = 0$ and subsequent strong beats and overdamped decays arising from nuclear responses. The Kerr transients were normalized relative to the intensity of the electronic response at $t = 0$. Figure 3.3 reveals that the relative intensities of the nuclear responses in relation to the electronic responses increase with increasing temperature. This temperature-dependent behavior was

confirmed for all of the studied ILs regardless of their counteranions (see Appendix C). The Kerr transients after 3 ps were fitted by a biexponential function. The above time constants were almost independent of temperature within the experimental and fitting errors. For example, the fast and slow time constants of $[C_4MIm][PF_6]$ are 1.46 ± 0.20 and 6.12 ± 1.01 ps, respectively. The offset parameter a_0 increases with increasing temperature. However, in the case of molecular liquids (1-methylimidazole and propionitrile), the Kerr transients decay faster, and both fast and slow time constants become faster with increasing temperature overall. No overdamped relaxation decay was observed for CCl_4 in this temperature range because of its spherical top (tetrahedral) structure. The biexponential fit parameters for all of the Kerr transients measured in this study, except for the transients for the case of CCl_4, are summarized in Appendix C.

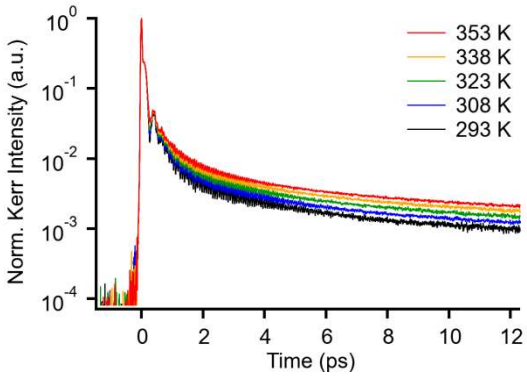

Figure 3.3. Kerr transients for $[C_4MIm][PF_6]$ at 293 (black), 308 (blue), 323 (green), 338 (yellow), and 353 K (red).

The Kerr transients were analyzed using the Fourier transform deconvolution procedure established by McMorrow and Lotshaw, described in Chapter 2.[9] Figure 3.4 shows the Fourier transform Kerr spectra of (a) $[C_4MIm][BF_4]$, (b) $[C_4MIm][DCA]$, and (c) $[C_4MIm][NTf_2]$ in the frequency range of 0–200 cm^{-1}. The IL spectral line shapes at 293 K in this study are similar to those previously reported at room temperature.[52,54,56,71] In addition to the above ILs shown in Figure 3.4, the low-frequency spectra of all ILs show a similar temperature dependence, although the line shape of each spectrum is different. That is, the spectral intensity in the low-frequency region below ~50 cm^{-1} increases and that in the high-frequency region above ~70 cm^{-1} decreases (or, in other words, the spectral density in the high-frequency region shifts to the lower frequency side) with rising temperature. A similar temperature dependence was

observed for the low-frequency spectra of other imidazolium-based ILs with the $[NTf_2]^-$ anion reported by Quitevis and coworkers.[66-67]

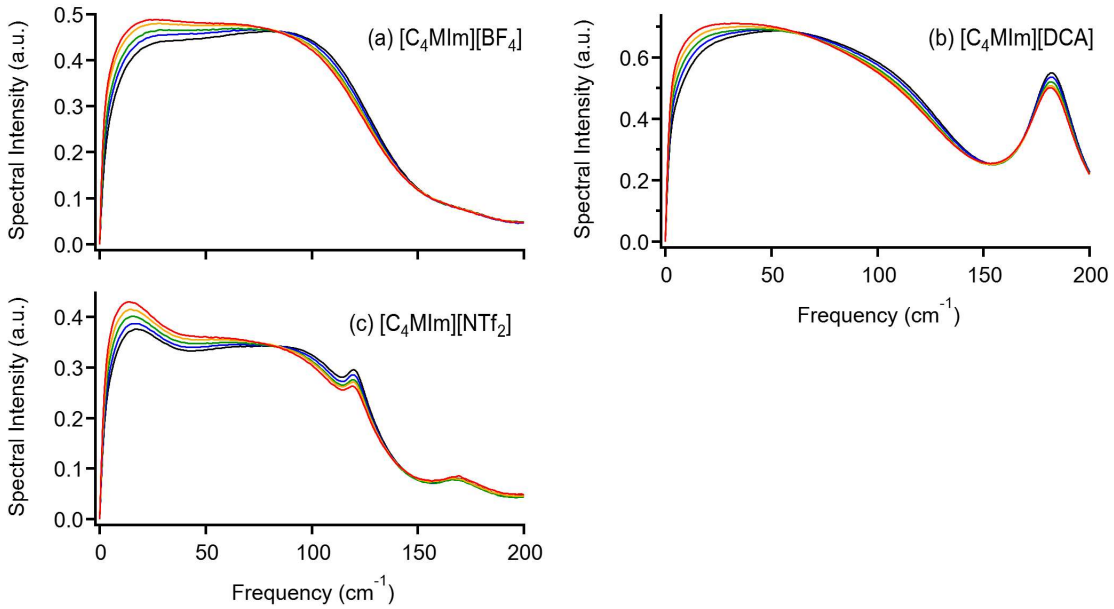

Figure 3.4. Low-frequency Kerr spectra in the frequency range of 0–200 cm^{-1} for (a) $[C_4MIm][BF_4]$, (b) $[C_4MIm][DCA]$, and (c) $[C_4MIm][NTf_2]$ at 293 (black), 308 (blue), 323 (green), 338 (yellow), and 353 K (red).

It is also noticeable from Figure 3.4 (actually, Figures 3.5 and 3.6 as well, vide infra) that there is an isoscattering point in the spectrum of each IL. An isosbestic point in an absorption spectrum appears when a perturbation (temperature in this study) affects two components or states in the spectrum. Thus, it could be considered that the results of the temperature-dependent features of the IL spectra are attributed to the two distinguishable temperature-dependent intermolecular vibrational motions. However, the Kerr spectra in this study are actually normalized at the electronic response in the time-domain data, and thus the Kerr spectral intensity is relative to the electronic response intensity but not absolute. Furthermore, it is hard to think that two intermolecular vibrational motions in liquids are not coupled or interacting. Therefore, it is not clear whether the isoscattering point observed in this study is real or an artifact.

To determine the effect of the length of the imidazolium cation alkyl group, Figure 3.5 compares the temperature-dependent low-frequency spectra of (a) $[C_4MIm][PF_6]$, (b) $[C_6MIm][PF_6]$, and (c) $[C_7MIm][PF_6]$. The differences in the line shapes of the above spectra

for the 1-alkyl-3-methylimidazolium hexafluorophosphates at room temperature shown in Figure 3.5 have been previously observed and attributed to the different frequencies of the intramolecular vibrational mode (bending of the alkyl group and imidazolium ring).[54] Figure 3.5 reveals that the same temperature dependence was observed for the spectra of the three ILs, namely, an increase in the spectral intensity in the low-frequency region below ~50 cm^{-1} and a redshift of the spectra in the high-frequency region above ~70 cm^{-1}.

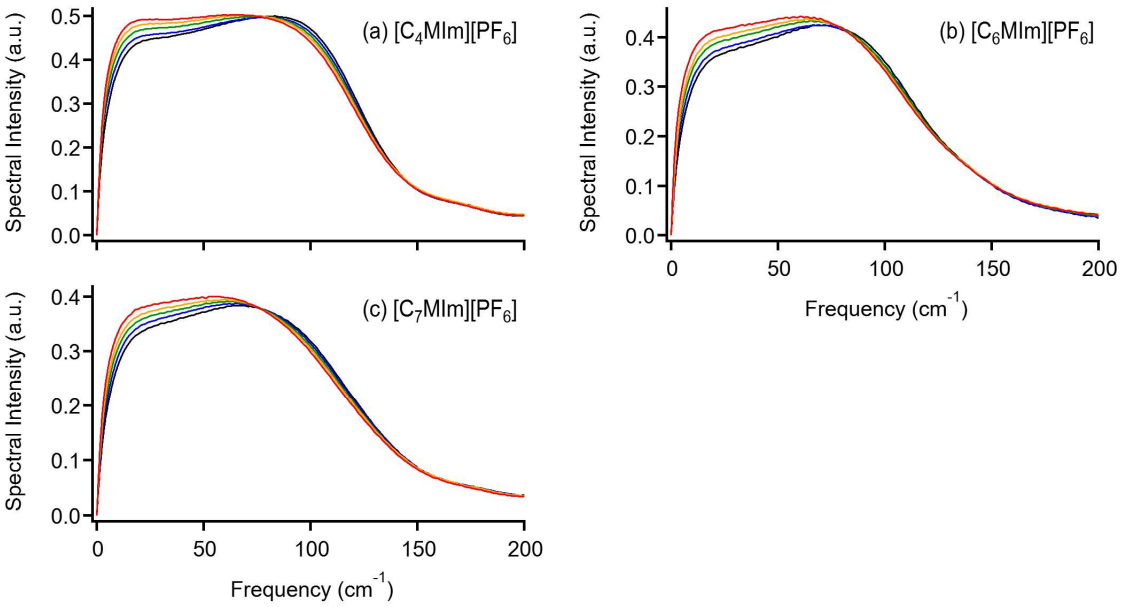

Figure 3.5. Low-frequency Kerr spectra in the frequency range of 0–200 cm^{-1} for (a) $[C_4MIm][PF_6]$, (b) $[C_6MIm][PF_6]$, and (c) $[C_7MIm][PF_6]$ at 293 (black), 308 (blue), 323 (green), 338 (yellow), and 353 K (red).

Figure 3.6 shows the temperature-dependent spectra of (a) 1-methylimidazole, (b) propionitrile, and (c) CCl_4. Note that no spectrum is provided for CCl_4 at 353 K because its boiling point at ambient pressure is 350 K.[91] It is found that the temperature dependence of the spectra of 1-methylimidazole was very similar to that of the ILs studied herein. However, propionitrile and CCl_4 showed a clearly different temperature dependence. Namely, the corresponding spectral intensity in the low-frequency region below 50 cm^{-1} increased, similarly to the case of ILs and 1-methylimidazole, whereas the intensity in the high-frequency region above 70 cm^{-1} was largely unchanged.

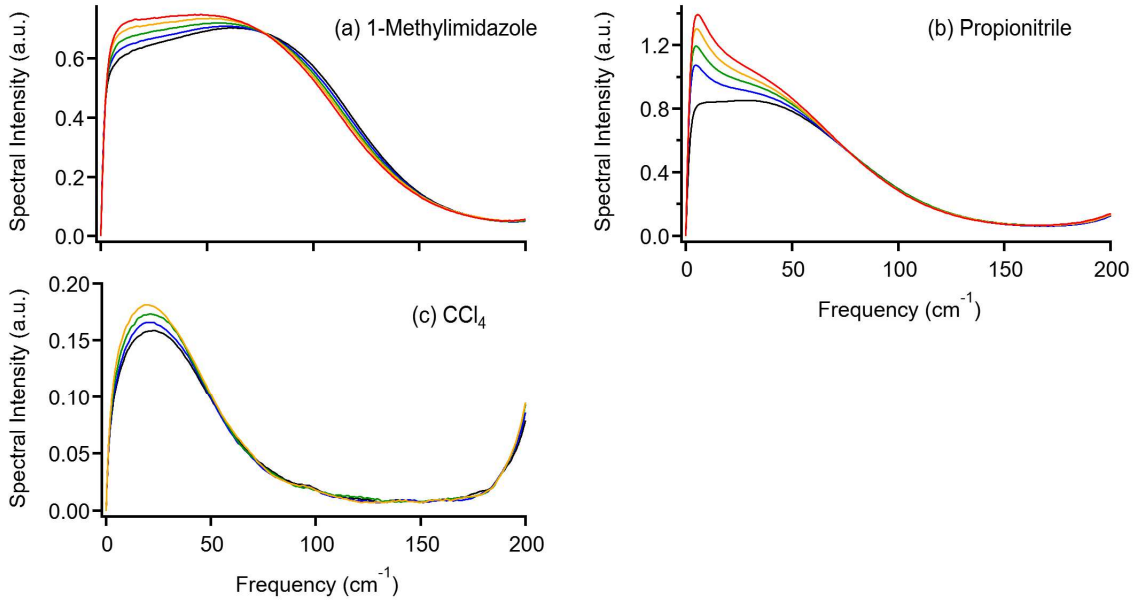

Figure 3.6. Low-frequency Kerr spectra in the frequency range of 0–200 cm^{-1} for (a) 1-methylimidazole, (b) propionitrile, and (c) CCl_4 at 293 (black), 308 (blue), 323 (green), 338 (yellow), and 353 K (red).

A line shape analysis of the low-frequency Kerr spectra is performed to discuss the temperature dependence quantitatively, as described in Chapter 2. The fit parameters and the values of M_1 for the studied ILs and molecular liquids are summarized in Appendix C. Each fit component obtained by the line shape analysis of low-frequency spectra of liquids/solutions is sometimes discussed. However, M_1 is used to discuss the temperature dependent spectral features in the ILs in this study. This is because it does not always mean that each function obtained by line shape analysis corresponds to an intermolecular vibrational mode. It is known from MD simulations that orientational and translational vibrational motions in liquids are strongly overlapped and coupled.[18,92-95] The cross-term, which is a kind of coupling motion, often appears in the spectrum with a negative amplitude that is hard to characterize by line shape analysis. Furthermore, two-component systems, such as binary mixtures[13,96-97] and ILs,[60-62,98-99] are even more complicated. Therefore, I focus here on the general or overall feature of the temperature-dependent low-frequency spectra of the ILs.

Figure 3.7 shows the temperature dependence of M_1 for the ILs with (a) spherical top anions, (b) less symmetric anions, (c) anions having conformers, and (d) cations with different alkyl group lengths. For comparison purposes, the M_1 plots for 1-methylimidazole are also shown in the figure, and the linear fits are also displayed by solid lines. The slopes obtained

from linear fits are similar (approximately −0.056 ± 0.007 cm^{-1}/K), except for [C_4MIm][SCN] and [C_4MIm][DCA]. This contrasts with the viscosities and thermal properties that significantly depend on the cation-anion combinations (Figure 3.2 and Table 3.1). Moreover, 1-methylimidazole also shows a similar slope of −0.057 cm^{-1}/K. The slopes obtained for the M_1 temperature dependence of the studied ILs and molecular liquids are summarized in Table 3.2.

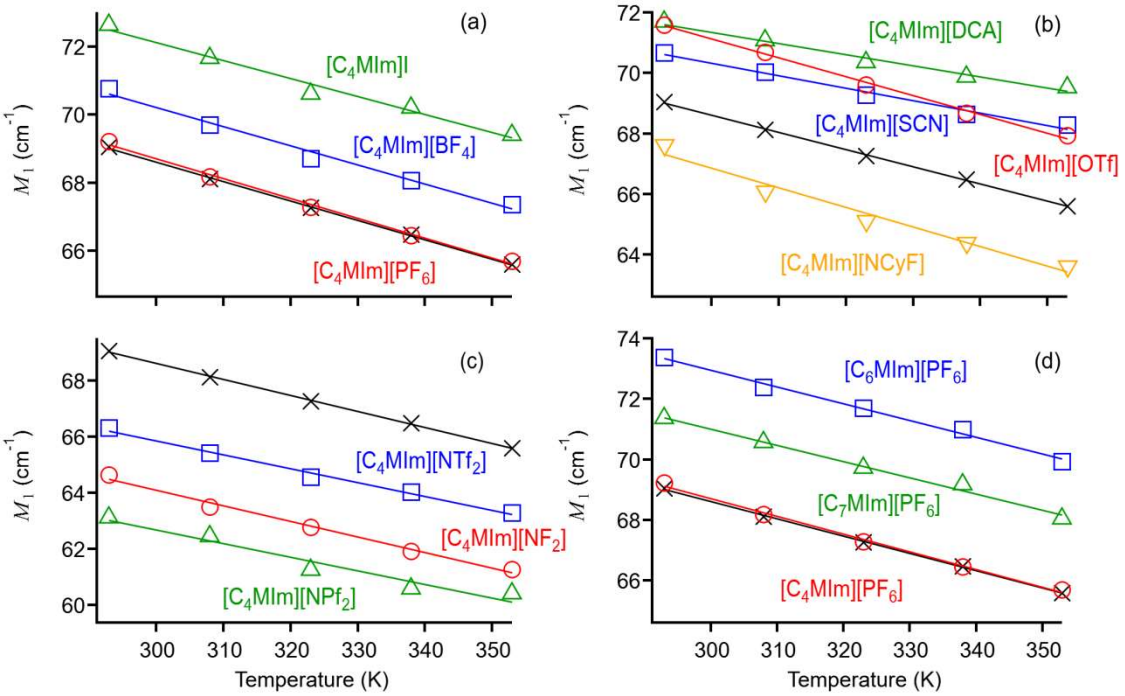

Figure 3.7. Plots of first moment vs. temperature for ILs with (a) spherical top anions, (b) less symmetric anions, (c) anions having conformers, and (d) cations with different alkyl chain lengths. Plots for 1-methylimidazole (black crosses) are included in all figures for comparison. Linear fits are shown by solid lines.

Table 3.2. Slopes Estimated from Linear Fits for the First Moments, M_1, to Temperature for ILs and Molecular Liquids

spherical top anion		lower symmetric anion	
sample	slope (cm^{-1}/K)	sample	slope (cm^{-1}/K)
$[C_4MIm][PF_6]$	−0.058	[C4MIm][OTf]	−0.062
$[C_4MIm][BF_4]$	−0.056	[C4MIm][SCN]	−0.041
[C4MIm]I	−0.053	[C4MIm][DCA]	−0.037
$[C_6MIm][PF_6]$	−0.055	[C4MIm][NCyF]	−0.065
$[C_7MIm][PF_6]$	−0.054		
anion having conformers		molecular liquid	
sample	slope (cm^{-1}/K)	sample	slope (cm^{-1}/K)
$[C_4MIm][NF_2]$	−0.056	1-methylimidazole	−0.057
$[C_4MIm][NTf_2]$	−0.050	propionitrile	−0.104
$[C_4MIm][NPf_2]$	−0.048	CCl_4	−0.056

3.3.3. Temperature-Dependent DOS Spectrum of $[C_4MIm][PF_6]$ Calculated by MD Simulations.

Figure 3.8 compares the DOS spectra of (a) $[C_4MIm][PF_6]$ at 293, 323, and 353 K, which are decomposed into the contributions of (b) $[C_4MIm]^+$ and (c) $[PF_6]^-$ to see the effects of each constituent ion. The DOS profiles of $[C_4MIm][PF_6]$, $[C_4MIm]^+$, and $[PF_6]^-$ are in good agreement with those calculated previously for these species.[61] Note that the DOS spectra are not directly related to the Kerr spectra because the latter are based on this fs-RIKES selection rule (depolarized Raman signal), whereas the former feature equal contributions of all vibrational states existing within the frequency region (Fourier transform power spectrum of the time correlation function of the velocity of ionic species). Nonetheless, the comparison of temperature-dependent low-frequency Kerr spectra with the calculated DOS spectra is useful.

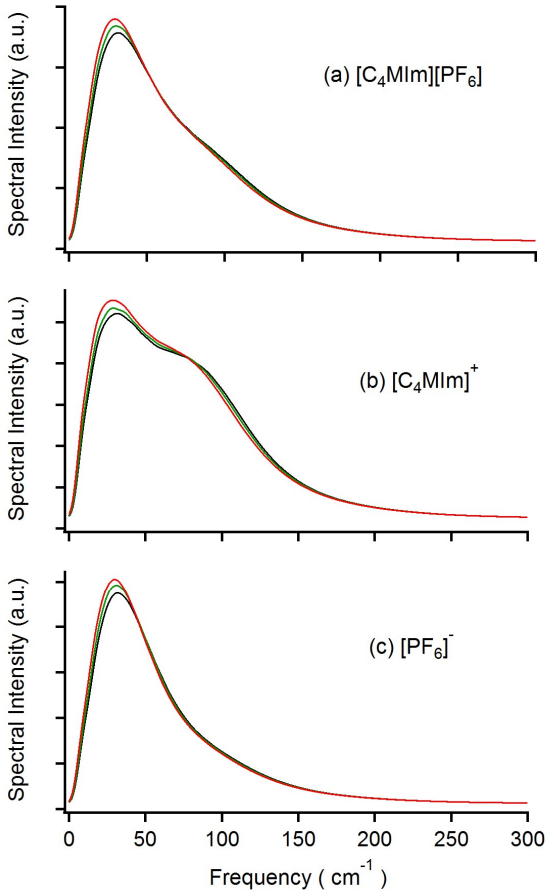

Figure 3.8. Calculated temperature-dependent DOS spectra of (a) $[C_4MIm][PF_6]$, (b) $[C_4MIm]^+$, and (c) $[PF_6]^-$. Black, green, and red lines denote the spectra at 293, 323, and 353 K, respectively.

As shown in Figure 3.8, the spectral intensities in the low-frequency region below 50 cm^{-1} increase with increasing temperature for both cation and anions (and thus for the entire IL). Moreover, the shoulder at ~80 cm^{-1} in the cation DOS spectrum for the cation shifts to the lower frequency side with increasing temperature. The temperature-dependent spectral features of the $[C_4MIm][PF_6]$ DOS spectra qualitatively agree with the results of the fs-RIKES experiments, which is further discussed in Section 3.4.2.

3.4. Discussion

3.4.1. Fragilities of ILs.

The viscosities of ILs are well-known to change drastically with temperature.[29] Thus, it is valuable to discuss the relationship between the temperature dependence of the intermolecular vibrational dynamics and the temperature dependence of the viscosities of ILs. The behavior of the change of viscosity is represented by "fragility".[100] When liquids are cooled to their glass

transition temperature, their viscosities increase. If the liquids show Arrhenius-type behavior, they are referred to “strong” liquids: such as SiO_2. On the other hand, the liquids show non-Arrhenius-type behavior, that is, their viscosities increase rapidly near their glass transition temperature, they are referred to “fragile” liquids: such as *o*-terphenyl. The fragility can be represented by D parameter appeared in VTF fit (eq 3.1): the fragility is proportional to D^{-1}. The fragility is also depicted by so-called Angell plot,[90] that is, logarithmic scale of viscosities $\ln(\eta)$ vs the inverse of temperature normalized by glass transition temperature T_g/T, such as Figure 3.9 (vide infra).

Figure 3.9 shows the Angell plots[90] for the studied ILs with the exception of $[C_4MIm][OTf]$ and $[C_4MIm][NCyF]$, which do not exhibit glass transitions. Plots for the two extreme cases, SiO_2[101-102] and *o*-terphenyl,[103-105] which show strong and fragile features, respectively, are also shown. Figure 3.9a reveals that the studied ILs are rather fragile compared to SiO_2 but stronger than *o*-terphenyl. Furthermore, the ILs roughly show a single curve in large-scale plots (Figure 3.9a). However, careful examination of the magnified plots in Figure 3.9b shows that the curve is dependent on the nature of IL anions. The obtained data indicate that ILs containing spherical top anions are stronger than the ones containing other anions (less symmetric and flexible ones). Considering that the liquid fragility is proportional to D^{-1}, the results of this study are reasonable, indicating that more compact (smaller) anions make the corresponding imidazolium-based ILs stronger.

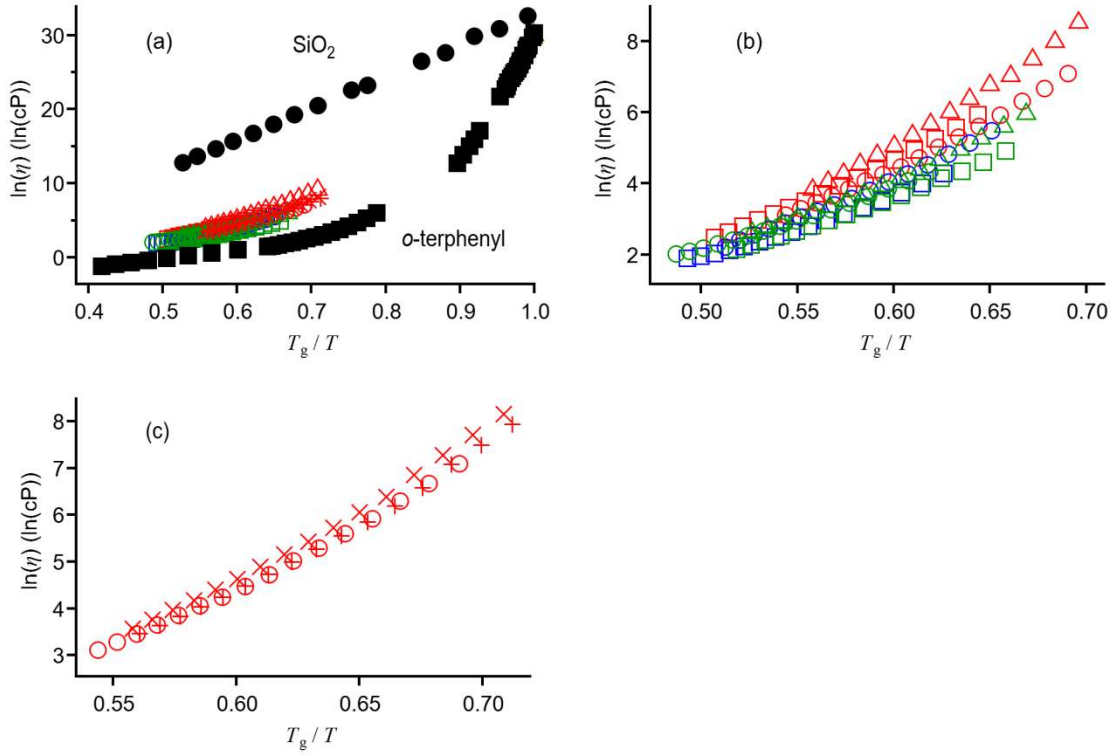

Figure 3.9. (a) Full-scale plots of ln(η) vs T_g/T. Expanded scale plots for (b) $[C_4MIm]^+$-based ILs with various anions and (c) $[PF_6]^-$ salts of 1-alkyl-3-methyl- imidazolium cations. Filled circles, SiO_2;[101-102] filled squares, *o*-terphenyl;[103-105] red circles, $[C_4MIm][PF_6]$; red squares, $[C_4MIm][BF_4]$; red triangles, $[C_4MIm]I$; blue circles, $[C_4MIm][SCN]$; blue squares, $[C_4MIm][DCA]$; green circles, $[C_4MIm][NF_2]$; green squares, $[C_4MIm][NTf_2]$; green triangles, $[C_4MIm][NPf_2]$; red pluses, $[C_6MIm][PF_6]$; red crosses, $[C_7MIm][PF_6]$.

Figure 3.9c compares the plots for $[C_4MIm][PF_6]$, $[C_6MIm][PF_6]$, and $[C_7MIm][PF_6]$ to illustrate the effect of the alkyl group attached to the cation. The differences between these ILs are not large, with $[C_7MIm][PF_6]$ being the strongest IL. The results of VTF fits in Table 3.1 show that the *D* parameter increases with the length of the IL alkyl group, indicating that longer alkyl groups result in stronger liquids because of stronger van der Waals interactions. Previously, Triolo and coworkers studied the small- to wide-angle X-ray diffraction patterns of ILs and found that the intensity in the low Q peak (attributed to the segregation structure) for imidazolium-based ILs gains intensity and shifts to lower Q for longer alkyl groups of the imidazolium cation.[35] These results indicate that the micro-segregation structures in ILs are clearer in the imidazolium-based ILs with cations having longer alkyl groups. Because the

fragility parameter is related to the dynamic heterogeneity,[106] the present results might indicate a relation between the fragility and dynamic heterogeneity of ILs.

3.4.2. Temperature Dependence of Low-Frequency Spectra.

Before to discussing the results of this study, some previous reports on the temperature dependence of the low-frequency spectra of imidazolium-based ILs studied by fs-RIKES are summarized. Quitevis and coworkers reported the temperature dependence of the *normalized* low-frequency spectra characterized by fs-RIKES for 1-methyl-3-pentylimidazolium ([C_5MIm])-based ILs with $[NTf_2]^-$,[66] bromide (Br^-), and $[PF_6]$.[67] The authors showed that the spectra of [C_5MIm]Br and [C_5MIm][PF_6] were temperature independent. However, the spectrum of [C_5MIm][NTf_2] was temperature dependent, with the spectral intensity in the high-frequency region above 60 cm^{-1} decreasing with increasing temperature. Note that normalization is performed relative to the highest peak intensity in the low-frequency spectrum, with the contribution of overdamped relaxation subtracted from the entire spectrum. The authors attributed the results to the difference in the liquid natures of the ILs, with [C_5MIm]Br and [C_5MIm][PF_6] having a larger solid-like nature, whereas [C_5MIm][NTf_2] having a more liquid-like one. At first glance, the results of Quitevis and coworkers and our group seem to be different. However, the temperature-dependent spectral features are quite similar for the *normalized* low-frequency spectra. It should be recalled that the Kerr transients are normalized with respect to the intensity at $t = 0$ before Fourier transform deconvolution analysis. Therefore, the normalized low-frequency Kerr spectra are actually renormalized. In this study, the low-frequency spectra without renormalization are discussed, as shown in Figures 3.4–6. Essentially, the temperature dependence behaviors of imidazolium-based ILs with the $[NTf_2]^-$ anion obtained by Quitevis et al. and our group are in good agreement. On the other hand, the intriguing temperature-dependent spectral features of [C_5MIm]Br and [C_5MIm][PF_6] seem to be different from the results of [C_4MIm][PF_6] in this study. The temperature-dependent spectral features of various ILs are discussed below.

3.4.2.1. Effects of Various Anions.

As shown in Figure 3.4 and Appendix C, the low-frequency Kerr spectra for all studied $[C_4MIm]^+$-based ILs with ten different anions are temperature dependent, as are the spectra of the three molecular liquids. As mentioned in Section 3.3.2, the temperature-dependent spectral features of all ILs are similar, also resembling those of 1-methylimidazole, but being clearly

different from those of propionitrile and CCl_4. These results indicate that the temperature dependence of the low-frequency spectra of the ILs is largely affected by the imidazolium ring. On the basis of this assumption, the mechanism of this temperature dependence of the low-frequency spectra of the imidazolium-based ILs is considered. The low-frequency spectral shapes of the ILs studied here are bimodal or trapezoidal, being common features of ILs based on aromatic cations with simple alkyl groups.[107] Indeed, not only aromatic-cation-based ILs, but also most aromatic molecular liquids show broad line shapes in their low-frequency spectra.[11,15,17] According to an MD simulation of liquid benzene,[18] the frequency region above 60 cm^{-1} in the low-frequency spectral bands is assigned to the librational motion of the aromatic ring. According to a recent study combining fs-RIKES experiments and MD simulations for liquid benzene at various temperatures,[108] the high-frequency portion of the low-frequency spectrum of liquid benzene (described as an antisymmetrized Gaussian function) shifts to the low-frequency side with increasing temperature, and this result is qualitatively reproduced by the MD simulation. These results show that density (free volume), and not temperature (purely thermal effect), is the dominant factor. Ratajska-Gadomska also simulated the temperature-dependent Kerr spectrum of liquid benzene based on the quasi-crystalline model, and a redshift of the high-frequency component was observed with increasing temperature.[109] As mentioned in Section 3.3.2, the spectral intensity in the high-frequency region of the intermolecular vibrational spectra of the studied ILs decreases with increasing temperature, which has also been reported for some molecular liquids.[14-15,63,65] These results indicate that the librational motion of the imidazolium ring becomes slower with increasing temperature, probably due to the increase in the IL free volumes, which increases the libration displacement magnitude and weakens the intermolecular interactions (thus making the librational motion slower). Note that unlike the diffusion process, the vibrational motion (e.g., harmonic oscillator) becomes slower (or lower in the frequency region) with weakening of the intermolecular interaction.

On the other hand, several different types of molecular motions, such as translational motion, rotational motion, and their cross-term, contribute to the spectral density in the low-frequency region below ~50 cm^{-1}.[18] Moreover, the crossover process from the intermolecular vibrational motions to the collective structural relaxation also contribute to this frequency region.[50,106] As seen in Figure 3.4 and Appendix C, the spectral intensity in the low-frequency region of the IL low-frequency spectra increases with increasing temperature, attributed to the activation (less hindrance) of translational motions of ions with increasing temperature, which makes the caging effect weaker. In fact, some studies describe the influences of the translational

motions on the low-frequency region of the intermolecular vibrational band.[23,52,61,110-111] The spectra of $[C_4MIm]^+$-based ILs with $[XF_6]^-$ anions showed that the intensities in the frequency region below 20 cm^{-1} decrease when $[PF_6]^-$ is substituted with heavier anions, $[AsF_6]^-$ and $[SbF_6]^-$.[52] This is attributed to the lesser activation of the interaction-induced motions in $[C_4MIm][AsF_6]$ and $[C_4MIm][SbF_6]$ than $[C_4MIm][PF_6]$.[52,61] Another helpful case is the comparison of the spectra of polymer, oligomer, and monomer solutions. It is reported that the spectral intensities in the low-frequency region of the intermolecular vibrational spectra of polymer and oligomer solutions are lower than those of the corresponding monomer solutions, which is consistent with their mass.[23,110-111] These results suggest that the increases of intensity in the low-frequency region with increasing temperature are accounted for by the activation of the interaction-induced (translational) motions.

To provide more details for the temperature-dependent spectral features of the low-frequency spectra, Figure 3.10 shows the difference spectra for 308, 323, 338, and 353 K relative to the spectra at 293 K for (a) $[C_4MIm][BF_4]$, (b) $[C_4MIm][NTf_2]$, (c) $[C_4MIm][SCN]$, (d) $[C_4MIm][DCA]$, (e) 1-methylimidazole, and (f) propionitrile. The difference spectra for the other ILs studied here are provided in Appendix C. $[C_4MIm][BF_4]$ and $[C_4MIm][NTf_2]$ display representative difference spectra, showing a large increase in the low-frequency (~5 cm^{-1}) region, a slight increase in the intermediate-frequency (~50 cm^{-1}) region, and a decrease in the high-frequency (~110 cm^{-1}) region. The temperature dependence of the difference spectra for 1-methylimidazole is close to that for the ILs, indicating that the librational motion activity decreases and the translational motion and/or the cross-term increases with rising temperature. Thus, the effect of temperature on the low-frequency Kerr spectra of the imidazolium-based ILs is largely attributed to the motion of the imidazolium ring. However, two specific features are found for the temperature dependence of the difference spectra upon closer examination.

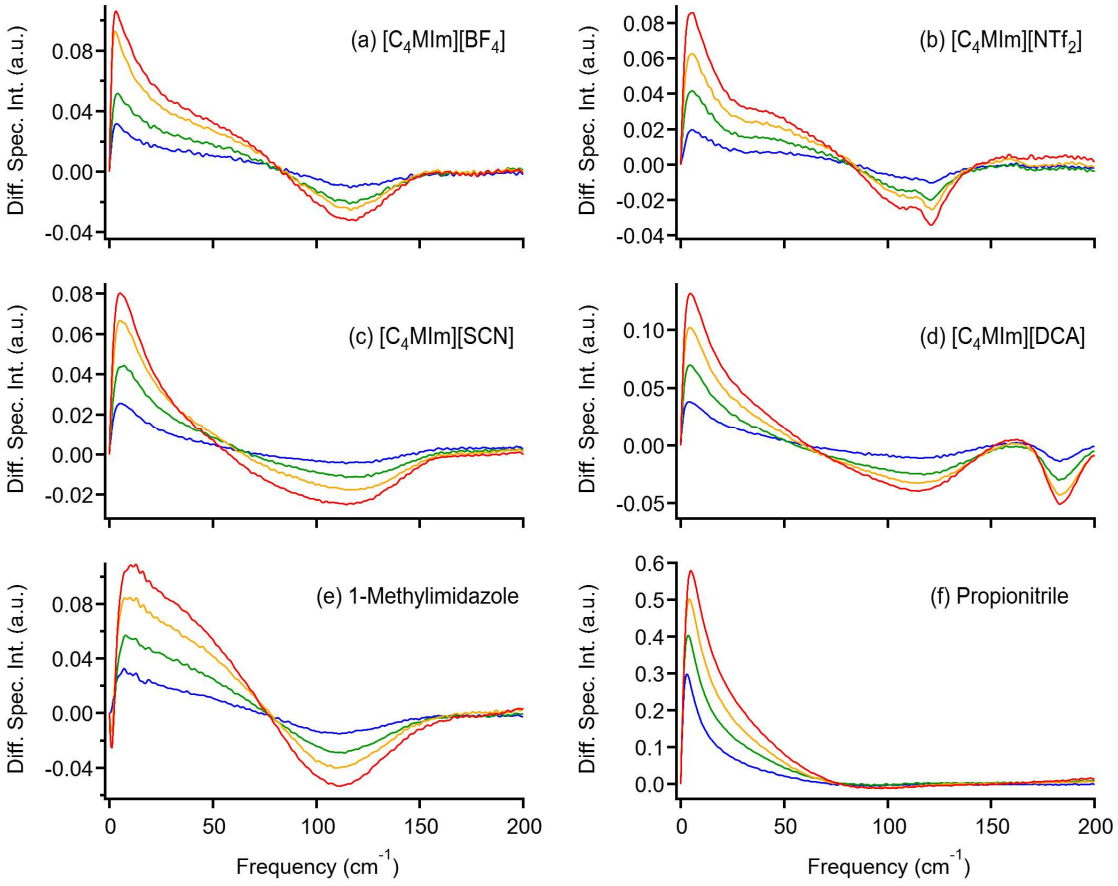

Figure 3.10. Difference Kerr spectra of (a) [C_4MIm][BF_4], (b) [C_4MIm][NTf_2], (c) [C_4MIm][SCN], (d) [C_4MIm][DCA], (e) 1-methylimidazole, and (f) propionitrile for the spectra at 308 (blue), 323 (green), 338 (yellow), and 353 (red) K relative to those at 293 K.

First, the ILs show a steeper intensity change in the ~5 cm^{-1} frequency region with increasing temperature than 1-methylimidazole. Moreover, the changes observed for ILs are more similar to those detected for the smaller propionitrile than for the larger and planar 1-methylimidazole. This indicates that the anions also contribute to the temperature-dependent spectrum in the ~5 cm^{-1} frequency region. One can think that the spherical top anions contribute to the Kerr spectra very weakly. As shown in Figure 3.6, a low-frequency spectral band with a peak at ~15 cm^{-1} without the strong spectral density in the high-frequency region is observed in liquid CCl_4. It is thus plausible that the temperature effect in the low-frequency (~5 cm^{-1}) region features the contributions of both IL cations and anions.

Next, on comparing the difference spectra of [C_4MIm][BF_4] and [C_4MIm][NTf_2] with those of [C_4MIm][SCN] and [C_4MIm][DCA], a clear dissimilarity is found in the intermediate-frequency (~50 cm^{-1}) region. This would be attributed to the librational motions of the $[SCN]^-$

and $[DCA]^-$ anions. These anions are expected to contribute to the Kerr spectra in large because they do not have spherical top symmetry. Thus, their contributions might lie in the intermediate-frequency region, and shift to a lower frequency with increasing temperature, similarly to the librational motions of the imidazolium ring. Notably, many nonaromatic aprotic molecular liquids show large spectral densities in the frequency range of approximately 5–80 cm^{-1}, which is lower than those of aromatic molecular liquids.[17] Accordingly, it is not surprising that the decrease in the spectral intensities with increasing temperature in the intermediate-frequency region is observed for the imidazolium-based ILs with nonspherical top anions that probably exhibit strong Kerr activities. The effects of these anions on temperature-dependent features will be further discussed in the case of pyrrolidinium-based ILs (Chapter 5).

On the other hand, it is surprising that the ILs with anions having two stable conformers, that is, $[NF_2]^-$, $[NTf_2]^-$, and $[NPf_2]^-$, show the temperature dependence of M_1 (slope) (Figure 3.7 and Table 3.2) and the difference spectra (Figure 3.10) similar to those of ILs with spherical top anions and 1-methylimidazole. This could be caused by the frequency of the anion vibrational motions. Because the librational motions of these anions are in the low-frequency region of ~20 cm^{-1},[54,71] the dissimilarity in the difference spectra caused by anions should also appear in this frequency region but not the intermediate-frequency region of ~50 cm^{-1}. Furthermore, M_1 should be more sensitive to the spectral change in the high-frequency region than in the low-frequency region. As a result, the temperature dependence of M_1 and the difference spectra of $[C_4MIm][NF_2]$, $[C_4MIm][NTf_2]$, and $[C_4MIm][NPf_2]$ are similar to those of the ILs with spherical top anions and 1-methylimidazole.

3.4.2.2. Effect of Alkyl Groups Attached to the Imidazolium Cation.

As seen in Section 3.4.2.1, the temperature-dependent spectral features of the imidazolium-based ILs including $[C_4MIm][PF_6]$ are clearly observed. It seems that the results are different from the results of $[C_5MIm][PF_6]$ reported by Xiao et al.[67] One can think that different alkyl groups attached to the imidazolium cation result in different temperature dependence of the low-frequency spectra of ILs. As shown in Figure 3.5, however, the temperature-dependent spectral features of $[C_4MIm][PF_6]$, $[C_6MIm][PF_6]$, and $[C_7MIm][PF_6]$ are quite similar. To be more specific, Figure 3.11 shows the difference spectra at 308, 323, 338, 353 K in relation to those at 293 K for (a) $[C_4MIm][PF_6]$, (b) $[C_6MIm][PF_6]$, and (c) $[C_7MIm][PF_6]$. The above figure reveals that all ILs show a similar temperature dependence of the difference spectra, with the intensity in the high-frequency region above ~80 cm^{-1}

decreasing and the intensity in the low-frequency region below ~70 cm^{-1} increasing with increasing temperature. Accordingly, it is concluded from the present results that the alkyl groups of the imidazolium cation do not significantly influence the temperature dependence of the low-frequency spectra.

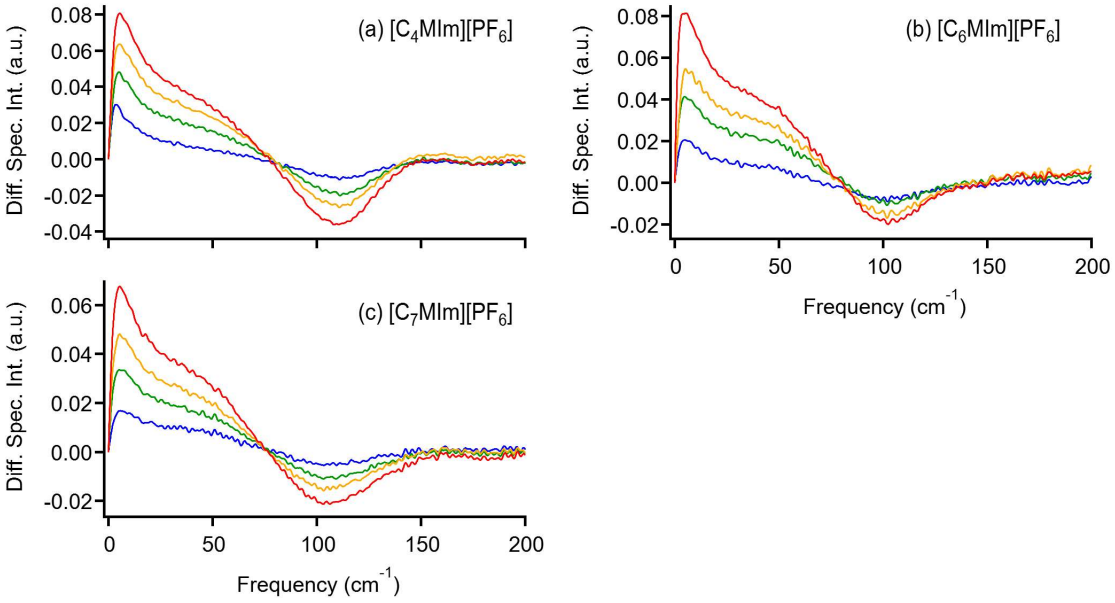

Figure 3.11. Difference Kerr spectra of (a) $[C_4MIm][PF_6]$, (b) $[C_6MIm][PF_6]$, and (c) $[C_7MIm][PF_6]$ for the spectra at 308 (blue), 323 (green), 338 (yellow), and 353 (red) K relative to those at 293 K.

As mentioned in the introduction of Section 3.4, the temperature-independent low-frequency Kerr spectrum of $[C_5MIm][PF_6]$ has previously been reported.[67] Although the reported sample was not exactly identical to the ILs used in the present study, the results for $[C_5MIm][PF_6]$ somewhat disagree with those obtained for $[C_4MIm][PF_6]$, $[C_6MIm][PF_6]$, and $[C_7MIm][PF_6]$. One might think that $[C_5MIm][PF_6]$ is an exception in the series of 1-alkyl-3-methylimidazolium hexafluorophosphates. However, several possible reasons would explain this inconsistency. The first one is the difference in the signal-to-noise ratios between the spectra of $[C_5MIm][PF_6]$ and the other ILs, $[C_4MIm][PF_6]$, $[C_6MIm][PF_6]$, and $[C_7MIm][PF_6]$. The signal-to-noise ratio in the spectra of $[C_4MIm][PF_6]$, $[C_6MIm][PF_6]$, and $[C_7MIm][PF_6]$ is higher than that of $[C_5MIm][PF_6]$, explaining the small differences in their spectra, such as those in the frequency region above 80 cm^{-1} for $[C_4MIm][PF_6]$, $[C_6MIm][PF_6]$, and $[C_7MIm][PF_6]$ (Figure 3.5). The second reason is the renormalization of the $[C_5MIm][PF_6]$

spectra.[67] If we consider the renormalized low-frequency spectra of $[C_6MIm][PF_6]$ and $[C_7MIm][PF_6]$, the spectral intensity difference in the low-frequency region below 50 cm^{-1}, which is clearly observed in the non-renormalized spectra in Figure 3.5, is expected to be small. Finally, the effect of the overdamped relaxation component provides the third reason to explain the observed behavior. The overdamped relaxation components over several picoseconds are excluded in the spectra of $[C_4MIm][PF_6]$, $[C_6MIm][PF_6]$, and $[C_7MIm][PF_6]$, whereas the subpicosecond components are removed in the case of $[C_5MIm][PF_6]$.[67] These differences between the spectra of $[C_5MIm][PF_6]$ and the other ILs, $[C_4MIm][PF_6]$, $[C_6MIm][PF_6]$, and $[C_7MIm][PF_6]$, probably lead to the different temperature-dependent spectral features. I therefore conclude that the renormalization of spectra measured by fs-RIKES introduces ambiguity into their temperature sensitivity, and the inconsistency in the temperature dependence of the low-frequency spectra between $[C_5MIm][PF_6]$ and $[C_4MIm][PF_6]$, $[C_6MIm][PF_6]$, and $[C_7MIm][PF_6]$ is probably due to these three possibilities.

3.4.2.3. Comparison of Experimental Kerr Spectra and Calculated DOS Spectra.

In contrast to sharp intramolecular vibrational modes, assigning broadened low-frequency spectra of liquids is not straightforward, because the low-frequency band includes different kinds of motions, such as translational and reorientational motions and their coupling motions. ILs show an even more complicated behavior, being composed of different species, that is, cations and anions. MD simulations are good at clarifying them. Herein, the temperature-dependent Kerr spectrum of $[C_4MIm][PF_6]$ with its temperature-dependent DOS spectrum is compared to elucidate the origin of the temperature-sensitive features in the low-frequency Kerr spectra.

A comparison of the Kerr spectra (Figure 3.5a) and DOS spectra (Figure 3.8a) of $[C_4MIm][PF_6]$ shows that their line shapes are quite different. As mentioned above, this likely arises from the difference in the selection rules between the spectra. Considering the polarizability anisotropies of the cation and anion,[52] the contribution of the cation to the intensity in the Kerr spectrum is expected to be much larger than that of the anion. It is thus reasonable that the Kerr spectrum (Figure 3.5a) of $[C_4MIm][PF_6]$ is more similar to the DOS spectrum of $[C_4MIm]^+$ (Figure 3.8b) rather than to that of $[C_4MIm][PF_6]$ (Figure 3.8a) or $[PF_6]^-$ (Figure 3.8c).

The focus of this study is the temperature dependence of spectra. The DOS spectra of $[C_4MIm]^+$ and $[PF_6]^-$ in Figure 3.8 show that the intensities in the ~30 cm^{-1} frequency region

increases with increasing temperature in both cases. As a result, the intensity in the ~30 cm^{-1} region for the entire $[C_4MIm][PF_6]$ DOS spectrum also increases at higher temperatures. This behavior agrees well with the temperature-dependent feature in the low-frequency region of the Kerr spectrum shown in Figure 3.5. Therefore, the MD simulations indicate that the temperature-dependent spectral change in the low-frequency region is actually attributable to both cation and anion species. On the other hand, the temperature-related changes in the high-frequency region (> 70 cm^{-1}) of the Kerr spectrum are quite similar to those of the DOS spectrum of $[C_4MIm]^+$, however, this feature is not reproduced in the DOS spectrum of $[PF_6]^-$. This is in good agreement with the assignment mentioned above. Accordingly, the temperature-dependent features of the low-frequency Kerr spectrum of $[C_4MIm][PF_6]$ are well accounted for by the results of MD simulations.

3.4.3. Fragility and Temperature Dependence of the Low-Frequency Spectrum.

In the last section, I would like to make a brief comment on the relation between the temperature dependence of the low-frequency spectra and the fragilities of ILs, because I believe that it is important to understand/determine the effect of intermolecular vibrations on the nature of liquid fragility. The temperature dependence degree of the low-frequency Kerr spectra (Table 3.2) and the values of the fragility-related parameter *D* (Table 3.1) for the studied ILs are hard to correlate. For example, ILs with spherical top anions show larger *D* values than the other ones, but the temperature dependence degrees of their low-frequency Kerr spectra are quite similar to those of several ILs with flexible anions ($[N(SO_2C_nF_{2n+1})_2]^-$: n = 0–2), $[NCyF]^-$, and $[OTf]^-$, and even to that of a molecular liquid, 1-methylimidazole. The *D* values seem to be dependent on the alkyl group length for the imidazolium cation in 1-alkyl-3-methylimidazolium hexafluorophosphates, but not on the temperature dependence degree of the low-frequency Kerr spectra. This suggests that caging motion such as libration does not directly influence the fragility of ILs to a large extent. Slower relaxation processes, such as the so-called α-relaxation (structural relaxation), that represent motions on a larger space (length) scale than the intermolecular vibration might be more appropriate for comparison with the fragility parameter. In fact, Ribeiro pointed out that the temperature-dependent intensity of the quasi-elastic scattering, which is mainly due to the contribution of the relaxational component rather than to that of intermolecular vibrations, is related to the fragility parameter for some ILs.[112]

3.5 Conclusions

In this study, the temperature dependence of the low-frequency spectra of imidazolium-based ILs with ten different anions is investigated by fs-RIKES. The spectral intensities in the frequency region below 20 cm^{-1} increase with increasing temperature due to the activation of the translational vibrational motions of IL ions at higher thermal energies. In addition, the spectra in the high-frequency region above 80 cm^{-1} shift to lower-frequency side with increasing temperature, attributed to the slower librational motion of the imidazolium ring due to the larger free volume and the weaker intermolecular interaction at higher temperatures. The results of the DOS spectra calculated for $[C_4MIm][PF_6]$ by MD simulation support the assignments of the temperature-dependent spectral features for the imidazolium-based ILs.

The difference between the spectra of ILs at certain temperatures and at 293 K revealed the temperature-dependent spectral features in greater detail. The temperature dependence of the difference spectra for 1-methylimidazole is rather similar to those for the ILs, suggesting that the effect of temperature on the low-frequency Kerr spectra of the imidazolium-based ILs is largely due to the motions of the imidazolium cation. However, $[C_4MIm][SCN]$ and $[C_4MIm][DCA]$ showed the difference from those of other ILs and 1-methylimidazole, with the difference spectral density in the intermediate-frequency region (~50 cm^{-1}) of these two ILs being distinguishable from that of other ILs, attributed to the librational motions of $[SCN]^-$ and $[DCA]^-$ anions. In fact, the temperature dependence degrees of the low-frequency spectra (that is the slope for the first moment of the spectrum to the temperature) of the ILs are in good agreement with the features of the difference spectra.

The temperature dependence of viscosities and the glass transition temperatures of the ILs were also estimated. On the basis of these physical properties and VTF fits, the fragility-related parameters (D parameter for the VTF fit) of the ILs were determined. The D parameter was particularly large for ILs with spherical top anions, as compared to those with other anions. It is also found that the D value increases for the longer alkyl groups of the IL imidazolium cations. On the other hand, there is no clear direct relationship between D and the temperature dependence of M_1 for the low-frequency spectrum of the studied ILs.

Chapter 4

Effects of Cations Species on Temperature-Dependent Low-Frequency Spectra: Imidazolium, Pyridinium, Pyrrolidinium, Ammonium, and Phosphonium Cations

J. Phys. Chem. B, **2018**, *122*, 6033–6047.

4.1. Introduction

The representative cations of ILs can be broadly classified into two groups: aromatic cations and nonaromatic cations. The physical and chemical properties of aromatic and nonaromatic cation based ILs differ in several ways. For example, the viscosities of aromatic cation based ILs are generally lower than those of nonaromatic cation based ILs with similar cations' formula weights and the same anions.[29] Although the electric conductivities of aromatic cation based ILs are higher than those of nonaromatic cation based ILs, the electrochemical potential windows of nonaromatic cation based ILs are larger than those of aromatic cation based ILs.[113] The microscopic structures of aromatic cation based ILs also exhibit greater spatial inhomogeneity than nonaromatic cation based ILs.[114]

In addition to their physical properties, aromatic and nonaromatic cation based ILs also present differences in their intermolecular vibrations.[53,115] The low-frequency Kerr spectra of aromatic cation based ILs are generally broader than those of nonaromatic cation based ILs.[53] This can be explained by the librational motions of the aromatic ring, which create additional components in the high-frequency region at about 100 cm^{-1}. In addition, the relationships between the low-frequency spectra and bulk properties of aromatic and nonaromatic cation based ILs are different.[53] Linear correlations between the first moment of the intermolecular vibration band and the square root of the surface tension divided by the density have been found in ILs, as well as in aprotic molecular liquids.[17] However, the first moments of aromatic cation based ILs are more insensitive to changes in the bulk properties than those of nonaromatic cation based ILs, although aromatic and nonaromatic molecular liquids do not exhibit such a difference. This is attributed to the microheterogeneity of ILs; that is, aromatic cation based ILs are more segregated at the molecular level than the respective nonaromatic cation based ILs,[114] and thus the information from the ionic region is more reflected in the low-frequency Kerr spectra than nonaromatic cation based ILs, which causes the differences in the correlations between the low-frequency Kerr spectra and the bulk properties.

In this chapter, the temperature dependence of the low-frequency spectra of standard ILs with representative cation structures using fs-RIKES is investigated. As samples, $[NTf_2]^-$ salts of 1-butyl-3-methylimidazolium ($[C_4MIm]^+$), 1-butyl-1-methyl- pyrrolidinium ($[Pyrr_{14}]^+$), 1-butylpyridinium ($[C_4Py]^+$), butyldiethylmethylammonium ($[N_{1224}]^+$), triethyloctylammonium ($[N_{2228}]^+$), and triethyloctylphosphonium ($[P_{2228}]^+$) cations, as shown in Figure 4.1. The main purpose of this study is to clarify how the differences in the structure of the cations of the ILs affect the temperature-dependent features of their low-frequency spectra. The universal and

structurally-dependent features of the temperature dependence of the low-frequency spectra are investigated on the basis of comparisons between (i) (aromatic) imidazolium and (nonaromatic) pyrrolidinium cations, (ii) imidazolium and pyridinium cations, (iii) (cyclic) pyrrolidinium and (branched) ammonium cations, (iv) ammonium cations with different alkyl groups of different lengths, and (v) ammonium and phosphonium cations. I have further searched the temperature-dependent low-frequency spectra of the molecular liquids: 1-methylimidazole, pyridine, 1-methylpyrrolidine, and butyldiethylamine, which are neutral analogues of the cations of the studied ILs. In addition, the fragility parameters of the ILs on the basis of measured temperature-dependent viscosities are estimated.

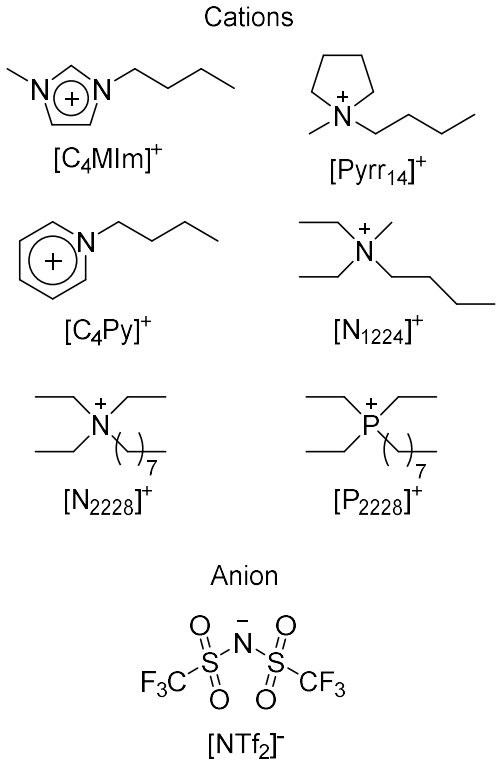

Figure 4.1. Structural formulas of the cations and anion of the ILs used in this study.

4.2. Experimental Section

$[C_4MIm][NTf_2]$ was purchased from Kanto Chemical and used as received. $[C_4Py][NTf_2]$, $[N_{2228}][NTf_2]$, and $[P_{2228}][NTf_2]$ were the same as previously used.[56,116] $[Pyrr_{14}][NTf_2]$ and $[N_{1224}][NTf_2]$ were synthesized according to the similar procedure.[56,116] The synthesized ILs were confirmed by ^1H NMR and elemental analysis measurements. Detailed synthetic procedures and assignments for these ILs are described Appendix A. The water contents of the

[C_4MIm][NTf_2], [$Pyrr_{14}$][NTf_2], [C_4Py][NTf_2], [N_{1224}][NTf_2], [N_{2228}][NTf_2], and [P_{2228}][NTf_2] were 16.5, 58.5, 19.6, 27.4, 41.4, and 29.9 ppm, respectively. The sample ILs were dried in vacuo for more than 36 h prior to measurements. 1-Methylimidazole (Aldrich) and pyridine (Wako) were used as received. 1-Methylpyrrolidine (TCI) and butyldiethylamine (Aldrich) were used after distillation.

4.3. Results and Discussion

4.3.1. Temperature Dependent Low-Frequency Spectra.

Figure 4.2 shows the Kerr transients of the ILs at 293, 308, 323, 338, and 353 K. They are the first reports of the temperature-dependent Kerr transients (and, of course, the Kerr spectra, vide infra) for the present ILs, except for [C_4MIm][NTf_2] that was previously reported by us.[117] Figure 4.2 shows that the Kerr transients for all of the present ILs are clearly temperature-dependent. Namely, the amplitude of the picosecond overdamped relaxation process increases with increasing temperature, while the valleys in the early time region (faster than 1 ps), which are due to the underdamped intramolecular and intermolecular vibrational modes, become shallower with rising temperature. The picosecond overdamped decays were analyzed using a biexponential function. The biexponential fit parameters are summarized in Table 4.1. The time constants were almost independent of temperature within the experimental errors and the fitting standard deviations, while the amplitudes for all the components increased with rising temperature.

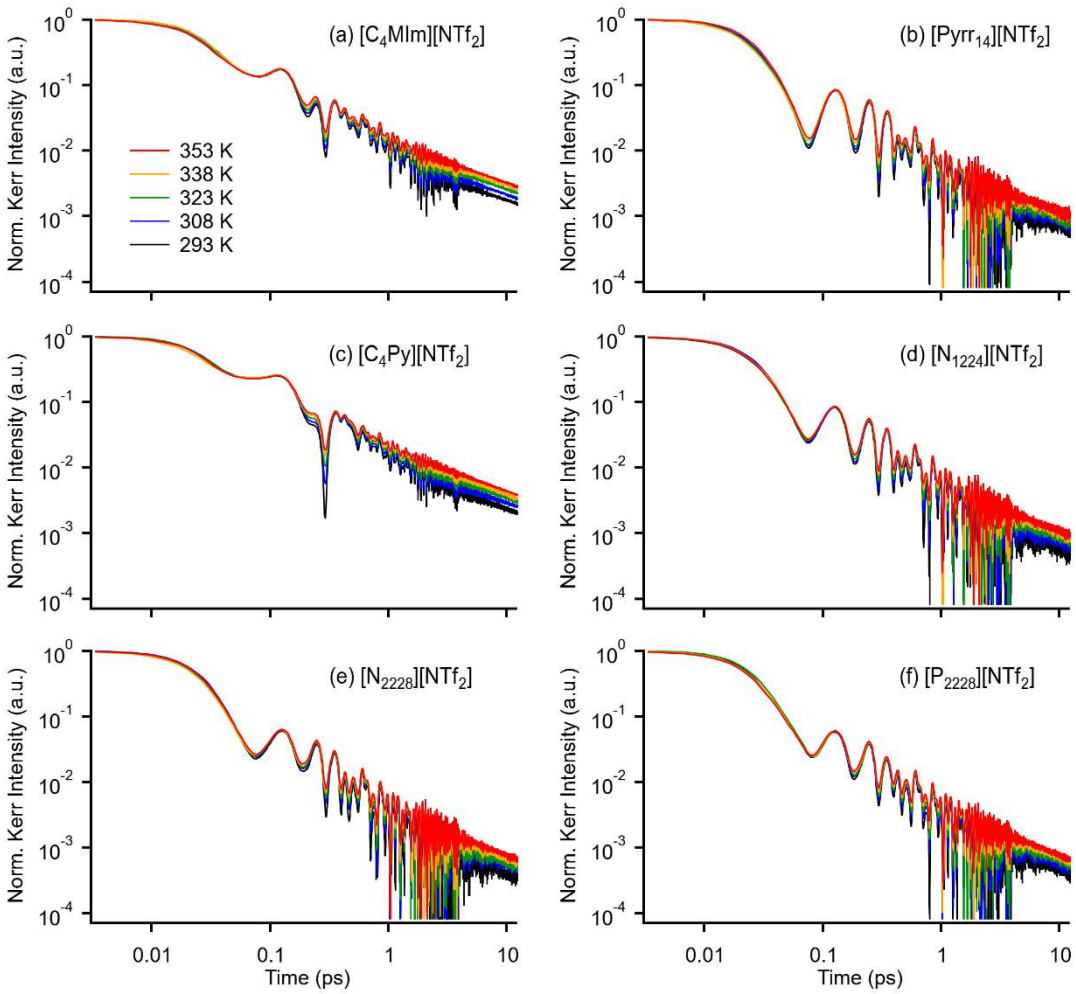

Figure 4.2. Log–log plots of Kerr transients for (a) $[C_4MIm][NTf_2]$, (b) $[Pyrr_{14}][NTf_2]$, (c) $[C_4Py][NTf_2]$, (d) $[N_{1224}][NTf_2]$, (e) $[N_{2228}][NTf_2]$, and (f) $[P_{2228}][NTf_2]$ at 293 K (black), 308 K (blue), 323 K (green), 338 K (yellow), and 353 K (red).

Table 4.1. Biexponential Fit Parameters for Kerr Transients of ILs at Various Temperatures

temperature (K)	a_0	a_1	τ_1 (ps)	a_2	τ_2 (ps)
		$[C_4MIm][NTf_2]$			
293	0.0009	0.0103	1.30	0.0030	8.24
308	0.0010	0.0134	1.20	0.0038	8.17
323	0.0012	0.0121	1.32	0.0045	8.23
338	0.0014	0.0120	1.36	0.0051	8.23
353	0.0015	0.0144	1.33	0.0058	8.29
		$[Pyrr_{14}][NTf_2]$			
293	0.0004	0.0101	0.93	0.0014	7.01
308	0.0004	0.0102	0.95	0.0017	6.91
323	0.0004	0.0109	0.94	0.0020	6.98
338	0.0006	0.0116	1.00	0.0021	6.84
353	0.0007	0.0126	0.94	0.0025	6.47
		$[C_4Py][NTf_2]$			
293	0.0012	0.0138	1.26	0.0044	7.18
308	0.0016	0.0159	1.26	0.0052	7.17
323	0.0020	0.0152	1.37	0.0060	7.14
338	0.0020	0.0203	1.22	0.0077	7.30
353	0.0023	0.0172	1.38	0.0082	7.20
		$[N_{1224}][NTf_2]$			
293	0.0002	0.0192	0.75	0.0014	6.85
308	0.0003	0.0230	0.78	0.0015	7.57
323	0.0004	0.0185	0.82	0.0019	6.79
338	0.0004	0.0251	0.77	0.0023	6.94
353	0.0005	0.0224	0.82	0.0024	7.21
		$[N_{2228}][NTf_2]$			
293	0.0002	0.0079	0.80	0.0009	7.03
308	0.0003	0.0106	0.78	0.0011	6.92
323	0.0003	0.0141	0.79	0.0012	7.11
338	0.0003	0.0137	0.82	0.0015	7.38
353	0.0004	0.0145	0.83	0.0017	7.21
		$[P_{2228}][NTf_2]$			
293	0.0003	0.0095	0.78	0.0010	6.52
308	0.0003	0.0095	0.80	0.0012	6.72
323	0.0004	0.0112	0.77	0.0014	5.89
338	0.0004	0.0136	0.71	0.0018	5.27
353	0.0004	0.0148	0.72	0.0020	5.46

The Fourier transform Kerr spectra of the ILs, resolved up to 600 cm^{-1}, are shown in Figure 4.5. Note that the contributions of the overdamped relaxation (the slower component and the offset of the biexponential fits) have been subtracted from the spectra in order to focus on the intermolecular vibrations. The spectra obtained at 293 K are similar to previously reported ones.[51,56,71,116] The vibrational bands in the range 250–370 cm^{-1} were assigned to the rocking of CF_3 and the twisting/wagging/rocking motions of the SO_2 groups of $[NTf_2]^-$.[118] A close examination of Figure 4.4 reveals some differences between $[C_4MIm][NTf_2]$, $[P_{2228}][NTf_2]$, and the other ILs, which will be discussed in Section 4.1.7.

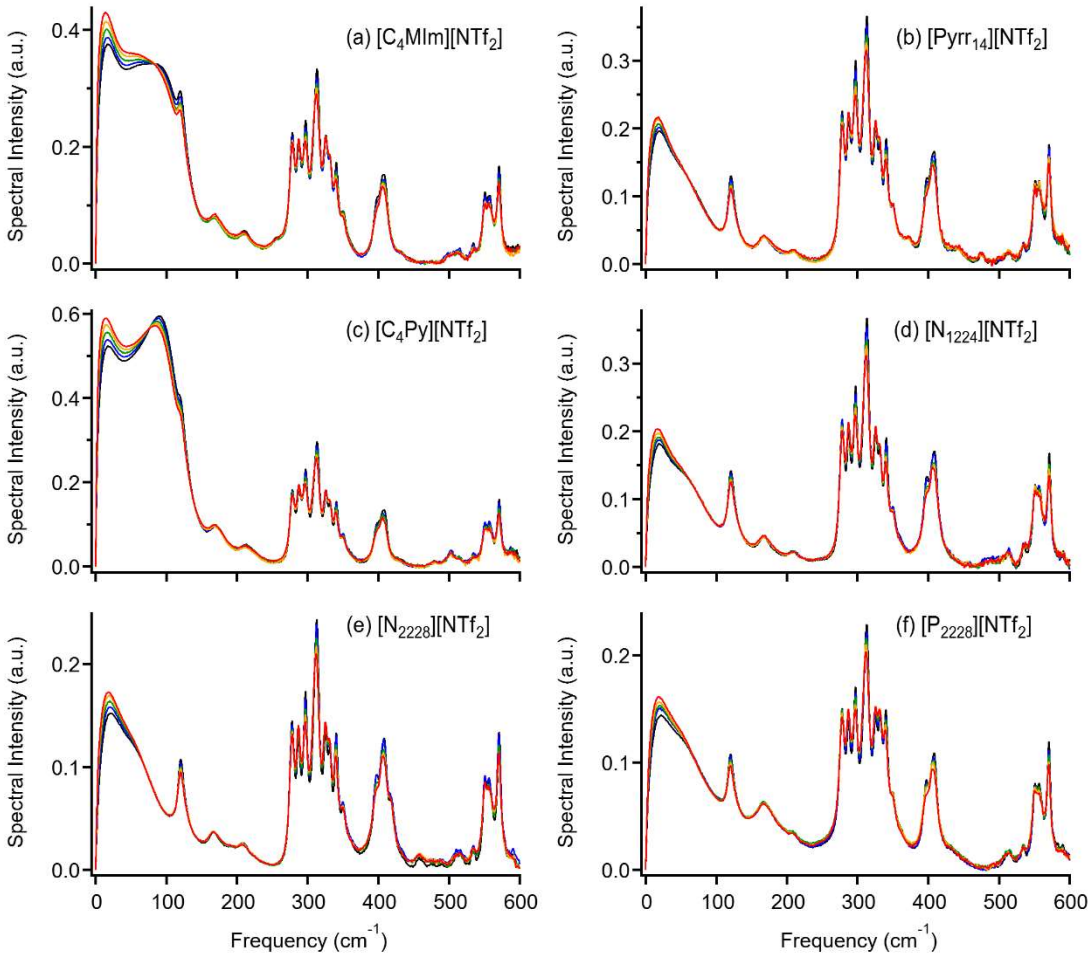

Figure 4.3. Low-frequency Kerr spectra in the frequency range of 0–600 cm^{-1} for (a) $[C_4MIm][NTf_2]$, (b) $[Pyrr_{14}][NTf_2]$, (c) $[C_4Py][NTf_2]$, (d) $[N_{1224}][NTf_2]$, (e) $[N_{2228}][NTf_2]$, and (f) $[P_{2228}][NTf_2]$ at 293 K (black), 308 K (blue), 323 K (green), 338 K (yellow), and 353 K (red).

Figure 4.4 displays the magnifications of the Fourier transform Kerr spectra of the ILs in the frequency range of 0–200 cm^{-1}. The broad band in this low-frequency region for each IL

was attributed mainly to intermolecular vibration, although clear intramolecular vibrational bands are observed at ca. 121 and 168 cm^{-1}. All of the present ILs showed temperature-dependent low-frequency Kerr spectra. However, their temperature-dependent features were unique. The temperature-dependent low-frequency spectral features will be discussed on the basis of the structures of the cations in the following section.

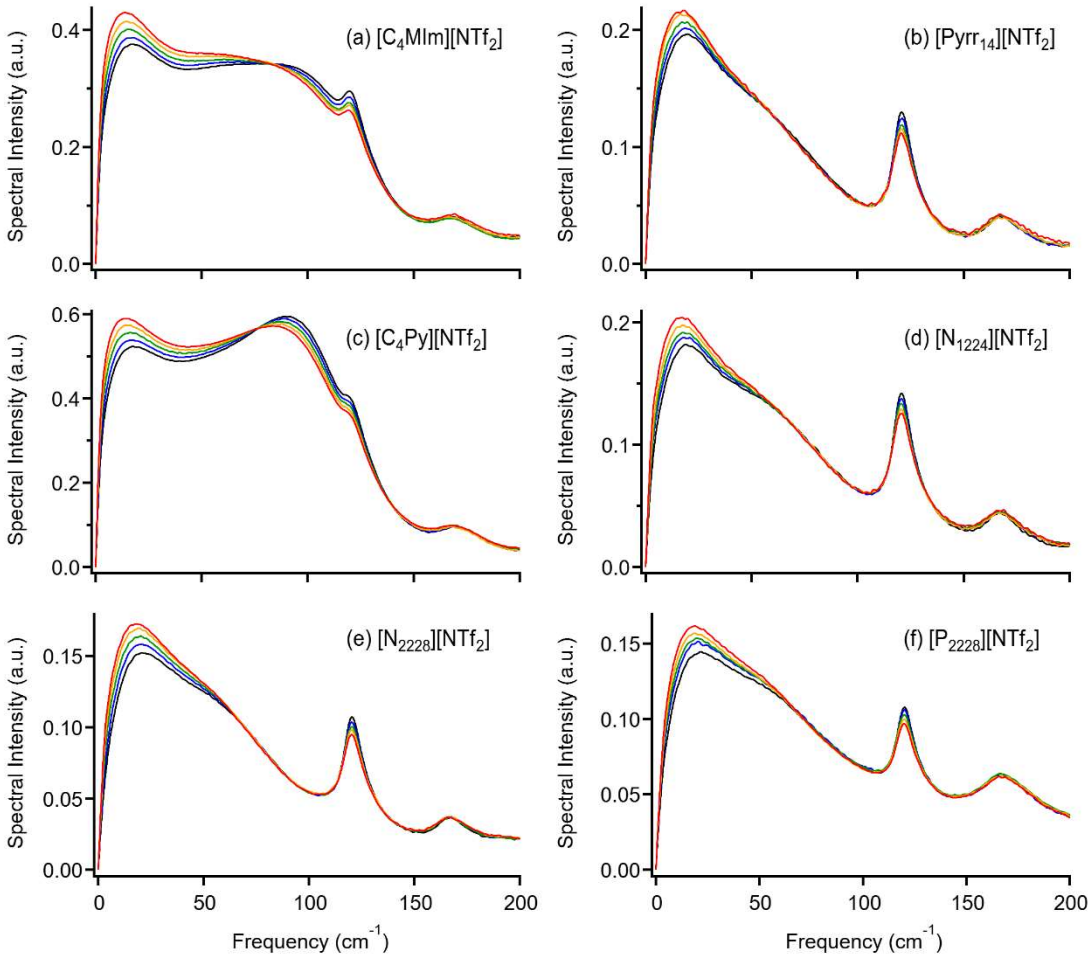

Figure 4.4. Low-frequency Kerr spectra in the frequency range of 0–200 cm^{-1} for (a) $[C_4MIm][NTf_2]$, (b) $[Pyrr_{14}][NTf_2]$, (c) $[C_4Py][NTf_2]$, (d) $[N_{1224}][NTf_2]$, (e) $[N_{2228}][NTf_2]$, and (f) $[P_{2228}][NTf_2]$ at 293 K (black), 308 K (blue), 323 K (green), 338 K (yellow), and 353 K (red).

4.3.1.1. Imidazolium Cation vs Pyrrolidinium Cation.

As shown in Figure 4.4a and b, the spectral line shapes of $[C_4MIm][NTf_2]$ and $[Pyrr_{14}][NTf_2]$ at room temperature (293 K) are very different, although both cations are based on five-membered-rings. $[C_4MIm][NTf_2]$ shows a bimodal spectrum at each temperature, while $[Pyrr_{14}][NTf_2]$ exhibits a triangular line shape. This difference can be accounted for by the

presence or absence of an aromatic ring, which gives a large contribution in the high-frequency region at ca. 100 cm^{-1}. Such broad (and often trapezoidal) low-frequency spectral line shapes are commonly observed not only in ILs but also in molecular liquids.[15,17,63,68,119-122] Several MD simulations indicated that the aromatic ring librations (reorientational motions) in aromatic cation based ILs[61-62] and aromatic molecular liquids[13,18,92,123] contribute strongly to the whole low-frequency spectra but the contributions of the collision (or interaction) induced motions (translational motions) are only in the lower frequency region. Because the aromatic ring libration is a molecular reorientational vibration, the spectral density is well correlated with the molecular polarizability anisotropy.[122] Therefore, the spectral densities of aromatic ILs and molecular liquids in the high frequency region, which exhibit bimodal or trapezoidal spectral line shapes, are mainly due to the aromatic ring librations.

Figure 4.4a and b also shows that the temperature-dependent spectral features of $[C_4MIm][NTf_2]$ and $[Pyrr_{14}][NTf_2]$ differ. In the case of $[C_4MIm][NTf_2]$, the spectral intensities in the low-frequency region below 50 cm^{-1} increase with increasing temperature, while those in the high-frequency region at approximately 100 cm^{-1} decrease or are shifted to lower frequency with rising temperature. This type of temperature dependence has been observed for imidazolium cation based ILs with various anions (Chapter 3). The spectral change in the low-frequency region is due to the activation of the translational motions of both the cation and anion with increasing temperature, while that in the high-frequency region is mainly due to imidazolium ring librations, which slow with increasing temperature because the free volume of the ILs becomes larger and the intermolecular interactions weaken. The spectral change in the high frequency region with temperature is due to the temperature sensitivity of the aromatic ring libration, but the change in the low-frequency region includes the contributions of both the anion and cation.

On the other hand, in the case of $[Pyrr_{14}][NTf_2]$, the spectral intensity in the low-frequency region (below 50 cm^{-1}) increases with rising temperature, while that of the high-frequency region (above 50 cm^{-1}) is nearly insensitive to temperature. As mentioned above, the aromatic ring contributes to the temperature-dependent spectral change in the high-frequency region. Therefore, the presence or absence of an aromatic ring determines whether temperature-dependent features are observed in the high frequency region of the low-frequency spectra of the ILs.

In the frequency region below 50 cm^{-1}, an increase in the spectral density with increasing temperature was observed for both the aromatic cation containing IL $[C_4MIm][NTf_2]$ and the

nonaromatic [$Pyrr_{14}$][NTf_2], as shown in Figure 4.4a and b. As discussed above, this was attributed to the thermal activation of the translational motions of the ion species. In this study, I determined that this temperature-dependent spectral feature is common to both aromatic and nonaromatic ILs with simple linear alkyl groups.

4.3.1.2. Imidazolium Cation vs Pyridinium Cation.

As seen in Figure 4.4a and c, the spectral line shapes of [C_4MIm][NTf_2] and [C_4Py][NTf_2] are different at all of the measured temperatures. The spectral intensity of [C_4Py][NTf_2] in the high-frequency region at ca. 80–100 cm^{-1} relative to the low-frequency region at ca. 20 cm^{-1} is greater than that of [C_4MIm][NTf_2] at all temperatures. This was attributed to the greater polarizability anisotropy of $[C_4Py]^+$ compared to that of $[C_4MIm]^+$.[54]

The temperature-dependent spectral features of both ILs are quite similar. As stated in section 4.3.1.1, the librational motion of the imidazolium ring mainly affects the temperature-dependent features of the low-frequency spectra. It is reasonable to assume that the librational motion of the pyridinium ring would also make a large contribution to the temperature dependence of the low-frequency spectra, thus explaining the similar temperature dependence of the low-frequency spectra of the imidazolium and pyridinium based ILs. The spectral change in the high frequency region at approximately 100 cm^{-1} with the variation of temperature for imidazolium and pyridinium is thus rather universal.

4.3.1.3. Pyrrolidinium Cation vs Ammonium Cation.

As shown in Figure 4.4c and d, the differences between the spectra of [$Pyrr_{14}$][NTf_2] and [N_{1224}][NTf_2] are small; however, [N_{1224}][NTf_2] shows a somewhat broader spectral line shape than that of [$Pyrr_{14}$][NTf_2]. This can be attributed to the difference in their molecular structures: the $[Pyrr_{14}]^+$ cation is cyclic, while the $[N_{1224}]^+$ cation has a branched chain structure. Generally, chain compounds have more conformers than cyclic ones due to the lower structural hindrance, which leads to broadening of their intramolecular vibrational modes. This feature was also observed in the low-frequency spectra of oligo(ethylene glycols) compared to cyclic crown ethers.[124]

As seen in Figure 4.4c and d, the temperature-dependent spectral features of [$Pyrr_{14}$][NTf_2] and [N_{1224}][NTf_2] are similar; that is, the spectral intensity in the low-frequency region below 50 cm^{-1} increases with increasing temperature, and the intensity of the high-frequency region is almost temperature-independent. The difference between the cyclic and chain structures of

the cations does not seem to affect the temperature dependence strongly. Differences among cation structures in nonaromatic cation based ILs may have little effect on the temperature dependence of their low-frequency spectra when their alkyl chain lengths are short.

4.3.1.4. Alkyl Group Length Dependence.

Comparing Figure 4.4d and e, the spectral line shapes of $[N_{1224}][NTf_2]$ and $[N_{2228}][NTf_2]$ are quite similar despite their different alkyl group lengths. Previously, Shirota and coworkers discussed the alkyl group dependence of the low-frequency spectra for aromatic cation based ILs.[54] The spectral line shapes of 1-alkyl-3-methylimidazolium based ILs with $[BF_4]^-$ anions showed the alkyl group length dependence. This was partly due to intramolecular bending modes between the alkyl groups and the imidazolium ring, whose frequencies depend on their length and weight. On the other hand, in this study, no apparent differences were observed between butyl ($[N_{1224}]^+$) and octyl ($[N_{2228}]^+$) groups. Upon close examination, the spectra of $[N_{2228}][NTf_2]$ were slightly broader than those of $[N_{1224}][NTf_2]$, which could be due to the fact that longer alkyl chains have more conformers than shorter ones. A plausible reason for the clearer alkyl group length dependence of the low-frequency spectra of imidazolium cation based ILs compared to ammonium-based ILs is that the intramolecular bending mode between the polarizable imidazolium ring and the alkyl group located in the low-frequency region below 150 cm^{-1} is relatively stronger than the low-frequency intramolecular vibrational modes of ammonium cations.

The temperature-dependent features of these ILs were similar. Thus, increasing the length of the alkyl side chain of the ammonium cation from a butyl to an octyl group had little influence on the temperature-dependent low-frequency spectral features. This may be rather surprising, because many physical properties of ILs, such as the melting point, viscosity, and surface tension, depend strongly on the alkyl group.[29] However, the difference between the butyl and octyl groups is probably not great enough to affect the temperature dependence of the intermolecular vibrational band, because the difference in the alkyl group length is not very large.

4.3.1.5. Ammonium Cations vs Phosphonium Cations.

Figure 4.4e and f show a clear difference in the spectral shapes of $[N_{2228}][NTf_2]$ and $[P_{2228}][NTf_2]$ in the high-frequency region; that is, the spectral intensity in the frequency range of 70–200 cm^{-1} relative to the peak intensity at ca. 20 cm^{-1} is greater for $[P_{2228}][NTf_2]$ than

$[N_{2228}][NTf_2]$ at all measured temperatures. The spectra of $[P_{2228}][NTf_2]$ has been reported to have greater contributions from intramolecular vibrations in the region of 150 cm^{-1} compared to $[N_{2228}][NTf_2]$.[116] ILs based on a different phosphonium cation, (2-ethoxyethoxy)ethyltriethylphosphonium, showed intramolecular vibrational modes of the cation at ca. 140 and 180 cm^{-1}, while these bands were not observed in ILs of an ammonium cation having the same functional groups ((2-ethoxyethoxy)ethyl- triethylammonium).[116] Thus, phosphonium cations likely possess lower frequency intramolecular vibrational modes than the corresponding ammonium cations with the same functional groups.

In terms of the temperature-dependent spectral features, $[N_{2228}][NTf_2]$ and $[P_{2228}][NTf_2]$ show a similar temperature dependence, as do $[Pyrr_{14}][NTf_2]$ and $[N_{1224}][NTf_2]$. The effects of the center atoms of the cations on the temperature dependence of the low-frequency spectral shapes seem to be very small.

4.3.1.6. Molecular Liquids.

I also characterized the temperature-dependent low-frequency spectra of molecular liquids that are analogues of the cations of the ILs used in this study in order to determine whether the temperature-dependent spectral features of the ILs are unique to ILs or general for all liquids. Figure 4.5 shows the temperature-dependent spectra of 1-methylimidazole, pyridine, 1-methylpyrrolidine, and butyldiethylamine, which are analogues of the imidazolium, pyridinium, pyrrolidinium, and ammonium cations, respectively. Note that the time-domain data of the molecular liquids are summarized in Appendix D. Also note that, like the IL spectra, the spectra of the molecular liquids do not include the slow overdamped relaxation process. 1-Methylimidazole and pyridine have trapezoidal spectral shapes, while those of the 1-methylpyrrolidine and butyldiethylamine are monomodal or triangular. As reported previously, aromatic molecular liquids generally show trapezoidal or bimodal spectra due to the librational motions of the aromatic rings, which provide large contributions to the high-frequency region of the low-frequency spectral bands.[15,17,63,68,119-122] The spectra of 1-methylimidazole and pyridine show the temperature dependence in both the low- and high-frequency region, similar to $[C_4MIm][NTf_2]$ and $[C_4Py][NTf_2]$. On the other hand, only the low-frequency region below 50 cm^{-1} is temperature-dependent for 1-methylpyrrolidine and butyldiethylamine, similarly to $[Pyrr_{14}][NTf_2]$ and $[N_{1224}][NTf_2]$ (as well as $[N_{2228}][NTf_2]$ and $[P_{2228}][NTf_2]$). This implies that the presence or absence of an aromatic ring is critical in determining the temperature-dependent

features of the low-frequency spectra, especially in the high frequency region above 50 cm^{-1}, in both ILs and molecular liquids.

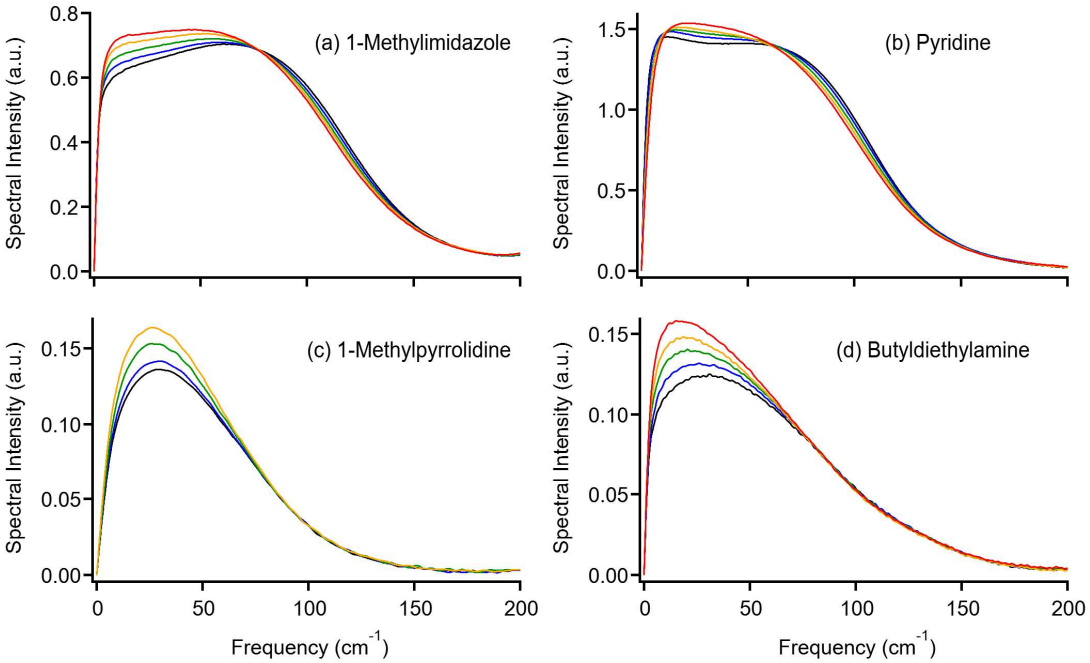

Figure 4.5. Low-frequency Kerr spectra in the frequency range of 0–200 cm^{-1} for (a) 1-methylimidazole, (b) pyridine, (c) 1-methylpyrrolidine, and (d) butyldiethylamine at 293 K (black), 308 K (blue), 323 K (green), 338 K (yellow), and 353 K (red).

4.3.1.7. Intramolecular Vibrational Bands.

Figure 4.3 shows evident intramolecular vibrational bands at 250–370 cm^{-1} for all the present ILs. Figure 4.6 shows magnifications of the spectra at 293 K to focus on these vibrational modes of the ILs, which originate from the $[NTf_2]^-$ anion. $[NTf_2]^-$ has two stable conformers, cisoid and transoid forms, and their conformational changes influence the spectral shapes in this region. The bands numbered 2, 5, 6, and 8 originate purely from the cisoid from, those numbered 3 and 7 originate solely from the transoid form, and 1 and 4 are overlapped cisoid and transoid bands.[56,118] It is noteworthy that the relative intensities of these vibrational bands are slightly different among the present ILs. For example, for $[P_{2228}][NTf_2]$, the intensity of band 6 is high relative to those of band 5 and band 7. In the case of $[Pyrr_{14}][NTf_2]$, the intensity of band 3 is high relative to that of band 4. The relative intensities of these bands are not correlated to the intensities of other bands originating from the same conformer. It is also noted that the intramolecular vibrational modes of all of the present cations likely occur in the

frequency range 250–370 cm^{-1}, similarly to that of $[C_4MIm]^+$.[54] Therefore, we conclude that the different relative intensity patterns for the present ILs are not due to different populations of the cisoid and transoid forms of the anion but caused by the presence of the intramolecular vibrational modes of cations.

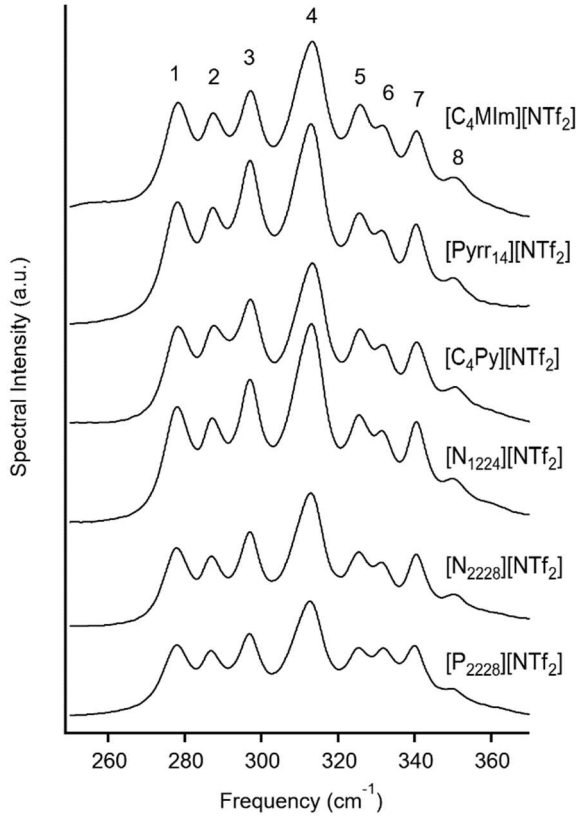

Figure 4.6. Low-frequency Kerr spectra in the frequency range of 250–370 cm^{-1}. From top to bottom, $[C_4MIm][NTf_2]$, $[Pyrr_{14}][NTf_2]$, $[C_4Py][NTf_2]$, $[N_{1224}][NTf_2]$, $[N_{2228}][NTf_2]$, and $[P_{2228}][NTf_2]$ at 293 K.

Figure 4.7 shows the spectra of the ILs in the frequency range 250–370 cm^{-1} at various temperatures, which clearly demonstrate that the spectral changes in the frequency range 250–370 cm^{-1} are similar for all of the ILs. The intensities of bands 3 and 7 decrease, while those of bands 2 and 6 increase with increasing temperature. The equilibrium between the two conformers changes with temperature, and thus, the spectra in the 250–370 cm^{-1} range are temperature-dependent, as has been discussed previously.[125] At higher temperature, the population of the cisoid form increases, while that of the transoid form decreases. The temperature sensitivity of the population ratio of the anion conformers seems to be similar

among all of the present ILs.

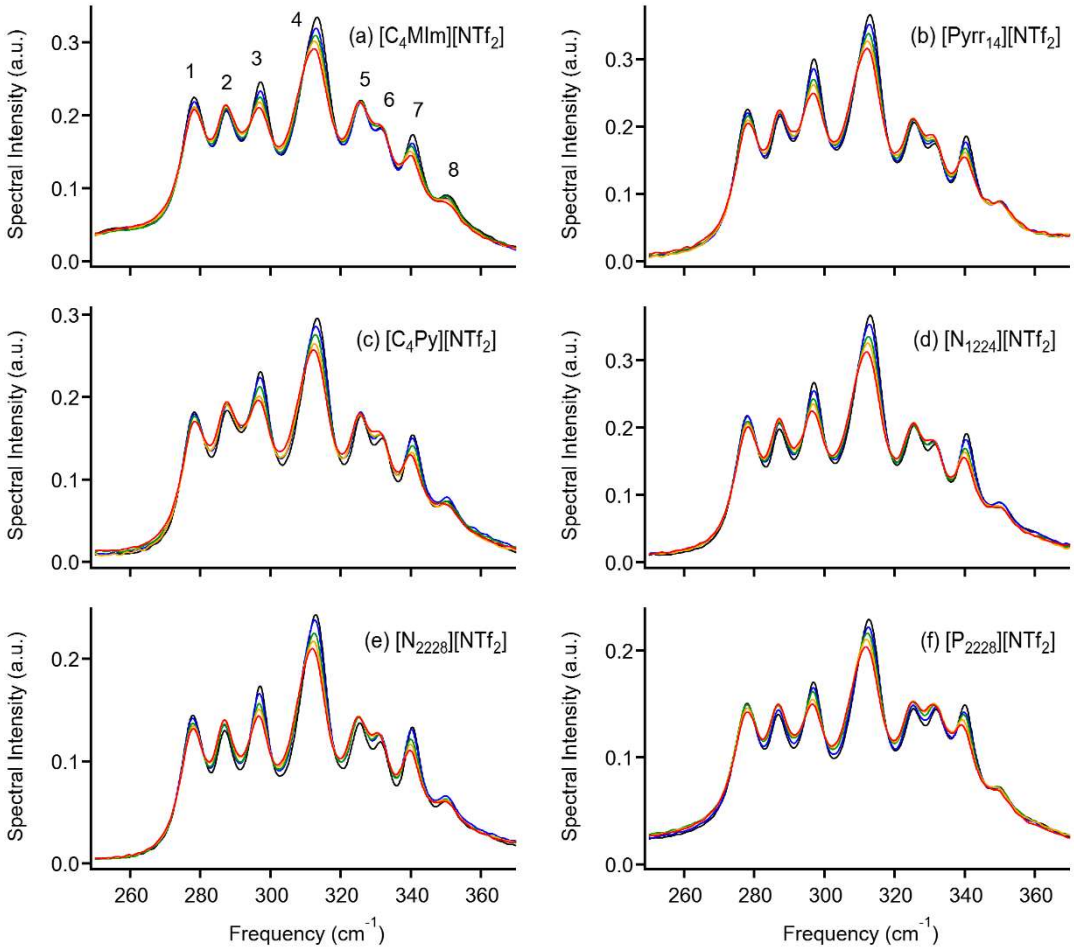

Figure 4.7. Low-frequency Kerr spectra in the frequency range of 250–370 cm^{-1} for (a) $[C_4MIm][NTf_2]$, (b) $[Pyrr_{14}][NTf_2]$, (c) $[C_4Py][NTf_2]$, (d) $[N_{1224}][NTf_2]$, (e) $[N_{2228}][NTf_2]$, and (f) $[P_{2228}][NTf_2]$ at 293 K (black), 308 K (blue), 323 K (green), 338 K (yellow), and 353 K (red).

4.3.2. Temperature Dependence of the First Moment.

On the basis of the analytical procedure described in Chapter 2, a line shape analysis of the low-frequency spectra is performed and estimated the M_1 values of the low-frequency spectra for the ILs. The fit results, fit parameters, and values of M_1 for the ILs and molecular liquids are summarized in Appendix D. To understand the quantitative features of the temperature dependence of the low-frequency spectra, plots of M_1 vs temperature for the ILs and cation analogue molecular liquids are shown in Figure 4.8. The linear fits, given by $M_1(T) = aT + M_{1,0}$, where T is the absolute temperature, a is the slope, and $M_{1,0}$ is the intercept of the relation, are also indicated in the figure. These fit parameters are summarized in Table 4.2. From

the figure and the table, [C_4MIm][NTf_2] and [C_4Py][NTf_2] were found to show larger slopes than [$Pyrr_{14}$][NTf_2], [N_{1224}][NTf_2], and [N_{2228}][NTf_2]. The increase in the spectral intensity in the low-frequency region of less than 50 cm^{-1} with rising temperature acts to reduce the M_1 value. In addition, the slowing of the librational motions of the aromatic rings leads to the red shift of the bands, which also lowers M_1. As a result, the changes of the first moments of [C_4MIm][NTf_2] and [C_4Py][NTf_2] are larger than those of the pyrrolidinium and ammonium based ILs. Of course, the intrinsic first moment $M_{1,0}$ is larger for the aromatic cation based ILs than the nonaromatic cation based ILs because of the presence of an aromatic ring.

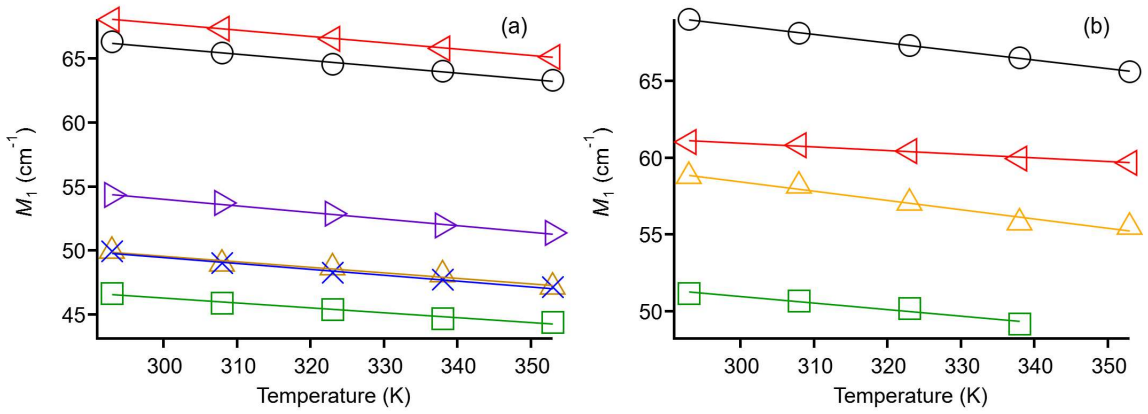

Figure 4.8. Plots of first moments vs temperature for (a) [C_4MIm][NTf_2] (black circles), [$Pyrr_{14}$][NTf_2] (green squares), [C_4Py][NTf_2] (red left-pointing triangles), [N_{1224}][NTf_2] (yellow triangles), [N_{2228}][NTf_2] (blue crosses) , and [P_{2228}][NTf_2] (purple right-pointing triangles) and (b) 1-methylimidazole (black circles), pyridine (red left-pointing triangles), 1-methylpyrrolidine (green squares), and butyldiethylamine (yellow triangles). Solid lines denote linear fits.

Table 4.2. Linear Fit Parameters for Temperature-Dependent First Moments M_1 for ILs and Cation Analogue Molecular Liquids

sample	a (cm^{-1} K^{-1})	$M_{1,0}$ (cm^{-1})
$[C_4MIm][NTf_2]$	−0.0495 ± 0.0025	80.7 ± 0.8
$[Pyrr_{14}][NTf_2]$	−0.0381± 0.0028	57.7± 0.9
$[C_4Py][NTf_2]$	−0.0493± 0.0008	82.5± 0.3
$[N_{1224}][NTf_2]$	−0.0434± 0.0045	62.6± 1.4
$[N_{2228}][NTf_2]$	−0.0459± 0.0029	63.2± 1.0
$[P_{2228}][NTf_2]$	−0.0513± 0.0020	69.4± 0.6
1-Methylimidazole	−0.0560± 0.0009	85.4± 0.3
Pyridine	−0.0235± 0.0016	68.0± 0.5
1-Methylpyrrolidine	−0.0427± 0.0064	63.8± 2.0
Butyldiethylamine	−0.0603± 0.0061	76.5± 2.0

Another significant point is that the slope for $[P_{2228}][NTf_2]$ was even greater than those of the aromatic cation based ILs, although $[P_{2228}]^+$ is a nonaromatic cation. As discussed in Section 4.3.1.5, $[P_{2228}][NTf_2]$ showed greater intramolecular vibration components in the region of 150 cm^{-1} than $[N_{2228}][NTf_2]$.[116] The contributions of the intramolecular vibrations are removed in the estimation of M_1 by fitting these components using Lorentzian functions; nonetheless the line shape fits are likely imperfect because of the broadness of these intramolecular vibrational bands and strong overlaps in this frequency region. On the other hand, it is also noted that the intermolecular interactions between the cation and anion are very different for $[P_{2228}][NTf_2]$ and $[N_{2228}][NTf_2]$.[126] It is thus not surprising that they show a different temperature dependence in the low-frequency spectral band. At the moment, I cannot clearly conclude the origin of the steeper slope of $[P_{2228}][NTf_2]$ compared to the other nonaromatic cation based ILs. However, we can at least suggest two possibilities: the peculiar nature of the intermolecular vibration for the phosphonium-cation-based IL, and the effect of the temperature dependence of the intramolecular vibrational bands of the phosphonium cation.

In contrast to the ILs, each molecular liquid shows unique a and $M_{1,0}$ values whether it is aromatic or nonaromatic. The results indicate that the temperature sensitivity of the low-frequency spectrum in the ILs is more affected by the ionic nature (Coulomb interaction) but less influenced by the structure of the cation (except for the difference in the aromaticity of the cation) than that in the neutral molecular liquids.

4.3.3. Temperature-Dependent Viscosities.

Figure 4.9 shows the temperature dependence of η for the ILs. The values at 293, 308, 323, 338, and 353 K are summarized in Table 4.1 for a comparison with the fs-RIKES results, and all data are listed in Appendix D. The viscosities of ILs generally show a non-Arrhenius dependence on temperature. Instead, the VTF equation[86-89] is commonly used to fit the temperature dependence of the η values of ILs,[90] and is given by eq. 3.1 in Chapter 3. The collected data were fitted using the logarithmic form of eq. 3.1, $\ln[\eta(T)] = \ln(\eta_0) + [DT_0/(T–T_0)]$, to properly treat the η data spanning several orders of magnitude.[127] Each data set includes the value of 1×10^{13} cP at the T_g of the liquid, according to the method of Angell and coworkers,[90] in order to estimate the fit parameters more precisely. The T_g values for each IL were taken from previous reports.[116-117,128-130] The VTF fitting parameters are summarized in Table 4.3.

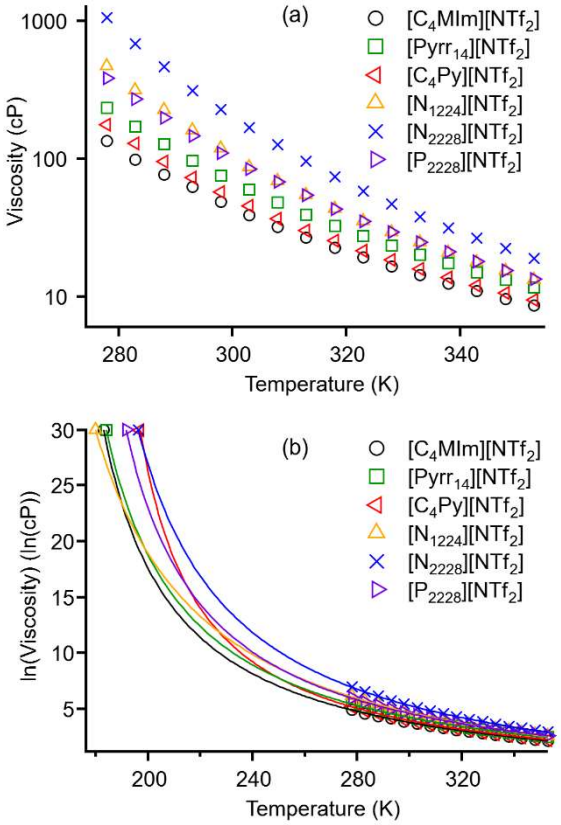

Figure 4.9. (a) Temperature-dependent viscosities for $[C_4MIm][NTf_2]$ (black circles), $[Pyrr_{14}][NTf_2]$ (green squares), $[C_4Py][NTf_2]$ (red left-pointing triangles), $[N_{1224}][NTf_2]$ (yellow triangles), $[N_{2228}][NTf_2]$ (blue crosses) , and $[P_{2228}][NTf_2]$ (purple right-pointing triangles). (b) VTF fits including the shear viscosity value of 10^{13} cP at the glass transition temperature are shown.

Table 4.3. Glass Transition Temperature T_g and VTF Fit Parameters for ILs

IL	T_g (K)	$\ln(\eta_0)$ (ln(cP))	D	T_0 (K)
$[C_4MIm][NTf_2]$	183[a]	−2.317	5.664	155.7
$[Pyrr_{14}][NTf_2]$	184[b]	−2.525	6.458	153.5
$[C_4Py][NTf_2]$	197[c]	−1.798	4.159	174.2
$[N_{1224}][NTf_2]$	180[d]	−4.085	10.26	138.3
$[N_{2228}][NTf_2]$	196[e]	−3.441	7.715	159.4
$[P_{2228}][NTf_2]$	192[e]	−2.671	6.312	160.5

[a]Reference 117. [b]Reference 129. [c]Reference 130. [d]Reference 128. [e]Reference 116.

As described in Chapter 3, the D parameter is a measure of the liquid fragility, which denotes the degree of deviation of the temperature-dependent viscosity from Arrhenius-type behavior.[131] Liquids with smaller D values are said to be more fragile, which means that their viscosities increase rapidly near the glass transition, while liquids with larger D values are said to be stronger. Among the studied ILs, the aromatic cation based ILs show smaller D values than the nonaromatic cation based ILs. A similar trend was reported previously: the fragilities of imidazolium, pyridinium, and ammonium cation based ILs were compared, and the pyridinium cation had the largest fragility, although a different type of anion, $[BF_4]^-$, was used.[90] Among the nonaromatic ILs, the ammonium cation based ILs showed larger D values than the pyrrolidinium and phosphonium cation based ILs. This might be related to the lower viscosities of the phosphonium-cation based ILs compared to the respective ammonium-cation based ILs.[116,132-133] Focusing on the relationship between the temperature dependence of the low-frequency spectra and the D parameters, the ILs with larger a and $M_{1,0}$ values show smaller D values. Both features can be attributed to the presence of aromatic cations. However, like imidazolium-based ILs with a variety of anions (Chapter 3), the clear direct correlation between the temperature sensitivity (the slope a in Figure 4.8) of the M_1 and the D parameter for the ILs studied here is not confirmed.

4.4 Conclusions

In this study, the temperature dependence of the low-frequency spectra of $[NTf_2]^-$ salts with a wide variety of cations is investigating using fs-RIKES to elucidate the effects of the cation structures on the temperature-dependent spectral features. For the aromatic cation based

ILs, the spectral intensities in the frequency region below 20 cm^{-1} increased with increasing temperature due to the activation of the translational vibrational motions of the ions at higher thermal energies. In addition, the high-frequency components above 80 cm^{-1} shifted to lower frequency with rising temperature, which was attributed to the slower librational motion of the aromatic ring due to the larger free volume and the weaker intermolecular interaction at higher temperature. On the other hand, in the case of the nonaromatic cation based ILs, the spectral intensities in the frequency region below 50 cm^{-1} increased with rising temperature; however, the intensities in the frequency region above 50 cm^{-1} showed little change. Furthermore, molecular liquids with structures similar to the cations of the ILs also showed temperature-dependent spectra, with spectral changes appearing in both the low- and high-frequency regions for 1-methylimidazole and pyridine, while only the low-frequency region below 50 cm^{-1} was temperature-dependent for 1-methylpyrrolidine and butyldiethylamine. Thus, it is concluded that the presence or absence of an aromatic ring determined the temperature-dependent features of the intermolecular vibrational spectra in both the ILs and molecular liquids. The M_1 values were more sensitive to temperature for the aromatic cation based ILs than the nonaromatic cation based ILs. In contrast, each molecular liquid shows a unique temperature sensitivity to the M_1 value. The fragility related parameter D was smaller for the aromatic cation based ILs than for the nonaromatic cation based ILs, which is consistent with previous reports. Thus, the presence or absence of an aromatic ring in the ILs governed both their temperature-dependent spectral features and their liquid properties. In the next chapter, I focus on pyrrolidinium based ILs, which is one of the nonaromatic cations, because the contributions of pyrrolidinium cations on the low-frequency spectra are small compared to aromatic cation. This means that the effects of anions are expected to be larger in pyrrolidinium based ILs than in imidazolium based ILs (Chapter 3).

Chapter 5

Temperature Dependence of Low-Frequency Spectra in Pyrrolidinium-Based Ionic Liquids: Effects of Anion Species

J. Phys. Chem. B, **2019**, *123*, 1307–1323.

5.1. Introduction

In this chapter, I study the temperature-dependent low-frequency spectra of nonaromatic cation based ILs with various anion species using fs-RIKES. Nonaromatic cations generally exhibit a much smaller Kerr signal than aromatic cations, as shown in Chapter 4. Thus, the contributions of anions to the spectra are expected to be more prominent in nonaromatic ILs than in aromatic ILs, which allows for a more precise discussion of the temperature-dependent spectral features originating from the anions. I chose 1-butyl-1-methylpyrrolidinium ($[Pyrr_{14}]^+$) and 1-(2-methoxyethyl)-1-methylpyrrolidinium ($[Pyrr_{1(1O2)}]^+$) as nonaromatic cations because they are commonly used cations (Figure 5.1). Note that the alkyl group (butyl group) is more commonly used than the ether group (2-methoxyethyl group), but $[Pyrr_{1(1O2)}]^+$-based ILs remain in the liquid state at room temperature with a wider variety of anions, particularly spherical top anions, than $[Pyrr_{14}]^+$-based ILs. I selected the following anion species: hexafluorophosphate ($[PF_6]^-$), tetrafluoroborate ($[BF_4]^-$), trifluoromethanesulfonate ($[OTf]^-$), dicyanamide ($[DCA]^-$), tricyanomethide ($[TCM]^-$), tris(pentafluoroethyl)trifluorophosphate ($[FAP]^-$), bis(fluorosulfonyl)amide ($[NF_2]^-$), bis(trifluoromethylsulfonyl)amide ($[NTf_2]^-$), bis(pentafluoroethylsulfonyl)amide ($[NPf_2]^-$), and cyclohexafluoropropane-1,3-bis(sulfonyl)amide ($[NCyF]^-$), as displayed in Figure 5.1. The main aims of this study are (i) to elucidate the temperature-dependent features of nonaromatic ILs and (ii) to clarify the effects of the anions on the temperature dependence of the low-frequency spectra. The temperature-dependent viscosities of the ILs are also measured and estimated their fragility to elucidate the relationship between the fragility parameter and the temperature dependence of the low-frequency spectrum in the ILs.

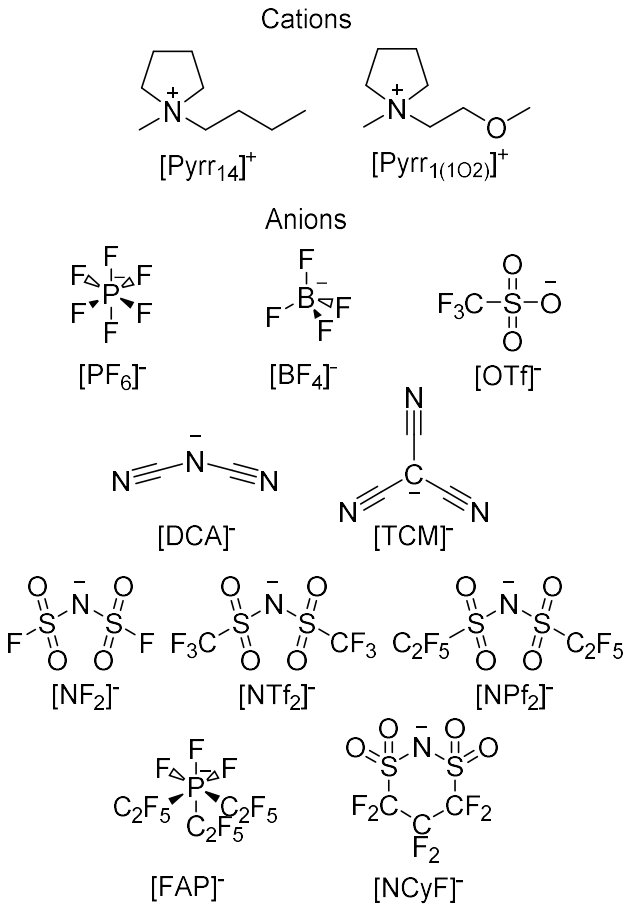

Figure 5.1. Structural formulas of cations and anions of ILs used in this study.

5.2. Experimental Methods

$[Pyrr_{14}][DCA]$, $[Pyrr_{14}][FAP]$, and $[Pyrr_{1(1O2)}][BF_4]$ were purchased from TCI, Merck, and Kanto Chemical, respectively, and used without further purification. $[Pyrr_{14}][TCM]$ (Iolitec) was purified according to a standard activated charcoal treatment. $[Pyrr_{14}][NTf_2]$ was that used in Chapter 4.[134] $[Pyrr_{14}][NF_2]$, $[Pyrr_{14}][NPf_2]$, $[Pyrr_{14}][NCyF]$, $[Pyrr_{14}][OTf]$, $[Pyrr_{1(1O2)}][NTf_2]$, $[Pyrr_{1(1O2)}][NF_2]$, $[Pyrr_{1(1O2)}][NCyF]$, and $[Pyrr_{1(1O2)}][PF_6]$ were synthesized by the procedures reported previously.[56,116] The structures of the synthesized ILs were confirmed by ^1H NMR and elemental analysis measurements. Details of the synthetic procedures and assignments for these ILs are summarized in Appendix A. The sample ILs were dried in vacuo at 313 K for over 36 hours before measurements.

Ab initio quantum chemistry calculations were performed at the B3LYP/6-311++G(d,p) level of theory to estimate the optimized structures and Raman-active normal modes of $[Pyrr_{14}]^+$ and $[Pyrr_{1(1O2)}]^+$ cations using the Gaussian 09 program suite.[135] The obtained atom coordinates of the optimized structures for the cations are provided in Appendix E.

5.3. Results

5.3.1. Temperature-Dependent Low-Frequency Spectra.

Figure 5.2 shows the Kerr transients of $[Pyrr_{1(1O2)}][BF_4]$, $[Pyrr_{14}][DCA]$, $[Pyrr_{1(1O2)}][NTf_2]$, and $[Pyrr_{14}][NCyF]$ at 293, 308, 323, 338, and 353 K as examples. The Kerr transients were normalized by the signal intensity at $t = 0$. Most of these modes of the present ILs decay within 10 ps except for the ILs with $[NCyF]^-$ anion, which show very strong beats due to intramolecular vibrational modes with long dephasing times. With increasing temperature, the amplitudes of the nuclear responses relative to the electronic responses at $t = 0$ increase for all ILs in this study. This feature has also been observed in aromatic cation based ILs.[117,125,134,136] The transients from 3 ps are fitted by a biexponential function. The fit parameters are tabulated in Appendix E. The obtained time constants do not change with the variation in temperature for all the studied ILs within the standard deviations of the fits. For example, τ_1 and τ_2 are 0.81 and 6.70 ps at 293 K and 0.85 and 6.69 ps at 338 K for $[Pyrr_{1(1O2)}][NTf_2]$. On the other hand, the values of the amplitude parameters typically increase with rising temperature. The temperature-independent nature of the time constants suggests that these components in the few picosecond region are not diffusive. The collective reorientation of ILs, which is temperature dependent, is typically of the order of nanoseconds.[49-50] Because the limitation of the delay time of the fs-RIKES setup used in this study is 300 ps, the complete reorientation processes of the ILs cannot be captured. However, when discussing the intermolecular vibrational dynamics, it is not necessary to obtain the long-time-window data over tens of picoseconds. The validity of the discussion of intermolecular vibrational spectra obtained from the Kerr transients without long-time-window data has been previously demonstrated.[125]

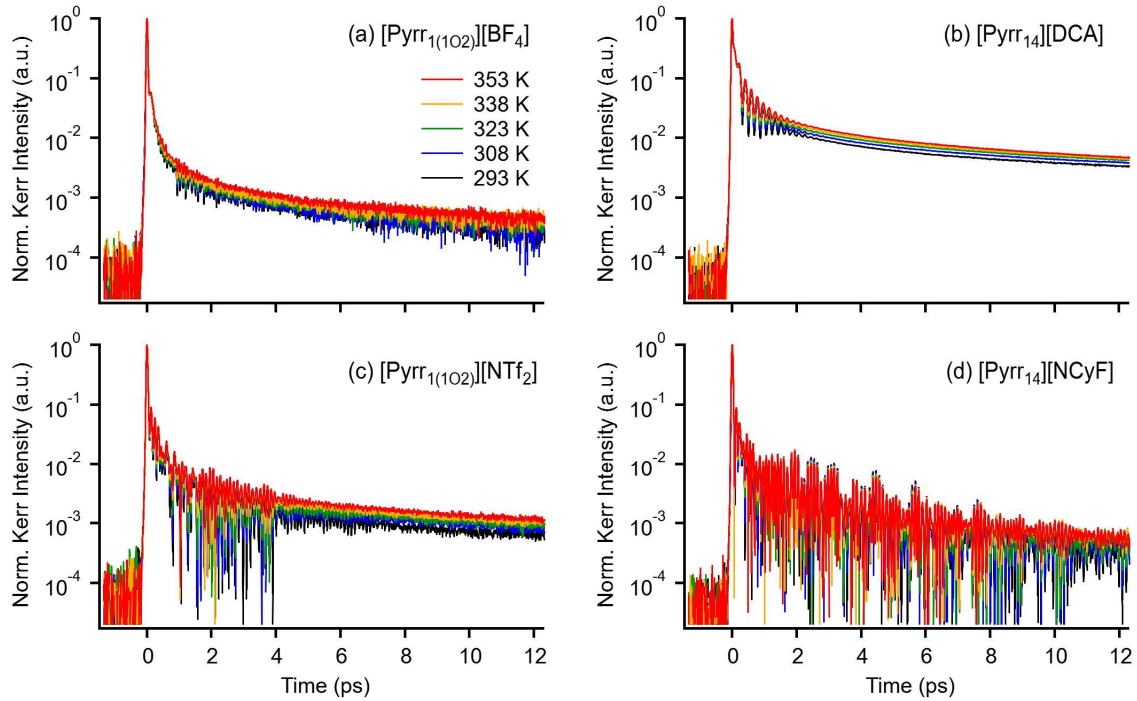

Figure 5.2. Normalized Kerr transients of (a) $[Pyrr_{1(1O2)}][BF_4]$, (b) $[Pyrr_{14}][DCA]$, (c) $[Pyrr_{1(1O2)}][NTf_2]$, and (d) $[Pyrr_{14}][NCyF]$ at 293 K (black), 308 K (blue), 323 K (green), 338 K (yellow), and 353 K (red).

The Fourier transform deconvolution analysis was performed as described in Chapter 2. The obtained Kerr spectra are all well resolved up to approximately 650 cm^{-1}. It is noted that the Kerr spectra discussed here are so-called reduced spectra which are the results of the subtractions of the contributions of the picosecond overdamped relaxation components from the entire Kerr spectra. The spectra of $[Pyrr_{1(1O2)}][BF_4]$, $[Pyrr_{14}][DCA]$, and $[Pyrr_{1(1O2)}][NTf_2]$ in the frequency range of 0–200 cm^{-1} are shown in Figure 5.3. The difference Kerr spectra at each temperature relative to those at 293 K for these ILs are also presented in Figure 5.3 so as to evaluate more closely the temperature dependence of the low-frequency spectra. The low-frequency Kerr spectra of $[Pyrr_{14}][NTf_2]$ and $[Pyrr_{1(1O2)}][NTf_2]$ at 295 K,[51] $[Pyrr_{14}][NTf_2]$ at 296 K,[56] and $[Pyrr_{14}][DCA]$ at 278 K[137] have already been reported, and the spectral line shapes of these ILs at 293 K obtained in this study are similar to those in the literature. All the ILs in this study show temperature-dependent spectra. As a common temperature-dependent feature of the spectra of the ILs, the spectral intensity in the low-frequency region below 50 cm^{-1} increases with rising temperature. On the other hand, the spectral intensity in the high-frequency region above 50 cm^{-1} remains almost unchanged except in the case of $[Pyrr_{14}][DCA]$ and $[Pyrr_{14}][TCM]$ (Figure 5.11, vide infra).

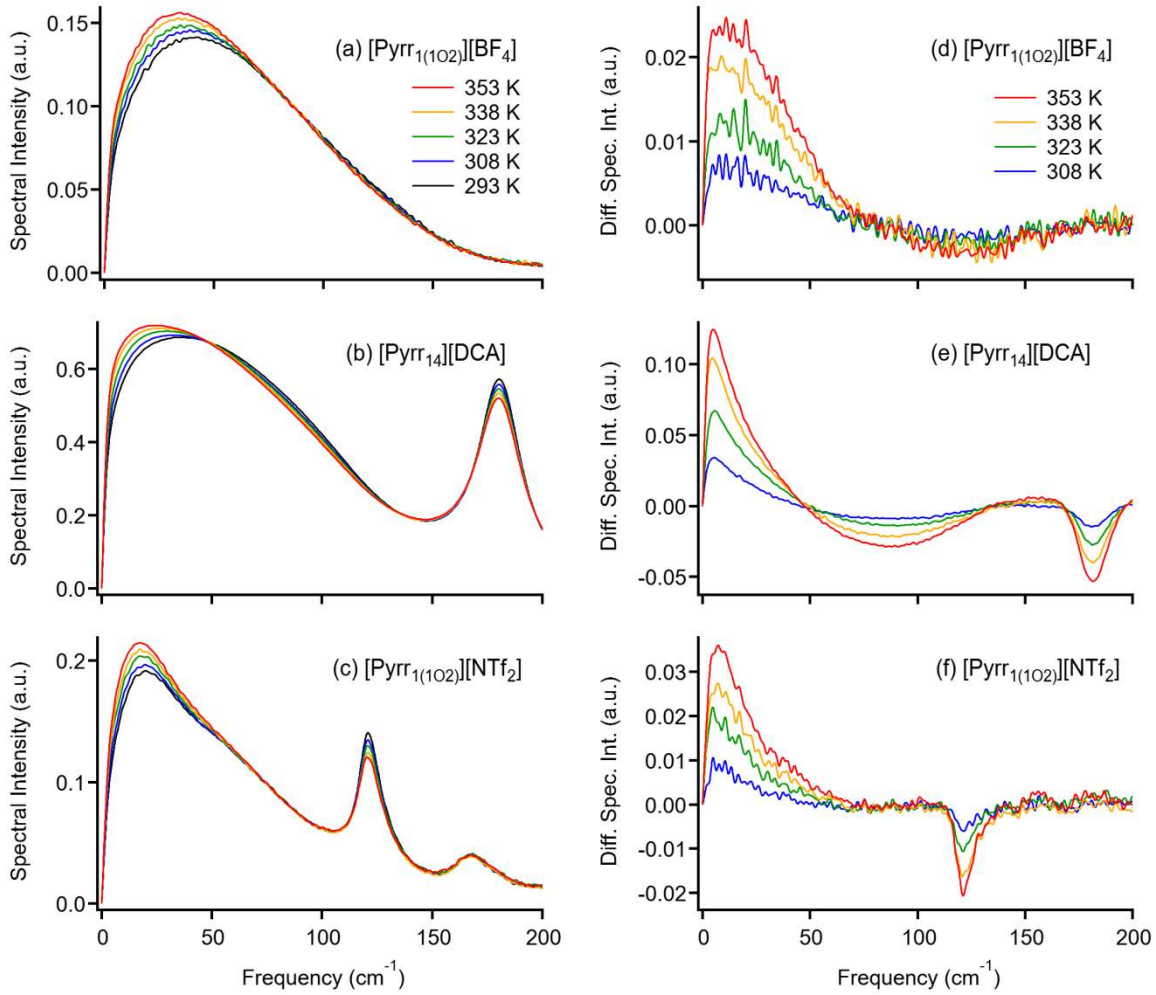

Figure 5.3. Temperature-dependent low-frequency spectra of (a) [$Pyrr_{1(1O2)}$][BF_4], (b) [$Pyrr_{14}$][DCA], and (c) [$Pyrr_{1(1O2)}$][NTf_2] at 293 K (black), 308 K (blue), 323 K (green), 338 K (yellow), and 353 K (red). Difference Kerr spectra of (d) [$Pyrr_{1(1O2)}$][BF_4], (e) [$Pyrr_{14}$][DCA], and (f) [$Pyrr_{1(1O2)}$][NTf_2] at 308 K (blue), 323 K (green), 338 K (yellow), and 353 K (red) relative to those at 293 K are also shown.

To represent numerically the spectral line shapes and discuss the temperature dependence of the low-frequency spectra quantitatively, a line shape analysis of the low-frequency spectra of the ILs below 200 cm^{-1} was performed. Details of the procedure of the line shape analysis have been reported in Chapter 2. Figure 5.4 shows the results of the line shape analyses for [$Pyrr_{1(1O2)}$][BF_4] and [$Pyrr_{14}$][DCA] as examples. The fit parameters and the M_1 values are summarized in Appendix E. Figure 5.5 shows the temperature dependence of M_1 of the ILs. The temperature dependence of M_1 for each IL was fitted by a linear function given by $M_1(T)$

= $aT + M_{1,0}$, where T is the absolute temperature, a is the slope that is an indicative of the temperature sensitivity of the low-frequency spectrum, and $M_{1,0}$ is the intrinsic first moment, that is, M_1 at 0 K. The obtained parameters are summarized in Table 5.1. For a reference, the M_1 values at 293 K are also listed in the table.

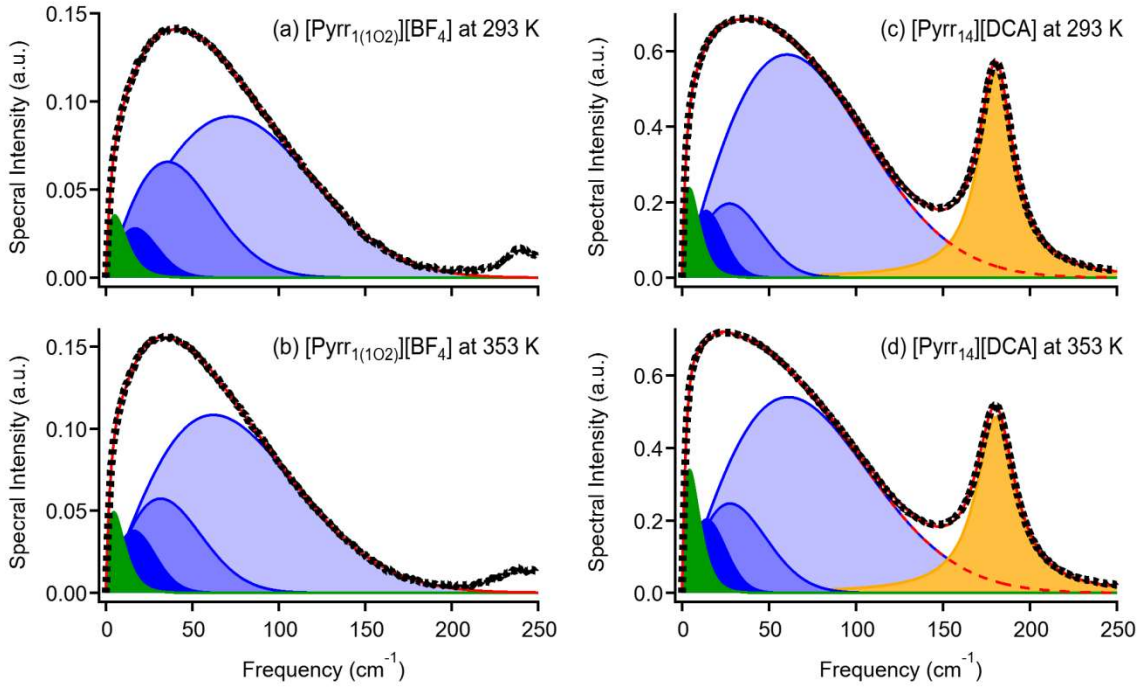

Figure 5.4. Line shape analysis results of the low-frequency spectra of (a) [Pyrr$_{1(1O2)}$][BF$_4$] at 293 K, (b) [Pyrr$_{1(1O2)}$][BF$_4$] at 353 K, (c) [Pyrr$_{14}$][DCA] at 293 K. and (d) [Pyrr$_{14}$][DCA] at 353 K. Black dots denote the experimentally obtained spectra. Green, blue, and orange areas denote Ohmic, antisymmetrized Gaussian, and Lorentzian functions, respectively. Red solid lines denote the entire fit. Red dashed lines denote the sum of the Ohmic and antisymmetrized Gaussian functions.

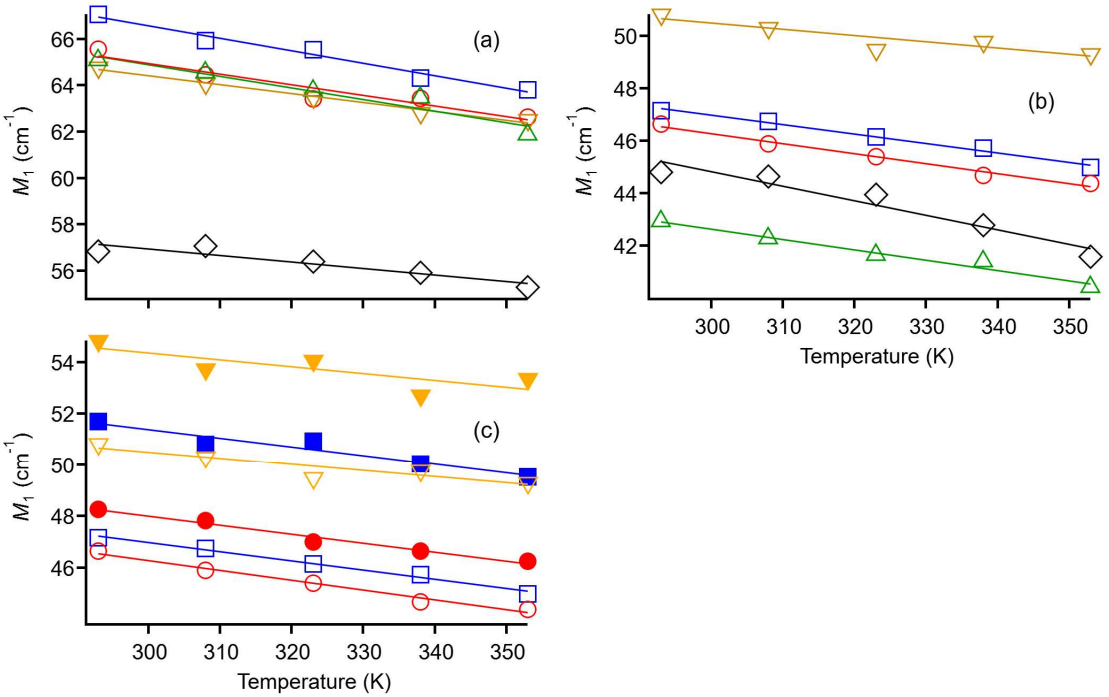

Figure 5.5. Plots of M_1 vs. temperature for (a) [Pyrr$_{1(1O2)}$][PF_6] (red circles), [Pyrr$_{1(1O2)}$][BF_4] (blue squares), [Pyrr$_{14}$][OTf] (green triangles), [Pyrr$_{14}$][DCA] (yellow inverted triangles), [Pyrr$_{14}$][TCM] (black diamonds) and (b) [Pyrr$_{14}$][NTf_2] (red circles), [Pyrr$_{14}$][NF_2] (blue squares), [Pyrr$_{14}$][NPf_2] (green triangles), [Pyrr$_{14}$][NCyF] (yellow inverted triangles), [Pyrr$_{14}$][FAP] (black diamonds). (c) Comparison of [Pyrr$_{14}$]$^+$- (open symbols) and [Pyrr$_{1(1O2)}$]$^+$-based ILs (filled symbols) with [NTf_2]$^-$ (red circles), [NF_2]$^-$ (blue squares), and [NCyF]$^-$ (yellow inverted triangles). Linear fits are shown by solids lines.

Table 5.1. Linear Fit Parameters for Temperature-Dependent First Moments M_1 and Slopes b for Temperature Dependence of Intensities of Difference Spectra Relative to 293K for ILs

IL	a (cm^{-1} K^{-1})	$M_{1,0}$ (cm^{-1})	M_1(293 K) (cm^{-1})	b (K^{-1})
$[Pyrr_{1(1O2)}][PF_6]$	−0.0457 ± 0.0076	78.7 ± 2.5	65.6	4.38×10^{-4}
$[Pyrr_{1(1O2)}][BF_4]$	−0.0539 ± 0.0049	82.7 ± 1.6	67.0	3.99×10^{-4}
$[Pyrr_{14}][OTf]$	−0.0499 ± 0.0077	79.8 ± 2.5	65.1	2.97×10^{-4}
$[Pyrr_{14}][DCA]$	−0.0384 ± 0.0027	75.9 ± 0.9	64.8	2.18×10^{-3}
$[Pyrr_{14}][TCM]$	−0.0283 ± 0.0062	65.4 ± 2.0	56.8	1.74×10^{-3}
$[Pyrr_{14}][FAP]$	−0.0554 ± 0.0086	61.4 ± 2.8	44.8	6.39×10^{-4}
$[Pyrr_{14}][NTf_2]$	−0.0381 ± 0.0028	57.7 ± 0.9	46.6	5.75×10^{-4}
$[Pyrr_{14}][NF_2]$	−0.0357 ± 0.0021	57.7 ± 0.7	47.2	9.77×10^{-4}
$[Pyrr_{14}][NPf_2]$	−0.0395 ± 0.0038	54.5 ± 1.2	42.9	7.10×10^{-4}
$[Pyrr_{14}][NCyF]$	−0.0239 ± 0.0065	57.6 ± 2.1	51.1	5.34×10^{-4}
$[Pyrr_{1(1O2)}][NTf_2]$	−0.0347 ± 0.0031	58.4 ± 1.0	48.2	5.95×10^{-4}
$[Pyrr_{1(1O2)}][NF_2]$	−0.0340 ± 0.0056	61.6 ± 1.8	51.7	8.81×10^{-4}
$[Pyrr_{1(1O2)}][NCyF]$	−0.0264 ± 0.0012	62.3 ± 3.8	54.8	5.86×10^{-4}

5.3.2. Temperature-Dependent Viscosities and Glass Transition Temperatures.

Figure 5.6 displays the temperature-dependent η of $[Pyrr_{1(1O2)}][BF_4]$, $[Pyrr_{14}][DCA]$, and $[Pyrr_{1(1O2)}][NTf_2]$ as examples. The measured η values for the ILs are summarized in Appendix E. The η values of the most ILs are reported including their temperature dependence.[129,138-143] As far as I know, the data of the temperature-dependent η of $[Pyrr_{1(1O2)}][PF_6]$, $[Pyrr_{1(1O2)}][NCyF]$, and $[Pyrr_{14}][NCyF]$ are reported here for the first time. The values in this study are in reasonably good agreement with the reported values considering the measured temperature and the experimental errors. The η of the ILs depends significantly on their anion species. When comparing η at 293 K, $[Pyrr_{1(1O2)}][PF_6]$ presents the largest value, while $[Pyrr_{14}][TCM]$ has the smallest η value in the present ILs. The tendency of η in 1-butyl-3-methylimidazolium ($[C_4MIm]^+$)-based ILs with different anions is reported in Chapter 3. The $[C_4MIm]^+$-based ILs with $[PF_6]^-$ and $[NPf_2]^-$ anions tend to be more viscous, while the ILs with $[NF_2]^-$ and $[DCA]^-$ anions are least viscous. This tendency is also valid for the pyrrolidinium-based ILs studied here. In addition, replacing the butyl group in the cations with a 2-

methoxyethyl group reduced the η of the ILs with $[NTf_2]^-$, $[NF_2]^-$, and $[NCyF]^-$ anions. The η values for the $[Pyrr_{1(1O2)}]^+$-based ILs are 60–80% of those of the $[Pyrr_{14}]^+$-based ILs.

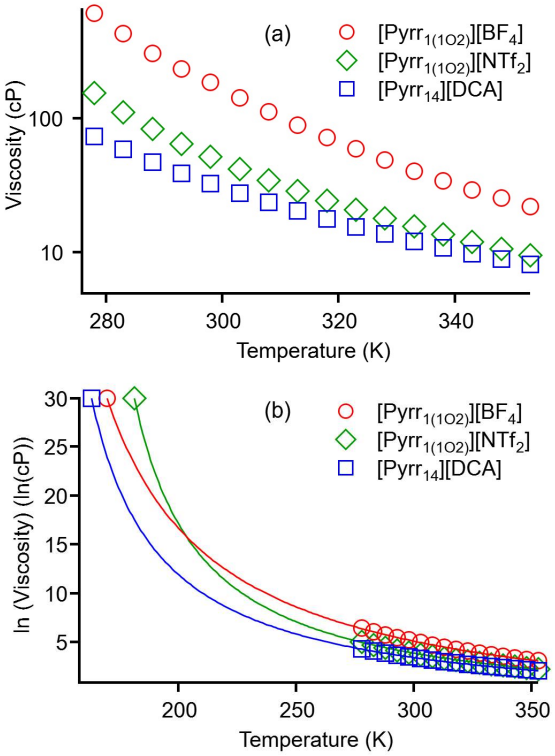

Figure 5.6. (a) Temperature-dependent viscosities of $[Pyrr_{1(1O2)}][BF_4]$ (red circles), $[Pyrr_{14}][DCA]$ (blue squares), and $[Pyrr_{1(1O2)}][NTf_2]$ (green diamonds). (b) VTF fits including the viscosity value of 10^{13} cP at the glass transition temperature are shown.

The temperature dependence of η of supercooled liquids does not follow the Arrhenius equation, but obeys the VTF model,[86-89]. The VTF equation is also commonly used to fit the temperature-dependent η of ILs.[90] To fit the temperature-dependent η data of the ILs considered in this study, the logarithmic form of eq. 3.1, $\ln[\eta(T)] = \ln(\eta_0) + DT_0/(T - T_0)$, was used because the η data span several orders of magnitude, resulting a poor fit at low η values. According to the method by Angell and co-workers, each data set includes the value of 1×10^{13} cP at the T_g of the liquid.[90] The VTF fits are illustrated in Figure 5.6b, and the obtained parameters are summarized in Table 5.2. Note that the fittings were carried out without the T_g data for some ILs that do not show glass transitions, and the obtained values are presented in parenthesis just for references in Table 5.2. I will next discuss the quantitative features based on the temperature-dependent η data with T_g values.

Table 5.2. Viscosity η at 293 K, Melting Point T_m, Glass Transition Temperature T_g, and VTF Fit Parameters for ILs[a]

IL	η (cP)	T_m (K)	T_g (K)	ln(η_0) (ln(cP))	D	T_0 (K)
[Pyrr$_{1(1O2)}$][PF_6]	753	307	-	(−5.390)	(24.807)	(95.6)
[Pyrr$_{1(1O2)}$][BF_4]	232	286	170	−3.783	12.752	123.2
[Pyrr$_{14}$][OTf]	227	264	177	−3.644	10.684	134.6
[Pyrr$_{14}$][DCA]	38.8	228	163	−2.159	6.870	134.4
[Pyrr$_{14}$][TCM]	33.0	-	173	−2.077	5.482	147.9
[Pyrr$_{14}$][FAP]	288	276	-	(−2.461)	(5.717)	(172.0)
[Pyrr$_{14}$][NTf_2]	97.1	264	184	−2.556	6.556	152.7
[Pyrr$_{14}$][NF_2]	61.4	-	165	−1.980	7.166	134.5
[Pyrr$_{14}$][NPf_2]	341	279	-	(−3.101)	(7.079)	(163.5)
[Pyrr$_{14}$][NCyF]	486	292	199	−2.623	6.863	164.7
[Pyrr$_{1(1O2)}$][NTf_2]	64.0	-	181	−2.349	5.973	153.1
[Pyrr$_{1(1O2)}$][NF_2]	47.9	275	-	(−1.743)	(5.638)	(146.1)
[Pyrr$_{1(1O2)}$][NCyF]	308	-	193	−2.638	7.107	158.5

[a]Values in paranthesis were estimated from the temperature-dependent η without T_g values for a reference.

Figure 5.7a shows the DSC curves of [Pyrr$_{14}$][NF_2], [Pyrr$_{1(1O2)}$][NTf_2], and [Pyrr$_{1(1O2)}$][NCyF] as examples of the ILs exhibiting glass transitions. The T_g of the ILs depends on the constituent cation and anion. The values of T_g for the ILs in this study are in the range of 160–200 K. Figure 5.7b shows the DSC curve of [Pyrr$_{14}$][NTf_2] as an example of an IL exhibiting a melting point. A sharp negative peak is observed at 264 K, which is ascribed to the melting point. It is reported that a sharp peak at 217 K is due to the crystallization during the heating cycle, and the broad band near 245 K is attributed to solid-solid transitions.[144-146] Note that not all ILs always show melting points in the DSC curves. Some ILs in this study show both glass transition and melting points and some of them show only a glass transition or a melting point within the scanning temperature range of the DSC measurements. The values of T_g and T_m are summarized in Table 5.2. The values for most of the present ILs have been previously reported[129,143,147-152] and the obtained values in this study are similar to those reported, whereas the T_g value of [Pyrr$_{1(1O2)}$][NCyF] is here reported for the first time. The T_m

value of [Pyrr$_{1(1O2)}$][PF$_6$] is 307 K, and thus it exists in the supercooled state at 293 K. The other ILs exhibit melting points under 293 K or no melting points within the temperature range of 143–323 K.

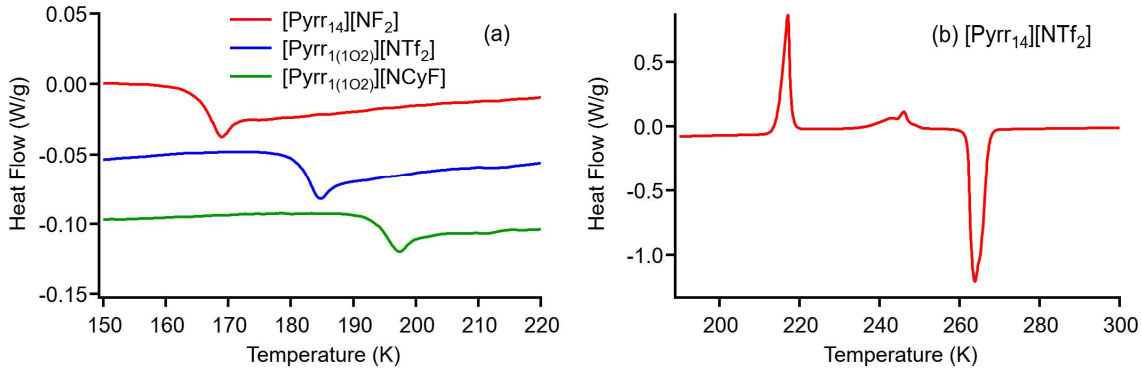

Figure 5.7. DSC heat flow charts of (a) [Pyrr$_{14}$][NF$_2$] (red), [Pyrr$_{1(1O2)}$][NTf$_2$] (blue) , and [Pyrr$_{1(1O2)}$][NCyF] (green) in the range of 150–220 K and (b) [Pyrr$_{14}$][NTf$_2$] in the range of 190–300 K.

5.3.3. Quantum Chemistry Calculations.

To see the effects of intramolecular vibrational modes of cation's side groups (butyl and 2-methoxyethyl groups) on the low-frequency spectra, quantum chemistry calculations at the B3LYP/6-311++G(d,p) level of theory were performed. Figure 5.8a shows the optimized structures of [Pyrr$_{14}$]$^+$ and [Pyrr$_{1(1O2)}$]$^+$ cations and Figure 5.8b shows the calculated Raman spectra in the frequency range of 0–700 cm^{-1}. The calculated Raman spectra will be compared to the low-frequency Kerr spectra of the [Pyrr$_{14}$]$^+$- and [Pyrr$_{1(1O2)}$]$^+$-based ILs in Section 5.4.1.2.

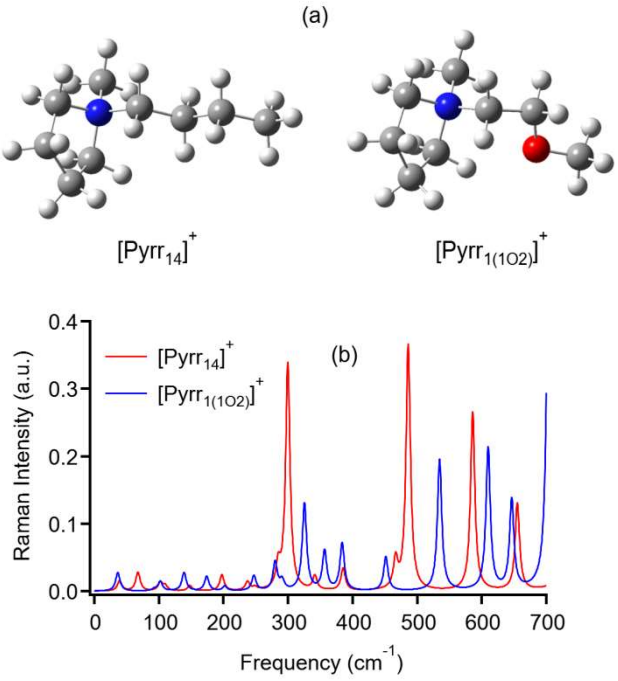

Figure 5.8. (a) Optimized structures of the $[Pyrr_{14}]^+$ and $[Pyrr_{1(1O2)}]^+$ cations at the B3LYP/6-311++G(d,p) level of theory and (b) calculated Raman spectra of the cations in the frequency range of 0–700 cm^{-1}.

5.4. Discussion

5.4.1. Temperature-Dependent Spectral Features of Pyrrolidinium-Based ILs.

Before discussing the results in detail, let's summarize the general temperature-dependent spectral features of the present pyrrolidinium-based ILs comparing with those of imidazolium-based ILs. As shown in Figure 5.3, the spectral intensity in the low-frequency region below ca. 50 cm^{-1} of $[Pyrr_{1(1O2)}][BF_4]$, $[Pyrr_{14}][DCA]$, and $[Pyrr_{1(1O2)}][NTf_2]$ increased with rising temperature. This is also true for the other present pyrrolidinium-based ILs (Figures 5.9 and 5.11–13, vide infra). Similar behaviors in various ILs (Chapter 3 and 4), and this was attributed to a thermal activation of the translational intermolecular vibrational motions of cations and anions and/or a decoupling of the intermolecular vibration and the structural relaxation process in the ILs.

In addition to the low-frequency region below ca. 50 cm^{-1}, imidazolium- and pyridinium-based ILs further show a redshift in the high-frequency region above 80 cm^{-1} with increasing temperature (Chapter 3 and 4). According to the results of MD simulations of aromatic cation based ILs[61-62] and aromatic molecular liquids,[13,18,92,123] the reorientational motions of aromatic ring contribute to the whole range of the low-frequency bands and the translational motions

appear in lower-frequency region. The redshift in the high-frequency region above 80 cm^{-1} for the imidazolium- and pyridinium-based ILs was attributed to the slowing down of the librational motions due to an increase of the free volume and/or weakened intermolecular interactions in the ILs.[117,125,134,136] The results of the pyrrolidinium-based ILs in this study show that the spectra in the high-frequency region above 50 cm^{-1} seem to be less sensitive to the temperature except for [$Pyrr_{14}$][DCA] and [$Pyrr_{14}$][TCM]. The pyrrolidinium skeleton is not planar. Thus, because there are no large contributions of the librational motions to the spectra in this frequency region, the spectra in the high-frequency region are less sensitive to the temperature. However, the spectrum of [$Pyrr_{14}$][DCA] in the high-frequency region indicated a slight redshift with rising temperature regardless of the absence of an aromatic ring, as shown in Figure 5.3. This is also true for [$Pyrr_{14}$][TCM] (Figure 5.11, vide infra). I will discuss this feature of [$Pyrr_{14}$][DCA] and [$Pyrr_{14}$][TCM] in Section 4.1.1.2.

Unlike common steady-state (depolarized) Raman spectrum measurements, the fs-RIKES measures simultaneously both the Stokes and anti-Stokes Raman scattering signals.[10,16,153] Thus, it might be presumed that the temperature dependence of the low-frequency spectra arises from the Bose-Einstein thermal occupation factor (see the Appendix E). However, the temperature-dependent spectrum of each IL differs, as seen in Figure 5.3 (and Figures 5.9 and 5.11–13, see below). Furthermore, each IL shows a unique line shape in the difference spectra at a certain temperature relative to 293 K (see Section 4.1.1) which are very different from the difference spectra for the Bose-Einstein thermal occupation factor at a certain temperature relative to 293 K. I am thus confident that the temperature-dependent features of the ILs mainly arise from the temperature-dependent intermolecular vibrations. Below, I will discuss in detail the temperature dependence of the low-frequency spectra of the pyrrolidinium-based ILs.

5.4.1.1. Effects of Different Anions.

The low-frequency spectral shapes below ca. 200 cm^{-1} for the pyrrolidinium-based ILs were found to substantially change depending on the anion species, where their temperature dependence is rather characteristic. The temperature-dependent features, such as line shapes and spectral intensity, of the low-frequency spectra of the pyrrolidinium-based ILs can be roughly classified into three representative types.

5.4.1.1.1. [Pyrr$_{1(1O2)}$][PF$_6$], [Pyrr$_{1(1O2)}$][BF$_4$], and [Pyrr$_{14}$][OTf].

Figures 5.3 and 5.9 present the temperature-dependent low-frequency spectra (< 200 cm^{-1}) and the difference spectra at each temperature relative to those of 293 K for [Pyrr$_{1(1O2)}$][PF$_6$], [Pyrr$_{1(1O2)}$][BF$_4$], and [Pyrr$_{14}$][OTf]. They show simple and monomodal spectra. [PF$_6$]$^-$ and [BF$_4$]$^-$ are spherical top anions and their contributions to the low-frequency Kerr spectra are expected to be small due to their symmetry. Thus the low-frequency spectra of these ILs reflect mainly the contributions of the pyrrolidinium cations, leading to similar simple spectral shapes for both [Pyrr$_{1(1O2)}$][PF$_6$] and [Pyrr$_{1(1O2)}$][BF$_4$]. This is in contrast with the case of the imidazolium-based ILs, where the spectral intensity in the low-frequency region below ca. 50 cm^{-1} relative to the high-frequency region at ca. 100 cm^{-1} is lower for [C$_4$MIm][PF$_6$] than [C$_4$MIm][BF$_4$].[54] This can be explained as follows. The spectral density in the low-frequency region below ca. 50 cm^{-1} includes the influence of the translational motions of the anions and/or the coupling motions with the cations.[54] Because the contributions to the spectral density from the imidazolium cations are much larger than those from the pyrrolidinium cations due to the larger polarizability anisotropy of the former cations than those of the latter cations,[53,56] indirect effects of anions through the coupling motions with cations on the spectral density in the low-frequency region would be greater for the imidazolium-based ILs than the pyrrolidinium-based ILs if the coupling strengths are similar in both the ILs. Because the contributions to the spectral density from the imidazolium cations are much larger than those from the pyrrolidinium cations, indirect effects of anions through the coupling motions with cations on the spectral density in the low-frequency region would be greater for the imidazolium-based ILs than the pyrrolidinium-based ILs. In other words, the pyrrolidinium cations have small spectral intensities compared to comparable imidazolium cations, hampering the elucidation of the effect of the anion species via coupling motions with the cation species. This would be the reason behind the clear difference between [PF$_6$]$^-$ and [BF$_4$]$^-$ is found in the imidazolium-based ILs but not found in the pyrrolidinium-based ILs.

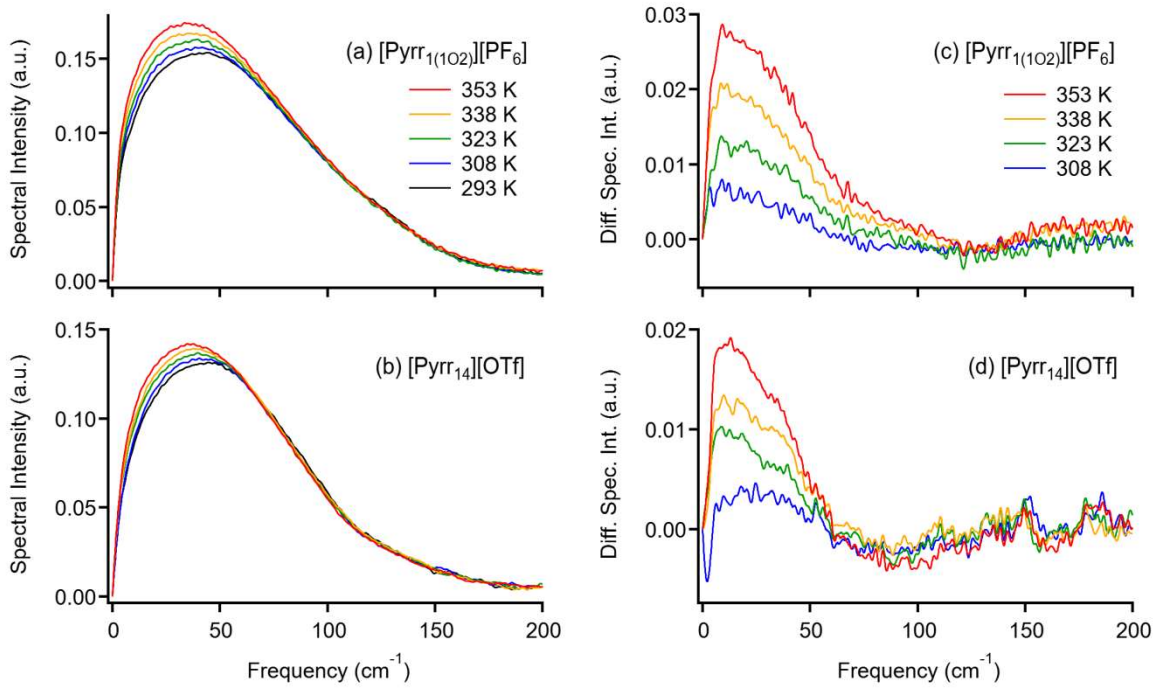

Figure 5.9. Temperature-dependent low-frequency spectra of (a) $[Pyrr_{1(1O2)}][PF_6]$ and (b) $[Pyrr_{14}][OTf]$ at 293 K (black), 308 K (blue), 323 K (green), 338 K (yellow), and 353 K (red). Difference Kerr spectra of (c) $[Pyrr_{1(1O2)}][PF_6]$ and (d) $[Pyrr_{14}][OTf]$ at 308 K (blue), 323 K (green), 338 K (yellow), and 353 K (red) relative to those at 293 K are also shown.

$[Pyrr_{14}][OTf]$ also exhibits a simple spectral shape regardless of the rather complex structure of $[OTf]^-$ anion (Figure 5.9b). The line shape of the low-frequency spectrum of $[Pyrr_{14}][OTf]$ is quite similar to those of $[Pyrr_{1(1O2)}][PF_6]$ and $[Pyrr_{1(1O2)}][BF_4]$, as well as the spectral intensity. In fact, the polarizability anisotropy of $[OTf]^-$ anion is very small compared to typical asymmetric anions ($[OTf]^-$: 0.309 Å^3; $[NTf_2]^-$: 4.065 Å^3 at the B3LYP/6-31+G(d,p) level of theory).[71] Therefore, it is not surprising that the contribution of $[OTf]^-$ anion to the low-frequency Kerr spectral density is not that large. In other words, the low-frequency spectral density of $[Pyrr_{14}][OTf]$ is mainly due to the cation, and thus it is quite similar to those of $[Pyrr_{1(1O2)}][PF_6]$ and $[Pyrr_{1(1O2)}][BF_4]$. The temperature-dependent spectral features of $[Pyrr_{1(1O2)}][PF_6]$, $[Pyrr_{1(1O2)}][BF_4]$, and $[Pyrr_{14}][OTf]$ are also similar, as shown in Figure 5.3d, 5.9c, and 5.9d. The shapes of the difference spectra for these ILs resemble, as well. In addition, the changes of the spectral intensities at peaks, $\Delta\text{Int} = I_T - I_{293}$, by temperature relative to 293 K for these ILs are also quite different from those of other ILs, as shown in Figure 5.10 that shows the temperature dependence of the intensities of difference spectra relative to 293 K for the present ILs. The slopes b estimated by liner fits, $\Delta\text{Int} = b(T - 293)$, are summarized in Table

5.1. It is clear from Figure 5.10a and b and Table 5.1 that $[Pyrr_{1(1O2)}][PF_6]$, $[Pyrr_{1(1O2)}][BF_4]$, and $[Pyrr_{14}][OTf]$ show less temperature sensitivity in spectral intensity by temperature (~4×10^{-4} K^{-1}) than other ILs (>5×10^{-4} K^{-1}). Such a similarity is also the result of the small contributions of these anions to the Kerr spectral density.

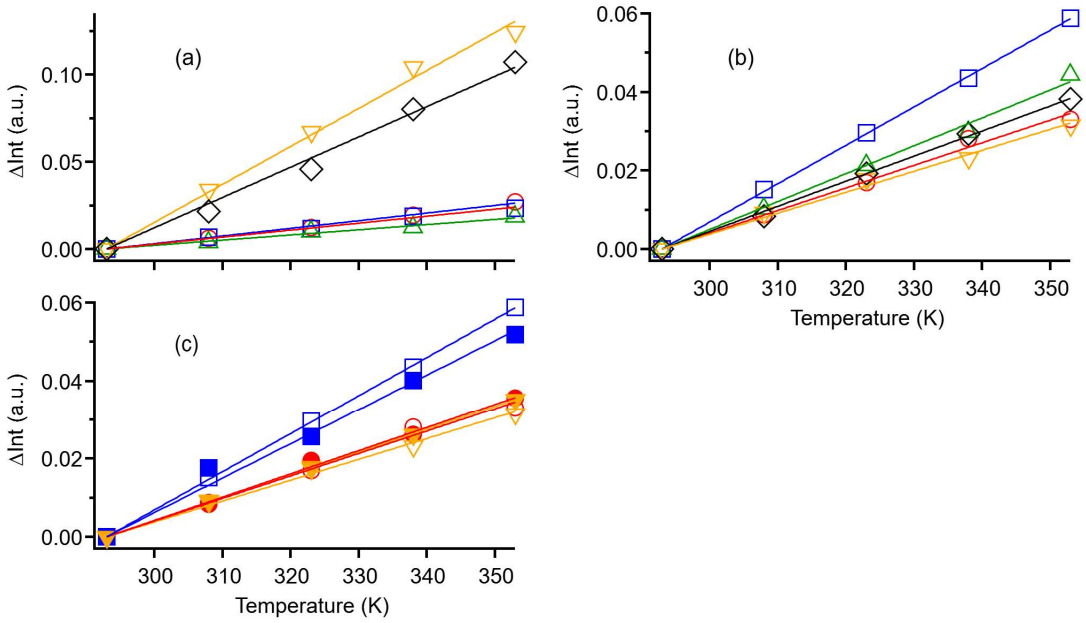

Figure 5.10. Temperature dependence of the change of the spectral intensity by temperature (maximum intensity in the difference spectrum) for (a) $[Pyrr_{1(1O2)}][PF_6]$ (red circles), $[Pyrr_{1(1O2)}][BF_4]$ (blue squares), $[Pyrr_{14}][OTf]$ (green triangles), $[Pyrr_{14}][DCA]$ (yellow inverted triangles), $[Pyrr_{14}][TCM]$ (black diamonds) and (b) $[Pyrr_{14}][NTf_2]$ (red circles), $[Pyrr_{14}][NF_2]$ (blue squares), $[Pyrr_{14}][NPf_2]$ (green triangles), $[Pyrr_{14}][NCyF]$ (yellow inverted triangles), $[Pyrr_{14}][FAP]$ (black diamonds). (c) compares $[Pyrr_{14}]^+$- (open symbols) and $[Pyrr_{1(1O2)}]^+$-based ILs (filled symbols) with $[NTf_2]^-$ (red circles), $[NF_2]^-$ (blue squares), and $[NCyF]^-$ (yellow inverted triangles). Linear fits are shown by solids lines.

5.4.1.1.2. [Pyrr$_{14}$][DCA] and [Pyrr$_{14}$][TCM].

The spectral shapes of $[Pyrr_{14}][DCA]$ and $[Pyrr_{14}][TCM]$ are also simple and monomodal aside from the remarkable intramolecular vibrational bands at 180 and 157 cm^{-1}, respectively, as shown in Figures 5.3b and 5.11a. These intramolecular vibrational bands are of the anions.[71] The spectrum of $[Pyrr_{14}][TCM]$ is narrower than that of $[Pyrr_{14}][DCA]$ in the high-frequency region above 50 cm^{-1}. This feature was also reported in several other imidazolium-based ILs.[71] In that report, the narrowing in the high-frequency region above 50 cm^{-1} for the spectrum of

[C_4MIm][TCM] compared to [C_4MIm][DCA] was attributed to more homogeneous liquid structure arising from the stacking of the imidazolium cation and $[TCM]^-$ anion through π-π interactions and planar structures.[71] However, a stacked complex in the pyrrolidinium-based ILs is unlikely formed through π-π interactions, since the pyrrolidinium cation does not possess π electrons and is not planar. Because the intensities of the low-frequency spectra of [$Pyrr_{14}$][DCA] and [$Pyrr_{14}$][TCM] are much greater than those of the [$Pyrr_{1(1O2)}$][PF_6], [$Pyrr_{1(1O2)}$][BF_4], and [$Pyrr_{14}$][OTf] spectra (Figures 5.3, 5.9, and 5.11), the librational motions of $[DCA]^-$ and $[TCM]^-$ anions likely contribute to the spectral densities. $[TCM]^-$ anion is bigger than $[DCA]^-$ anion, and thus the inertia moment of $[TCM]^-$ anion should be larger than that of $[DCA]^-$ anion. This can influence the librational frequency: $[TCM]^-$ anion is slower than $[DCA]^-$ anion. Previous quantum chemistry calculations at the B3LYP/6-31+G(d,p) level of theory support this scenario: the rotational constants of $[TCM]^-$ anion (2.834, 2.834, and 1.417 GHz for *X*, *Y*, and *Z* coordinates, respectively) are smaller than the respective rotational constants of $[DCA]^-$ anion (46.628, 2.917, and 2.745 GHz for *X*, *Y*, and *Z* coordinates, respectively).[71]

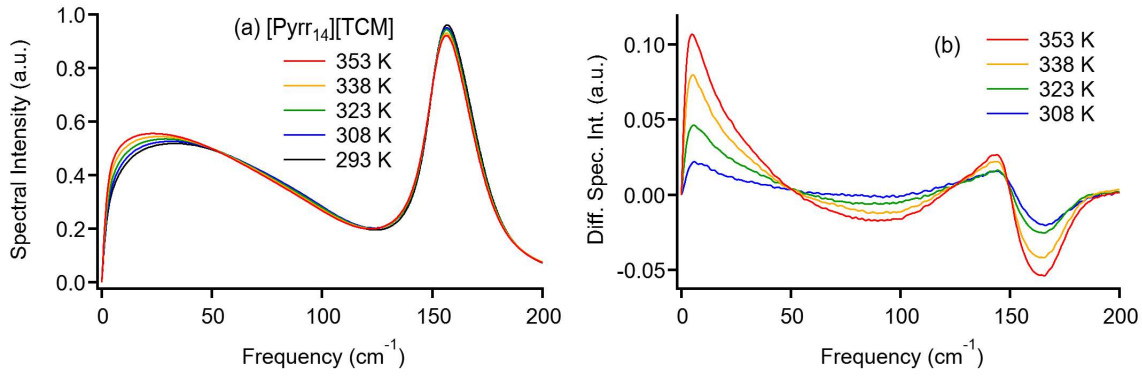

Figure 5.11. (a) Temperature-dependent low-frequency spectra of [$Pyrr_{14}$][TCM] at 293 K (black), 308 K (blue), 323 K (green), 338 K (yellow), and 353 K (red). (b) Difference Kerr spectra of [$Pyrr_{14}$][TCM] at 308 K (blue), 323 K (green), 338 K (yellow), and 353 K (red) relative to that at 293 K are also shown.

The temperature-dependent features of the low-frequency spectra of [$Pyrr_{14}$][DCA] and [$Pyrr_{14}$][TCM] are unique compared to those of the other present ILs, as seen in Figures 5.3 and 5.11. In addition to the increase in the spectral intensity in the low-frequency region below ca. 50 cm^{-1}, the spectrum in the high-frequency region above ca. 50 cm^{-1} shifts to lower frequency

side with increasing temperature. These features are clearly observed in the difference spectra; a large increase in the spectral intensity at ca. 5 cm^{-1} and a broad decrease in the frequency range of ca. 50–130 cm^{-1} with increasing temperature. The latter temperature dependence can be attributed to the effects of $[DCA]^-$ and $[TCM]^-$ anions because the other nonaromatic ILs with different anions do not exhibit this unique feature. In fact, such a redshift with increasing temperature was also observed in imidazolium- and pyridinium-based ILs, as mentioned in Chapter 3 and 4. It would be reasonable to think that the mechanism behind the spectral changes with increasing temperature in the aromatic cation based ILs is also valid for $[Pyrr_{14}][DCA]$ and $[Pyrr_{14}][TCM]$ as their spectra present a similar temperature dependence. As described in Chapter 8, benzene and 1,3-cyclohexadiene showed broad and trapezoidal spectra, while 1,4-cyclohexadiene and cyclohexene presented triangular shapes and cyclohexane showed a monomodal line shape. These features are rationalized based on their molecular structures. Benzene and 1,3-cyclohexadiene have conjugated double bonds, which lead to planar structures. These planar structures may broaden the spectra due to the librational motions. On the other hand, 1,4-cyclohexadiene, cyclohexene, and cyclohexane do not bear conjugated bonds, and thus they do not take rigid planar structures. This means that the contribution of the librational motions of nonaromatic rings to the spectra are not important. This explanation would also be valid for $[DCA]^-$ and $[TCM]^-$ anions. $[DCA]^-$ and $[TCM]^-$ anions are planar structures providing the Raman-active librational motions. Furthermore, a calculated density of state spectrum of 1-butyl-3-methylimidazolium-based IL with a flat anion, that is, nitrate, calculated by MD simulation is broader than the ILs with other anions including $[BF_4]^-$, $[PF_6]^-$, and $[NTf_2]^-$.[99] In addition, the polarizability anisotropy values of these anions are quite large (8.237 $Å^3$ for $[DCA]^-$ and 6.973 $Å^3$ for $[TCM]^-$ at the B3LYP/6-31+G(d,p) level of theory)[71] showing strong depolarized Raman intensities. These librational motions should slow down due to the increasing of the free volume and/or the weakening the intermolecular interaction of the ILs with rising temperature, as is the case of aromatic cation based ILs, which gives a redshift of the low-frequency spectra.[117] As a matter of fact, $[C_4MIm][SCN]$ and $[C_4MIm][DCA]$ also showed similar unique temperature-dependent features that can be attributed to the anions' motions. It should also be noted that the wider spectra of $[Pyrr_{14}][DCA]$ and $[Pyrr_{14}][TCM]$ than those of $[Pyrr_{1(1O2)}][PF_6]$, $[Pyrr_{1(1O2)}][BF_4]$, and $[Pyrr_{14}][OTf]$ are the result of the anions' librations. It is also noted that the extremely strong temperature dependence of the intensities for the two ILs ($\sim 2\times10^{-3}$ K^{-1}) compared to other ILs ($<1\times10^{-3}$ K^{-1}), as shown in Figure 5.10a

and b and Table 5.1, are accounted for by the large polarizability anisotropies in comparison with other anions.

5.4.1.1.3. [Pyrr$_{14}$][NTf$_2$], [Pyrr$_{14}$][NF$_2$], [Pyrr$_{14}$][NPf$_2$], [Pyrr$_{14}$][NCyF], and [Pyrr$_{14}$][FAP].

When comparing the low-frequency spectra below 200 cm^{-1} of [Pyrr$_{14}$][NTf$_2$], [Pyrr$_{14}$][NF$_2$], [Pyrr$_{14}$][NPf$_2$], and [Pyrr$_{14}$][NCyF] at 293 K shown in Figures 5.3 and 5.12, it is clearly found that the pyrrolidinium-based ILs with [NTf$_2$]$^-$, [NF$_2$]$^-$, [NPf$_2$]$^-$, and [NCyF]$^-$ anions show unique triangular spectral shapes with the peaks at 16–20 cm^{-1}. Such characteristic peaks have also been observed in the range of ca. 14–21 cm^{-1} for the imidazolium-based ILs with these anions, which were assigned to the anions' librations and/or the coupling of translational and reorientational motions.[54,71] This is also likely true for the pyrrolidinium-based ILs. These anions' motions result in the low-frequency spectra of the ILs bearing these anions being quite different from those of the ILs with the other anions. The intensities of the low-frequency spectra mainly arising from the intermolecular vibrations of the pyrrolidinium ILs with [NTf$_2$]$^-$, [NF$_2$]$^-$, [NPf$_2$]$^-$, and [NCyF]$^-$ anions are varied with temperature change only in the low-frequency region below 50 cm^{-1}. Such a spectral change with the temperature was also observed in [Pyrr$_{1(1O2)}$][PF$_6$], [Pyrr$_{1(1O2)}$][BF$_4$], and [Pyrr$_{14}$][OTf], but the [DCA]$^-$ and [TCM]$^-$ salts further show a spectral change in the high-frequency region above 50 cm^{-1} with the temperature (Figures 5.3c and 5.12).

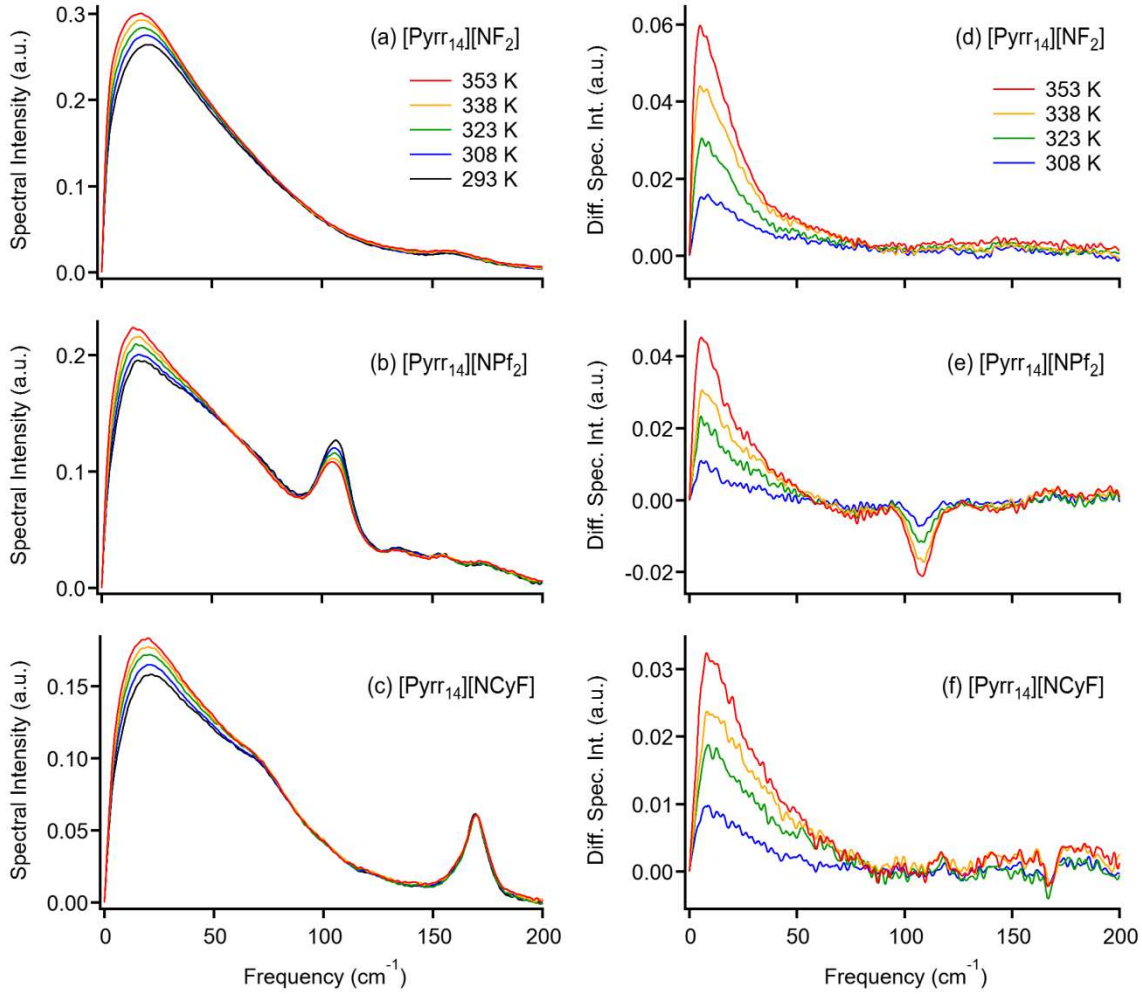

Figure 5.12. Temperature-dependent low-frequency spectra of (a) $[Pyrr_{14}][NF_2]$, (b) $[Pyrr_{14}][NPf_2]$, and (c) $[Pyrr_{14}][NCyF]$ at 293 K (black), 308 K (blue), 323 K (green), 338 K (yellow), and 353 K (red). Difference Kerr spectra of (d) $[Pyrr_{14}][NF_2]$, (e) $[Pyrr_{14}][NPf_2]$, and (f) $[Pyrr_{14}][NCyF]$ at 308 K (blue), 323 K (green), 338 K (yellow), and 353 K (red) relative to those at 293 K are also shown.

However, the line shapes of the difference spectra of the pyrrolidinium-based ILs with $[NTf_2]^-$, $[NF_2]^-$, $[NPf_2]^-$, and $[NCyF]^-$ anions are triangular with the peaks at ca. 10 cm^{-1} and obviously different from those of $[Pyrr_{1(1O2)}][PF_6]$, $[Pyrr_{1(1O2)}][BF_4]$, and $[Pyrr_{14}][OTf]$, as seen in Figures 5.3f and 5.12. As mentioned in the Introduction of Section 5.4, one possibility of increasing the spectral intensities in the low-frequency region by heating is the thermal activation of the translational vibrational motions of cations and anions. This is expected to be affected by the formula weights of ions, that is, the translational vibrational motions are likely slower for heavier ions. $[NTf_2]^-$, $[NF_2]^-$, $[NPf_2]^-$, and $[NCyF]^-$ anions are heavier (> 180 g/mol)

than other anions (< 150 g/mol) except in the case of $[FAP]^-$ (445.01 g/mol). Thus, the spectral densities due to the translational vibrations of $[NTf_2]^-$, $[NF_2]^-$, $[NPf_2]^-$, and $[NCyF]^-$ anions seem to appear in the lower frequency region compared to those of $[PF_6]^-$, $[BF_4]^-$, and $[OTf]^-$ anions. Of course, the librations of $[NTf_2]^-$, $[NF_2]^-$, $[NPf_2]^-$, and $[NCyF]^-$ anions likely appear in ca. 20 cm^{-1} region[54,71] and they can contribute to the difference spectra, but this should provide a negative change, as shown in the librations of imidazolium cations[117,125,134,136] and $[DCA]^-$ and $[TCM]^-$ anions (Figures 5.3 and 5.11). Thus, the contributions of the librations of $[NTf_2]^-$, $[NF_2]^-$, $[NPf_2]^-$, and $[NCyF]^-$ anions to the difference spectra are negligibly small.

Finally, we briefly mention the spectral features of $[Pyrr_{14}][FAP]$ whose anion has a rather complicated structure. Figure 5.13 presents the temperature-dependent low-frequency spectra below 200 cm^{-1} and the difference spectra for $[Pyrr_{14}][FAP]$. Previously, the imidazolium-based ILs with $[FAP]^-$ were found to show a bimodal spectral shape, where the strong intensity at 10 cm^{-1} was attributed to the intermolecular vibration of $[FAP]^-$ anion, as in the case of the ILs with $[NTf_2]^-$, $[NF_2]^-$, $[NPf_2]^-$, and $[NCyF]^-$ anions.[54] It is seen from Figures 5.12 and 5.13 that the line shape of the low-frequency spectrum of $[Pyrr_{14}][FAP]$ is similar to that of the $[Pyrr_{14}][NTf_2]$, $[Pyrr_{14}][NF_2]$, $[Pyrr_{14}][NPf_2]$, and $[Pyrr_{14}][NCyF]$ spectra. However, the relative intensity at ca. 18 cm^{-1} in the low-frequency spectrum of $[Pyrr_{14}][FAP]$ is slightly lower than those in the low-frequency region at ca. 20 cm^{-1} of the $[Pyrr_{14}][NTf_2]$, $[Pyrr_{14}][NF_2]$, $[Pyrr_{14}][NPf_2]$, and $[Pyrr_{14}][NCyF]$ spectra. For this, two possibilities exist. One is the lower activity of the translational vibrational motion of the heavier $[FAP]^-$ anion compared to the other anions. Such phenomena have indeed been observed in $[C_4MIm]^+$-based ILs with $[PF_6]^-$, $[AsF_6]^-$, and $[SbF_6]^-$ anions[52,61] and polymer solutions.[23,110-111] The other one is the relatively small polarizability anisotropy of $[FAP]^-$ anion (3.138 $Å^3$ at the B3LYP/6-31+G(d,p) level of theory,[54] which is slightly smaller than $[NTf_2]^-$ anion: 4.065 $Å^3$).[71] It is hard to conclude which effect is dominant at present, but both the effects likely exist. The temperature-dependent spectral feature and the difference spectra of $[Pyrr_{14}][FAP]$ are however similar to those of $[Pyrr_{14}][NTf_2]$, $[Pyrr_{14}][NF_2]$, $[Pyrr_{14}][NPf_2]$, and $[Pyrr_{14}][NCyF]$. The temperature sensitivity in intensity for this group of ILs (5–10 × 10^{-4} K^{-1}) is in between the group of $[Pyrr_{1(1O2)}][PF_6]$, $[Pyrr_{1(1O2)}][BF_4]$, and $[Pyrr_{14}][OTf]$ (~4 × 10^{-4} K^{-1}) and that of $[Pyrr_{14}][DCA]$ and $[Pyrr_{14}][TCM]$ (~2 × 10^{-3} K^{-1}), as shown in Figure 5.10a and b and Table 5.1.

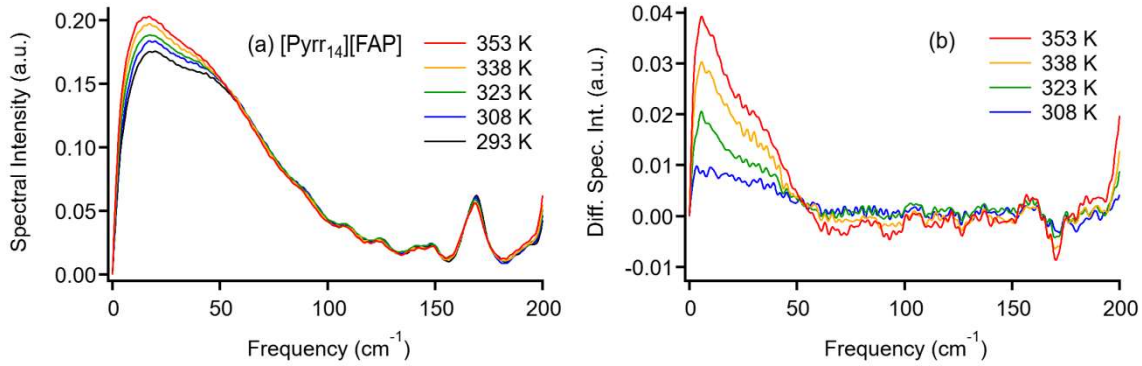

Figure 5.12. (a) Temperature-dependent low-frequency spectra of [$Pyrr_{14}$][FAP] at 293 K (black), 308 K (blue), 323 K (green), 338 K (yellow), and 353 K (red). (b) Difference Kerr spectra of [$Pyrr_{14}$][FAP] at 308 K (blue), 323 K (green), 338 K (yellow), and 353 K (red) relative to that at 293 K.

5.4.1.2. Comparison between Butyl and 2-Methoxyethyl Groups in Cation.

The substitution of alkyl groups in cations with their homologous ether groups in side groups of cations generally changes the physical properties of ILs.[116,154-156] In particular, the melting point, glass transition temperature, and viscosity of ILs are lowered by replacing the alkyl chain with the corresponding ether group. This can be ascribed to the flexibility of the ether group compared to the corresponding alkyl group. On the other hand, upon comparing the spectra between the $[Pyrr_{14}]^+$- and $[Pyrr_{1(1O2)}]^+$-based ILs with same anions, it is clear that the effects of ether substitution on the low-frequency spectra are not particularly large, as shown in Figure 5.14a. Figure 5.14a shows the low-frequency spectra at 293 K for [$Pyrr_{14}$][NF_2] and [$Pyrr_{1(1O2)}$][NF_2]. The spectral intensity of [$Pyrr_{1(1O2)}$][NF_2] in the range of 70–150 cm^{-1} is slightly larger than that of [$Pyrr_{14}$][NF_2]. This feature is also observed in the cases of [$Pyrr_{1(1O2)}$][NTf_2] vs. [$Pyrr_{14}$][NTf_2] and [$Pyrr_{1(1O2)}$][NCyF] vs. [$Pyrr_{14}$][NCyF]. The effects of ether substitutions on the low-frequency spectra of nonaromatic ILs have previously been investigated.[116] By comparing the low-frequency spectra of triethyloctylammonium bis(trifluoromethylsulfonyl)amide [N_{2228}][NTf_2] and (2-ethoxy-ethoxy)ethyltriethylammonium bis(trifluoromethylsulfonyl)amide [$N_{222(2O2O2)}$][NTf_2], and those of triethyloctylphosphonium bis(trifluoromethylsulfonyl)amide [P_{2228}][NTf_2] and (2-ethoxyethoxy)ethyltriethylphosphonium bis(trifluoromethylsulfonyl)amide [$P_{222(2O2O2)}$]-[NTf_2], the M_1 values of the low-frequency spectra were observed to shift to higher frequencies upon substituting the (2-ethoxyethoxy)ethyl groups for octyl groups in both ammonium- and phosphonium-based ILs. These spectral differences are consistent with those for the

pyrrolidinium-based ILs studied here, although the number of oxygen atoms introduced is different.

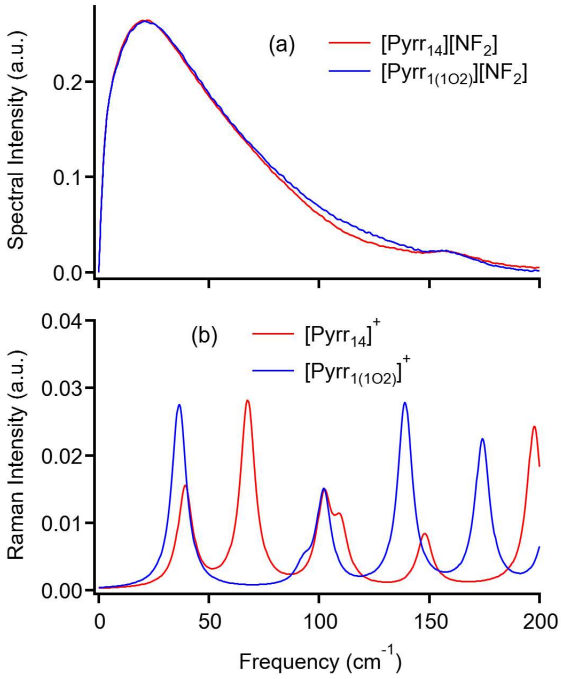

Figure 5.14. (a) Comparison of the low-frequency spectra of $[Pyrr_{14}][NF_2]$ (red) and $[Pyrr_{1(1O2)}][NF_2]$ (blue) at 293 K in the range of 0–200 cm^{-1} and (b) calculated Raman spectra for $[Pyrr_{14}]^+$ (red) and $[Pyrr_{1(1O2)}]^+$ (blue) cations at the B3LYP/6-311++G(d,p) level of theory in the frequency range of 0–200 cm^{-1}.

Let us consider the origin of the spectral difference between $[Pyrr_{14}]^+$- and $[Pyrr_{1(1O2)}]^+$-based ILs together with the quantum chemistry calculation results. Figure 5.14b shows the calculated Raman spectra of the optimized structures of $[Pyrr_{14}]^+$ and $[Pyrr_{1(1O2)}]^+$ cations in the expanded frequency range of 0–200 cm^{-1} in Figure 5.8. Several intramolecular vibrational modes with strong Raman intensities are observed in the high-frequency region above 300 cm^{-1}, while the modes in the low-frequency region below 200 cm^{-1} show weak intensities, as shown in Figure 5.8. Looking closely at the calculated spectra below 200 cm^{-1}, however, a difference in intramolecular modes between $[Pyrr_{14}]^+$ and $[Pyrr_{1(1O2)}]^+$ cations is observed in Figure 5.14b. The intramolecular modes at 139 cm^{-1} (rocking mode of the pyridinium ring together with the 2-methoxyethyl group) and 174 cm^{-1} (bending mode of the pyrrolidinium ring and the 2-methoxyethyl group) of $[Pyrr_{1(1O2)}]^+$ cation make relatively large contributions, while that at 148 cm^{-1} of $[Pyrr_{14}]^+$ cation is relatively small. Considering that the scaling factor for the

frequencies calculated at the B3LYP/6-311+G(d,p) level of theory is 0.9679,[157] the differences observed in the experimental spectra between $[Pyrr_{14}]^+$ and $[Pyrr_{1(1O2)}]^+$ cations seem to be attributed to the intramolecular vibrational modes of the cations.

In addition to the intramolecular vibrational modes, the temperature-dependent features of the low-frequency spectra arising mainly from the intermolecular vibrations of the $[Pyrr_{14}]^+$- and $[Pyrr_{1(1O2)}]^+$-based ILs are almost the same (see Appendix E). It is also clear from Table 5.1 that the temperature dependence of the M_1 of the low-frequency spectra is similar for the $[Pyrr_{14}]^+$- and $[Pyrr_{1(1O2)}]^+$-based ILs with the same anions. It is also found from Figure 5.10c and Table 5.1 that the temperature sensitivities in intensities between $[Pyrr_{14}]^+$- and $[Pyrr_{1(1O2)}]^+$-based ILs with the same anions are similar. Accordingly, the discussion on the effects of anions on the temperature-dependent spectral features discussed in Section 5.4.1.1 is reasonable without having to differentiate the cations.

5.4.1.3. Temperature Dependence of the First Moments of Low-Frequency Spectra.

Now, let us see the temperature dependence of the low-frequency spectra semi-quantitatively based on the M_1 values of the IL spectra. The slopes of the linear fits can be considered to represent the sensitivity of the low-frequency spectra to the temperature. The values of the slopes roughly depend on the anion species. This is in contrast to the case of imidazolium-based ILs.[117] Namely, the temperature dependence of M_1 for imidazolium-based ILs is largely governed by the imidazolium ring. The temperature dependence of M_1 for the imidazolium-based ILs with various anions is similar, except for some specific anions, e.g., $[DCA]^-$ and $[SCN]^-$ anions. Because the pyrrolidinium cations in the present ILs exhibit much smaller spectral densities in the low-frequency spectra than the imidazolium cations previously studied, it is not surprising that the pyrrolidinium-based ILs show an anion dependence of the temperature sensitivities in the low-frequency spectra. By comparing the temperature sensitivities of the low-frequency spectra of the pyrrolidinium-based ILs (*a* values, Table 5.1) with those of the imidazolium-based ILs, the *a* values are less negative for the pyrrolidinium-based ILs than for the imidazolium-based ILs.[117] Below, we will see the features of the different anion species.

The slopes for the ILs with $[PF_6]^-$, $[BF_4]^-$, and $[OTf]^-$ anions are about -0.05 $cm^{-1}K^{-1}$, which are values more negative (namely, steeper slopes) than those of the ILs with $[NTf_2]^-$, $[NF_2]^-$, and $[NPf_2]^-$ anions (-0.03 to -0.04 $cm^{-1}K^{-1}$), as shown in Table 5.1. In fact, such a feature has also been observed in the imidazolium-based ILs (-0.055 $cm^{-1}K^{-1}$ for ILs with

spherical top anions; −0.051 $cm^{-1}K^{-1}$ for ILs with $[NTf_2]^-$, $[NF_2]^-$, and $[NPf_2]^-$ anions),[117] although the difference between the former and latter anion groups is much larger for the pyrrolidinium-based ILs than for the imidazolium-based ILs. The difference between the pyrrolidinium- and imidazolium-based ILs might be due to the fact that the contributions to the low-frequency spectra of the pyrrolidinium cations are much smaller than those of the imidazolium cations relative to those of the anions. The lower temperature sensitivities of the spectra for the $[PF_6]^-$, $[BF_4]^-$, and $[OTf]^-$ salts compared to the $[NTf_2]^-$, $[NF_2]^-$, and $[NPf_2]^-$ salts may arise from the intrinsic natures of the anions.

$[Pyrr_{14}][DCA]$ and $[Pyrr_{14}][TCM]$ show less negative slopes than the $[PF_6]^-$, $[BF_4]^-$, and $[OTf]^-$ salts but similar to those of with the $[NTf_2]^-$, $[NF_2]^-$, and $[NPf_2]^-$ salts. As stated in Chapter 3, however, $[C_4MIm][DCA]$ and $[C_4MIm][SCN]$ show less negative slopes than the $[C_4MIm]^+$-based ILs with other different anions including $[PF_6]^-$, $[BF_4]^-$, $[OTf]^-$, $[NTf_2]^-$, $[NF_2]^-$, and $[NPf_2]^-$ anions. Because $[DCA]^-$ and $[TCM]^-$ anions, as well as $[SCN]^-$ anion, exhibit large polarizability anisotropies,[71] the lower temperature dependence of M_1 for the $[DCA]^-$, $[TCM]^-$, $[SCN]^-$ salts may largely arise from the temperature dependence of the anions' intermolecular vibrational motions.

As displayed in Table 5.1, the intrinsic first moment $M_{1,0}$ values for the pyrrolidinium cation based ILs with $[PF_6]^-$, $[BF_4]^-$, and $[OTf]^-$ anions are approximately 80 cm^{-1} which are larger than those for the ILs with the other anions. The values of $M_{1,0}$ for the $[NTf_2]^-$, $[NF_2]^-$, $[NPf_2]^-$, $[NCyF]^-$, and $[FAP]^-$ salts are approximately 60 cm^{-1}, and those for $[Pyrr_{14}][DCA]$ and $[Pyrr_{14}][TCM]$ are ca. 76 and 65 cm^{-1}, respectively. The line shapes of the low-frequency spectra of $[Pyrr_{1(1O2)}][PF_6]$, $[Pyrr_{1(1O2)}][BF_4]$, and $[Pyrr_{14}][OTf]$ are broad and peaked at higher frequencies compared to those of the other $[Pyrr_{14}]$-ILs and $[Pyrr_{1(1O2)}]$-ILs in nature (Figure 5.3), and thus the high $M_{1,0}$ value in the three ILs is not surprising. The $[NTf_2]^-$, $[NF_2]^-$, $[NPf_2]^-$, $[NCyF]^-$, and $[FAP]^-$ salts show characteristic intermolecular vibrations at ca. 20 cm^{-1} due to the anions, as mentioned in Section 4.1.1.3, which is likely to be lower the values of $M_{1,0}$. The $M_{1,0}$ value for $[Pyrr_{14}][DCA]$ is larger than that for $[Pyrr_{14}][TCM]$, which would reflect the narrowing of the high-frequency region of the spectra due to the slower libration of $[TCM]^-$ anion compared to $[DCA]^-$ anion, which arises from the larger inertia moment of $[TCM]^-$ anion relative to that of $[DCA]^-$ anion, as described in Section 5.4.1.1.2.

Upon comparing the $M_{1,0}$ of $[Pyrr_{14}]^+$-based ILs and $[Pyrr_{1(1O2)}]^+$-based ILs with the same anions ($[NTf_2]^-$, $[NF_2]^-$, and $[NCyF]^-$), the values for the former are smaller than those for the latter. This feature partially arises from the fact that the low-frequency spectra of the

$[Pyrr_{1(1O2)}]^+$-based ILs are broader than those of the $[Pyrr_{14}]^+$-based ILs, as discussed in Section 5.4.1.2.

5.4.2. Fragility of ILs.

As is the case with imidazolium-based ILs (Chapter 3), the fragility of the pyrrolidinium-based ILs are estimated to clarify the relation between the intermolecular vibrational dynamics and the fragility of ILs. Figure 5.15 illustrates the so-called Angell plots[90] for the ILs, except for the ILs not exhibiting glass transitions (Table 5.2). The plots for SiO_2[101,158] and *o*-terphenyl[103,159-160] are also included in the figure; SiO_2 is one of the strongest compounds, while *o*-terphenyl is one of the most fragile ones. The ILs in this study exist in the fragile region rather than in the strong region, as is the case of other reported ILs.[90,107,112,117,134] $[Pyrr_{1(1O2)}][BF_4]$ is stronger than the ILs with other less symmetric anions. $[Pyrr_{14}][TCM]$ is the most fragile among the pyrrolidinium-based ILs studied here. It is also found that $[Pyrr_{14}][NTf_2]$ is more fragile than $[Pyrr_{14}][NF_2]$. These features of the effects of the anions on the fragilities have also been observed in imidazolium-based ILs.[117]

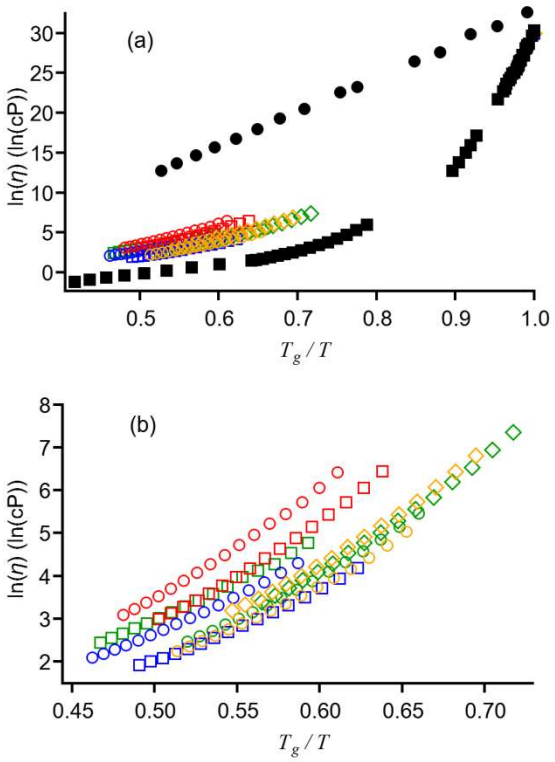

Figure 5.15. (a) Plots of ln(η) vs. T_g/T for SiO_2[101,158] (filled black circles), *o*-terphenyl[103,159-160] (filled black squares), [$Pyrr_{1(1O2)}$][BF_4] (red circles), [$Pyrr_{14}$][OTf] (red squares), [$Pyrr_{14}$][DCA] (blue circles), [$Pyrr_{14}$][TCM] (blue squares), [$Pyrr_{14}$][NTf_2] (green circles), [$Pyrr_{14}$][NF_2] (green squares), [$Pyrr_{14}$][NCyF] (blue diamonds), [$Pyrr_{1(1O2)}$][NTf_2] (yellow circles), [$Pyrr_{1(1O2)}$][NCyF] (yellow diamonds). (b) Magnification scale is given for a clarity of the IL data.

Generally, the ether substitution of alkyl groups in cations significantly affects the physical properties including the fragility.[116,154-156] For example, [$N_{222(2O2O2)}$][NTf_2] and [$P_{222(2O2O2)}$][NTf_2] are more fragile than the corresponding [N_{2228}][NTf_2] and [P_{2228}][NTf_2].[116] Thus, the ether substitution tends to render the ILs more fragile. In this study, the *D* parameter of [$Pyrr_{1(1O2)}$][NTf_2] is smaller than that of [$Pyrr_{14}$][NTf_2], as expected. However, the *D* value of [$Pyrr_{1(1O2)}$][NCyF] is slightly larger than that of [$Pyrr_{14}$][NCyF], contrary to what one would expect. Taking the experimental and fitting errors into consideration, the effects of 2-methoxyethyl group substitution in a butyl group seem to be small relative to (2-ethoxyethoxy)ethyl substitution in an octyl group.[116]

Regarding the relationship between the fragility and the temperature dependence of the low-frequency spectra, no clear correlation between *D* and *a* parameters in imidazolium-based

ILs (Chapter 3). To confirm this relation for the present pyrrolidinium-based ILs, Figure 5.16 plots D^{-1} against a for the pyrrolidinium ILs showing the glass transitions. A linear relation between D^{-1} and a can be identified when the data for [Pyrr$_{14}$][NCyF] and [Pyrr$_{1(1O2)}$][NCyF] are excluded, shown as a solid line rather than a broken line in Figure 5.16. These deviations of [Pyrr$_{14}$][NCyF] and [Pyrr$_{1(1O2)}$][NCyF] are likely due to contributions of the intramolecular vibrational mode of anion at ca. 70 cm^{-1}: the present line shape analysis cannot completely distinguish the intermolecular vibrational component from the low-frequency spectra due to the intramolecular vibrational mode. The linear correlation between the D^{-1} and a parameters indicates a relationship between the fragility and the temperature dependence of the low-frequency spectra in nonaromatic ILs. At the moment, I have no clear reason why there is a linear correlation between the D^{-1} and a parameters, but one can think that this might be an indicative of the coupling between the intermolecular vibration and structural relaxation.

The inconsistency between the pyrrolidinium-based ILs and the imidazolium-based ILs is likely due to the absence/presence of an imidazolium ring. As discussed in Section 5.4.1.3, the imidazolium ring libration governs the temperature sensitivity (a parameter) of the low-frequency spectra in the imidazolium-based ILs. Unlike the imidazolium cations, the pyrrolidinium cations do not exhibit a strong intensity in the low-frequency spectra. As a result, the variations of the low-frequency spectra with the temperature for the pyrrolidinium-based ILs are reflected by the contributions of both cations and anions.

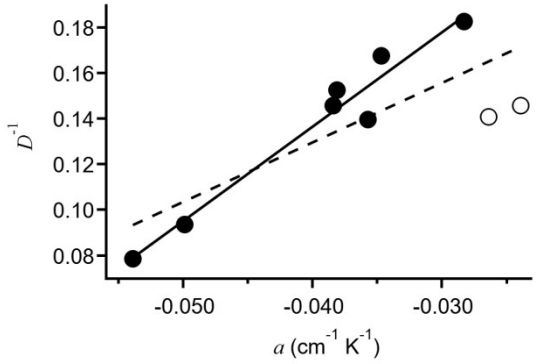

Figure 5.16. Plots of D^{-1} vs. a for [Pyrr$_{1(1O2)}$][BF$_4$], [Pyrr$_{14}$][OTf], [Pyrr$_{14}$][DCA], [Pyrr$_{14}$][TCM], [Pyrr$_{14}$][NTf$_2$], [Pyrr$_{14}$][NF$_2$], and [Pyrr$_{1(1O2)}$][NTf$_2$] (filled circles), and [Pyrr$_{14}$][NCyF] and [Pyrr$_{1(1O2)}$][NCyF] (open circles). Linear fits are also given (broken line: a fit for all data; solid line: a fit excluding the data for [Pyrr$_{14}$][NCyF] and [Pyrr$_{1(1O2)}$][NCyF]).

5.5. Conclusions

In this study, I explored the temperature-dependent features of the low-frequency spectra of pyrrolidinium-based ILs with 10 different anions by fs-RIKES to clarify the effects of anions on the temperature dependence of the low-frequency spectra. The spectral intensity in the low-frequency region below 50 cm^{-1} increased with rising temperature for all the present ILs. This feature has been reasonably explained by the thermal activation of the translational vibrational motions of ions. On the other hand, the spectra in the high-frequency region above ca. 50 cm^{-1} are almost insensitive to the temperature for all the present ILs except for $[Pyrr_{14}][DCA]$ and $[Pyrr_{14}][TCM]$. These ILs show a redshift of the high-frequency region above ca. 50 cm^{-1} of the low-frequency bands with increasing temperature. Because the structures of $[DCA]^-$ and $[TCM]^-$ anions are planar, they should exhibit Raman-active librational motions. These librational motions are redshifted in the high-frequency region of the spectra with increasing temperature, as is the case with the aromatic ring libration in imidazolium-based ILs. The sensitivities of the M_1 values to the temperature for the ILs with spherical top anions and $[OTf]^-$ are higher than those for the ILs with the other anions. The same tendency was also observed in the case of imidazolium-based ILs (Chapter 3), however, this difference between them is more pronounced in the pyrrolidinium-based ILs, which may reflect a smaller influence of the pyrrolidinium cations on the Kerr spectra compared to the imidazolium cations. The values of the intrinsic first moments are smaller for the ILs with $[NTf_2]^-$, $[NF_2]^-$, $[NPf_2]^-$, $[NCyF]^-$, and $[FAP]^-$ anions than those for other ILs, which is likely attributed to the intermolecular vibrations of these anions located at ca. 20 cm^{-1}. The temperature sensitivities of the low-frequency spectra of $[Pyrr_{1(1O2)}][PF_6]$, $[Pyrr_{1(1O2)}][BF_4]$, and $[Pyrr_{14}][OTf]$ are particularly significant out of the 13 pyrrolidinium-based ILs investigated in this study.

The temperature-dependent viscosities and the glass transition temperatures were also measured. The D parameters related to the fragilities of the ILs have been determined by the VTF fits for the temperature-dependent viscosities. We have found a linear correlation between the temperature sensitivity parameter a of M_1 and the fragility parameter D^{-1} for the pyrrolidinium-based ILs, except for the ILs showing no glass transition and the $[NCyF]^-$ salts.

Chapter 6

Comparison of Temperature-Dependent Low-Frequency Spectra between Dicationic and Monocationic Ionic Liquids

J. Phys. Chem. B, **2015**, *119*, 9835–9846.

6.1. Introduction

Most of ILs which have been essential target of IL research including ultrafast dynamics consist of one cation and one anion, that is, monocationic. More recently, however, dicationic ILs, which are composed of one dication and two monoanions, have been getting more attention because of their interesting features such as higher decomposition temperature, higher surface tension, and higher viscosity than corresponding monocationic ILs.[72,161-166] Shirota and coworkers have investigated the low-frequency spectra of dicationic ILs by fs-RIKES in 2011 and compared to those of the corresponding monocationic ILs, making the following observations from the comparison:[167] First, almost no dependence of the low-frequency spectrum of the dicationic ILs on the alkylene linker was observed. However, the different alkyl groups of the imidazolium cation gave different line shapes in the low-frequency spectra. Second, the spectral intensity in the low-frequency (less than 20 cm^{-1}) region relative to that in the medium-frequency (at approximately 80 cm^{-1}) region was slightly lower in the dicationic ILs than in the reference monocationic ILs. In that study, the anion species in the ILs were fixed, and the number of alkyl-group carbon atoms in the monocations was the same as the number of the carbon atoms in the alkylene linkers of the dications per charge; for example, the 1-methyl-3-propylimidazolium ($[C_3MIm]^+$) monocation had three carbon atoms in the propyl group, whereas the 1,6-bis(3-methylimidazolium-1-yl)hexane ($[C_6(MIm)_2]^{2+}$) dication had six carbon atoms in the alkylene linker. In a molecular dynamics (MD) simulation study,[62] they concluded that the difference between the low-frequency spectra of the monocationic and dicationic ILs was due to the suppression of the anion motion and the coupling motion between the anion and the cation, rather than to just the change in the cation.

In this chapter, the temperature dependence of the low-frequency spectra of the bis(trifluoromethylsulfonyl)amide ($[NTf_2]^-$) salts of 1-methyl-3-propylimidazolium and 1-hexyl-3-methylimidazolium monocations and 1,6-bis(3-methylimidazolium-1-yl)hexane and 1,12-bis(3-methylimidazolium-1-yl)dodecane dications has been investigated by fs-RIKES. The primary goals in this study are the following: (i) understanding the general features of the temperature-dependent spectra in the $[NTf_2]^-$ salts of imidazolium cations, (ii) clarifying the difference in the temperature dependence of the low-frequency spectra between dicationic and monocationic ILs, and (iii) finding the alkylene- linker/alkyl-group dependence of the low-frequency spectra. In addition, temperature-dependent viscosities of ILs are also measured to find the relation between the intermolecular vibrational dynamics and the fragility in the case of dicationic ILs.

6.2. Experimental Methods

The ILs used here were 1-methyl-3-propylimidazolium bis(trifluoromethylsulfonyl)amide ($[C_3MIm][NTf_2]$), 1-hexyl-3-methylimidazolium bis(trifluoromethylsulfonyl)amide ($[C_6MIm][NTf_2]$), 1,6-bis(3-methylimidazolium-1-yl)hexane bis(trifluoromethylsulfonyl)-amide ($[C_6(MIm)_2][NTf_2]_2$), and 1,12-bis(3-methylimidazolium-1-yl)-dodecane bis(trifluoromethylsulfonyl)amide ($[C_{12}(MIm)_2][NTf_2]_2$). The structural formulas of the cations and anion are shown in Figure 6.1. The IL samples used in this study were synthesized previously, and the details of the synthesis procedures and assignments of the ILs have been reported elsewhere.[72] Prior to the viscosity measurements, the ILs were dried at a vacuum oven in 313 K for 36 h. The water contents of the ILs were estimated with a Karl Fischer titration coulometer (Hiranuma, AQ-300) as 77, 83, 53, and 49 ppm for $[C_3MIm][NTf_2]$, $[C_3MIm][NTf_2]$, $[C_6(MIm)_2][NTf_2]_2$, and $[C_{12}(MIm)_2][NTf_2]_2$, respectively.

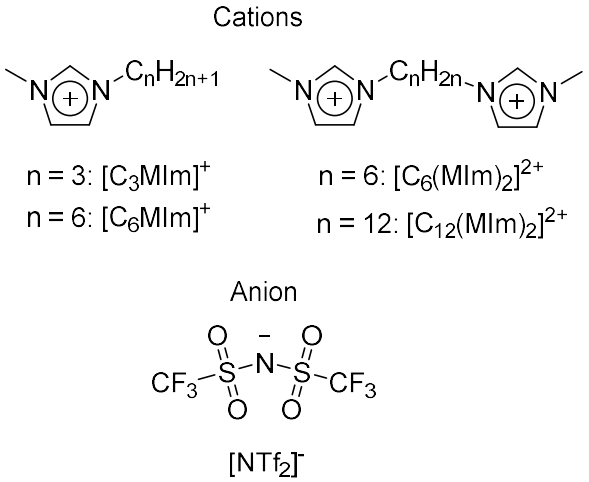

Figure 6.1. Chemical structures of the cations and anion of sample ILs used in this study.

6.3. Results and Discussion

6.3.1. Temperature Dependence of Shear Viscosities

Figure 6.2 shows the temperature dependence of η for $[C_3MIm][NTf_2]$, $[C_6MIm][NTf_2]$, $[C_6(MIm)_2][NTf_2]_2$, and $[C_{12}(MIm)_2][NTf_2]_2$. As clearly shown in the figure, the temperature dependence of η for the monocationic ILs is significantly different from that for the dicationic ILs. For each of the ILs, the temperature dependence of η shows non-Arrhenius behavior. Thus, the VTF equation[86-89] is used to fit the temperature dependence of η,as is the case with the previous chapters. The logarithmic form of eq. 3.1, $\ln(\eta(T)) = \ln(\eta_0) + D/((T/T_0) - 1)$, has been

used to fit the data to obtain a good fit across the shear viscosity data spanning orders of magnitude. According to the report by Angell and coworkers, each data set included a value of 1×10^{13} cP at the liquid's glass transition temperature T_g.[90] The fit parameters and T_g values[72] are summarized in Table 6.1. It is clear from the fit parameters in the table that the temperature-dependent parameters of η for the four ILs are unique. The fragility, which is inversely proportional to D,[90] decreases with the longer alkyl group and alkylene linker of the ILs, and the critical temperature T_0 and intrinsic viscosity η_0 are higher in the dicationic ILs than in the monocationic ILs.

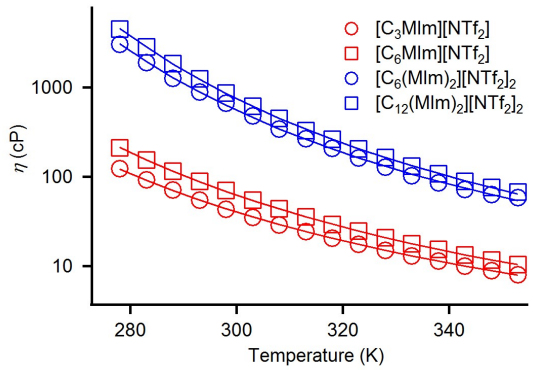

Figure 6.2. Plots of shear viscosity vs temperature for $[C_3MIm][NTf_2]$ (red circles), $[C_6MIm][NTf_2]$ (red squares), $[C_6(MIm)_2][NTf_2]_2$ (blue circles), and $[C_{12}(MIm)_2][NTf_2]_2$ (blue squares). Solid lines denote the VTF fits to eq 3.1 for each IL.

Table 6.1. Glass Transitions Temperature (T_g) and VTF Fit Parameters for $[C_3MIm][NTf_2]$, $[C_6MIm][NTf_2]$, $[C_6(MIm)_2][NTf_2]_2$, and $[C_{12}(MIm)_2][NTf_2]_2$

IL	T_g [a] (K)	η_0 (cP)	D	T_0 (K)
$[C_3MIm][NTf_2]$	185.8	0.1075	5.185	160.0
$[C_6MIm][NTf_2]$	190.4	0.1004	5.398	163.1
$[C_6(MIm)_2][NTf_2]_2$	209.9	0.2940	4.947	181.1
$[C_{12}(MIm)_2][NTf_2]_2$	212.0	0.2780	5.106	182.2

[a] Reference 72.

6.3.3. Temperature Dependence of Low-Frequency Spectra

Figure 6.3 shows the Kerr transients of the ILs measured at 293, 308, 323, 338, and 353 K. As shown in the figure, the intensity of the nuclear responses relative to the electronic responses of the ILs increases with rising temperature. Each Kerr transient after 3 ps was analyzed by a biexponential function. The parameters of the fits are summarized in Table 6.2. There are additional slower components of the Kerr transients, but the effect of the slower relaxation process on the low-frequency Kerr spectrum, which is due mainly to the contribution of the interionic vibrations, is negligibly small. There are some interesting features in the biexponential relaxation process. First, within experimental and fitting error, both the fast and slow time constants for the four ILs are almost independent of temperature. This indicates that the relaxation process in this time range is not diffusive. Second, the offset parameter (a_0) increases with increasing temperature. Because the Kerr intensities in this study are normalized at the instantaneous electronic response, the magnitude of the slow relaxation process relative to the electronic response becomes larger with increasing temperature. This temperature-dependent feature of the slow relaxation process observed in fs-RIKES has been recognized in molecular liquids.[168-169] Because the shear viscosities of liquids decrease with increasing temperature, the magnitude of the response of ions or molecules in liquids to the perturbation by a femtosecond laser pulse will be larger. As a result, the magnitude of the slow collective relaxation process increases.

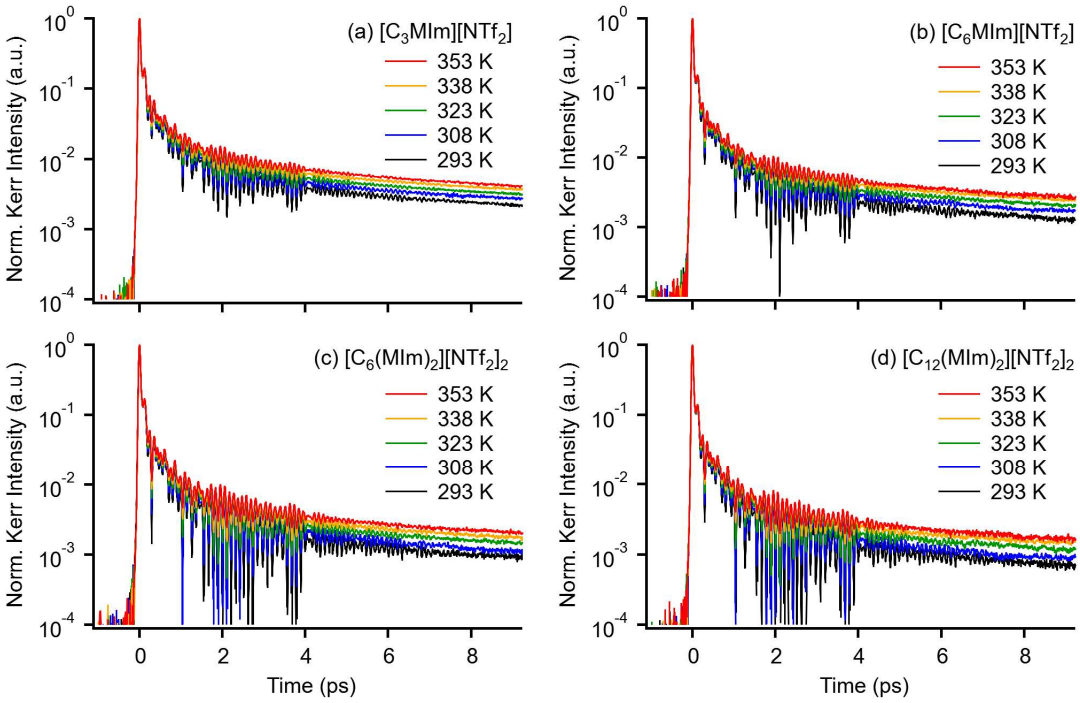

Figure 6.3. Kerr transients at 293 K (black), 308 K (blue), 323 K (green), 338 K (yellow), and 353 K (red) for (a) $[C_3MIm][NTf_2]$, (b) $[C_6MIm][NTf_2]$, (c) $[C_6(MIm)_2][NTf_2]_2$, and (d) $[C_{12}(MIm)_2][NTf_2]_2$.

Table 6.2. Biexponential Fit Parameters for Kerr Transients in Monocationic and Dicationic ILs at Various Temperatures

temperature (K)	a_0	a_1	τ_1 (ps)	a_2	τ_2 (ps)
		$[C_3MIm][NTf_2]$			
293	0.00049	0.01900	1.11	0.00419	10.0
308	0.00067	0.01700	1.22	0.00483	10.5
323	0.00073	0.01373	1.33	0.00578	10.4
338	0.00082	0.01526	1.35	0.00676	10.5
353	0.00084	0.01490	1.42	0.00782	10.3
		$[C_6MIm][NTf_2]$			
293	0.00017	0.00818	1.05	0.00291	10.4
308	0.00021	0.00782	1.20	0.00347	10.4
323	0.00026	0.00518	1.37	0.00419	10.5
338	0.00060	0.00831	1.47	0.00431	10.6
353	0.00065	0.00688	1.76	0.00460	10.8
		$[C_6(MIm)_2][NTf_2]_2$			
293	0.00016	0.00465	1.41	0.00175	10.6
308	0.00017	0.00608	1.48	0.00227	10.0
323	0.00032	0.00798	1.45	0.00248	11.5
338	0.00039	0.00626	1.63	0.00300	11.1
353	0.00048	0.00763	1.58	0.00342	11.4
		$[C_{12}(MIm)_2][NTf_2]_2$			
293	0.00020	0.00393	1.40	0.00125	10.0
308	0.00023	0.00832	1.34	0.00151	10.4
323	0.00028	0.00568	1.28	0.00219	10.1
338	0.00051	0.00938	1.33	0.00232	10.2
353	0.00053	0.00513	1.64	0.00285	9.57

The Kerr transients were further analyzed based on the Fourier transform deconvolution analysis to obtain the Kerr spectra. Figure 6.4 shows the temperature-dependent Kerr spectra of the ILs. It is evident that the spectra are well-resolved up to 600 cm^{-1}. In the 250–370 cm^{-1} range, there are many bands due to the anion. These vibrational bands have been assigned to the intraionic vibrational modes comprising rocking motions of the CF_3 group and the

twisting/wagging/rocking motions of the SO_2 groups of the anion.[56]

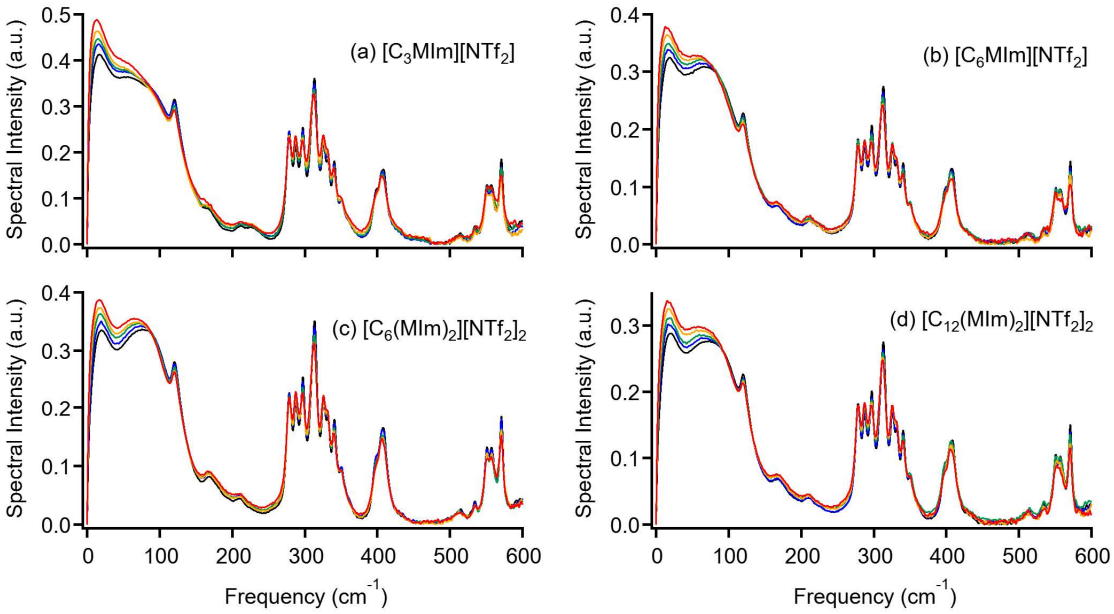

Figure 6.4. Fourier transform Kerr spectra after the subtraction of multiexponential components at 293 K (black), 308 K (blue), 323 K (green), 338 K (yellow), and 353 K (red) for (a) $[C_3MIm][NTf_2]$, (b) $[C_6MIm][NTf_2]$, (c) $[C_6(MIm)_2][NTf_2]_2$, and (d) $[C_{12}(MIm)_2][NTf_2]_2$.

Figure 6.5 displays the 250–370 cm^{-1} region of the Kerr spectra of the ILs in more detail. Several previous reports have revealed that the intraionic vibrational bands in this frequency range include contributions from the conformers (*cisoid* and *transoid* forms) of the $[NTf_2]^-$ anion.[56,118,170-172] Lassegues et al. have carefully distinguished the bands of the *cisoid* and *transoid* forms of the $[NTf_2]^-$ anion of 1-ethyl-3-methylimidazolium bis(trifluoro-methylsulfonyl)amide obtained by different cooling processes.[118] Bands at 279, 288, 310, 326, 332, and 351.5 cm^{-1} were assigned to the *cisoid* conformer, and bands at 276, 297, 314, and 340.5 cm^{-1} to the *transoid* form. Therefore, the bands labeled 1 and 4 in Figure 6.5a are overlapping vibrational modes of the *cisoid* and *transoid* forms. It is clear from Figure 6.5 that, for all four ILs, the intensities of bands 3, 4, and 7 decrease with increasing temperature, whereas the intensities of bands 2, 5, and 6 show the opposite trend. These results indicate that the population of the *cisoid* form increases and that of the *transoid* form decreases with increasing temperature.

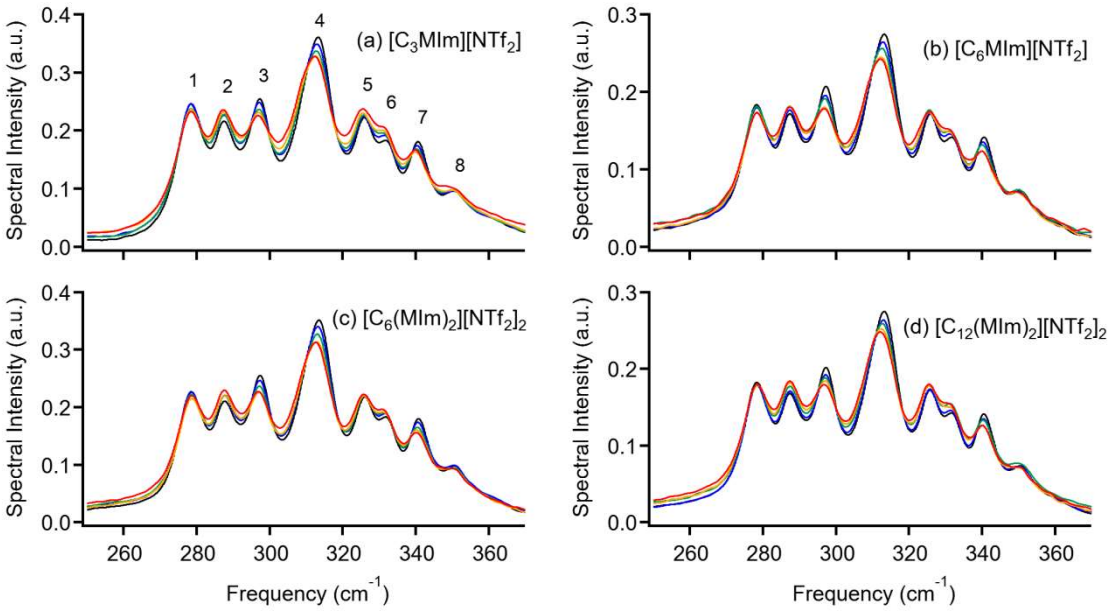

Figure 6.5. Fourier transform Kerr spectra in the frequency range of 250–370 cm^{-1} for (a) $[C_3MIm][NTf_2]$, (b) $[C_6MIm][NTf_2]$, (c) $[C_6(MIm)_2][NTf_2]_2$, and (d) $[C_{12}(MIm)_2][NTf_2]_2$ at 293 K (black), 308 K (blue), 323 K (green), 338 K (yellow), and 353 K (red).

In contrast to the intraionic vibrational bands, broad interionic vibrational bands are observed in Figure 6.4 in the low-frequency region, at less than 200 cm^{-1}. The expanded spectra in this range are shown in Figure 6.6. It is evident from the figure that the spectral intensity in the region less than 50 cm^{-1} increases with increasing temperature, regardless of whether the cations are monocationic or dicationic.

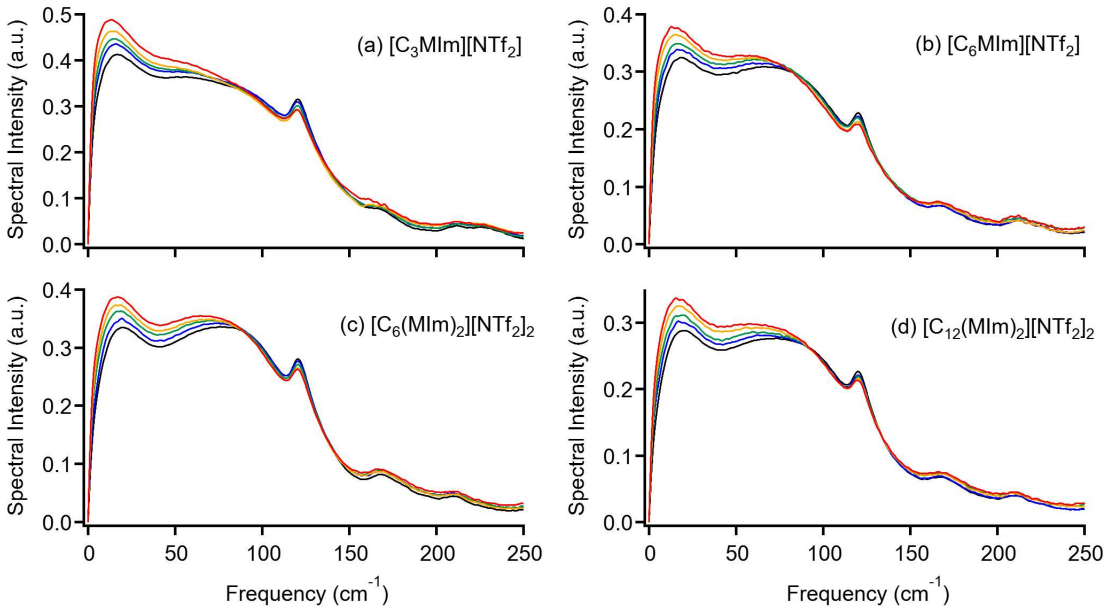

Figure 6.6. Low-frequency Kerr spectra after the subtraction of multiexponential components in the frequency range of 0–250 cm^{-1} for (a) $[C_3MIm][NTf_2]$, (b) $[C_6MIm][NTf_2]$, (c) $[C_6(MIm)_2][NTf_2]_2$, and (d) $[C_{12}(MIm)_2][NTf_2]_2$ at 293 K (black), 308 K (blue), 323 K (green), 338 K (yellow), and 353 K (red).

The unique bands in the 15–20 cm^{-1} range and the bimodal spectral shape in the low-frequency region below 200 cm^{-1} are commonly observed for imidazolium-cation-based ILs with the $[NTf_2]^-$ anion. On the basis of comparisons with the spectra of $[C_4MIm]^+$-cation-based ILs having the $[NTf_2]^-$, trifluoromethanesulfonate, and tris(trifluoromethylsulfonyl)methide anions,[71] the 15–20 cm^{-1} band for ILs with the $[NTf_2]^-$ anion can be attributed to the librational motions of the anion and/or the coupling of the translational and librational motions. In the present results, the spectral intensity in the frequency range of 15–20 cm^{-1} relative to that in the frequency range of 50–100 cm^{-1} increases with temperature for all four ILs. Thus, it is rather natural to think that the anion-related motions become more active at higher temperatures. On the other hand, in the 50–100 cm^{-1} region, which is assigned to the major contribution of the imidazolium ring libration,[48,53,71,173] the spectral density shifts to the lower-frequency side and its intensity increases as the temperature rises. Next, this spectral feature is discussed further based on the results of line shape analysis.

The line shape analyses of the low-frequency Kerr spectra were performed to provide a numerical representation of the low-frequency Kerr spectra and to estimate characteristic frequencies, such as the first moments M_1, to enable a semiquantitative discussion of the

temperature dependence. Model functions for the line shape analyses used in this study are composed of the sum of an Ohmic function[70] and antisymmetrized Gaussian functions.[16] A Lorentzian function was also used for clear intraionic vibrational modes. Details of the line shape analysis made in this study were described in Chapter 2.[17,53,174] Figure 6.7 shows some examples of the results of the line shape analysis. Line shape fits to the other low-frequency Kerr spectra also produced fitting results of similar quality. The time integration was performed up to 1000 cm^{-1}. The fitting parameters are summarized in Appendix F.

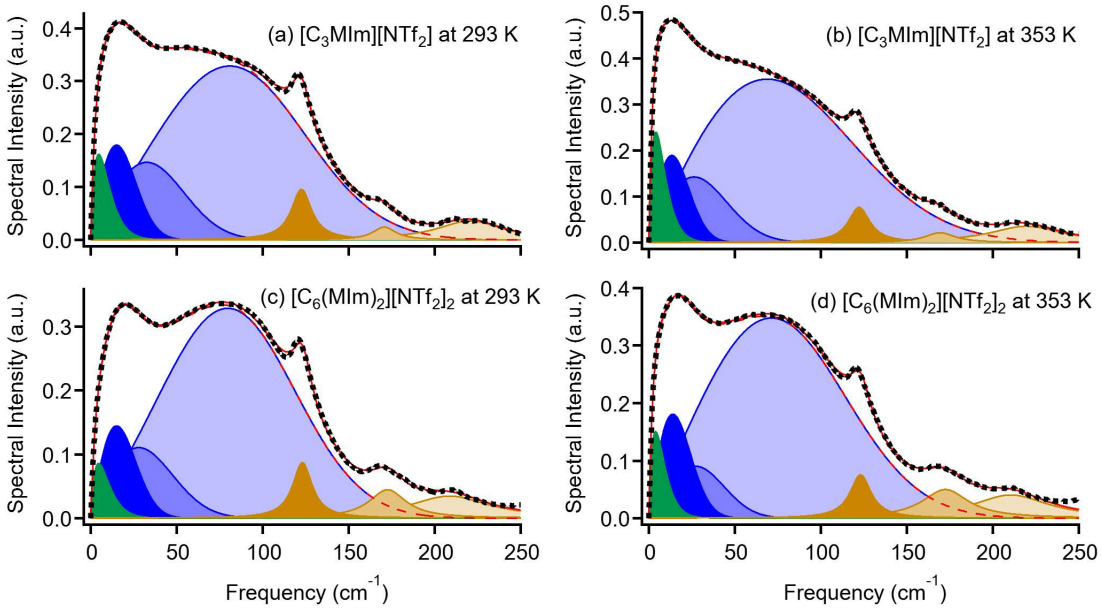

Figure 6.7. Line shape analysis results for the low-frequency spectra of (a) $[C_3MIm][NTf_2]$ at 293 K, (b) $[C_3MIm][NTf_2]$ at 353 K, (c) $[C_6(MIm)_2][NTf_2]_2$ at 293 K, and (d) $[C_{12}(MIm)_2][NTf_2]_2$ at 353 K. Black dots, data; solid red lines, entire fits; green areas, Ohmic functions; blue areas, antisymmetrized Gaussian functions; brown areas, Lorentzian functions (intraionic vibrations); and dashed red lines, sums of Ohmic and antisymmetrized Gaussian functions (assumed to be mainly the interionic components).

The line shape analyses show that there are two distinct temperature-dependent effects on the low-frequency Kerr spectra of the ILs. First, the spectral density in the decomposed component with the lowest frequency shows a particularly strong increase with temperature. In this frequency region, which is tentatively described by the Ohmic function, the origin of the molecular motion or spectral density cannot be identified in a simple manner. In molecular liquids, translational (collision-induced and interaction-induced) and rotational (librational)

motions (intermolecular vibrations) and their cross-term (coupling) contribute to the spectral intensity in this region.[18,92-93,175-176] The diffusive orientational dynamics occurs successively to these molecular motions in liquids. This is also true for ILs, although there are some differences in the spectral shapes between neutral molecular liquids and ILs.[61-62,98-99] A unique librational motion due to the anion appears in this frequency region (at approximately 15–20 cm^{-1}) in the case of the molten [NTf_2] salts (and also bis(perfluoroalkylsulfonyl)amide and tris(trifluoromethylsulfonyl)methide salts).[71] In fact, such a unique spectral band is not observed for ILs with other common anions such as tetrafluoroborate,[177-180] dicyanoamide,[51,55,71,180] thiocyanate,[71] trifluoromethylsulfonate,[48,71] hexafluorophosphate,[48,52,67,116,181] and bromide.[51,67,181] However, the results of the line shape analyses (Figure 6.7) show that the amplitude of the lowest-frequency band significantly increases with increasing temperature rather than that of the second-lowest band, which is mainly attributed to the librational and/or coupling of translational and librational motions of the anion. Thus, it might be plausible that the translational vibrational motions, which often appear in the low-frequency rather than high-frequency region, become more active with increasing temperature. In fact, the low-frequency spectra of polymer solutions also show a similar feature:[23,110-111] namely, the spectral intensities in the low-frequency region less than 50 cm^{-1} of the low-frequency Kerr spectra of polymer solutions are low compared to those of their reference model monomer solutions. The difference in the low-frequency spectra between the polymer and model monomer solutions is attributed to the difference in the activity of the translational motions: the translational motion in polymer solutions is suppressed because of the heavier mass.

In addition to the interionic vibrational motion, the crossover process from intermolecular vibrational motion (β-relaxation) to collective structural relaxation (α-relaxation) also appears in this time (frequency) range.[49] It seems reasonable that the higher activity in the crossover process provides faster structural relaxation with increasing temperature. Furthermore, decoupling of the intermolecular vibrational motion and the structural relaxation process might occur. With increasing temperature, the ILs can be more liquid-like and less supercooled (or solid-like) nature. As a result, the non-Markovian feature (or the memory)[1] of the ILs decreases with rising temperature. Further studies such as anion-dependence experiments and molecular dynamics simulations show promise in addressing this spectral feature in more detail.

Second, the peak of the highest-frequency component at approximately 80 cm^{-1} shifts to lower frequency with rising temperature. The amplitude of this component also increases with

increasing temperature. In other words, the width of this component (and, in fact, of all low-frequency spectral bands) decreases with higher temperature. This component is governed by the libration of the aromatic ring of the cation.[48,53,71,173] The results indicate that, in the present ILs, the librational motion of the ring is slowed, and its activity is increased, with increasing temperature. This might be due to the weakening of the interionic interaction at higher temperatures. A similar temperature dependence in the low-frequency spectra of neutral aromatic solvents such as aniline,[63] benzene,[14] tetrahydrofuran,[65] and pyridine[15] has also been reported. One plausible explanation for this behavior is that at higher temperatures, the larger free volume in liquids allows a greater magnitude (a larger displacement) of librational motion in the aromatic ring. As a result, the vibrational motion shifts to a lower frequency.

Another possibility is motional narrowing.[182-183] As in absorption in NMR spectroscopy, motional narrowing occurs in the intramolecular vibrational mode in liquids. Although the spectral band discussed here is due to an intermolecular (interionic) vibration, motional narrowing of the band would not be surprising. In fact, Ricci et al. explained the temperature dependence of the low-frequency spectrum of liquid benzene observed by fs-RIKES with a motional narrowing scheme.[64] Fourkas and coworkers also accounted for the temperature-dependent intermediate relaxation process (low-frequency region of the low-frequency Kerr spectrum) of six symmetric-top molecular liquids, including acetonitrile, benzene, and chloroform, by a scheme of motional narrowing.[184] This should also be applicable to ILs similarly to neutral molecular liquids.

To examine the temperature dependence of the characteristic frequencies M_1 of the low-frequency spectra for the four ILs, plots of M_1 versus T for the ILs are shown in Figure 6.8. Linear fits are also included in the figure. The slopes estimated from the fits are approximately −0.05 cm^{-1}/K for the four ILs: −0.049 cm^{-1}/K for $[C_3MIm][NTf_2]$; −0.053 cm^{-1}/K for $[C_6MIm][NTf_2]$; −0.053 cm^{-1}/K for $[C_6(MIm)_2][NTf_2]_2$; and −0.048 cm^{-1}/K for $[C_{12}(MIm)_2][NTf_2]_2$. The slopes (or temperature dependence) of M_1 for the four ILs are quite similar within the experimental (and fitting) error. In fact, this feature is completely different from that in viscosity. As shown in Figure 6.2 and Table 6.1, the temperature dependence of the shear viscosity for each IL is unique. Namely, the results indicate that, unlike for shear viscosity, the temperature dependence of the low-frequency spectra is not sensitive to the length of the alkyl group and alkylene linker or to the difference between monocations and dications. In comparison to shear viscosity, the interionic (or intermolecular) vibrational spectrum provides information on a shorter length scale. Furthermore, the low-frequency Kerr spectra of aromatic-

cation-based ILs are dominated by features that provide information about the local ionic region.[53] Thus, it is not very surprising that the four ILs studied here do not show large differences in the temperature dependence of their low-frequency spectra.

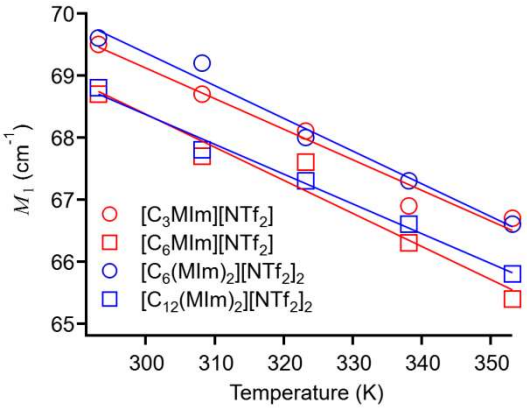

Figure 6.8. Temperature dependence of the first moment, M_1, of the low-frequency spectrum after the subtraction of slow relaxation and clear intraionic vibrational modes. Red circles, [C_3MIm][NTf_2]; red squares, [C_6MIm][NTf_2]; blue circles, [C_6(MIm)$_2$][NTf_2]$_2$; and blue squares, [C_{12}(MIm)$_2$][NTf_2]$_2$. Linear fits are also shown by solid lines.

6.4. Conclusion

The temperature dependence of the low-frequency spectra of [C_3MIm][NTf_2], [C_6MIm][NTf_2], [C_6(MIm)$_2$][NTf_2]$_2$, and [C_{12}(MIm)$_2$][NTf_2]$_2$ was investigated by fs-RIKES. As has been shown for most molten [NTf_2] salts of imidazolium cations, the line shapes of the present ILs are essentially bimodal. The relative intensities in the low frequency region less than 20 cm^{-1} of the low-frequency spectra of each of the ILs studied increase with rising temperature. On the basis of line shape analysis, this is probably due to an increase in the activity of the intermolecular translational vibrational motion and/or the deactivation/activation of the coupling motion of translational and librational motions. It is also plausible that the intermolecular vibrational motion and structural relaxation process decouple because of decrease in the non-Markovian feature (loss of memory) at higher temperatures. In addition to the spectral feature in the low-frequency region, it was found that the high-frequency component peaking at approximately 80 cm^{-1} shifts to lower frequency with increasing temperature for each IL. This shift is attributed to weaker interionic interaction at higher temperatures. The first moment of the low-frequency spectra shifts to lower frequency with

rising temperature for each of the ILs studied. The temperature dependence (slopes of the relations between the first moment and the temperature) of the monocationic and dicationic ILs is similar. The temperature dependence of the shear viscosities of the ILs was also studied. The data were analyzed according to the Vogel–Tammann–Fulcher scheme. The fragility decreases with longer alkyl groups and longer alkylene linkers, and the critical temperature and intrinsic viscosity of the dicationic ILs are higher than those of the monocationic ILs.

Chapter 7

Effects of Aromaticity in Cations and Their Functional Groups on Temperature Dependence of Low-Frequency Spectra of Ionic Liquids

J. Chem. Phys. **2018**, *148*, 193805/1–10.

7.1. Introduction

In this chapter, I investigated the temperature dependence of the low-frequency Kerr spectra of ILs whose cations have two systematically different cyclic groups, and I also investigate their combinations to determine the effects of charged and neutral aromatic rings in cations of the ILs on the temperature-dependent low-frequency spectral features. Previously, Shirota and coworkers used fs-RIKES to investigate the low-frequency spectra of the $[NTf_2]^-$ salts of 1-cyclohexylmethyl-1-methylpyrrolidinium $[CHxmMPyrr]^+$, 1-cyclohexyl- methyl-3-methylimidazolium $[CHxmMIm]^+$, *N*-cyclohexylmethylpyridinium $[CHxmPy]^+$, 1-benzyl-1-methylpyrrolidinium $[BzMPyrr]^+$, 1-benzyl-3-methylimidazolium $[BzMIm]^+$, and *N*-benzylpyridinium $[BzPy]^+$ cations (Figure 7.1) at 293 K.[107] In that study, they found that the librations of the charged aromatic rings, i.e., imidazolium and pyridinium rings, appear at approximately 80 cm^{-1}, but that of the neutral aromatic ring, i.e., the benzyl group, appears at approximately 60 cm^{-1}.[107] Expanding this study, in this chapter, the temperature dependence of the low-frequency spectra of these ILs is further explored. The particular aim of this study is to investigate the effects of placing charged and neutral aromatic rings on IL cations by probing the temperature dependence of their low-frequency spectral features. As discussed above, the librational motions of aromatic rings will show the red shift of the high-frequency side of the spectra. Thus, how the difference of the red shift between charged and neutral aromatic rings appear in the temperature dependence is interesting.

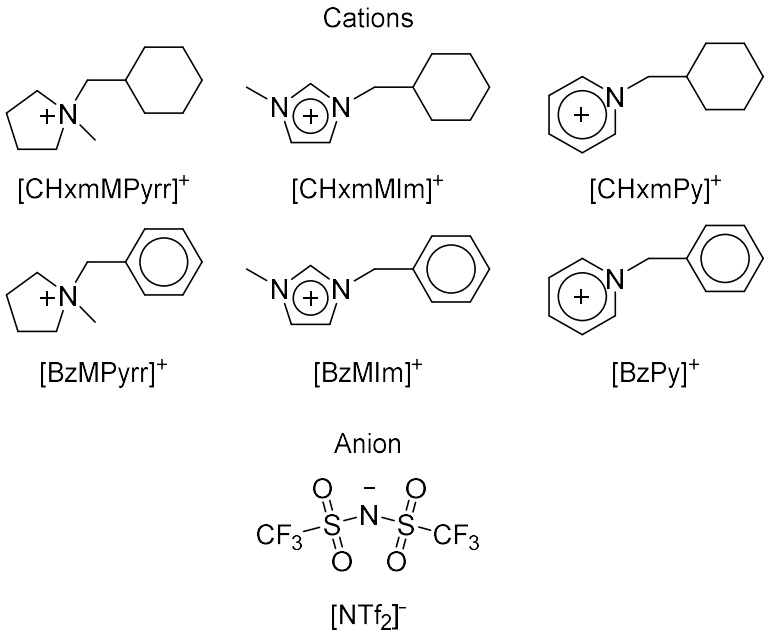

Figure 7.1. Chemical formulas of the IL cations and anion used in this study.

7.2. Experiments

Details of the preparations of the sample ILs have been reported elsewhere.[107] The sample ILs were kindly donated from Dr Wishart and Ms. Ramati (Brookhaven National Laboratory). The water contents of the ILs were generally below 100 ppm.[107] Before fs-RIKES measurements, the sample ILs were injected into a 3-mm optical-path-length quartz cell via a 0.2-μm inorganic membrane filter, and then dried at 313 K (323 K for [CHxmPy][NTf_2] because of its melting point of 314.9 K[107]) for over 36 h in a vacuum oven.

7.3. Results and Discussion

Figure 7.2 shows the Kerr transients normalized at the intensity at $t = 0$ for ILs at 293, 308, 323, 338, and 353 K. The Kerr transient of [CHxmPy][NTf_2] at 293 K was not measured because the supercooled state of [CHxmPy][NTf_2] is not sufficiently stable for fs-RIKES experiments.[107] In each Kerr transient, the spike at $t = 0$ is due to the electronic response, and successive nuclear motions including underdamped and overdamped motions are involved. Strong underdamped motions, especially motions with duration less than 4 ps, are mainly due to intramolecular vibrational modes. Because the depolarized Raman-active modes within the spectral width of a pump pulse are excited or deexcited, depending on the initial state, by a femtosecond optical pulse in fs-RIKES, the Kerr signal includes both the Stokes and anti-Stokes Raman components. It should be noted that these oscillations are not noise, but the real response derived from the samples. Figure 7.2 indicates that the intensities of the nuclear responses relative to the electronic responses increase with rising temperature. This temperature-dependent behavior was confirmed for all of the studied ILs regardless of their cations, as shown in Figure 7.2. The Kerr transients after 3 ps were fitted by a biexponential function. The fit parameters are summarized in Appendix G.

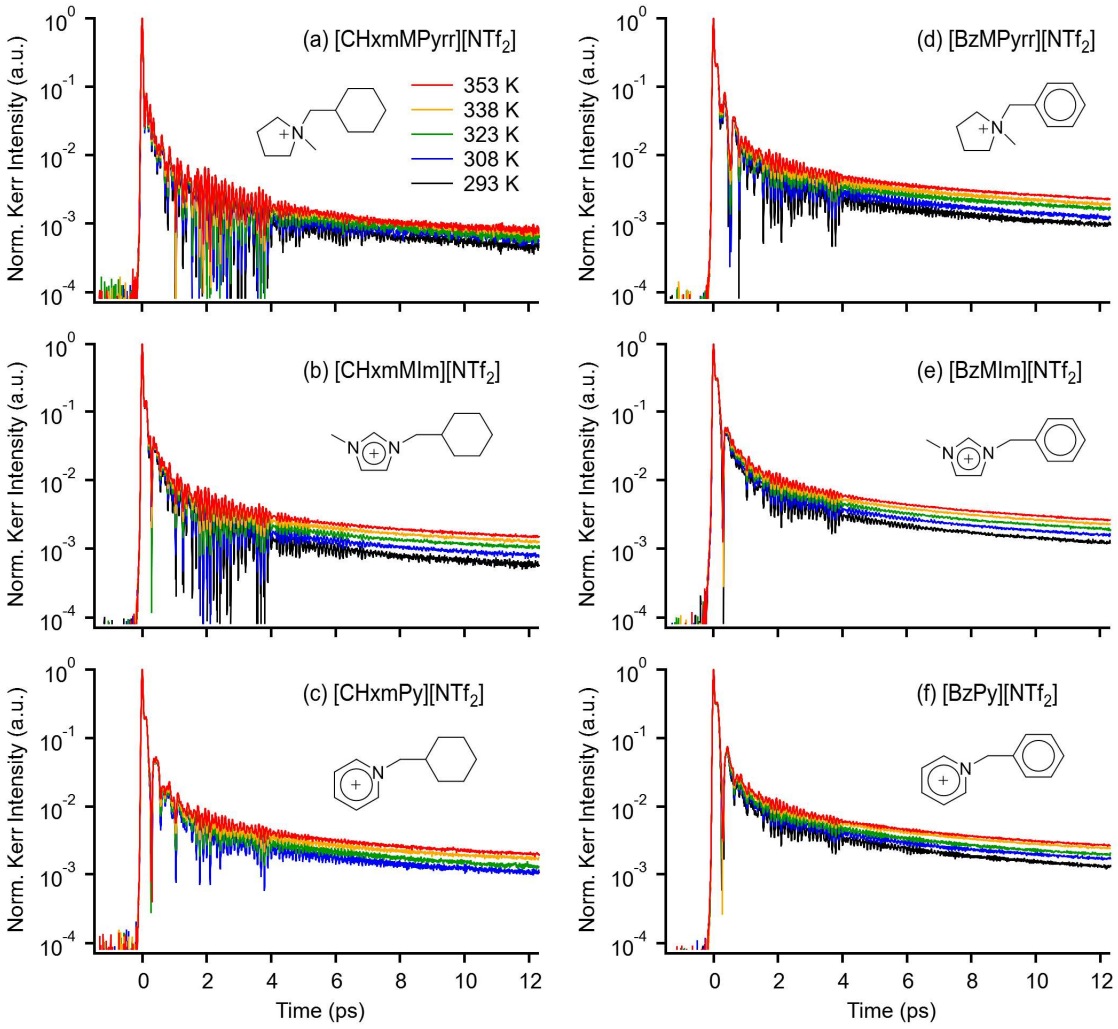

Figure 7.2. Kerr transients of (a) [CHxmMPyrr][NTf_2], (b) [CHxmMIm][NTf_2], (c) [CHxmPy][NTf_2], (d) [BzMPyrr][NTf_2], (e) [BzMIm][NTf_2], and (f) [BzPy][NTf_2] at 293 K (black), 308 K (blue), 323 K (green), 338 K (orange), and 353 K (red).

The Kerr transients were converted to the Kerr spectra by the standard Fourier-transform deconvolution analysis developed by Lotshaw and McMorrow, described in Chapter 2.[9,185] Figure 7.3 shows the temperature dependence of the Fourier-transform Kerr spectra (also referred to as the reduced Kerr spectra) with the frequency range of 0–650 cm^{-1}. The obtained spectra are not renormalized further, and thus the low-frequency spectral densities here are relative to the electronic response. Note that the spectra in Figure 7.3 are those with picosecond overdamped components (a_0 and $a_2\exp(-t/\tau_2)$) that are removed from the entire spectra, but the faster picosecond components are left in the spectra because the time scale is similar to the vibrational dephasing process in liquids and solutions. It should also be noted that although ILs typically possess a slower relaxation process with a time constant of the order of

nanoseconds,[49,180,186-189] the Kerr transients were measured within the time range from ca. −1 ps to 12 ps. This is because the focusing point in this study is the intermolecular vibrational band, not the diffusive reorientation process. Broad bands observed in the frequency region below 150 cm^{-1} are mainly due to intermolecular vibrational motions. In contrast, sharp bands that appear mostly in the frequency band above 100 cm^{-1} are intramolecular vibrational modes. Vibrational bands in the frequency range between 250 and 350 cm^{-1} are eye-grabbing. They are due to the anion's intramolecular vibrational modes. The assignments of the intramolecular vibrational bands were made previously.[107]

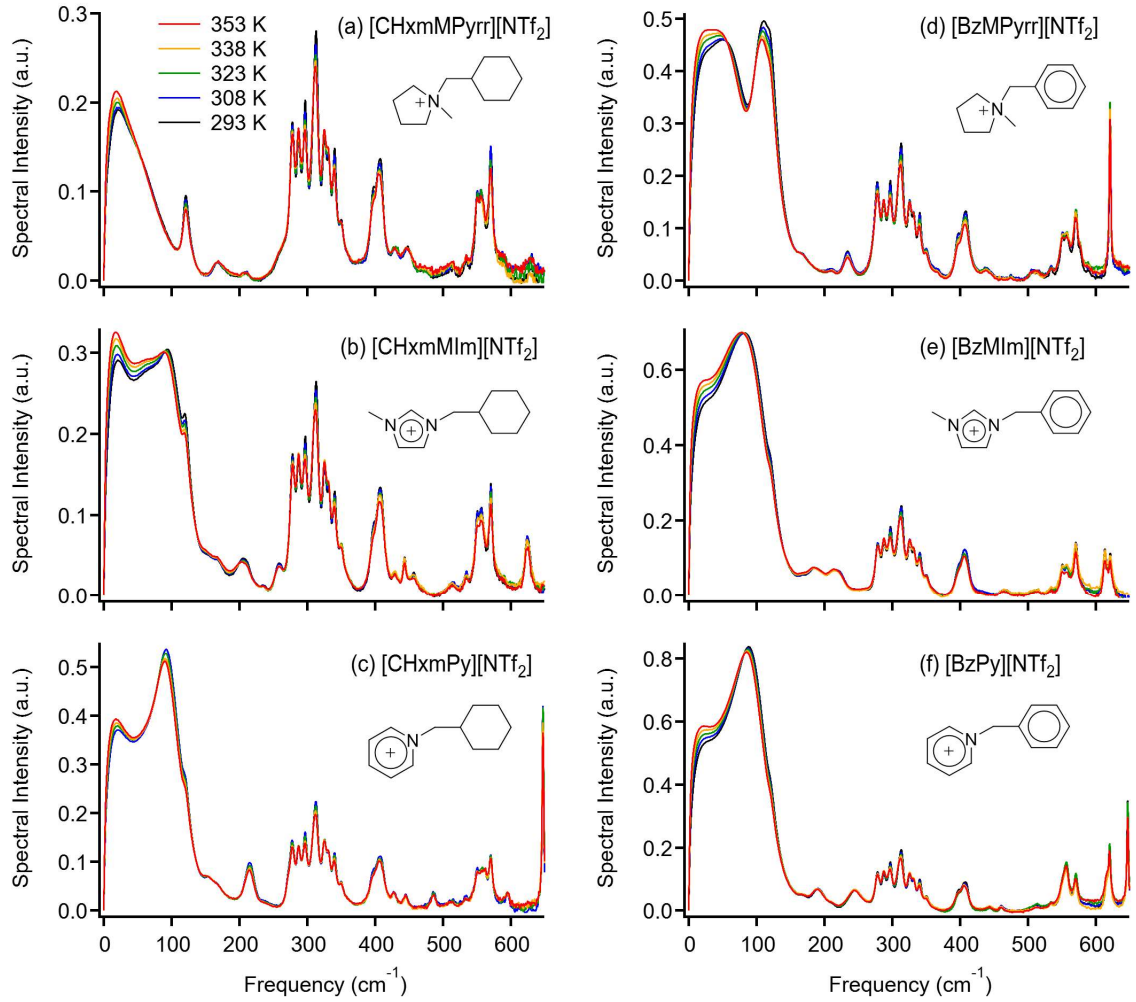

Figure 7.3. Fourier transform Kerr spectra in the frequency range of 0–650 cm^{-1} for (a) [CHxmMPyrr][NTf_2], (b) [CHxmMIm][NTf_2], (c) [CHxmPy][NTf_2], (d) [BzMPyrr][NTf_2], (e) [BzMIm][NTf_2], and (f) [BzPy][NTf_2] at 293 K (black), 308 K (blue), 323 K (green), 338 K (orange), and 353 K (red).

Figure 7.4 shows the magnification of the Kerr spectra of the ILs with the frequency range between 0 and 200 cm^{-1}. The spectral shapes for most ILs are rather complicated because the cations have two bulky cyclic functional groups, and they include intramolecular vibrational modes in the frequency region below 150 cm^{-1}. Previously, Shiota and coworkers measured the low-frequency spectra of these ILs at 293 K.[107] In that report, the frequencies of the librational motions of the charged aromatic ring (imidazolium and pyridinium rings) and the neutral aromatic ring (benzyl group) are different, and the charged aromatic rings show the peak of the librational band at ca. 80 cm^{-1}, but the neutral one is shown at ca. 60 cm^{-1}. The ILs whose cations have a charged aromatic ring ([CHxmMIm][NTf_2] and [CHxmPy][NTf_2]) show bimodal line-shape spectra, and the ILs whose cations have both charged and neutral aromatic rings show more ambiguous bimodal line-shape spectra. That is, the valley between the low-frequency peak at ca. 20 cm^{-1} and the high-frequency peak at ca. 80 cm^{-1} is buried with the spectral density at ca. 60 cm^{-1} owing to the neutral aromatic ring libration. However, [CHxmMPyrr][NTf_2] shows a simpler lineshape for the low-frequency spectrum. Note that the intensity due to the aromatic ring libration in low-frequency Kerr spectra of aromatic liquids is much stronger than the spectral intensity of the low-frequency Kerr spectra of nonaromatic liquids.[190] Thus, the spectral intensity of [CHxmMPyrr][NTf_2] is much lower than that of the other ILs. In the same way, the ILs whose cation has an aromatic ring ([CHxmMIm][NTf_2], [CHxmPy][NTf_2], and [BzMPyrr][NTf_2]) show the lower spectral intensity than the ILs whose cation has two aromatic rings ([BzMIm][NTf_2] and [BzPy][NTf_2]). It is known that the spectral intensities in the low-frequency Kerr spectra of 1-alkyl-3-methylimidazolium cation based ILs are weaker than that of the respective *N*-alkylpyridinium cation based ILs.[54] As shown in Figure 7.4, accordingly, the tendency of the spectral intensities of the present six ILs is: [CHxmMPyrr][NTf_2] < [CHxmMIm][NTf_2] < [CHxmPy][NTf_2] ≈ [BzMPyrr][NTf_2] < [BzMIm][NTf_2] < [BzPy][NTf_2].[107]

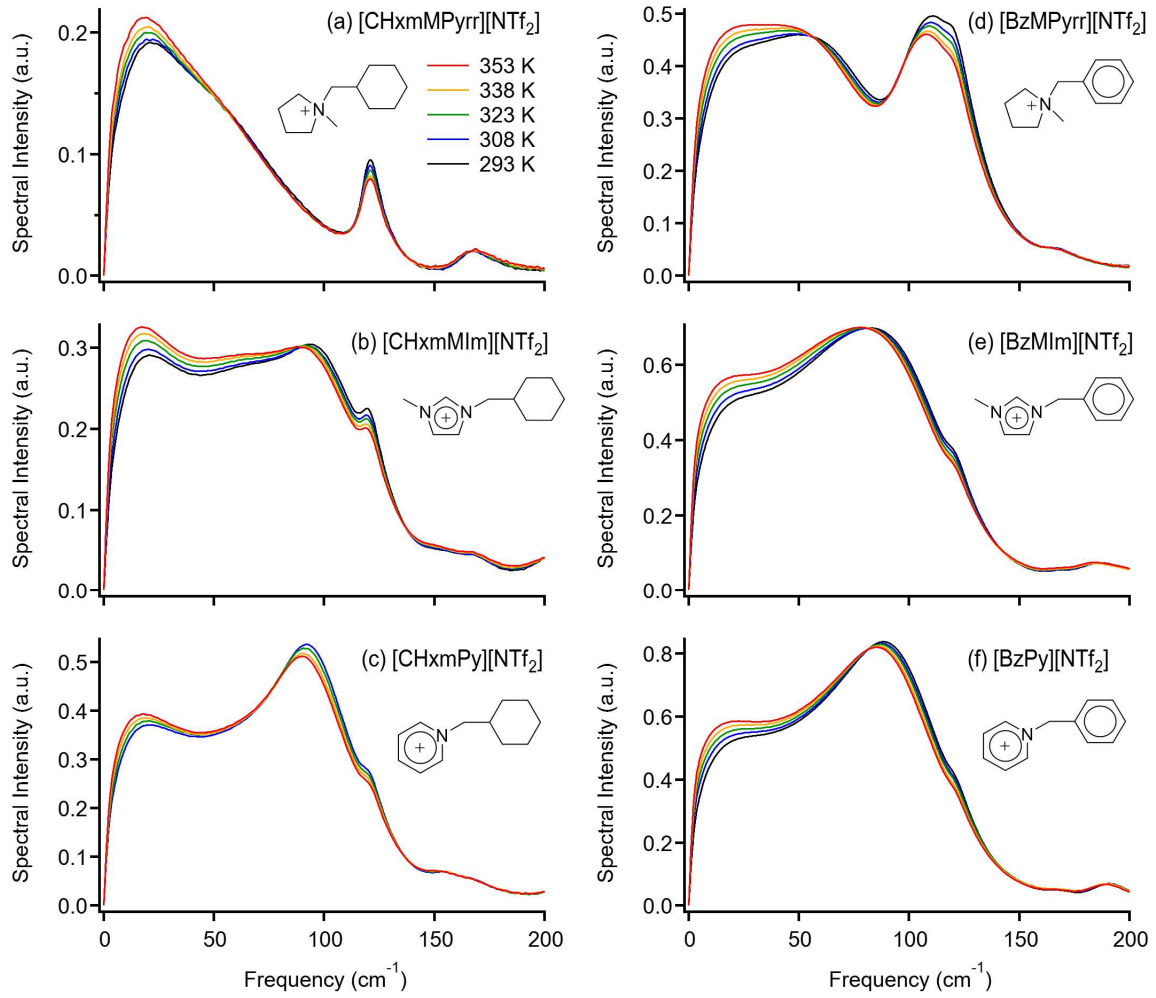

Figure 7.4. Low-frequency Kerr spectra in the frequency range of 0–200 cm^{-1} for (a) [CHxmMPyrr][NTf_2], (b) [CHxmMIm][NTf_2], (c) [CHxmPy][NTf_2], (d) [BzMPyrr][NTf_2], (e) [BzMIm][NTf_2], and (f) [BzPy][NTf_2] at 293 K (black), 308 K (blue), 323 K (green), 338 K (orange), and 353 K (red).

From Figure 7.4, it can be seen that the broad low-frequency spectra, which are mainly due to intermolecular vibrations of all six ILs, are clearly temperature dependent. However, upon close analysis of the spectra, it is found that the temperature-dependent spectral feature of the nonaromatic IL, [CHxmMPyrr][NTf_2], is different from that of the other five ILs. That is, [CHxmMPyrr][NTf_2] shows the spectral change only in the low-frequency region below ca. 50 cm^{-1}; however, the spectral feature of other ILs in terms of their temperature dependence is that the spectral intensity in the low-frequency region below ca. 50 cm^{-1} increases with rising temperature, but the spectral density in the high-frequency region greater than ca. 80 cm^{-1} decreases, or the peak at the high-frequency region of ca. 80 cm^{-1} (depending on IL) is red-

shifting.

In molecular liquids, it is well known that the low-frequency spectra are temperature dependent.[15,63-65,191-193] In many liquids, the spectral intensity increases and spectral band width narrows with increasing temperature more or less. The temperature-dependent Kerr spectral or signal feature has often been accounted for by the motional narrowing.[64,183-184] Yoshioka et al. have categorized molecular liquids based on the temperature-dependent features of the low-frequency spectra.[194] They attributed the temperature-dependent spectral features to molecular rigidity, the hydrogen-bonding network, and coupling between phonon and intramolecular modes. In a specific or more molecular aspect, Fourkas and coworkers have recently examined the red shift of the high frequency component, which is mainly due to the libration, of the low-frequency spectrum of liquid benzene with increasing temperature observed by fs-RIKES experiments by molecular dynamics simulations.[108] They concluded that the effect of density is dominant rather than the energetic effects of temperature itself.

Comparing the results in this study with those in Chapter 3, it is found that the temperature-dependent spectral features of the aromatic cation-based ILs, [CHxmMIm][NTf_2], [CHxmPy][NTf_2], [BzMIm][NTf_2], and [BzPy][NTf_2], are similar to that of imidazolium-based ILs. On the other hand, as noted above, [CHxmMPyrr][NTf_2] shows a spectral change with temperature only in the low-frequency region below 50 cm^{-1}, and it is temperature insensitive in the high-frequency region greater than 50 cm^{-1}, which is similar to that of pyrrolidinium-based ILs. As discussed in Chapter 4, the unique temperature-independent spectral feature in the high-frequency region above 50 cm^{-1} for [CHxmMPyrr][NTf_2] is attributed to the absence of the aromatic ring libration.

With the exception of [CHxmPy][NTf_2], Figure 7.5 shows the difference spectra for 308, 323, 338, and 353 K relative to the IL spectra at 293 K. Because of its higher melting point, the difference spectra of [CHxmPy][NTf_2] are calculated relative to the spectrum at 308 K. As mentioned before, normalization is performed for the Kerr transients before Fourier transform deconvolution analysis, and the difference spectra are obtained from the spectra without renormalization. The positive intensity indicates that the spectral intensity increases with rising temperature, and the negative intensity denotes a decreasing spectral intensity. Note that the sharp negative intensity at ca. 120 cm^{-1} is due to the intramolecular vibrational mode of the anion.[51,71] The temperature dependence of the intensity of the band would be attributed to that of the populations of the *cisoid* and *transoid* forms of the anion[118] and/or the spectral broadening due to the thermal activation. From Figure 7.6, it can be seen that the spectral intensity in the

low-frequency region below 20 cm^{-1} significantly increases with rising temperature for all six ILs. It is also found that the spectral densities at approximately 100 cm^{-1} decrease with increasing temperature in [CHxmMIm][NTf_2] and [CHxmPy][NTf_2], but [BzMPyrr][NTf_2] shows a decreasing spectral intensity at approximately 70 cm^{-1}. These spectral changes of [CHxmMIm][NTf_2], [CHxmPy][NTf_2], and [BzMPyrr][NTf_2] can be attributed to the changes in the librational motions of aromatic rings with changing temperature, since the librational bands of the imidazolium and pyridinium rings are located at higher frequencies compared to the phenyl ring.[107]

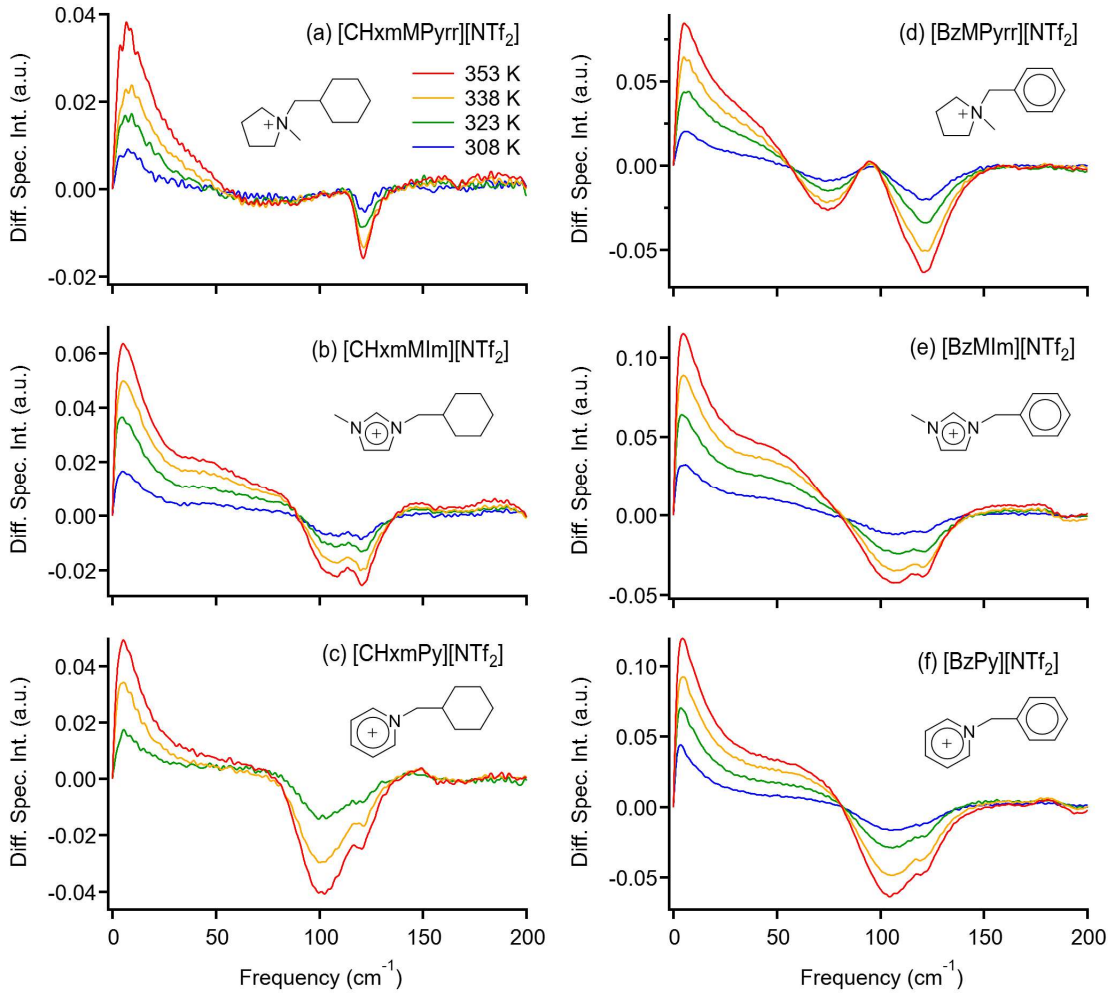

Figure 7.5. Difference Kerr spectra in the frequency range of 0–200 cm^{-1} for (a) [CHxmMPyrr][NTf_2], (b) [CHxmMIm][NTf_2], (c) [CHxmPy][NTf_2], (d) [BzMPyrr][NTf_2], (e) [BzMIm][NTf_2], and (f) [BzPy][NTf_2] for the spectra at 308 K (blue), 323 K (green), 338 K (orange), and 353 K (red) relative to that at 293 K.

[BzMIm][NTf_2] and [BzPy][NTf_2] show a negative spectral change at approximately 100 cm^{-1}, but not at 70 cm^{-1}, although the cations possess both charged and neutral aromatic rings. Further, if comparing the difference spectra between [CHxmMIm][NTf_2] and [BzMIm][NTf_2] or [CHxmPy][NTf_2] and [BzPy][NTf_2], it is found that the difference spectra of these ILs are similar. This indicates that the spectral changes caused by varying the temperature for the charged and neutral aromatic rings do not occur independently, but the charged aromatic ring dominates the temperature dependence of the line shape of the spectrum. If the charged and neutral aromatic rings librated independently and their temperature dependence was different, [BzMIm][NTf_2] and [BzPy][NTf_2] would show the negative band peaked at ca. 70 cm^{-1} in the difference Kerr spectra. Because the librational motions of the charged aromatic rings appear at the higher frequency than that of neutral aromatic ring libration and are the highest frequency intermolecular vibrational motion, the motions are less coupled to the other intermolecular vibrational motions. On the other hand, the librational motion of the neutral aromatic ring can be more interfered with by the other intermolecular vibrational motions, since it overlaps with the other intermolecular motions in the frequency region. As a result, the spectral change in the neutral aromatic ring libration with the temperature variation become less significant than that for the charged aromatic ring librations.

The shapes of the low-frequency spectra displayed in Figure 7.4 were further analyzed by modeling them to the sum of an Ohmic function[70] and antisymmetrized Gaussian functions.[16] When there is a clear intramolecular vibrational mode in the low-frequency region, then either an antisymmetrized Gaussian function or a Lorentzian function are used to obtain the fit. As an example, Figure 7.6 shows the line shape analysis results obtained for the low-frequency spectrum of [BzMIm][NTf_2] at 293 and 353 K. Fits for all of the low-frequency spectra in this study have similar quality. It should be noted that in the previous study, an antisymmetrized Gaussian function at ca. 95 cm^{-1} with a relatively small amplitude was added for the spectra of [CHxmMIm][NTf_2] and [CHxmPy][NTf_2] as an intramolecular mode,[107] but in this study that function is not included because it led to unstable fits with some unreasonable parameters. Fitting without that function gave the same goodness-of-fit values as when it was included, so it was considered superfluous. Therefore, I determine that intramolecular vibrational modes contribute to the low-frequency spectral densities. However, this is unlikely to significantly influence the temperature dependence of the spectra because of their relatively small amplitude, and the relative tendency of the spectral change to the temperature variation does not vary widely. The results of the line shape analysis for ILs at various temperatures are summarized in

Appendix G. Note that simple and exact assignments of intermolecular vibrational modes in the low-frequency broadened spectrum of liquids based on the line shape analysis results are often beyond safe discussion and spectral assignment, because the intermolecular vibrational modes in liquids, including ILs, are strongly coupled, and the spectral band is significantly influenced by the couplings.[18,61-62,94,98,195-197] Perhaps some exceptions might be allowed to discuss a specific mode, such the 7-azaindole dimer that forms cooperative hydrogen-bonding dimer in the gas phase and nonpolar solvents.[26-27] Nonetheless, it is helpful to understand the spectral features of particular frequency region (e.g., low-frequency and high-frequency regions) and to obtain the overall spectral quantity, such as the first moment M_1. The M_1 values of the low-frequency spectra for the ILs were also estimated on the basis of the line-shape analysis results.

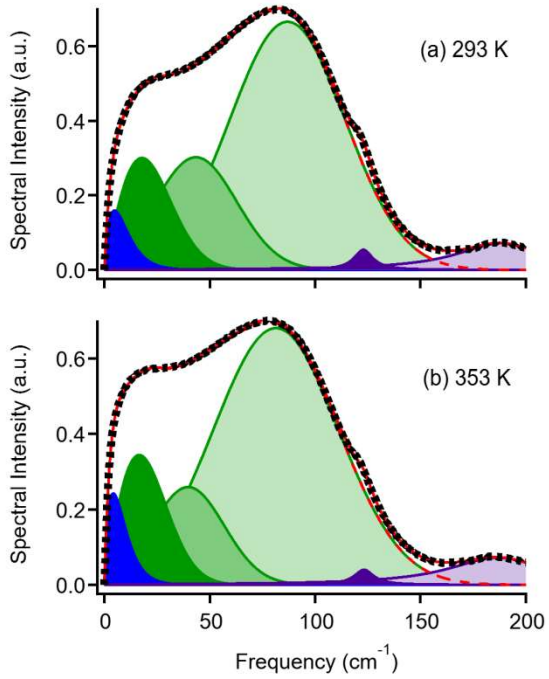

Figure 7.6. Line shape analysis results obtained for the low-frequency Kerr spectra in the frequency range of 0–200 cm^{-1} for [BzMIm][NTf_2] at (a) 293 K and (b) 353 K. Dots denote the experimentally obtained spectra, red lines denote the entire fits, blue areas denote the Ohmic components, green areas denote the antisymmetrized Gaussian components, purple areas denote the Lorentzian component, and red broken lines denote the sums of Ohmic and antisymmetrized Gaussian components.

With respect to the fit parameters for the line-shape analysis (Appendix G), it should be

noted that two parameters show clear tendencies regarding the variation of temperature for all the ILs. As mentioned above, discussion on each fit component is not respective to each vibrational mode, but it is helpful to understand the spectral feature qualitatively. One is the amplitude of the Ohmic component (the lowest frequency component at ca. 5 cm^{-1}). This component's intensity increases with rising temperature. In fact, this feature is clear in the difference spectra shown in Figure 7.5. In the calculated spectra of the density of states of $[C_4MIm][PF_6]$ and ionic components, i.e., cation and anion, at several temperatures using molecular dynamics simulations,[198] the spectral intensities in the low-frequency region for both the cation and anion increase with rising temperature. Although the present ILs are not the same, I expect that the motions of both cations and anions influence the temperature dependence in the low-frequency spectral density.

The other parameter is the frequency of the highest frequency antisymmetrized Gaussian component. For ILs, the characteristic frequency shifts to the lower frequency with increasing temperature, except for $[CHxmMPyrr][NTf_2]$, which does not show the high-frequency libration. I also found that the amplitude parameter in this component does not change much with a variation of temperature. Because the spectral density in the high-frequency region above 80 cm^{-1} for aromatic cation-based ILs originated mainly from the libration of the aromatic ring,[53] I conclude that the spectral change in the high-frequency region is due to the red shift of the aromatic ring librational motion, rather than the change in the amplitude of the spectral density.

Figure 7.7 shows the plots of M_1 vs. temperature for ILs. The linear fits ($M_1 = aT + M_{1,0}$) are also shown in the figure, and the fit parameters are summarized in Table 7.1. Though the number of data is not large and some data have considerable error ranges, it would be worth discussing the qualitative feature of the temperature dependence of M_1 in the ILs. a is the slope of the relation of M_1 to temperature, i.e., the temperature-sensitivity parameter, and $M_{1,0}$ is the intercept of the relation, i.e., the intrinsic first moment of the spectrum. From the figure and table, it can be seen that the slope a for $[CHxmMPyrr][NTf_2]$ is the most gradual among these ILs. The a values for the other ILs in this study are similar to that of $[C_4MIm]^+$-based ILs, including $[NTf_2]^-$ salt, as well as the neutral analogue, 1-methylimidazole.[198] Therefore, it is natural to assume that the temperature dependence of the intermolecular vibrational band of ILs whose cations have aromatic rings are governed by the temperature dependence of the aromatic ring libration; thus, the nonaromatic cation-based IL, i.e., $[CHxmMPyrr][NTf_2]$, shows a different temperature dependence of M_1 for the other ILs. In Section 3.4.3, the temperature

sensitivity (slope of M_1 to temperature: a) was compared with the fragility parameter, which is obtained from the temperature-dependent viscosity, for imidazolium-based ILs, and no correlation between them was found.[198] In fact, the fragility is an important physical parameter for glass-forming liquids, which is the classification of many ILs.[100,106] In this study, when the spectral temperature-sensitivity parameter a is compared with the fragility parameter,[107] there are no clear tendencies or correlations among the present six ILs. Because the length (or space) scale of the intermolecular vibration is very small compared to that of the structural relaxation, the temperature dependence of the M_1 of the intermolecular vibrational band would not directly relate to the fragility parameter. In addition, it is noted that the temperature range in the present experiments is much higher than the glass transition temperatures of the ILs (205–220 K).[107] This obscures the glass transition and its related phenomena, and properties including the fragility.

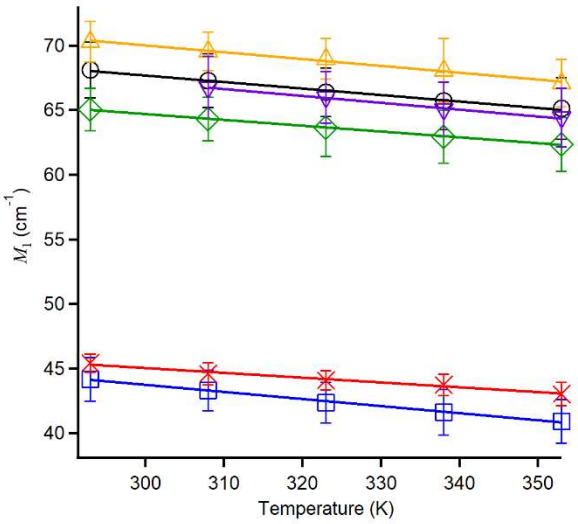

Figure 7.7. Plots of first moment M_1 vs. temperature for [CHxmMPyrr][NTf_2] (red crosses), [CHxmMIm][NTf_2] (green diamonds), [CHxmPy][NTf_2] (purple inverted triangles), [BzMPyrr][NTf_2] (blues squares), [BzMIm][NTf_2] (black circles), and [BzPy][NTf_2] (yellow triangles). Linear fits are shown by the solid lines.

Table 7.1. Fit parameters for the temperature dependence of the first moment M_1 of the broad, low-frequency spectral band for each IL.

IL	a (cm^{-1} K^{-1})	$M_{1,0}$ (cm^{-1})
[CHxmMPyrr][NTf_2]	−0.0374	56.3
[CHxmMIm][NTf_2]	−0.0454	78.3
[CHxmPy][NTf_2]	−0.0529	83.0
[BzMPyrr][NTf_2]	−0.0550	60.3
[BzMIm][NTf_2]	−0.0506	82.9
[BzPy][NTf_2]	−0.0528	85.9

Besides the spectral temperature-sensitivity parameter a, it is also found that the $M_{1,0}$ values for [CHxmMPyrr][NTf_2] and [BzMPyrr][NTf_2] are approximately 60 cm^{-1}, but that for the other four ILs are approximately 80 cm^{-1}. This difference is attributed to the origin of the cation moiety: pyrrolidinium vs. imidazolium and pyridinium. This indicates that the charged aromatic rings of the cations have a greater influence on the intrinsic low-frequency spectrum than the neutral aromatic rings of the cations. Previously, Shirota and coworkers compared M_1 with the bulk parameter, which is the square root of the surface tension divided by the density $(\gamma/d)^{1/2}$ for [CHxmMPyrr][NTf_2], [CHxmMIm][NTf_2], [CHxmPy][NTf_2], [BzMPyrr][NTf_2], [BzMIm][NTf_2], and [BzPy][NTf_2] at room temperature. They found that the relation between M_1 and $(\gamma/d)^{1/2}$ for pyrrolidinium-based ILs is different from that for imidazolium- and pyridinium-based ILs.[107] These experimental results indicate that the charged aromatic ring plays an important role on the low-frequency spectral feature (and thus microscopic intermolecular interaction and structure) in ILs compared to the neutral aromatic ring.

7.4. Conclusions

In this chapter, I studied the temperature dependence of the low-frequency spectra of six systematic ILs whose cations have different cyclic functional groups to determine the effects of aromaticity using fs-RIKES. All six of the ILs show temperature-dependent low-frequency Kerr spectra. However, the low-frequency spectrum of [CHxmMPyrr][NTf_2] shows a temperature dependence only in the low-frequency region below 50 cm^{-1}, but the other five ILs show temperature dependence for both the low-frequency region below 50 cm^{-1} and the high-frequency region above 80 cm^{-1} (greater than 50 cm^{-1} in the case of [BzMPyrr][NTf_2]). This indicates that the aromatic ring libration influences the temperature dependence of the low-

frequency spectral density in the high-frequency region. From the difference spectra for the higher temperatures relative to the spectra at 293 K, it is confirmed that the temperature-sensitive frequency region for [CHxmMIm][NTf_2] and [CHxmPy][NTf_2] is approximately 100 cm^{-1}, and that for [BzMPyrr][NTf_2] is approximately 70 cm^{-1}. The results are well explained with the previous assignments for the librational bands of the aromatic rings in the ILs at room temperature.[107] For the six ILs, the plots of M_1 vs. temperature show that the low-frequency spectrum for the nonaromatic [CHxmMPyrr][NTf_2] is less temperature dependent than the other ILs. This is accounted for by the absence of an aromatic ring whose librational motion is temperature sensitive. It was also found that the intrinsic first moment of the low-frequency spectrum is lower for pyrrolidinium-based ILs than for imidazolium- and pyridinium-based ILs.

Chapter 8

Effects of Conjugations on Intermolecular Vibrational Dynamics for Six-Membered-Ring Molecular Liquids

J. Phys. Chem. B, **2015**, *119*, 4713–4724.

8.1. Introduction

In this chapter, how aromaticity, conjugation, and resulting molecular structures affect the low-frequency spectral shapes will be discussed by investigating the intermolecular vibrational dynamics of six-membered-ring molecular liquids. It is commonly expected in fs-RIKES experiments that aromatic liquids are usually easy to analyze, as their signal is very large. However, it is not fully clarified how aromaticity in molecular liquids affects the low-frequency Kerr spectrum or the polarizability anisotropy response. Simon and coworkers have studied the intermolecular vibrational bands of benzene, 1,4-cyclohexadiene, 1,5-cyclooctadiene, benzonitrile, and *o*-methylbenzonitrile by means of fs-RIKES.[199] They attributed the broad spectral features of the low-frequency spectra in aromatic liquids to aromatic–aromatic interactions. Chang and Castner have investigated substituted benzenes and cyclohexanes, such as toluene, cyclohexane, and methylcyclohexane.[120] They observed the damped transients at 400–500 fs in the pure nuclear responses in the aromatic liquids but no such damped nuclear responses in the nonaromatic liquids. Recently, Zhong and Fourkas have studied molecular liquids with different geometries, including nonaromatic tetrahydrofuran and aromatic furan.[65] Like the other liquids mentioned above, the low-frequency spectrum of furan is broader than that of tetrahydrofuran.

Here, I have investigated the low-frequency dynamics of five systematically different six-membered-ring molecular liquids by means of fs-RIKES to elucidate the effects of aromaticity or conjugation on the low-frequency spectra and ultrafast molecular dynamics. The target liquids include benzene, 1,3-cylcohexadiene, 1,4-cyclohexadiene, cyclohexene, and cyclohexane, as shown in Figure 8.1. It is noted that the low-frequency spectra of 1,3-cyclohexadiene and cyclohexene are reported for the first time, as far as I know. In addition to fs-RIKES, the dynamics of solvents in the low-frequency region have often been characterized by a more popular spectroscopic method, the time-dependent fluorescence Stokes shift (TDFSS) measurements of a solvatochromic probe molecule, which corresponds to the solvation dynamics.[6,200] Recently, a more sophisticated spectroscopic technique, ultrafast photon echo measurement, has also been developed to characterize the solvation dynamics in solutions.[201-203] In contrast to fs-RIKES, the TDFSS probes a dipole moment time-correlation function predominantly. When we are interested in the dynamics of a nonpolar or less polar solvent, however, TDFSS is difficult to use because of its sensitivity, as the solvation energy or the magnitude of the fluorescence Stokes shift of the solute due to nonpolar and less polar solvents are much less than those of polar solvents.[204] As far as I know, the solvation dynamics

data of the solvents used in this study have not been reported, except for benzene.[205] Thus, I believe that the dynamical data of the liquids reported here are helpful to understanding the molecular aspects of the intermolecular dynamics in nonpolar or less-polar liquids and useful as new data, besides the new information on the effects of aromaticity of six-membered-ring molecular liquids on low-frequency intermolecular dynamics.

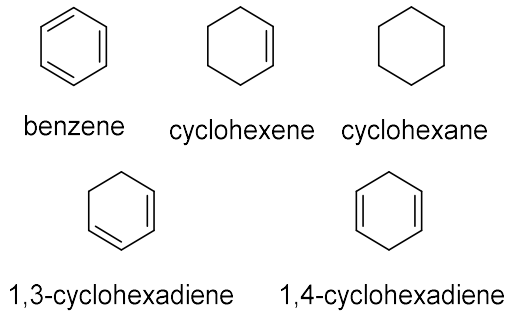

Figure 8.1. Chemical structural formulas of the six-membered-ring molecular liquids: benzene, 1,3-cyclohexadiene, 1,4-cyclohexadiene, cyclohexene, and cyclohexane.

To help understand the nature of the Kerr spectra, quantum chemistry calculations have also been performed to estimate the polarizability anisotropy volumes and intramolecular vibrational modes. Furthermore, the bulk properties, such as shear viscosity η, density d, and surface tension γ, have been measured to compare with the low-frequency spectra and the overdamped relaxation times.

8.2. Experimental Section

Benzene (Wako, >99.7%), 1,3-cylohexadiene (Sigma-Aldrich, 97%), 1,4-cyclohexadiene (TCI, >98%), cyclohexene (TCI, >98%), and cyclohexane (Sigma-Aldrich, >99.7%) were used as received.

Ab initio quantum chemistry calculations of the present six-membered-ring molecules in the gas phase condition were performed at the B3LYP/6-311++G(d,p) level of theory to obtain the optimized structures, Raman-active normal modes, and polarizability tensor elements of the six-membered ring molecules using the *Gaussian 03* program suite.[206] The obtained atom coordinates of the optimized structures of the molecules are summarized in Appendix H.

8.3. Results

Table 8.1 lists the bulk property data, including η, d, and γ, of benzene, 1,3-cylohexadiene, 1,4-cyclohexadiene, cyclohexene, and cyclohexane measured in this study. The formula weights and molar volumes are also listed in the table. d of all five liquids and the η and γ of liquid benzene, cyclohexene, and cyclohexane were reported,[91] and the values estimated in this study are quite similar to the reported ones. As far as I know, the values of η and γ of liquid 1,3-cyclohexadiene and 1,4-cyclohexadiene have never been reported. I believe that the values of the bulk properties of liquid 1,3-cyclohexadiene and 1,4-cyclohexadiene measured in this study are adequate on the basis of agreement with the present and reported data of benzene, cyclohexene, and cyclohexane. The van der Waals volumes V_{vdW} of the five molecules, which are calculated by the van der Waals increments,[207] are also listed in Table 8.1 to determine the occupation factors of the volumes V_{vdW}/V_m.

Table 8.1. Formula Weight FW, Density d, Molar Volume V_m, Shear Viscosity η, and Surface Tension γ of Six-Membered-Ring Molecular Liquids at 293 K

liquid	FW	$V_{vdW}N_A$ (cm^3/mol)	d [a,b] (g/cm^3)	V_m (cm^3/mol)	$V_{vdW}N_A/V_m$	η [c,d] (cP)	γ [e,f] (mN/m)
benzene	78.11	48.4	0.878	89.0	0.544	0.617	28.2
1,3-cyclohexadiene	80.13	52.8	0.840	95.4	0.553	0.633	25.3
1,4-cyclohexadiene	80.13	52.8	0.850	94.3	0.560	0.616	27.2
cyclohexene	82.14	57.1	0.805	102	0.560	0.661	26.1
cyclohexane	84.16	61.4	0.773	109	0.563	0.963	24.7

[a] 293.0±0.3 K. [b] ±1%. [c] 293.0±0.2 K. [d] ±5%. [e] 293.0±0.3 K. [f] ±3%.

Figure 8.2a shows the long-time-window Kerr transients of benzene, 1,3-cyclohexadiene, 1,4-cyclohexadiene, cyclohexene, and cyclohexane. The transients from 3 to 25 ps were fitted by a biexponential function, and the fit parameters are summarized in Table 8.2. The slowest time constant τ_2 seems to be slower with lower aromaticity in the six-membered-ring molecules. However, Figure 8.2a and Table 8.2 clearly show that the amplitude of the slowest relaxation in cyclohexane is much smaller than that in the other liquids. The small amplitude of the slowest relaxation of cyclohexane is attributed to its small polarizability anisotropy.

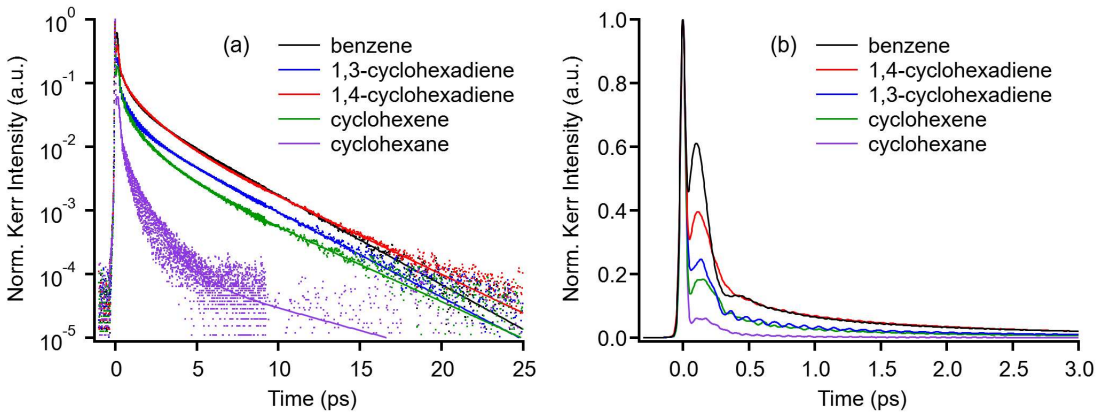

Figure 8.2. (a) Normalized Kerr transients (dots) for benzene (black), 1,3-cyclohexadiene (blue), 1,4-cyclohexadiene (red), cyclohexene (green), and cyclohexane (purple). Biexponential fits from 3 to 25 ps are also shown by the corresponding colored solid lines. (b) Magnification of the Kerr transients from −0.3 to 3.0 ps.

Table 8.2. Biexponential Fit Parameters for Kerr Transients of Six-Membered-Ring Molecular Liquids at 293 K

liquid	a_1	τ_1 (ps)	a_2	τ_2 (ps)
benzene	0.05144	1.12	0.04361	3.09
	±0.00150	±0.02	±0.00048	±0.01
1,3-cyclohexadiene	0.02251	1.22	0.02000	3.26
	±0.00096	±0.05	±0.00049	±0.03
1,4-cyclohexadiene	0.07652	1.39	0.02658	3.58
	±0.00037	±0.01	±0.00037	±0.02
cyclohexene	0.02559	1.41	0.00775	3.74
	±0.00033	±0.03	±0.00030	±0.05
cyclohexane	0.00388	1.12	0.00014	6.23
	±0.00084	±0.11	±0.00005	±1.44

Figure 8.2b shows the short-time-window Kerr transients from −0.5 to 3 ps for benzene, 1,3-cyclohexadiene, 1,4-cyclohexadiene, cyclohexene, and cyclohexane. It is seen from the figure that (i) the Kerr transient clearly depends on the molecular liquid and (ii) the tendency of the Kerr signal intensities of the nuclear responses at the earliest time stage (~50–200 fs) relative to the signal intensities of the electronic responses (spike at $t = 0$) for the five liquids is benzene > 1,4-cyclohexadiene > 1,3-cyclohexadiene > cyclohexene > cyclohexane.

Because each Kerr transient shows a complicated feature that includes underdamped and overdamped motions, as shown in Figure 8.2b, they have been analyzed by the standard Fourier transform deconvolution method[9,185] to elucidate the Kerr spectra based on a previously reported procedure.[17,53,174] Figure 8.3 shows the Kerr spectra in the frequency range of 0–700 cm^{-1} for benzene, 1,3-cyclohexadiene, 1,4-cyclohexadiene, cyclohexene, and cyclohexane. The Kerr spectra of benzene,[14,17,68-69,119,199,208-215] 1,4-cyclohexadiene,[199] and cyclohexane[65,120] in the low-frequency region were reported, and the reported spectra are quite similar to the present ones. The sharp bands are due to the intramolecular modes, while the broad bands in the frequency range of less than 200 cm^{-1} are due to the intermolecular vibrational bands. The clear intramolecular vibrational bands are listed in Table 8.3.

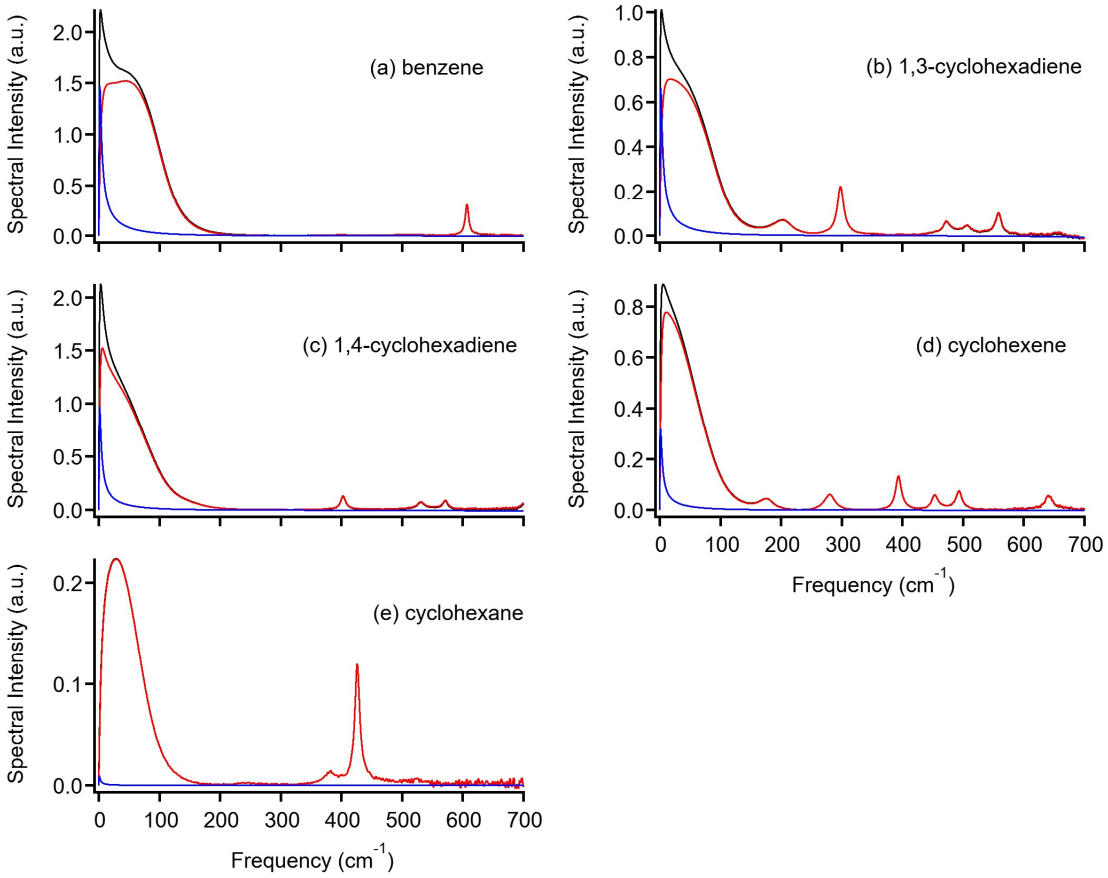

Figure 8.3. Fourier transform Kerr spectra in the frequency range of 0–700 cm^{-1} for (a) benzene, (b) 1,3-cyclohexadiene, (c) 1,4-cyclohexadiene, (d) cyclohexene, and (e) cyclohexane. The black lines denote the entire spectra, the blue line denotes the contributions of the slow relaxation components, and the red lines denote the spectra subtracted the slow relaxation components from the entire spectra.

Table 8.3. Observed and Calculated Intramolecular Vibrational Modes for Six-Membered-Ring-Molecular Liquids

benzene			1,3-cyclohexadiene			1,4-cyclohexadiene		
exp	calc	mode	exp	calc	mode	exp	calc	mode
607	622	ring def (ip) (deg)	200	196	ring twist (C–C)	403	407	ring rocking
			298	301	ring rocking	531	543	ring def (ip) (sym)
			472	480	ring def (asym)	571	580	ring def (ip) (asym)
			506	522	ring twist (C=C)	707	722	CH wagging (op)
			558	572	ring def (sym)			
				674	CH wagging (op)			

cyclohexene			cyclohexane		
exp	calc	mode	exp	calc	mode
174	165	ring rocking	382	371	ring rocking
280	278	ring torsion (C4,5)	426	432	ring def (deg)
394	399	ring torsion (C3,6)			
453	458	ring def (asym)			
493	502	ring def (sym)			
640	654	CH wagging + C(3,6) bd			
718	730	CH wagging + C(4,5) bd			

def: deformation. bd: bending. sym: symmetric. asym: asymmetric. deg: degeneracy. ip: in-plane. op: out-of-plane.

The line shape of the broad intermolecular vibrational band, excluding the contribution of the collective orientational relaxation (the slow contribution of the biexponential component), in the frequency range of approximately 0–200 cm^{-1} has been analyzed by the sum of Ohmic[70] and antisymmetrized Gaussian functions.[16] A Lorentzian function was further added when a clear intramolecular vibrational band was observed in the Kerr spectra. The details of the line shape analysis have been described in Chapter 2.[17,53,174] The line shape analysis results are shown in Figure 8.4, and the fit parameters are summarized in Appendix H. In Figure 8.4f, the normalized relative intensity is determined as that the sum of the strongest intensities of each fit function component equals unity. It is also noted that the peak frequency in Figure 8.4g denotes the peak frequency of each component, not the characteristic frequency of each fit function. The values of the first moment M_1 of the low-frequency spectrum have been calculated and are listed in Table 8.4. Note that the estimated M_1 is for the intermolecular vibrational band, which is the spectrum with the contributions of the collective orientational relaxation (slow exponential component) and the intramolecular vibrational mode removed.

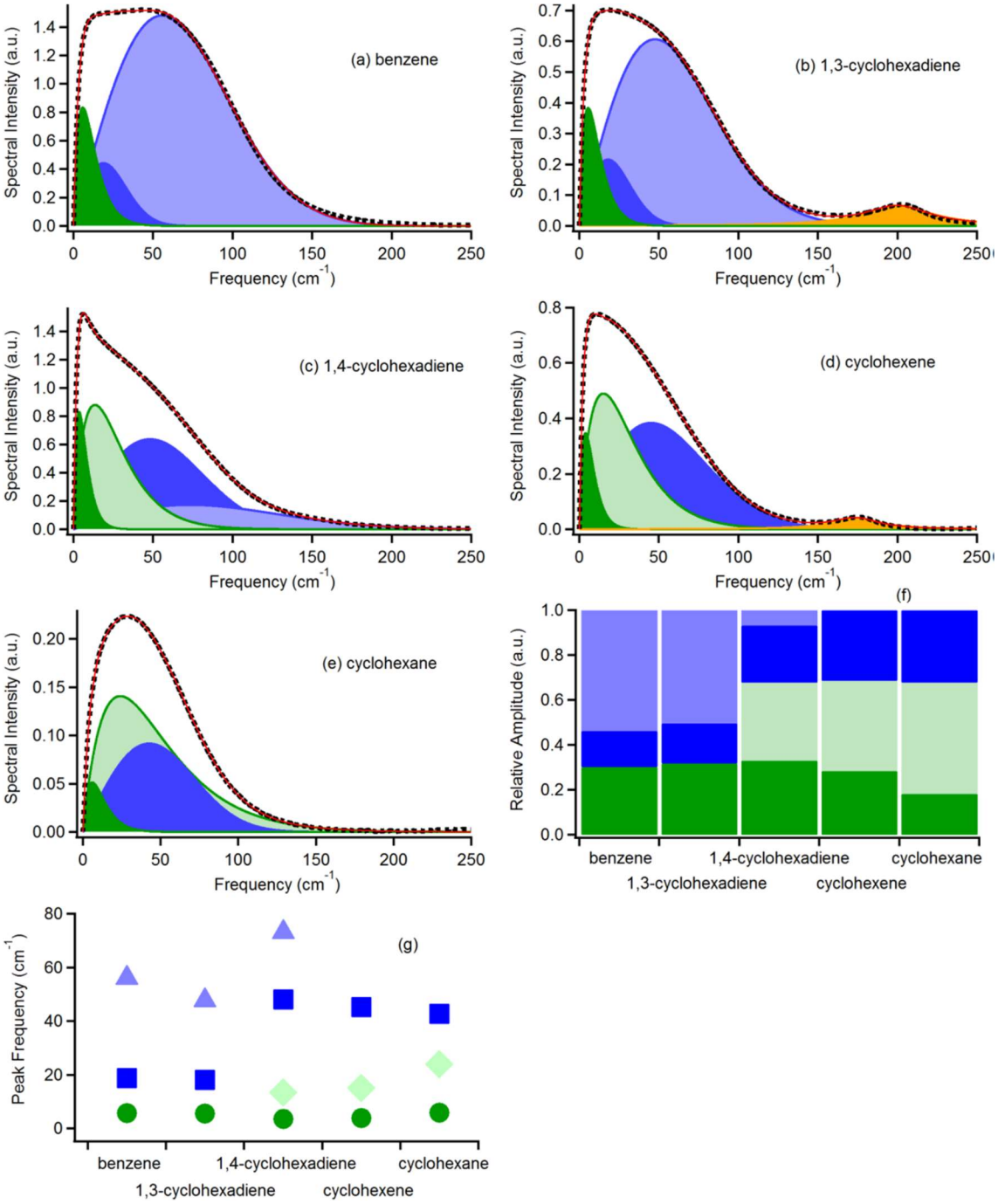

Figure 8.4. Low-frequency Kerr spectra in the frequency range of 0–250 cm^{-1} for (a) benzene, (b) 1,3-cyclohexadiene, (c) 1,4-cyclohexadiene, (d) cyclohexene, and (e) cyclohexane. Black dots denote the spectra, red lines denote the entire fits, green areas denote Ohmic functions, blue areas denote antisymmetrized Gaussian functions, and brown areas denote Lorentzian functions (for intramolecular vibrational modes). (f) Bar chart of each fit component of the relative amplitude and (g) plots of the peak frequencies are also given.

Table 8.4. First Moments M_1 of Experimental Low-Frequency Spectra, Calculated Mean Polarizabilities α_0, Polarizability Anisotropies α_{anis}, and Their Values Relative to Benzene for Six-Membered-Ring Molecular Liquids

liquid	M_1 (cm^{-1})	α_0 (α_0/α_0(benzene))	α_{anis} ($\alpha_{anis}/\alpha_{anis}$(benzene))	r_{integ}/r_{integ}(benzene)
benzene	59.0	9.819	5.459	1
		(1)	(1)	
1,3-cyclohexadiene	51.0	10.289	3.926	0.451
		(1.05)	(0.72)	
1,4-cyclohexadiene	50.6	9.996	5.022	0.861
		(1.02)	(0.92)	
cyclohexene	42.9	10.267	3.086	0.380
		(1.05)	(0.565)	
cyclohexane	46.7	10.375	1.324	0.069
		(1.06)	(0.243)	

To see the relative intensity of the nuclear response to the electronic response of the Kerr signal of the five six-membered-ring molecular liquids, the line shape analysis results are further subjected to an inverse Fourier transform analysis. The nuclear response in the time domain $r(t)$ is obtained by an inverse Fourier transform analysis of the imaginary part of the Fourier transform Kerr spectrum:[10]

$$r(t) = F^{-1}\{\mathrm{Im}[D(\omega)]\}H(t) \tag{8.1}$$

where $H(t)$ is the Heaviside step function. Note that the nuclear response here does not include the electronic response. Figure 8.5 shows the nuclear responses of the five six-membered-ring molecular liquids. In addition to the entire nuclear responses, the responses of the intermolecular vibrational dynamics and the reorientation are also shown in the figure. The time integrals of the intermolecular vibrational response and the nuclear response exclude the intramolecular vibrations, that is, the sum of the nuclear responses of the intermolecular vibrational dynamics and estimated reorientations, and the values for the five sample liquids are summarized in Table 8.4 together with the mean polarizabilities and polarizability anisotropies (vide infra) to find the relative magnitudes of the nuclear responses (or the depolarized Raman spectra) of the intermolecular dynamics and the intermolecular vibrational

dynamics. The nuclear responses in the time domain due to the intermolecular vibrational dynamics of the five liquids are directly compared in Figure 8.5f.

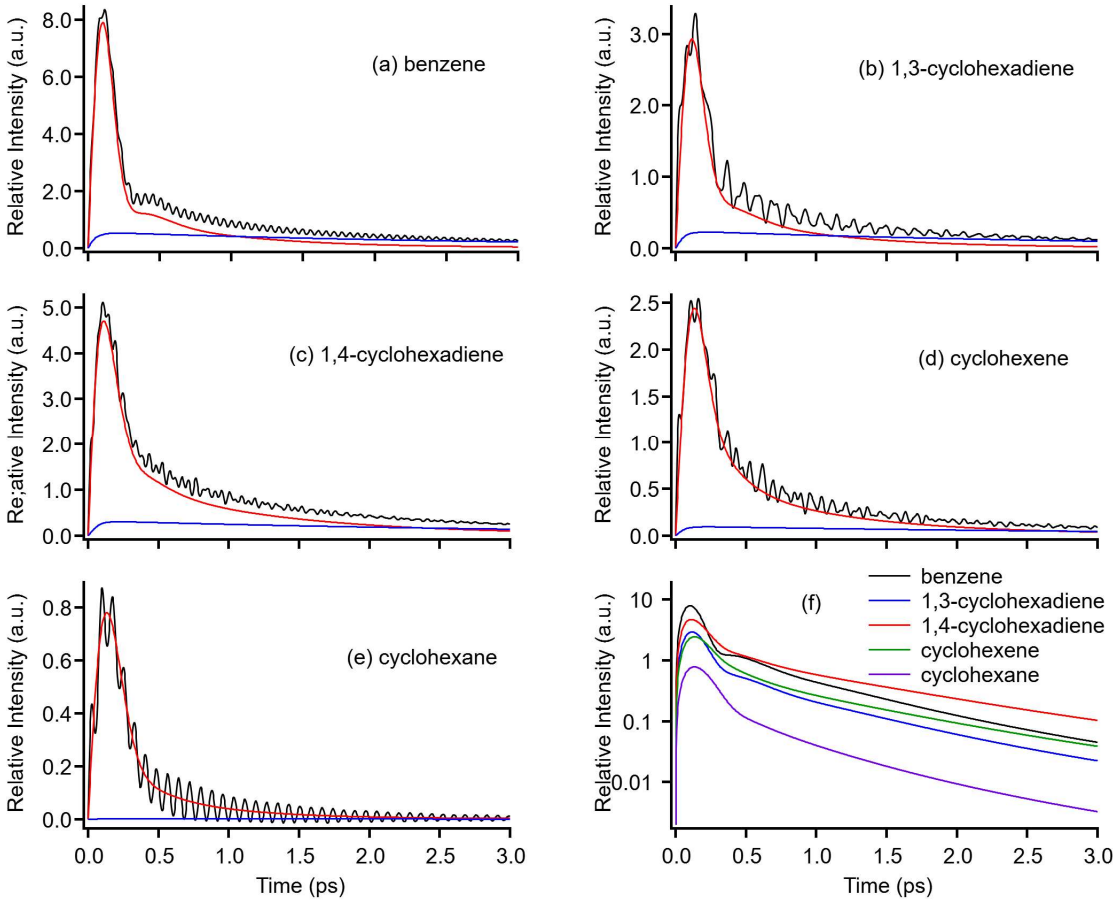

Figure 8.5. Nuclear responses of liquid (a) benzene, (b) 1,3-cyclohexadiene, (c) 1,4-cyclohexadiene, (d) cyclohexene, and (e) cyclohexane. Black lines denote the entire responses, blue lines denote the diffusive orientational relaxations (the slow components in the biexponential fits to the overdamped transients), and red lines denote the intermolecular vibrational dynamics. (f) Semilogarithmic plots of the intermolecular nuclear responses due to the intermolecular vibrations of benzene (black), 1,3-cyclohexadiene (blue), 1,4-cyclohexadiene (red), cyclohexene (green), and cyclohexane (purple). Contributions of the electronic responses, diffusive orientational relaxations, and the intramolecular vibrational modes are excluded from the nuclear responses.

Figure 8.6 displays the calculated Raman spectra of the optimized benzene, 1,3-cyclohexadiene, 1,4-cyclohexadiene, cyclohexene, and cyclohexane molecules based on the B3LYP/6-311++G(d,p) level of theory. The observed intramolecular vibrational bands in the

Kerr spectra have been assigned on the basis of the quantum chemistry calculations and previous reports. The assignments for the intramolecular vibrational bands are summarized in Table 8.3. The values of the polarizability tensor elements α_{ij} are summarized in Appendix H, but the mean polarizability α_0, which is defined as $(\alpha_{xx} + \alpha_{yy} + \alpha_{zz})/3$, and polarizability anisotropies α_{anis}, which are defined as $\{[(\alpha_{xx} - \alpha_{yy})^2 + (\alpha_{yy} - \alpha_{zz})^2 + (\alpha_{zz} - \alpha_{xx})^2 + 6(\alpha_{xy}^2 + \alpha_{yz}^2 + \alpha_{zx}^2)]/2\}^{1/2}$,[216] are summarized in Table 8.4.

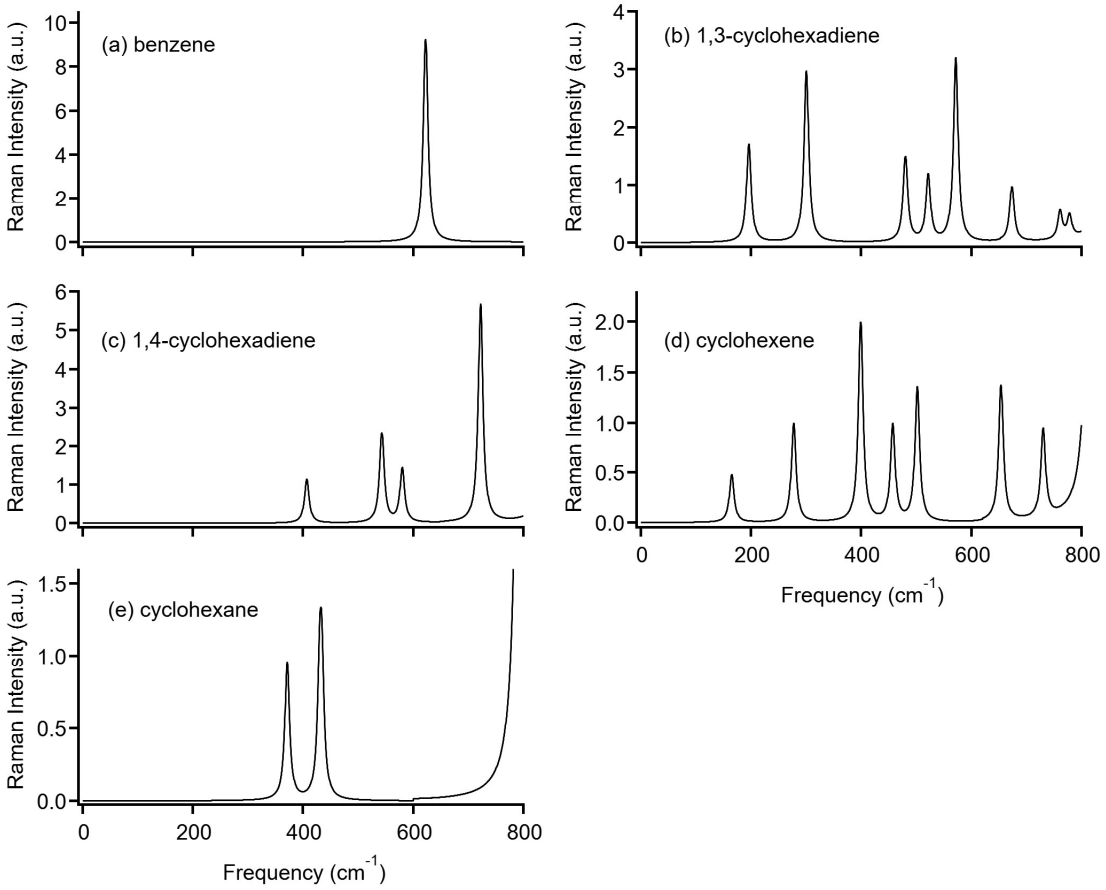

Figure 8.6. Calculated Raman spectra of benzene, 1,3-cyclohexadiene, 1,4-cyclohexadiene, cyclohexene, and cyclohexane molecules by quantum chemistry calculations based on the B3LYP/6-311++G(d,p) level of theory.

8.4. Discussion

8.4.1. Low-Frequency Kerr Spectra and Intermolecular Vibrational Dynamics.

As shown in Figures 8.3 and 8.4, the line shapes of the low-frequency Kerr spectral bands for the five liquids are very different, despite their all being six-membered rings. The line shape

of benzene is trapezoidal (or gently bimodal), while that of cyclohexane shows a monomodal spectrum. The trapezoidal (or bimodal) line shape feature for benzene is mainly attributed to the strong magnitude of the highest frequency component and the small amplitude of the intermediate components, as shown in Figure 8.4. The ratio in the amplitudes of the highest, intermediate, and lowest frequency components for benzene are 1:0.30:0.56. 1,4-Cyclohexadiene is clearly triangular, while cyclohexene seems to be in between cyclohexane and 1,4-cyclohexadiene. 1,3-Cyclohexadiene can be seen as trapezoidal, but it is in between the trapezoidal benzene and the triangular 1,4-cyclohexadiene. The ratio in the amplitudes of the highest, intermediate, and lowest frequency components for cyclohexane, which shows the monomodal line shape, are 1:1.54:0.56. The ratio in the amplitudes of the highest (G_2 component), low antisymmetrized Gaussian (G_1 component), high Ohmic (O_2 component), and lowest frequency (O_1 component) components for 1,4-cyclohexane, which shows the triangular line shape, are 1:3.69:5.09:4.80.

According to a theoretical work based on molecular dynamics simulations and instantaneous normal mode analysis of liquid benzene by Ryu and Stratt,[18] the translational vibrational motion and the cross-term that is the coupling motion between the translational and reorientational vibrational motions are located in the low-frequency region, while the high-frequency region signals are mostly due to the reorientational vibrational motion such as libration. In addition, most aromatic liquids, except for hexafluorobenzene, show broad bimodal line shapes in the low-frequency Kerr spectra.[17] Therefore, the broad bimodal spectral (or trapezoidal) feature of the low-frequency spectrum for liquid benzene is mainly attributed to the benzene ring libration. In addition to liquid benzene, liquid 1,3-cyclohexadiene also shows a broadened spectral line shape. In contrast, liquid 1,4-cyclohexadiene, a structural isomer of 1,3-cyclohexadiene, shows a triangular spectral shape. As mentioned in the Introduction, the low-frequency spectra of aromatic molecular liquids are broad relative to their nonaromatic analogs: benzene and 1,4-cyclohexadiene;[199] toluene and methylcyclohexane;[120] and furan and tetrahydrofuran.[65] One can think that the planar structure from C1 to C4 due to the aromaticity in the 1,3-cyclohexadiene is likely indicative of distinct (caging) librational motion.

In cyclohexane, the spectral shape is monomodal with a low intensity in the low-frequency region less than approximately 20 cm^{-1} compared to the other evaluated liquids. In this region, the spectral features are indeed complicated. The molecular motions appearing in this frequency region often include intermolecular vibrational motions, such as translational and orientational vibrational motions, and their coupling motion and also the crossover process from the

intermolecular vibration to the diffusive reorientational dynamics. Furthermore, the contribution of the diffusive orientational dynamics in cyclohexane is very small in comparison to that of the other evaluated liquids, as displayed in Figures 8.2a and 8.3. In fact, a nonpolar solvent, carbon tetrachloride, at room temperature shows a similar spectral feature, although it does not show the diffusive orientational dynamics because of its spherical top nature.[68] One can think that the intermolecular vibrations in nonpolar solvents with negligible polarizability anisotropy do not significantly influence or couple with the diffusive orientational dynamics, and thus the crossover process from the intermolecular vibrational motion and the translational motions such as collision-induced and interaction-induced motions do not affect the anisotropic motion.

In Figure 8.5, one can clearly compare the nuclear responses due to the intermolecular vibrations in the time domain of the five liquids. As seen in the figure, the damped transients or bumps of approximately 0.5 ps are observed in benzene clearly and in 1,3-cyclohexadiene barely. The damped features of the two liquids come from the trapezoidal shapes, the strong spectral densities at approximately 50 cm^{-1}. Thus, the intermolecular vibrational motions of 1,4-cyclohexadiene, cyclohexene, and cyclohexane dephase quickly, but the intermolecular vibrational motions (likely librational motions) of benzene and 1,3-cyclohexadiene maintain the periodic motions. Like the present results, Chang and Castner reported that the damped nuclear responses with a bump of 0.4–0.5 ps were observed in toluene, benzonitrile, and benzyl alcohol, but not in cyclohexane or methylcyclohexane.[120] They attributed this feature (librational caging effect) to the stronger intermolecular forces (on the basis of the bimolecular system) of aromatic liquids relative to nonaromatic liquids. On the other hand, the boiling points (T_b) and the enthalpies of vaporization (ΔH_{vap}) of benzene, cyclohexene, and cyclohexane are similar: T_b(benzene) = 353.24 K, T_b(cyclohexene) = 356.13 K, T_b(cyclohexane) = 353.88 K, $\Delta H_{vap,298K}$(benzene) = 33.83 kJ/mol, $\Delta H_{vap,298K}$(cyclohexene) = 33.47 kJ/mol, and $\Delta H_{vap,298K}$(cyclohexane) = 33.01 kJ/mol.[91] This indicates that the intermolecular force would not likely be the reason for the caging librational motion in the present liquids. Therefore, as shown in Figures 8.3 and 8.4 and discussed above, the planar structures seem to be the key to the caging librational motion; molecular geometry plays an important role in the intermolecular vibrational spectrum and the ultrafast nuclear response.

In addition to the time domain trajectory features of the nuclear responses of the five liquids, it would be worthwhile to discuss the intensities of the nuclear responses. Essentially, the intensities of the intermolecular nuclear responses shown in Figures 8.5 are relative to the

electronic responses. As seen in Figure 8.5f, the tendency of the intensities at the first peak of the nuclear responses is benzene > 1,4-cyclohexadiene > 1,3-cyclohexadiene > cyclohexene > cyclohexane. At first glance, this may seem confusing because the aromaticity (or conjugation) of 1,3-cylohexadine is greater than that of 1,4-cyclohexadiene. In fact, the Kerr transient in the present polarization condition corresponds to the polarizability anisotropy response. It is thus more reasonable to compare the intensities due to the nuclear responses in the time domain to the polarizability anisotropies. Figure 8.7 shows plots of the time integrals of the nuclear responses $r(t)$ relative to that of benzene $r_{\mathrm{integ}}/r_{\mathrm{integ}}(\mathrm{benzene})$ versus the squares of the calculated polarizability anisotropies on the basis of quantum chemistry calculations (Table 8.4) relative to that of benzene $(\alpha_{\mathrm{anis}}/\alpha_{\mathrm{anis}}(\mathrm{benzene}))^2$. Note that the square, not the value, of α_{anis} is used in the relation between the signal intensity and the electric field of the signal. Figure 8.7 also shows the one-to-one linear correlation line, $r_{\mathrm{integ}}/r_{\mathrm{integ}}(\mathrm{benzene}) = (\alpha_{\mathrm{anis}}/\alpha_{\mathrm{anis}}(\mathrm{benzene}))^2$, not the linear fit. It is clear from the figure that $r_{\mathrm{integ}}/r_{\mathrm{integ}}(\mathrm{benzene})$ is well correlated to $(\alpha_{\mathrm{anis}}/\alpha_{\mathrm{anis}}(\mathrm{benzene}))^2$. This is not surprising, but it should be also noted that the time integral nuclear responses here include all the nuclear responses, the intramolecular vibrational modes, intermolecular vibrational dynamics, and diffusive orientational relaxations.

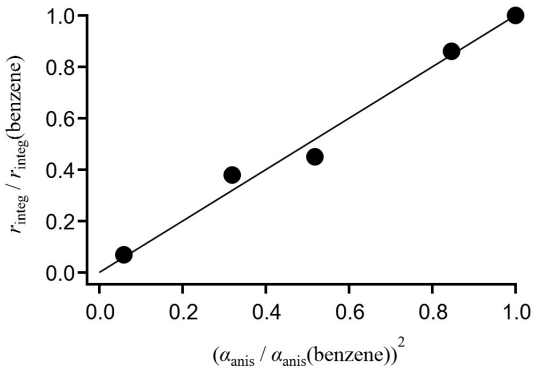

Figure 8.7. Plots of the time integrals of the nuclear responses $r(t)$ relative to that of benzene $r_{\mathrm{integ}}/r_{\mathrm{integ}}(\mathrm{benzene})$ versus the squares of the calculated polarizability anisotropies on the basis of quantum chemistry calculations relative to that of benzene $(\alpha_{\mathrm{anis}}/\alpha_{\mathrm{anis}}(\mathrm{benzene}))^2$. Line denotes the linear correlation between the two ($r_{\mathrm{integ}}/r_{\mathrm{integ}}(\mathrm{benzene}) = (\alpha_{\mathrm{anis}}/\alpha_{\mathrm{anis}}(\mathrm{benzene}))^2$), not the fit.

8.4.2. Comparison of the Low-Frequency Spectrum with a Bulk Parameter.

Previously, Shirota and coworkers reported a single linear relation between M_1 of the low-frequency Kerr spectrum and a bulk parameter $(\gamma/d)^{1/2}$ for aprotic molecular liquids including both aromatic and nonaromatic molecular liquids.[17] However, if FW is chosen instead of d, the relations for the aromatic and nonaromatic molecular liquids are different. In both cases, the essential idea of these plots is a simple consideration of the intermolecular vibrational band as a harmonic oscillator.[17]

Figure 8.8 shows the plots for M_1 vs $(\gamma/d)^{1/2}$ and $(\gamma/FW)^{1/2}$ for the present molecular liquids together with the previously reported correlation for aprotic molecular liquids.[17] The data of all evaluated liquids essentially obey the reported correlation. When strictly looking at the datum of liquid cyclohexene, however, the M_1 is slightly small compared to the bases of the $(\gamma/d)^{1/2}$ and $(\gamma/FW)^{1/2}$ scales. In particular, it is clear that the datum of cyclohexene is even far from the relation between M_1 and $(\gamma/FW)^{1/2}$ for nonaromatic molecular liquids, but the data of the other liquids are aligned with the respective correlations.

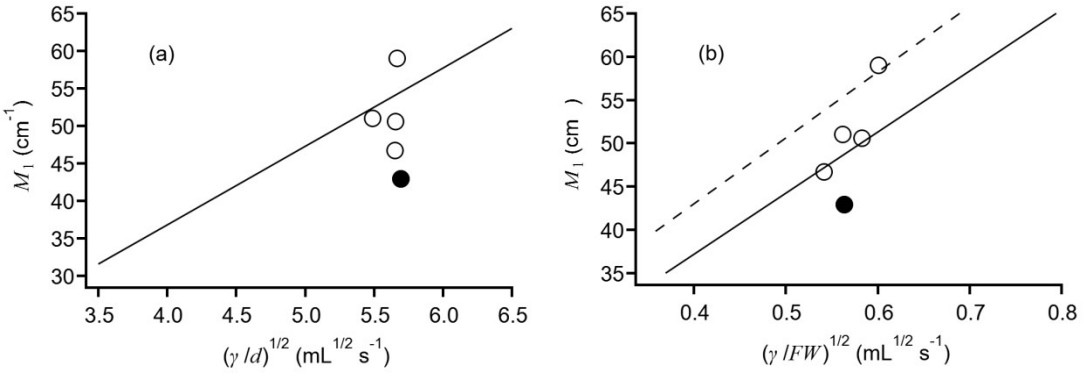

Figure 8.8. Plots of M_1 vs (a) $(\gamma/d)^{1/2}$ and (b) $(\gamma/FW)^{1/2}$ for the five six-membered-ring molecular liquids. Open circles denote benzene, 1,3-cyclohexadiene, 1,4-cyclohexadiene, and cyclohexane, and filled circles denote cyclohexene. Solid line in (a) the plots of M_1 vs $(\gamma/d)^{1/2}$ is the fit on the basis of 40 aprotic molecular liquids, and solid line and broken line in (b) the plots of M_1 vs $(\gamma/FW)^{1/2}$ are the fits on the basis of 20 nonaromatic aprotic molecular liquids and 20 aromatic aprotic molecular liquids.[17]

Unlike aprotic molecular liquids, ILs show different relations between M_1 and $(\gamma/d)^{1/2}$ for aromatic and nonaromatic ILs.[53] In the case of nonaromatic ILs, M_1 depends strongly on $(\gamma/d)^{1/2}$. In contrast, the slope of the correlation between M_1 and $(\gamma/d)^{1/2}$ for aromatic ILs is very small;

M_1 depends very weakly on $(\gamma/d)^{1/2}$. The difference between aromatic and nonaromatic ILs was attributed to the differences in the magnitudes of the segregation structures and the (depolarized) Raman activities between them. Namely, aromatic ILs are in general more segregated than nonaromatic ILs,[114] and aromatic moieties such as imidazolium and pyridinium rings have strong RIKES signals relative to nonaromatic groups, e.g., ammonium, pyrrolidinium, and phosphonium.[53,56,107] As a result, the low-frequency spectra of aromatic ILs by means of fs-RIKES predominantly involve information on the ionic region, while the low-frequency Kerr spectra of nonaromatic ILs contain rather homogeneous information in contrast. Thus, the microscopic structure in liquids influences the low-frequency spectral feature and the correlation between M_1 and the bulk parameters significantly. One possible reason for the atypical relation between M_1 and $(\gamma/d)^{1/2}$ for liquid cyclohexene might be because its molecule has both an aromatic (polarizable) part (–HC=CH–) and an aliphatic part (–$(CH_2)_4$–), which may behave like a nonaromatic ionic liquid.

8.4.3. Diffusive Relaxation.

The present fs-RIKES detects the polarizability anisotropy relaxation in liquids. The overdamped relaxation is thus attributed to the orientational dynamics in liquids. However, it should be noted that the fs-RIKES observes the "collective" orientational dynamics, not the single particle reorientation observed in fluorescence anisotropy measurements. According to the Stokes-Einstein-Debye (SED) hydrodynamic model, the rotational time τ_r of a single particle is expressed by[217-219]

$$\tau_r = V\eta/k_B T \tag{8.2}$$

where V is the volume of the particle, η is the shear viscosity of the medium, k_B is the Boltzmann constant, and T is the absolute temperature. The collective orientational relaxation time τ_{col} is correlated with τ_r:[217]

$$\tau_{col} = (g_2/j_2)\tau_r \tag{8.3}$$

where g_2 is the static pair orientational correlation parameter and j_2 is the dynamical orientational pair parameter.[217] The parameters g_2 and j_2 for all the present liquids except for liquid benzene are not available as far as I know.[217] Recently, Fourkas and coworkers discussed the slow relaxations of liquid benzene, perdeuterated benzene, hexafluorobenzene, and mesitylene together with the parameter g_2/j_2.[14] The value of g_2/j_2 of liquid benzene is

approximately 1, but the values of g_2/j_2 at room temperature for mesitylene, trifluorobenzene, and hexafluorobenzene are approximately 1.5, 2, and 2, respectively. g_2/j_2 depends on the liquid itself and is sensitive to the microscopic structure. Nonetheless, I believe it is a good starting point to assume that the values of g_2/j_2 are unity (per the simple SED hydrodynamic model, eq 8.3 for the present five liquids.

Figure 8.9 shows plots of the fast and slow relaxation time constants τ_1 and τ_2 vs $V_m\eta$. The temperature in this study is constant, and thus the denominators in eq 8.2 for all the liquids are constant. As displayed in Figure 8.9a, the values of τ_1 of the present five liquids are all approximately 1.1 to 1.4 ps. Therefore, the dynamics in the fast component are not simply diffusive. As described in Section 3, the fast components are included in the intermolecular vibrational dynamics (low-frequency spectra).

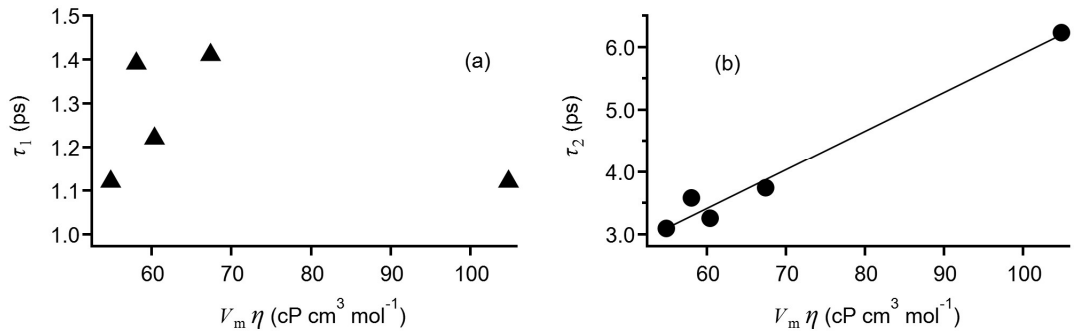

Figure 8.9. Plots of (a) fast time constant τ_1 and (b) slow time constant τ_2 vs $V_m\eta$ for benzene, 1,3-cyclohexadiene, 1,4-cyclohexadiene, cyclohexene, and cyclohexane.

On the other hand, the time constants of the slow components τ_2 of the present five liquids seems to obey the SED hydrodynamic behavior, although the correlation is not perfect (τ_2 of 1,4-cyclohexadiene is slightly slow compared to the data of the other liquids on the basis of the SED model: plot in the second from left). In solutions (not neat liquids), some cases show non-SED hydrodynamic behavior in the relaxation times by means of fs-RIKES.[63,220] However, the slowest relaxation times of most neat liquids observed by fs-RIKES display the SED-like behavior.

It might be natural to think that the datum apart from the SED relation for liquid 1,4-cyclohexadiene is attributed to the microscopic structure or interaction. When I look at the values of $V_{vdW}N_A/V_m$ for the five molecules, however, they are 0.544–0.563, and that of 1,4-cyclohexadiene is not particularly different (0.560) from the values of the other liquids, as

shown in Table 8.1. Thus, the behavior of 1,4-cyclohexadiene is unlikely to be due to the (static) microscopic intermolecular interactions and structure. The dynamical parameter j_2 might lead to a slight deviation in 1,4-cyclohexadiene from the other liquids, but it should also remind that the deviation of the datum of 1,4-cyclohexadiene from the data of the other liquids is not very large.

8.5 Conclusions

In this chapter, I investigated the intermolecular vibrational and orientational dynamics of liquid benzene, 1,3-cyclohexadiene, 1,4-cyclohexadiene, cyclohexene, and cyclohexane by means of fs-RIKES. To find the relation between the low-frequency intermolecular vibrational band and the bulk properties, the densities, shear viscosities, and surface tensions were also characterized. The line shape of the low-frequency spectra less than 200 cm^{-1} due to the intermolecular vibrations differs in each molecular liquid, but the liquid benzene and 1,3-cyclohexadiene show rather trapezoidal shapes. This probably comes from the strong magnitudes of the librational motions coming from the planar structures due to the conjugations. This contributes to the underdamped nuclear responses, which are obtained by the inverse Fourier transformation of the low-frequency spectra of liquid benzene and 1,3-cyclohexadiene. The line shapes of the low-frequency spectra of 1,4-cyclohexadiene and cyclohexene are triangular, and that of cyclohexane is monomodal. The monomodal spectral feature of cyclohexane is attributed to its small polarizability anisotropy that is responsible for the small magnitude of the diffusive orientational dynamics and thus the crossover process from the intermolecular vibrations to the diffusive orientational dynamics. In addition to the line shapes of the low-frequency spectra of the present liquids, I confirmed that the time integrals of the pure nuclear responses, which include the intramolecular vibrational modes, intermolecular vibrational dynamics, and diffusive orientational relaxation, are well correlated to the squares of the polarizability anisotropies. From the plots of the first moment versus the bulk properties (M_1 vs $(\gamma/d)^{1/2}$ and $(\gamma/FW)^{1/2}$), I also found that the data for liquid cyclohexene deviate slightly from the relations. One can think that the structure of cyclohexene, with hydrophobic and aromatic parts, might cause an inhomogeneous structure in the liquid state. The fast components of the overdamped transients, which are characterized by a biexponential fit after 3 ps, do not vary among the five liquids, all having a time constant of approximately 1.1–1.4 ps. On the other hand, the time constants of the slow components of the overdamped transients roughly but not perfectly linearly correlate to the products of the molar volumes and shear viscosities.

The intramolecular vibrational modes observed by fs-RIKES were also assigned on the basis of quantum chemistry calculations.

Chapter 9

Summary

In this thesis, the temperature dependence of the intermolecular vibrational dynamics in the various ionic liquids (ILs) was investigated by femtosecond Raman-induced Kerr effect spectroscopy. In order to perform systematic investigations, the following three topics were mainly focused: (i) The temperature dependence of the low-frequency spectra for the imidazolium-based ILs with 10 different anions was examined. (ii) The effects of the cation structures on the temperature-dependent features of the low-frequency spectra of ILs were studied. (iii) The temperature dependence of the low-frequency spectra for the pyrrolidinium-based ILs with 10 different anions and the effects of the anions on the temperature-dependent features of the low-frequency spectra were investigated. In addition to the ILs, several molecular liquids as the neutral analogues of the cation and anion of ILs were also investigated to clarify how the nature of ILs influences the temperature-dependent features of ILs. Furthermore, the temperature-dependent features of the spectra for the dicationic ILs were investigated and compared to those of the corresponding monocationic ILs. The effects of aromaticity in cations and their functional groups on the temperature dependence of the low-frequency spectra were also studied. In addition to the IL studies, the effects of conjugations in six-membered-ring molecular liquids were investigated to elucidate how the number and the position of double bonds affect the low-frequency spectra.

With increasing temperature, the spectral intensity in the low-frequency region below approximately 50 cm^{-1} increases for all of the ILs, regardless of aromaticity of cations, or anion species. This feature was reproduced in the DOS spectra calculated by MD simulation. The thermal activation of the translational motions of the ions is a plausible explanation. For aromatic ILs, the lower-frequency shift of the spectra above approximately 50 cm^{-1} is also observed. This contribution to temperature-dependent features is significantly large compared to nonaromatic cations and anions: the temperature dependence of the first moments of the imidazolium-based ILs are similar to that of 1-methylimidazole, which suggest that the temperature-dependent features of the spectra for imidazolium-based ILs are dominated by the motions of imidazolium cations.

For nonaromatic ILs, the spectral intensity in the high-frequency region below 50 cm^{-1} does not change very much with temperature, which is attributed to the absence of aromatic rings. Thanks to the lack of strong contributions to the low-frequency spectra in nonaromatic cations, the effects of anions on the temperature dependence of the spectra are clearly recognized in the pyrrolidinium-based ILs. Dicyanamide, tricyanomethide, and thiocyanate have especially large contributions to the spectra. The redshifts of the librational motions of

these anions are observed even in the imidazolium-based ILs. This is likely attributed to their planar structures. It is clarified by comparing the low-frequency spectral shapes of six-membered-ring molecular liquids that the planarity of molecules makes the low-frequency spectra broad because of the contribution of the librational motion, compared to nonplanar molecules. It is clarified that the influence of the librational motions on the temperature dependence is universally observed if the samples has planar structures, regardless of their charge.

However, the librational motions of anions having cyano groups appear in the frequency of ~80 cm^{-1} (shown in Figure 5.3 and 5.11), whereas those of aromatic cations exist in ~110 cm^{-1} (shown in Figure 3.10). This may seem strange because the lighter anions having cyano groups seem to librate more quickly. In fact, it is clarified that the librational motions of charged aromatic rings are located in the higher-frequency region than those of neutral aromatic rings. This implies that the frequencies of the librational motions depend on their charge state: positive, negative, or neutral. It would be interesting to see the effects of charge on the librational motions by experimental and theoretical methods.

Other interesting points of the temperature-dependent features would be an isoscattering point in the temperature-dependent spectra of imidazolium-based ILs. In this thesis, details were not discussed because the intensity of Kerr spectra is not absolute but relative to the electronic response, and the situations that an isoscattering point indicates, two states that do not couple or interact are affected by temperature, seem too simple. However, the fact remains that all of the imidazolium (and pyridinium) ILs show an isoscattering points in their low-frequency spectra. In order to elucidate whether an isoscattering points in the temperature-dependent low-frequency spectra is real or an artifact, the theoretical approaches seem to be necessary.

References

1. Nitzan, A., *Chemical Dynamics in Condensed Phases. Relaxation, Transfer and Reactions in Condensed Molecular Systems.* Oxford University Press: Oxford, 2006.
2. Fleming, G. R.; Wolynes, P. G., *Physics Today* **1990,** *43*, 36-43.
3. Yoshihara, K.; Tominaga, K.; Nagasawa, Y., *Bull. Chem. Soc. Jpn.* **1995,** *68*, 696-712.
4. Castner, E. W., Jr.; Maroncelli, M., *J. Mol. Liq.* **1998,** *77*, 1-36.
5. Maroncelli, M.; MacInnis, J.; Fleming, G. R., *Science* **1989,** *243*, 1674-1681.
6. Maroncelli, M., *J. Mol. Liq.* **1993,** *57*, 1-37.
7. Barthel, J.; Bachhuber, K.; Buchner, R.; Hetzenauer, H., *Chem. Phys. Lett.* **1990,** *165*, 369-373.
8. McMorrow, D.; Lotshaw, W. T.; Kenney-Wallace, G. A., *IEEE J. Quantum. Electron.* **1988,** *24*, 443-454.
9. McMorrow, D.; Lotshaw, W. T., *J. Phys. Chem.* **1991,** *95*, 10395-10406.
10. Lotshaw, W. T.; McMorrow, D.; Thantu, N.; Melinger, J. S.; Kitchenham, R., *J. Raman Spectrosc.* **1995,** *26*, 571-583.
11. Smith, N. A.; Meech, S. R., *Int. Rev. Phys. Chem.* **2002,** *21*, 75-100.
12. Kalpouzos, C.; Lotshaw, W. T.; McMorrow, D.; Kenney-Wallace, G. A., *J. Phys. Chem.* **1987,** *91*, 2028-2030.
13. Elola, M. D.; Ladanyi, B. M.; Scodinu, A.; Loughnane, B. J.; Fourkas, J. T., *J. Phys. Chem. B* **2005,** *109*, 24085-24099.
14. Loughnane, B. J.; Scodinu, A.; Fourkas, J. T., *J. Phys. Chem. B* **2006,** *110*, 5708-5720.
15. Zhong, Q.; Fourkas, J. T., *J. Phys. Chem. B* **2008,** *112*, 15342-15348.
16. Chang, Y. J.; Castner, E. W., Jr., *J. Chem. Phys.* **1993,** *99*, 7289-7299.
17. Shirota, H.; Fujisawa, T.; Fukazawa, H.; Nishikawa, K., *Bull. Chem. Soc. Jpn.* **2009,** *82*, 1347-1366.
18. Ryu, S.; Stratt, R. M., *J. Phys. Chem. B* **2004,** *108*, 6782-6795.
19. Hunt, N. T.; Jaye, A. A.; Meech, S. R., *Phys. Chem. Chem. Phys.* **2007,** *9*, 2167-2180.
20. Hunt, N. T.; Jaye, A. A.; Meech, S. R., *J. Phys. Chem. B* **2003,** *107*, 3405-3418.
21. Hunt, N. T.; Jaye, A. A.; Meech, S. R., *Chem. Phys. Lett.* **2003,** *371*, 304-310.
22. Hunt, N. T.; Meech, S. R., *J. Chem. Phys.* **2004,** *120*, 10828-10836.
23. Shirota, H.; Castner, E. W., Jr., *J. Am. Chem. Soc.* **2001,** *123*, 12877-12885.
24. Hunt, N. T.; Meech, S. R., *Chem. Phys. Lett.* **2004,** *400*, 368-373.
25. Turton, D. A.; Senn, H. M.; Harwood, T.; Lapthorn, A. J.; Ellis, E. M.; Wynne, K., *Nat.*

Commun. **2014,** *5*, 3999.

26. Kato, T.; Shirota, H., *J. Chem. Phys.* **2011,** *134*, 164504-164501-164509.

27. Shirota, H.; Fukuda, T.; Kato, T., *J. Phys. Chem. B* **2013,** *117*, 16196-16205.

28. Welton, T., *Chem. Rev.* **1999,** *99*, 2071-2083.

29. Wasserscheid, P.; Welton, T., *Ionic Liquids in Synthesis*. 2 ed.; Wiley-VCH: Weinheim, 2008.

30. Wilkes, J. S., *Green Chem.* **2002,** *4*, 73-80.

31. Walden, P., *Bull. Acad. Imper. Sci. (St. Petersburg)* **1914**, 405-422.

32. Wilkes, J. S.; Zaworotko, M. J., *J. Chem. Soc., Chem. Commun.* **1992**, 965-967.

33. Hallett, J. P.; Welton, T., *Chem. Rev.* **2011,** *111*, 3508-3576.

34. Lopes, J. N. A. C.; Padua, A. A. H., *J. Phys. Chem. B* **2006,** *110*, 3330-3335.

35. Triolo, A.; Russina, O.; Bleif, H.-J.; Di Cola, E., *J. Phys. Chem. B* **2007,** *111*, 4641-4644.

36. Russina, O.; Lo Celso, F.; Plechkova, N. V.; Triolo, A., *J. Phys. Chem. Lett.* **2017,** *8*, 1197-1204.

37. Ingram, J. A.; Moog, R. S.; Ito, N.; Biswas, R.; Maroncelli, M., *J. Phys. Chem. B* **2003,** *107*, 5926-5932.

38. Jin, H.; Li, X.; Maroncelli, M., *J. Phys. Chem. B* **2007,** *111*, 13473-13478.

39. Zhang, X.-X.; Liang, M.; Ernsting, N. P.; Maroncelli, M., *J. Phys. Chem. B* **2013,** *117*, 4291-4304.

40. Yamamoto, K.; Tani, M.; Hangyo, M., *J. Phys. Chem. B* **2007,** *111*, 4854-4859.

41. Stoppa, A.; Hunger, J.; Buchner, R.; Hefter, G.; Thoman, A.; Helm, H., *J. Phys. Chem. B* **2008,** *112*, 4854-4858.

42. Turton, D. A.; Sonnleitner, T.; Ortner, A.; Walther, M.; Hefter, G.; Seddon, K. R.; Stana, S.; Plechkova, N. V.; Buchner, R.; Wynne, K., *Faraday Discuss.* **2012,** *154*, 145-153.

43. Sonnleitner, T.; Turton, D. A.; Hefter, G.; Ortner, A.; Waselikowski, S.; Walther, M.; Wynne, K.; Buchner, R., *J. Phys. Chem. B* **2015,** *119*, 8826-8841.

44. Hyun, B. R.; Dzyuba, S. V.; Bartsch, R. A.; Quitevis, E. L., *J. Phys. Chem. A* **2002,** *106*, 7579-7585.

45. Xiao, D.; Rajian, J. R.; Li, S. F.; Bartsch, R. A.; Quitevis, E. L., *J. Phys. Chem. B* **2006,** *110*, 16174-16178.

46. Xiao, D.; Hines, L. G., Jr.; Bartsch, R. A.; Quitevis, E. L., *J. Phys. Chem. B* **2009,** *113*, 4544-4548.

47. Bardak, F.; Xiao, D.; Hines, L. G., Jr.; Son, P.; Bartsch, R. A.; Quitevis, E. L.; Yang, P.;

Voth, G. A., *ChemPhysChem* **2012,** *13*, 1687-1700.

48. Giraud, G.; Gordon, C. M.; Dunkin, I. R.; Wynne, K., *J. Chem. Phys.* **2003,** *119*, 464-477.

49. Cang, H.; Li, J.; Fayer, M. D., *J. Chem. Phys.* **2003,** *119*, 13017-13023.

50. Fayer, M. D., *Chem. Phys. Lett.* **2014,** *616-617*, 259-274.

51. Shirota, H.; Funston, A. M.; Wishart, J. F.; Castner, E. W., Jr., *J. Chem. Phys.* **2005,** *122*, 184512/1-12.

52. Shirota, H.; Nishikawa, K.; Ishida, T., *J. Phys. Chem. B* **2009,** *113*, 9831-9839.

53. Shirota, H., *ChemPhysChem* **2012,** *13*, 1638-1648.

54. Shirota, H.; Kakinuma, S.; Takahashi, K.; Tago, A.; Jeong, H.; Fujisawa, T., *Bull. Chem. Soc. Jpn.* **2016,** *89*, 1106-1128.

55. Shirota, H.; Castner, E. W., Jr., *J. Phys. Chem. A* **2005,** *109*, 9388-9392.

56. Fujisawa, T.; Nishikawa, K.; Shirota, H., *J. Chem. Phys.* **2009,** *131*, 244519/1-14.

57. Shim, Y.; Jeong, D.; Manjari, S.; Choi, M. Y.; Kim, H. J., *Acc. Chem. Res.* **2007,** *40*, 1130-1137.

58. Shim, Y.; Kim, H. J., *J. Phys. Chem. B* **2008,** *112*, 11028-11038.

59. Maroncelli, M.; Zhang, X.-X.; Liang, M.; Roy, D.; Ernsting, N. P., *Faraday Discuss.* **2012,** *154*, 409-424.

60. Ishida, T., *J. Non-Cryst. Solids* **2011,** *357*, 454-462.

61. Ishida, T.; Nishikawa, K.; Shirota, H., *J. Phys. Chem. B* **2009,** *113*, 9840-9851.

62. Ishida, T.; Shirota, H., *J. Phys. Chem. B* **2013,** *117*, 1136-1150.

63. Smith, N. A.; Meech, S. R., *J. Phys. Chem. A* **2000,** *104*, 4223-4235.

64. Ricci, M.; Bartolini, P.; Chelli, R.; Cardini, G.; Califano, S.; Righini, R., *Phys. Chem. Chem. Phys.* **2001,** *3*, 2795-2802.

65. Zhong, Q.; Fourkas, J. T., *J. Phys. Chem. B* **2008,** *112*, 8656-8663.

66. Rajian, J. R.; Li, S. F.; Bartsch, R. A.; Quitevis, E. L., *Chem. Phys. Lett.* **2004,** *393*, 372-377.

67. Xiao, D.; Rajian, J. R.; Cady, A.; Li, S.; Bartsch, R. A.; Quitevis, E. L., *J. Phys. Chem. B* **2007,** *111*, 4669-4677.

68. Shirota, H., *J. Chem. Phys.* **2005,** *122*, 044514/1-12.

69. Shirota, H., *J. Phys. Chem. A* **2011,** *115*, 14262-14275.

70. Bucaro, J. A.; Litovitz, T. A., *J. Chem. Phys.* **1971,** *54*, 3846-3853.

71. Fukazawa, H.; Ishida, T.; Shirota, H., *J. Phys. Chem. B* **2011,** *115*, 4621-4631.

72. Shirota, H.; Mandai, T.; Fukazawa, H.; Kato, T., *J. Chem. Eng. Data* **2011,** *56*, 2453-2459.

73. Abraham, M. J.; Spoel, D. v. d.; E. Lindahl, B. H.; team, t. G. d., *GROMACS User Manual, verion 5.0.6, www.gromacs.org*. 2015.

74. Canongia Lopes, J. N.; Deschamps, J.; Padua, A. A. H., *J. Phys. Chem. B* **2004,** *108*, 2038-2047.

75. Canongia Lopes, J. N.; Deschamps, J.; Padua, A. A. H., *J. Phys. Chem. B* **2004,** *108*, 11250.

76. Darden, T.; York, D.; Pedersen, L., *J. Chem. Phys.* **1993,** *98*, 10089-10092.

77. Nose, S., *Mol. Phys.* **1984,** *52*, 255-268.

78. Hoover, W. G., *Phys. Rev. A* **1985,** *31*, 1695-1697.

79. Parrinello, M.; Rahman, A., *J. Appl. Phys.* **1981,** *52*, 7182-7190.

80. McQuarrie, D. A., *Statistical Mechanics*. University Science Books: Sausalito, 2000.

81. Tokuda, H.; Tsuzuki, S.; Susan, M. A. B. H.; Hayamizu, K.; Watanabe, M., *J. Phys. Chem. B* **2006,** *110*, 19593-19600.

82. Nazet, A.; Sokolov, S.; Sonnleitner, T.; Makino, T.; Kanakubo, M.; Buchner, R., *J. Chem. Eng. Data* **2015,** *60*, 2400-2411.

83. Carvalho, P. J.; Regueira, T.; Santos, L. M. N. B. F.; Fernandez, J.; Coutinho, J. A. P., *J. Chem. Eng. Data* **2010,** *55*, 645-652.

84. Harris, K. R.; Kanakubo, M.; Woolf, L. A., *J. Chem. Eng. Data* **2007,** *52*, 1080-1085.

85. Rocha, M. A. A.; Ribeiro, F. S.; Ferreira, A. I. M. C. L.; Coutinho, J. P.; Santos, L. M. N. B. F., *J. Mol. Liq.* **2013,** *188*, 196-202.

86. Vogel, H., *Physik. Z.* **1921,** *22*, 645-646.

87. Tamman, G.; Hesse, W., *Z. Anorg. Allg. Chem.* **1926,** *156*, 245-257.

88. Fulcher, G. S., *J. Am. Ceram. Soc.* **1925,** *8*, 339-355.

89. Scherer, G. W., *J. Am. Ceram. Soc.* **1992,** *75*, 1060-1062.

90. Xu, W.; Cooper, E. I.; Angell, C. A., *J. Phys. Chem. B* **2003,** *107*, 6170-6178.

91. Lide, D. R., *CRC Handbook of Chemistry and Physics*. 89 ed.; CRC Press: Boca Raton, 2008.

92. Tao, G.; Stratt, R. M., *J. Phys. Chem. B* **2006,** *110*, 976-987.

93. Elola, M. D.; Ladanyi, B. M., *J. Chem. Phys.* **2005,** *122*, 224506/1-15.

94. Elola, M. D.; Ladanyi, B. M., *J. Phys. Chem. B* **2006,** *110*, 15525-15541.

95. Torii, H.; Tasumi, M., *J. Phys. Chem. A* **2000,** *104*, 4174-4181.

96. Skaf, M. S.; Vechi, S. M., *J. Chem. Phys.* **2003,** *119*, 2181-2187.
97. Idrissi, A.; Damay, P., *J. Non-Cryst. Solids* **2006,** *352*, 4486-4489.
98. Hu, Z.; Huang, X.; Annapureddy, H. V. R.; Margulis, C. J., *J. Phys. Chem. B* **2008,** *112*, 7837-7849.
99. Sarangi, S. S.; Reddy, S. K.; Balasubramanian, S., *J. Phys. Chem. B* **2011,** *115*, 1874-1880.
100. Angell, C. A., *Science* **1995,** *267*, 1924-1935.
101. Urbain, G.; Bottinga, Y.; Richet, P., *Geochim. Cosmochim. Acta* **1982,** *46*, 1061-1072.
102. Doremus, R. H., *J. Appl. Phys.* **2002,** *92*, 7619-7629.
103. Greet, R. J.; Turnbull, D., *J. Phys. Chem.* **1967,** *46*, 1243-1251.
104. Laughlin, W. T.; Uhlmann, D. R., *J. Phys. Chem.* **1972,** *76*, 2317-2325.
105. Hedley, W. H.; Milnes, M. V.; Yanko, W. H., *J. Chem. Eng. Data* **1970,** *15*, 122-127.
106. Ngai, K. L., *Relaxation and Diffusion in Complex Systems*. Springer: New York, 2011.
107. Shirota, H.; Matsuzaki, H.; Ramati, S.; Wishart, J. F., *J. Phys. Chem. B* **2015,** *119*, 9173-9187.
108. Bender, J. S.; Cohen, S. R.; He, X.; Fourkas, J. T.; Coasne, B., *J. Phys. Chem. B* **2016,** *120*, 9103-9114.
109. Ratajska-Gadomska, B., *J. Chem. Phys.* **2002,** *116*, 4563-4576.
110. Shirota, H.; Castner, E. W., Jr., *J. Chem. Phys.* **2006,** *125*, 034904/1-14.
111. Shirota, H.; Ushiyama, H., *J. Phys. Chem. B* **2008,** *112*, 13542-13551.
112. Ribeiro, M. C. C., *J. Chem. Phys.* **2010,** *133*, 024503/1-6.
113. Galiński, M.; Lewandowski, A.; Stępniak, I., *Electrochim. Acta* **2006,** *51*, 5567-5580.
114. Triolo, A.; Russina, O.; Fazio, B.; Appetecchi, G. B.; Carewska, M.; Passerini, S., *J. Chem. Phys.* **2009,** *130*, 164521/1-6.
115. Fumino, K.; Reimann, S.; Ludwig, R., *Phys. Chem. Chem. Phys.* **2014,** *16*, 21903-21929.
116. Shirota, H.; Fukazawa, H.; Fujisawa, T.; Wishart, J. F., *J. Phys. Chem. B* **2010,** *114*, 9400-9412.
117. Kakinuma, S.; Ishida, T.; Shirota, H., *J. Phys. Chem. B* **2017,** *121*, 250-264.
118. Lassegues, J. C.; Grondin, J.; Holomb, R.; Johansson, P., *J. Raman Spectrosc.* **2007,** *38*, 551-558.
119. McMorrow, D.; Lotshaw, W. T., *Chem. Phys. Lett.* **1993,** *201*, 369-376.
120. Chang, Y. J.; Castner, E. W., Jr., *J. Phys. Chem.* **1996,** *100*, 3330-3343.
121. Smith, N. A.; Lin, S. J.; Meech, S. R.; Shirota, H.; Yoshihara, K., *J. Phys. Chem. A* **1997,**

101, 9578-9586.
122. Kakinuma, S.; Shirota, H., *J. Phys. Chem. B* **2015,** *119*, 4713-4724.
123. Elola, M. D.; Ladanyi, B. M., *J. Chem. Phys.* **2005,** *122*, 224508/1-15.
124. Shirota, H., *J. Phys. Chem. B* **2005,** *109*, 7053-7062.
125. Shirota, H.; Kakinuma, S., *J. Phys. Chem. B* **2015,** *119*, 9835-9846.
126. Lee, H. Y.; Shirota, H.; Castner, E. W., Jr., *J. Phys. Chem. Lett.* **2013,** *4*, 1477-1483.
127. Shirota, H.; Wishart, J. F.; Castner, E. W., Jr., *J. Phys. Chem. B* **2007,** *111*, 4819-4829.
128. Zhou, Z.-B.; Matsumoto, H.; Tatsumi, K., *Chem. Eur. J.* **2005,** *11*, 752-766.
129. Zhou, Z.-B.; Matsumoto, H.; Tatsumi, K., *Chem. Eur. J.* **2006,** *12*, 2196-2212.
130. Tokuda, H.; Ishii, K.; Susan, M. A. B. H.; Tsuzuki, S.; Hayamizu, K.; Watanabe, M., *J. Phys. Chem. B* **2006,** *110*, 2833-2839.
131. Angell, C. A., *Chem. Rev.* **2002,** *102*, 2627-2649.
132. Fraser, K. J.; MacFarlane, D. R., *Aust. J. Chem.* **2009,** *62*, 309-321.
133. Tsunashima, K.; Sugiya, M., *Electrochem. Commun.* **2007,** *9*, 2353-2358.
134. Kakinuma, S.; Shirota, H., *J. Phys. Chem. B* **2018,** *122*, 6033-6047.
135. M. J. Frisch, G. W. T., H. B. Schlegel, G. E. Scuseria, M. A. Robb, J. R. Cheeseman, G. Scalmani, V. Barone, G. A. Petersson, H. Nakatsuji, X. Li, M. Caricato, A. Marenich, J. Bloino, B. G. Janesko, R. Gomperts, B. Mennucci, H. P. Hratchian, J. V. Ortiz, A. F. Izmaylov, J. L. Sonnenberg, D. Williams-Young, F. Ding, F. Lipparini, F. Egidi, J. Goings, B. Peng, A. Petrone, T. Henderson, D. Ranasinghe, V. G. Zakrzewski, J. Gao, N. Rega, G. Zheng, W. Liang, M. Hada, M. Ehara, K. Toyota, R. Fukuda, J. Hasegawa, M. Ishida, T. Nakajima, Y. Honda, O. Kitao, H. Nakai, T. Vreven, K. Throssell, J. A. Montgomery, Jr., J. E. Peralta, F. Ogliaro, M. Bearpark, J. J. Heyd, E. Brothers, K. N. Kudin, V. N. Staroverov, T. Keith, R. Kobayashi, J. Normand, K. Raghavachari, A. Rendell, J. C. Burant, S. S. Iyengar, J. Tomasi, M. Cossi, J. M. Millam, M. Klene, C. Adamo, R. Cammi, J. W. Ochterski, R. L. Martin, K. Morokuma, O. Farkas, J. B. Foresman, and D. J. Fox,, *Gaussian 09, Revision A.02*. Gaussian, Inc.: Wallingford CT, 2016.
136. Kakinuma, S.; Ramati, S.; Wishart, J. F.; Shirota, H., *J. Phys. Chem.* **2018,** *148*, 193805/1-10.
137. Sonnleitner, T.; Turton, D. A.; Waselikowski, S.; Hunger, J.; Stoppa, A.; Walther, M.; Wynne, K.; Buchner, R., *J. Mol. Liq.* **2014,** *192*, 19-25.
138. Gacino, F. M.; Regueira, T.; Lugo, L.; Comunas, M. J. P.; Fernandez, J., *J. Chem. Eng. Data* **2011,** *56*, 4984-4999.

139. Makino, T.; Kanakubo, M.; Umecky, T.; Suzuki, A.; Nishida, T.; Takano, J., *J. Chem. Eng. Data* **2012,** *57*, 751-755.
140. Appetecchi, G. B.; Montanino, M.; Carewska, M.; Moreno, M.; Alessandrini, F.; Passerini, S., *Electrochim. Acta* **2011,** *56*, 1300-1307.
141. Nazet, A.; Sokolov, S.; Sonnleitner, T.; Friesen, S.; Buchner, R., *J. Chem. Eng. Data* **2017,** *62*, 2549-2561.
142. Domanska, U.; Krolikowska, M.; Walczak, K., *J. Sol. Chem.* **2014,** *43*, 1929-1946.
143. Reiter, J.; Paillard, E.; Grande, L.; Winter, M.; Passerini, S., *Electrochim. Acta* **2013,** *91*, 101-107.
144. Henderson, W. A.; Passerini, S., *Chem. Mater.* **2004,** *16*, 2881-2885.
145. Martinelli, A.; Matic, A.; Jacobsson, P.; Börjesson, L.; Fernicola, A.; Scrosati, B., *J. Phys. Chem. B* **2009,** *113*, 11247-11251.
146. Vitucci, F. M.; Manzo, D.; Navarra, M. A.; Palumbo, O.; Trequattrini, F.; Panero, S.; Bruni, P.; Croce, F.; Paolone, A., *J. Phys. Chem. C* **2014,** *118*, 5749-5755.
147. Kunze, M.; Jeong, S.; Paillard, E.; Winter, M.; Passerini, S., *J. Phys. Chem. C* **2010,** *114*, 12364-12369.
148. Yuyama, K.; Masuda, G.; Yoshida, H.; Sato, T., *J. Power Sources* **2006,** *162*, 1401-1408.
149. Domanska, U.; Okuniewska, P.; Markowska, A., *Fluid Phase Equilib.* **2016,** *424*, 68-78.
150. MacFarlane, D. R.; Forsyth, S. A.; Golding, J.; Deacon, G. B., *Green Chem.* **2002,** *4*, 444-448.
151. Fletcher, S. I.; Sillars, F. B.; Hudson, N. E.; Hall, P. J., *J. Chem. Eng. Data* **2010,** *55*, 778-782.
152. Jeremias, S.; Carewska, M.; Conte, L.; Passerini, S.; Appetecchi, G. B., *RSC Adv.* **2013,** *3*, 17755-17761.
153. Cho, M.; Du, M.; Scherer, N. F.; Fleming, G. R.; Mukamel, S., *J. Chem. Phys.* **1993,** *99*, 2410-2428.
154. Cooper, E. I.; Angell, C. A., *Solid State Ionics* **1983,** *9&10*, 617-622.
155. Matsumoto, H.; Yanagida, M.; Tanimoto, K.; Nomura, M.; Kitagawa, Y.; Miyazaki, Y., *Chem. Lett.* **2000**, 922-923.
156. Funston, A. M.; Wishart, J. F., *ACS Symp. Ser.* **2005,** *901*, 102-116.
157. Andersson, M. P.; Uvdal, P., *J. Phys. Chem. A* **2005,** *109*, 2937-2941.
158. Doremus, R. H., *J. Appl. Phys.* **2002,** *92*, 7619-7629.
159. Laughlin, W. T.; Uhlmann, D. R., *J. Phys. Chem.* **1972,** *76*, 2317-2325.

160. Hedley, W. H.; Milnes, M. V.; Yanko, W. H., *J. Chem. Eng. Data* **1970,** *15*, 122-127.
161. Wang, R.; Gao, H.; Ye, C.; Shreeve, J. M., *Chem. Mater.* **2007,** *19*, 144.
162. Wang, R.; Jin, C.-M.; Twamley, B.; Shreeve, J. M., *Inorganic Chemistry* **2006,** *45*, 6396.
163. Payagala, T.; Huang, J.; Breitbach, Z. S.; Sharma, P. S.; Armstrong, D. W., *Chem. Mater.* **2007,** *19*, 5848-5850.
164. Anderson, J. L.; Ding, R.; Ellern, A.; Armstrong, D. W., *J. Am. Chem. Soc.* **2005,** *127*, 593.
165. Ito, K.; Nishina, N.; Ohno, H., *Electrochim. Acta* **2000,** *45*, 1295.
166. Lall, S. I.; Mancheno, D.; Castro, S. B.; V.; Cohen, J. I.; Engel, R., *Chem. Commun.* **2000**, 2413.
167. Shirota, H.; Ishida, T., *J. Phys. Chem. B* **2011,** *115*, 10860-10870.
168. Bartolini, P.; Ricci, M.; Torre, R.; Righini, R.; Santa, I., *J. Chem. Phys.* **1999,** *110*, 8653-8662.
169. Turton, D. A.; Hunger, J.; Stoppa, A.; Thoman, A.; Candelaresi, M.; Hefter, G.; Walther, M.; Buchner, R.; Wynne, K., *J. Mol. Liq.* **2011,** *159*, 2-8.
170. Rey, I.; Johansson, P.; Lindgren, J.; Lassegues, J. C.; Grondin, J.; Servant, L., *J. Phys. Chem. A* **1998,** *102*, 3249-3258.
171. Herstedt, M.; Smirnov, M.; Johansson, P.; Chami, M.; Grondin, J.; Servant, L.; Lassegues, J. C., *J. Raman Spectrosc.* **2005,** *36*, 762-770.
172. Fujii, K.; Fujimori, T.; Takamuku, T.; Kanzaki, R.; Umebayashi, Y.; Ishiguro, S.-I., *J. Phys. Chem. B* **2006,** *110*, 8179-8183.
173. Shirota, H.; Matsuzaki, H.; Ramati, S.; Wishart, J. F., *J. Phys. Chem. B* **2015**.
174. Shirota, H.; Fukazawa, H., Atom Substitution Effects in Ionic Liquids: A Microscopic View by Femtosecond Raman-Induced Kerr Effect Spectroscopy. In *Ionic Liquids: Theory, Properties, New Approaches*, Kokorin, A., Ed. InTech: Rijeka, Croatia, 2011; pp 201-224.
175. Geiger, L. C.; Ladanyi, B. M., *J. Chem. Phys.* **1987,** *87*, 191-202.
176. Geiger, L. C.; Ladanyi, B. M., *Chem. Phys. Lett.* **1989,** *159*, 413-420.
177. Shirota, H.; Castner, E. W., Jr., *J. Phys. Chem. B* **2005,** *109*, 21576-21585.
178. Shirota, H.; Biswas, R., *J. Phys. Chem. B* **2012,** *116*, 13765-13773.
179. Shirota, H., *J. Phys. Chem. B* **2013,** *117*, 7985-7995.
180. Turton, D. A.; Hunger, J.; Stoppa, A.; Hefter, G.; Thoman, A.; Walther, M.; Buchner, R.; Wynne, K., *J. Am. Chem. Soc.* **2009,** *131*, 11140-11146.
181. Xiao, D.; Rajian, J. R.; Hines, L. G., Jr.; Li, S.; Bartsch, R. A.; Quitevis, E. L., *J. Phys.*

Chem. B **2008,** *112*, 13316-13325.
182. Kubo, R., *J. Phys. Soc. Jpn.* **1954,** *9*, 935-944.
183. Kubo, R., A Stochastic Theory of Line-Shape and Relaxation. In *Fluctuation, Relaxation and Resonance in Magnetic Systems*, Haar, D. T., Ed. Oliver and Boyd: Edinburgh, 1961; p 23.
184. Loughnane, B. J.; Scodinu, A.; Farrer, R. A.; Fourkas, J. T.; Mohanty, U., *J. Chem. Phys.* **1999,** *111*, 2686-2694.
185. McMorrow, D.; Lotshaw, W. T., *Chem. Phys. Lett.* **1990,** *174*, 85-94.
186. Nicolau, B. G.; Sturlaugson, A.; Fruchey, K.; Ribeiro, M. C. C.; Fayer, M. D., *J. Phys. Chem. B* **2010,** *114*, 8350-8356.
187. Li, J.; Wang, I.; Fruchey, K.; Fayer, M. D., *J. Phys. Chem. A* **2006,** *110*, 10384-10391.
188. Sonnleitner, T.; Turton, D. A.; Waselikowski, S.; Hunger, J.; Stoppa, A.; Walther, M.; Wynne, K.; Buchner, R., *J. Mol. Liq.* **2014,** *192*, 19-25.
189. Sonnleitner, T.; Turton, D. A.; Hefter, G.; Ortner, A.; Waselikowski, S.; Walther, M.; Wynne, K.; Buchner, R., *J. Phys. Chem. B* **2015,** *119*, 8826-8841.
190. Kakinuma, S.; Shirota, H., *J. Phys. Chem. B* **2015,** *119*, 4713-4727.
191. Jaye, A. A.; Hunt, N. T.; Meech, S. R., *J. Chem. Phys.* **2006,** *124*, 024506.
192. Heisler, I. A.; Meech, S. R., *J. Phys. Chem. B* **2008,** *112*, 12976-12984.
193. Turton, D. A.; Martin, D. F.; Wynne, K., *Phys. Chem. Chem. Phys.* **2010,** *12*, 4191-4200.
194. Yoshioka, S.; Miyake, Y.; Watanabe, J.; Kinoshita, S., *J. Lumin.* **2001,** *94-95*, 771-774.
195. Madden, P. A.; Cox, T. I., *Mol. Phys.* **1981,** *43*, 287-305.
196. Geiger, L. C.; Ladanyi, B. M., *J. Chem. Phys.* **1988,** *89*, 6588-6599.
197. Ladanyi, B. M.; Klein, S., *J. Chem. Phys.* **1996,** *105*, 1552-1561.
198. Kakinuma, S.; Ishida, T.; Shirota, H., *J. Phys. Chem. B* **2017,** *121*, 250-264.
199. Cong, P.; Deuel, H. P.; Simon, J. D., *Chem. Phys. Lett.* **1995,** *240*, 72-78.
200. Barbara, P. F.; Jarzeba, W., *Adv. Photochem.* **1991,** *15*, 1-68.
201. Fleming, G. R.; Cho, M., *Annu. Rev. Phys. Chem.* **1996,** *47*, 109-134.
202. Ohta, K.; Tominaga, K., *Bull. Chem. Soc. Jpn.* **2005,** *78*, 1581-1594.
203. Nagasawa, Y., *J. Phoitochem. Photobiol., C* **2011,** *12*, 31-45.
204. Horng, M. L.; Gardecki, J. A.; Papazyan, A.; Maroncelli, M., *J. Phys. Chem.* **1995,** *99*, 17311-17337.
205. Reynolds, L.; Gardecki, J. A.; Frankland, S. J. V.; Horng, M. L.; Maroncelli, M., *J. Phys. Chem.* **1996,** *100*, 10337-10354.

206. Frisch, M. J.; Trucks, G. W.; Schlegel, H. B.; Scuseria, G. E.; Robb, M. A.; Cheeseman, J. R.; Montgomery, J. A., Jr.; Vreven, T.; Kudin, K. N.; Burant, J. C.; Millam, J. M.; Iyengar, S. S.; Tomasi, J.; Barone, V.; Mennucci, B.; Cossi, M.; Scalmani, G.; Rega, N.; Petersson, G. A.; Nakatsuji, H.; Hada, M.; Ehara, M.; Toyota, K.; Fukuda, R.; Hasegawa, J.; Ishida, M.; Nakajima, T.; Honda, Y.; Kitao, O.; Nakai, H.; Klene, M.; Li, X.; Knox, J. E.; Hratchian, H. P.; Cross, J. B.; Adamo, C.; Jaramillo, J.; Gomperts, R.; Stratmann, R. E.; Yazyev, O.; Austin, A. J.; Cammi, R.; Pomelli, C.; Ochterski, J. W.; Ayala, P. Y.; Morokuma, K.; Voth, G. A.; Salvador, P.; Dannenberg, J. J.; Zakrzewski, V. G.; Dapprich, S.; Daniels, A. D.; Strain, M. C.; Farkas, O.; Malick, D. K.; Rabuck, A. D.; Raghavachari, K.; Foresman, J. B.; Ortiz, J. V.; Cui, Q.; Baboul, A. G.; Clifford, S.; Cioslowski, J.; Stefanov, B. B.; Liu, G.; Liashenko, A.; Piskorz, P.; Komaromi, I.; Martin, R. L.; Fox, D. J.; Keith, T.; Al-Laham, M. A.; Peng, C. Y.; Nanayakkara, A.; Challacombe, M.; Gill, P. M. W.; Johnson, B.; Chen, W.; Wong, M. W.; Gonzalez, C.; Pople, J. A., *GAUSSIAN 03*. Gaussian, Inc.: Pittsburgh, PA, 2003.
207. Edward, J. T., *J. Chem. Educ.* **1970,** *47*, 261-270.
208. Vohringer, P.; Scherer, N. F., *J. Phys. Chem.* **1995,** *99*, 2684-2695.
209. Kinoshita, S.; Kai, Y.; Ariyoshi, T.; Shimada, Y., *Int. J. Mod. Phys. B* **1996,** *10*, 1229-1272.
210. Neelakandan, M.; Pant, D.; Quitevis, E. L., *Chem. Phys. Lett.* **1997,** *265*, 283-292.
211. Rajian, J. R.; Hyun, B. R.; Quitevis, E. L., *J. Phys. Chem. A* **2004,** *108*, 10107-10115.
212. Ronne, C.; Jensby, K.; Loughnane, B. J.; Fourkas, J.; Faurskov Nielsen, O.; Keiding, S. R., *J. Chem. Phys.* **2000,** *113*, 3749-3756.
213. Zhong, Q.; Fourkas, J. T., *J. Phys. Chem. B* **2008,** *112*, 15529-15539.
214. Manfred, K.; He, X.; Fourkas, J. T., *J. Phys. Chem. B* **2010,** *114*, 12096-12103.
215. Shirota, H., *J. Phys. Chem. B* **2013,** *117*, 7985-7995.
216. Long, D. A., *The Raman Effect*. John Wiley & Sons: West Sussex, 2002.
217. Kivelson, D.; Madden, P. A., *Ann. Rev. Phys. Chem.* **1980,** *31*, 523-558.
218. Dote, J. L.; Kivelson, D.; Schwartz, R. N., *J. Phys. Chem.* **1981,** *85*, 2169-2180.
219. Fleming, G. R., *Chemical Applications of Ultrafast Spectroscopy*. Oxford University Press: New York, 1986.
220. Turton, D. A.; Wynne, K., *J. Phys. Chem. B* **2014,** *118*, 4600-4604.
221. Shirota, H.; Kato, T., *J. Phys. Chem. A* **2011,** *115*, 8797-8807.

Appendix

A. Sample Preparation

A.1. Ionic Liquids used in Chapter 3

A.1.1. 1-Butyl-3-methylimidazolium cyclohexafluoropropane-1,3-bis(sulfonyl)amide, [C_4MIm][NCyF].

[C_4MIm]Cl (1.87 g, 10.7 mmol) was dissolved in water and aqueous solution of lithium cyclohexafluoropropane-1,3-bis(sulfonyl)amide (3.54 g, 11.8 mmol) was added. After the mixture was stirred at room temperature for 14 hours, aqueous layer was decanted. The ionic liquid layer was washed with water three times, and then the ionic liquid was dissolved in dichloromethane and washed with water three times. The dichloromethane was evaporated. The ionic liquid was then dried in vacuo at 313 K for more than 2 days. The yield was 92.6% (4.27 g). ^{1}H-NMR (400 MHz, DMSO-d_6): δ = 0.90 (t, J = 7.4 Hz, 3H, $NCH_2CH_2CH_2CH_3$), 1.26 (m, 2H, $NCH_2CH_2CH_2CH_3$), 1.76 (m, 2H, $NCH_2CH_2CH_2CH_3$), 3.84 (s, 3H, NCH_3), 4.15 (t, J = 7.1 Hz, 2H, $NCH_2CH_2CH_2CH_3$), 7.69 (t, J = 1.7 Hz, 1H, $CH_3NCHCHN$), 7.76 (t, J = 1.7 Hz, 1H, $CH_3NCHCHN$), 9.10 (s, 1H, CH_3NCHN). Elemental analysis: $C_{11}H_{15}F_6N_3O_4S_2$: Calcd. C 30.63, H 3.51, N 9.74. Found: C 30.44, H 3.29, N 9.60.

A.1.2. 1-Heptyl-3-methylimidazolium hexafluorophosphate, [C_7MIm][PF_6].

1-Heptyl-3-methylimidazolium bromide was synthesized as a precursor for [C_7MIm][PF_6], at first. 1-Methylimidazole was distilled before use. 1-Bromoheptane (9.68 g, 54.0 mmol) was added to an acetonitrile solution of 1-methylimidazole (3.68 g, 44.8 mmol) at nitrogen atmosphere in a flask equipped with a reflux condenser and magnetic stirrer. The solution was heated to 333–343 K in an oil bath for 15 hours while stirring. The solution was allowed to cool to room temperature, and then condensed by evaporation. The ionic liquid was washed with diethyl ether for three times, and then dried in vacuo at 313 K for more than 2 days. The obtained 1-heptyl-3-methylimidazolium bromide was successively used for the preparation of [C_7MIm][PF_6]. 1-Heptyl-3-methylimidazolium bromide (8.15 g, 31.2 mmol) was dissolved in water and aqueous solution of sodium hexafluorophosphate (6.18 g, 36.8 mmol) was added. After the mixture was stirred at room temperature for about 4 hours, aqueous layer was decanted. The ionic liquid layer was dissolved in dichloromethane and washed with water several times. The dichloromethane was evaporated. The residual ionic liquid was mixed with activated charcoal in acetonitrile and stirred at room temperature overnight. The solution was filtered and evaporated. The ionic liquid was then dried in vacuo at 313 K for more than 2 days. The yield

was 86.3% (8.79 g). ^{1}H-NMR (400 MHz, DMSO-d_6): δ = 0.85 (t, J = 6.9 Hz, 3H, $NC_6H_{12}CH_3$), 1.24 (m, 8H, $NCH_2CH_2C_4H_8CH_3$), 1.76 (m, 2H, $NCH_2CH_2C_5H_{11}$), 3.83 (s, 3H, NCH_3), 4.13 (t, J = 7.2 Hz, 2H, $NCH_2C_6H_{13}$), 7.67 (t, J = 1.7 Hz, 1H, $CH_3NCHCHN$), 7.74 (t, J = 1.7 Hz, 1H, $CH_3NCHCHN$), 9.07 (s, 1H, CH_3NCHN). Elemental analysis: $C_{11}H_{21}F_6N_2P$: Calcd. C 40.49, H 6.49, N 8.59. Found: C 40.12, H 6.35, N 8.51.

A.2. Ionic Liquids used in Chapter 4

A.2.1. 1-Butyl-1-methylpyrrolidinium bis(trifluoromethylsulfonyl)amide, [Pyrr$_{14}$][NTf$_2$].

At first, 1-butyl-1-methylpyrrolidinium bromide ([Pyrr$_{14}$]Br) was synthesized as a precursor for [Pyrr$_{14}$][NTf$_2$]. 1-Methylpyrrolidine was distilled before use. 1-Bromobutane (7.57 g, 55.3 mmol) was added to an acetonitrile solution of 1-methylpyrrolidine (4.28 g, 50.3 mmol) at nitrogen atmosphere in a flask equipped with a reflux condenser and magnetic stirrer. The solution was heated to 323–333 K in an oil bath for 16 hours while stirring. The solution was allowed to cool to room temperature and evaporated. The obtained solid was recrystallized from acetonitrile and diethyl ether, and then dried in vacuo at 313 K for more than 2 days. The obtained [Pyrr$_{14}$]Br (4.59 g, 20.7 mmol) was dissolved in water and aqueous solution of lithium bis(trifluoromethylsulfonyl)amide (6.56 g, 22.8 mmol) was added. After the mixture was stirred at room temperature for 15 hours, aqueous layer was decanted. The ionic liquid layer was dissolved in dichloromethane and washed with water five times. The dichloromethane was then evaporated. The ionic liquid was mixed with activated charcoal in acetonitrile and stirred at room temperature overnight. The solution was filtered and evaporated. The ionic liquid was finally dried in vacuo at 313 K for more than 2 days. The yield was 71.7% (7.52 g). ^{1}H-NMR (400 MHz, DMSO-d_6): δ = 0.93 (t, J = 7.4 Hz, 3H, $NCH_2CH_2CH_2CH_3$), 1.32 (sext, J = 7.4 Hz, 2H, $NCH_2CH_2CH_2CH_3$), 1.68 (m, 2H, $NCH_2CH_2CH_2CH_3$), 2.08 (br, 4H, $N(CH_2CH_2)_2$), 2.97 (s, 3H, NCH_3), 3.28 (m, 2H, $NCH_2CH_2CH_2CH_3$), 3.37–3.50 (m, 4H, $N(CH_2CH_2)_2$). Elemental analysis: $C_{11}H_{20}F_6N_2O_4S_2$: Calcd. C 31.28, H 4.77, N 6.63. Found: C 31.19, H 4.67, N 6.53.

A.2.2. Butyldiethylmethylammonium bis(trifluoromethylsulfonyl)amide, [N$_{1224}$][NTf$_2$].

The same procedure was followed as described for [Pyrr$_{14}$][NTf$_2$], except for the use of diethylmethylamine instead of 1-methylpyrrolidine. ^{1}H-NMR (400 MHz, DMSO-d_6): δ = 0.93 (t, J = 7.4 Hz, 3H, $NCH_2CH_2CH_2CH_3$), 1.20 (m, 6H, NCH_2CH_3), 1.31 (sext, J = 7.4 Hz, 2H, $NCH_2CH_2CH_2CH_3$), 1.59 (m, 2H, $NCH_2CH_2CH_2CH_3$), 2.89 (s, 3H, NCH_3), 3.15 (m, 2H,

NC*H*$_2$CH$_2$CH$_2$CH$_3$), 3.26 (q, *J* = 7.3 Hz, 4H, NC*H*$_2$CH$_3$). Elemental analysis: $C_{11}H_{22}F_6N_2O_4S_2$: Calcd. C 31.13, H 5.23, N 6.60. Found: C 31.03, H 5.17, N 6.55.

A.3 Ionic Liquids used in Chapter 5

A.3.1. 1-Butyl-1-methylpyrrolidinium bromide, [Pyrr$_{14}$]Br.

[Pyrr$_{14}$]Br was synthesized as a precursor for [Pyrr$_{14}$][NF$_2$], [Pyrr$_{14}$][NPf$_2$], [Pyrr$_{14}$][NCyF], and [Pyrr$_{14}$][OTf]. 1-Methylpyrrolidine was distilled before use. 1-Bromobutane (7.57 g, 55.3 mmol) was added to an acetonitrile solution of 1-methylpyrrolidine (4.28 g, 50.3 mmol) at nitrogen atmosphere in a flask equipped with a reflux condenser and magnetic stirrer. The solution was heated to 323–333 K in an oil bath for 16 hours while stirring. The solution was allowed to cool to room temperature and evaporated. The obtained solid was recrystallized from acetonitrile and diethyl ether, and then dried in vacuo at 313 K for more than 2 days. The yield was 83.4 % (9.32 g).

A.3.2. 1-(2-Methoxyethyl)-1-methylpyrrolidinium bromide, [Pyrr$_{1(1O2)}$]Br.

[Pyrr$_{1(1O2)}$]Br was synthesized as a precursor for [Pyrr$_{1(1O2)}$][NTf$_2$]. The same procedure was followed as described for [Pyrr$_{14}$]Br, except for the use of 1-methylpyrrolidine (7.10 g, 83.4 mmol) and 2-bromoethyl methyl ether (7.2 mL, 75.8 mmol). The yield was 69.4% (11.8 g).

A.3.3. 1-(2-Methoxyethyl)-1-methylpyrrolidinium bromide, [Pyrr$_{1(1O2)}$]Cl.

[Pyrr$_{1(1O2)}$]Cl was synthesized as a precursor for [Pyrr$_{1(1O2)}$][NF$_2$], [Pyrr$_{1(1O2)}$][NCyF], and [Pyrr$_{1(1O2)}$][PF$_6$]. 2-chloroethyl methyl ether (10 mL, 110.0 mmol) was added to an acetonitrile solution of 1-methylpyrrolidine (8.53 g, 100.2 mmol) at nitrogen atmosphere in a flask equipped with a reflux condenser and magnetic stirrer. The solution was heated to 343–353 K in an oil bath for 2 days while stirring. The solution was allowed to cool to room temperature and evaporated. The obtained solid was washed with diethyl ether. The obtained solids were mixed with activated charcoal in acetonitrile and stirred at room temperature overnight. The solution was filtered and evaporated, and then dried in vacuo at 313 K for more than 2 days. The yield was 46.4% (8.35 g).

A.3.4. 1-Butyl-1-methylpyrrolidinium bis(fluorosulfonyl)amide, [Pyrr$_{14}$][NF$_2$].

[Pyrr$_{14}$]Br (3.60 g, 16.2 mmol) was dissolved in water and aqueous solution of potassium bis(fluorosulfonyl)amide (4.28 g, 19.5 mmol) was added. After the mixture was stirred at room

temperature for about 17 hours, aqueous layer was decanted. The ionic liquid layer was dissolved in dichloromethane and washed with water five times. The dichloromethane was evaporated. The obtained ionic liquid was then dried in vacuo at 313 K for more than 2 days. The yield was 94.8% (4.95 g). ^{1}H-NMR (400 MHz, DMSO-d_6): δ = 0.93 (t, J = 7.4 Hz, 3H, $NCH_2CH_2CH_2CH_3$), 1.31 (sext, J = 7.4 Hz, 2H, $NCH_2CH_2CH_2CH_3$), 1.67 (m, 2H, $NCH_2CH_2CH_2CH_3$), 2.08 (br, 4H, $N(CH_2CH_2)_2$), 2.97 (s, 3H, NCH_3), 3.28 (m, 2H, $NCH_2CH_2CH_2CH_3$), 3.37–3.50 (m, 4H, $N(CH_2CH_2)_2$). Elemental analysis: $C_9H_{20}F_2N_2O_4S_2$: Calcd. C 33.53, H 6.25, N 8.69. Found: C 33.18, H 6.17, N 8.44.

A.3.5. 1-Butyl-1-methylpyrrolidinium bis(pentafluoroethylsulfonyl)amide, [Pyrr$_{14}$][NPf$_2$].

The same procedure was followed as described for [Pyrr$_{14}$][NF$_2$], except for the use of [Pyrr$_{14}$]Br (3.22 g, 14.5 mmol) and lithium bis(pentafluoroethylsulfonyl)amide (6.20g, 16.0 mmol). The yield was 95.3% (7.21 g). ^{1}H-NMR (400 MHz, DMSO-d_6): δ = 0.93 (t, J = 7.4 Hz, 3H, $NCH_2CH_2CH_2CH_3$), 1.32 (sext, J = 7.4 Hz, 2H, $NCH_2CH_2CH_2CH_3$), 1.67 (m, 2H, $NCH_2CH_2CH_2CH_3$), 2.08 (br, 4H, $N(CH_2CH_2)_2$), 2.97 (s, 3H, NCH_3), 3.28 (m, 2H, $NCH_2CH_2CH_2CH_3$), 3.36–3.50 (m, 4H, $N(CH_2CH_2)_2$). Elemental analysis: $C_{13}H_{20}F_{10}N_2O_4S_2$: Calcd. C 29.89, H 3.86, N 5.36. Found: C 29.83, H 3.75, N 5.43.

A.3.6. 1-Butyl-1-methylpyrrolidinium cyclohexafluoropropane-1,3-bis(sulfonyl)amide, [Pyrr$_{14}$][NCyF].

The same procedure was followed as described for [Pyrr$_{14}$][NF$_2$], except for the use of [Pyrr$_{14}$]Br (3.20 g, 14.4 mmol) and lithium cyclohexafluoropropane-1,3-bis(sulfonyl)amide (4.75 g, 15.9 mmol). The yield was 97.3% (6.10 g). ^{1}H-NMR (400 MHz, DMSO-d_6): δ = 0.93 (t, J = 7.4 Hz, 3H, $NCH_2CH_2CH_2CH_3$), 1.31 (sext, J = 7.4 Hz, 2H, $NCH_2CH_2CH_2CH_3$), 1.68 (m, 2H, $NCH_2CH_2CH_2CH_3$), 2.08 (br, 4H, $N(CH_2CH_2)_2$), 2.97 (s, 3H, NCH_3), 3.28 (m, 2H, $NCH_2CH_2CH_2CH_3$), 3.39–3.50 (m, 4H, $N(CH_2CH_2)_2$). Elemental analysis: $C_{12}H_{20}F_6N_2O_4S_2$: Calcd. C 33.18, H 4.64, N 6.45. Found: C 33.06, H 4.56, N 6.38.

A.3.7. 1-Butyl-1-methylpyrrolidinium trifluoromethanesulfonate, [Pyrr$_{14}$][OTf].

[Pyrr$_{14}$]Br (5.0 g, 22.5 mmol) was dissolved in water and aqueous solution of sodium trifluoromethanesulfonate (4.3 g, 25.0 mmol) was added in the [Pyrr$_{14}$]Br solution. After the mixture was stirred at room temperature for 3 hours and extracted with dichloromethane. The obtained layer was washed with water five times. The solvent dichloromethane was then evaporated. The residual ionic liquid and activated carbon were added in acetonitrile and stirred

at room temperature overnight. The solution was then filtered and evaporated. The colorless ionic liquid was then obtained and dried in vacuo at 313 K for more than 2 days. The yield was 16.5 % (1.08 g). ^{1}H-NMR (500 MHz, DMSO-d_6): δ = 0.93 (t, J = 7.4 Hz, 3H, $NCH_2CH_2CH_2CH_3$), 1.32 (sext, J = 7.4 Hz, 2H, $NCH_2CH_2CH_2CH_3$), 1.68 (m, 2H, $NCH_2CH_2CH_2CH_3$), 2.08 (br, 4H, $N(CH_2CH_2)_2$), 2.97 (s, 3H, NCH_3), 3.28 (m, 2H, $NCH_2CH_2CH_2CH_3$), 3.39–3.48 (m, 4H, $N(CH_2CH_2)_2$). Elemental analysis: $C_{10}H_{20}F_3NO_3S$: Calcd. C 41.23, H 6.92, N 4.81. Found: C 41.13, H 6.53, N 4.82.

A.3.8. 1-(2-Methoxyethyl)-1-methylpyrrolidinium bis(trifluoromethylsulfonyl)amide, [Pyrr$_{1(1O2)}$][NTf$_2$].

The same procedure was followed as described for [Pyrr$_{14}$][NF$_2$], except for the use of [Pyrr$_{1(1O2)}$]Br (4.59 g, 20.5 mmol) and lithium bis(trifluoromethylsulfonyl)amide (7.30 g, 25.44 mmol). The yield was 87.8% (7.62 g). ^{1}H-NMR (400 MHz, DMSO-d_6): δ = 2.07 (br, 4H, $N(CH_2CH_2)_2$), 3.01 (s, 3H, $NCH_2CH_2OCH_3$), 3.30 (s, 3H, NCH_3), 3.42–3.50 (m, 4H, $N(CH_2CH_2)_2$), 3.55 (m, 2H, $NCH_2CH_2OCH_3$), 3.74 (m, 2H, $NCH_2CH_2OCH_3$). Elemental analysis: $C_{10}H_{18}F_6N_2O_5S_2$: Calcd. C 28.30, H 4.28, N 6.60. Found: C 27.96, H 4.17, N 6.51.

A.3.9. 1-(2-Methoxyethyl)-1-methylpyrrolidinium bis(fluorosulfonyl)amide, [Pyrr$_{1(1O2)}$][NF$_2$].

The same procedure was followed as described for [Pyrr$_{14}$][NF$_2$], except for the use of [Pyrr$_{1(1O2)}$]Cl (4.75 g, 26.4 mmol) and potassium bis(fluorosulfonyl)amide (6.10 g, 27.8 mmol). The obtained liquid was mixed with activated charcoal in acetonitrile and stirred at room temperature overnight. The solution was filtered and evaporated and then dried in vacuo at 313 K for more than 2 days. The yield was 75.6% (6.48 g). ^{1}H-NMR (400 MHz, DMSO-d_6): δ = 2.09 (br, 4H, $N(CH_2CH_2)_2$), 3.02 (s, 3H, $NCH_2CH_2OCH_3$), 3.31 (s, 3H, NCH_3), 3.42–3.50 (m, 4H, $N(CH_2CH_2)_2$), 3.55 (m, 2H, $NCH_2CH_2OCH_3$), 3.74 (m, 2H, $NCH_2CH_2OCH_3$). Elemental analysis: $C_8H_{18}F_2N_2O_5S_2$: Calcd. C 29.62, H 5.59, N 8.64. Found: C 29.31, H 5.41, N 8.30.

A.3.10. 1-(2-Methoxyethyl)-1-methylpyrrolidinium cyclohexafluoropropane-1,3-bis(sulfonyl)amide, [Pyrr$_{1(1O2)}$][NCyF].

The same procedure was followed as described for [Pyrr$_{14}$][NF$_2$], except for the use of [Pyrr$_{1(1O2)}$]Cl (2.74 g, 15.2 mmol) and lithium cyclohexafluoropropane- 1,3-bis(sulfonyl)amide (4.86 g, 16.2 mmol). The obtained liquid was mixed with activated charcoal in acetonitrile and stirred at room temperature overnight. The solution was filtered and evaporated and then dried in vacuo at 313 K for more than 2 days. The yield was 79.9% (5.31 g). ^{1}H-NMR (400 MHz,

DMSO-d_6): δ = 2.07 (br, 4H, N(CH_2CH_2)$_2$), 3.01 (s, 3H, $NCH_2CH_2OCH_3$), 3.30 (s, 3H, NCH_3), 3.42–3.50 (m, 4H, N(CH_2CH_2)$_2$), 3.55 (m, 2H, $NCH_2CH_2OCH_3$), 3.74 (m, 2H, $NCH_2CH_2OCH_3$). Elemental analysis: $C_{11}H_{18}F_6N_2O_5S_2$: Calcd. C 30.28, H 4.16, N 6.42. Found: C 30.05, H 3.94, N 6.24.

A.3.11. 1-(2-Methoxyethyl)-1-methylpyrrolidinium hexafluorophosphate, [Pyrr$_{1(1O2)}$][PF$_6$].
The same procedure was followed as described for [Pyrr$_{14}$][NF_2], except for the use of [Pyrr$_{1(1O2)}$]Cl (4.70 g, 26.2 mmol) and sodium hexafluorophosphate (4.67 g, 27.8 mmol). The obtained liquid was mixed with activated charcoal in acetonitrile and stirred at room temperature overnight. The solution was filtered and evaporated and then dried in vacuo at 313 K for more than 2 days. The yield was 67.6% (5.12 g). ^{1}H-NMR (400 MHz, DMSO-d_6): δ = 2.07 (br, 4H, N(CH_2CH_2)$_2$), 3.01 (s, 3H, $NCH_2CH_2OCH_3$), 3.30 (s, 3H, NCH_3), 3.43–3.49 (m, 4H, N(CH_2CH_2)$_2$), 3.54 (m, 2H, $NCH_2CH_2OCH_3$), 3.74 (m, 2H, $NCH_2CH_2OCH_3$). Elemental analysis: $C_8H_{18}F_6NOP$: Calcd. C 33.23, H 6.27, N 4.84. Found: C 33.17, H 6.16, N 4.82.

B. Adequacy of Kerr Spectra without Slow Overdamped Relaxation Process Data

The adequacy of spectra obtained using only a short time window (varying from −1.0 to 9.2 ps) is shown. This is achieved by comparing the low-frequency Kerr spectra obtained with and without the wide time window Kerr transient (~300 ps). Unlike simple molecular liquids, the slowest relaxation time of ILs observed by RIKES is in the subnanosecond to nanosecond time scale and is dependent on the IL.[49,187] It is ideal to measure the complete Kerr transient from femtoseconds to nanoseconds. However, the limitation of the time delay of the fs-RIKES apparatus used in this study is 300 ps, and the Kerr signal in the time range of decades of picoseconds or even longer measured with the present fs-RIKES setup is essentially tiny because of the short perturbation by an ultrafast pulse. In addition, compared to single-temperature experiments, a greater number of data sets is required to observe a temperature dependence. Thus, the adequacy of the spectra obtained from the Kerr transients with short- and long-time-window data was examined for a discussion of the temperature-dependent spectra.

Figure B.1 shows logarithmic plots of the Kerr transients with and without the wide-time-window Kerr transient for $[C_3MIm][NTf_2]$. The Kerr transients after 3 ps were analyzed according to the multiexponential function

$$a_0 + \sum_{i=1}^{n} a_i \exp(-t/\tau_i) \tag{B.1}$$

where a_0 is the offset amplitude, a_i is the amplitude of the ith component, and τ_i is the time constant of the ith component. For data with the wide-time-window transients, a quadruple exponential function was used to fit the Kerr transients. On the other hand, a biexponential function has been used to fit the Kerr transients without the wide-time-window Kerr transient. The fits are also shown in Figure B.1. The fitting parameters for the Kerr transients of $[C_3MIm][NTf_2]$ are a_0 = 0.00013, a_1 = 0.01180, τ_1 = 1.24 ps, a_2 = 0.00314, τ_2 = 4.92 ps, a_3 = 0.00127, τ_3 = 20.66 ps, a_4 = 0.00086, and τ_4 = 122.57 ps for the Kerr transient with the wide-time-window transient, and a_0 = 0.00049, a_1 = 0.01900, τ_1 = 1.12 ps, a_2 = 0.00419, and τ_2 = 10.04 ps for the Kerr transient without the wide-time-window transient.

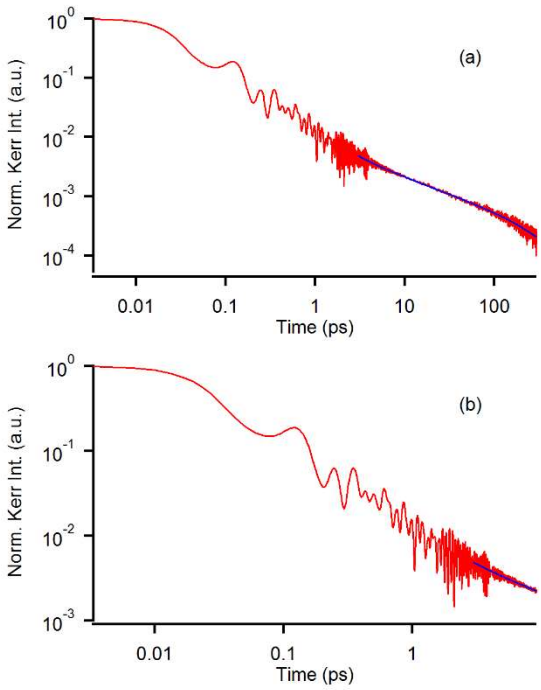

Figure B.1. Logarithmic plots of the Kerr transient (red) of [C_3MIm][NTf_2]. (a) Kerr transient with a wide-time-window transient (from −1.5 to 300 ps) and (b) Kerr transient without wide-time-window transient (from −1.5 to 8 ps). Multiexponential function fits are shown by blue lines.

Using the Kerr transients with and without the wide-time-window Kerr transient and multiexponential fit parameters, a Fourier transform deconvolution analysis, as established by McMorrow and Lotshaw,[9,185] has been conducted. Figure B.2 shows the Fourier transform Kerr spectra obtained from the Kerr transients with and without the wide-time-window Kerr transient for [C_3MIm][NTf_2].

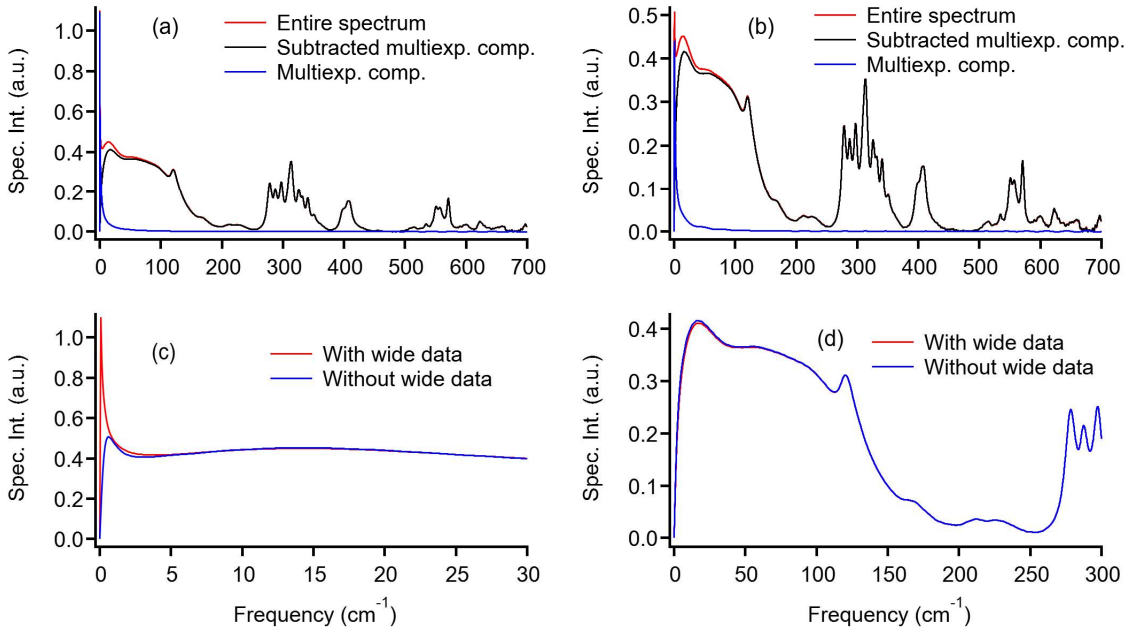

Figure B.2. Fourier transform Kerr spectra of [C_3MIm][NTf_2] (a) with a wide-time-window transient (from −1.5 to 300 ps) and (b) without a wide-time-window transient (from −1.5 to 8 ps). (c) Comparison of the entire Kerr spectra in the low-frequency region with and without a wide-time-window transient. (d) Comparison of Kerr spectra after the subtraction of multiexponential components with and without a wide-time-window transient.

As is evident in Figure B.2a and b, the difference in the spectra between the Kerr transients with and without the wide-time-window data is clear in the very low-frequency region. Strong spectral intensity appears in the Kerr transient with the wide-time-window data because of the overdamped relaxation process with a time scale of tens to hundreds of picoseconds. As is clearly shown in Figure B.2c, in the spectrum obtained from the Kerr transient without the wide-time-window data, the band at ca. 0.6 cm^{-1} (corresponding to ca. 56 ps) is well-resolved. On the other hand, the lowest part (<0.1 cm^{-1}) of the spectrum obtained from the Kerr transient with the wide-time-window data seems not to be completely resolved, as the first nonzero frequency datum at 0.0762 cm^{-1} (corresponding to 437 ps) has the highest spectral intensity.

Studies of the low-frequency Kerr spectra of condensed phases often discuss the intermolecular (or interionic) vibrational parts unaffected by the contributions of the picosecond overdamped relaxation process. In this thesis, Kerr spectra obtained by subtraction of the multiexponential component that is overlapped by intermolecular (or interionic) vibrations in the frequency/time domain are discussed. The Kerr spectra obtained from the Kerr

transients with and without the wide-time-window data are critically compared in Figure B.2d. Note that the fast component ($a_1\exp(-t/\tau_1)$) is including in the low-frequency spectra. So far, this component has been incorporated into the low-frequency spectrum in not only ILs[52,56,71,116,167,173] (except for earlier works) but also molecular liquids.[17] This is because the dynamics in molecular liquids expressed by an exponential function with the time constant of several hundred femtoseconds to a few picosecond is often non-Stokes–Einstein–Debye hydrodynamic behavior.[124,190,221] This indicates that the nature of the dynamics is not (diffusive) orientational, but possibly intermolecular vibrational or crossover process from the intermolecular vibration to the orientational dynamics. The Kerr spectra are superimposed at frequencies of above approximately 70 cm^{-1}. Below this frequency, there is minimal difference between the two spectra. The spectral intensity in the peak at ca. 16 cm^{-1} is approximately 1.2% lower in the Kerr spectrum obtained from the Kerr transients with the wide-time-window data than that obtained without the wide-time-window data. Accordingly, data obtained from the Kerr transient without the wide-time-window data can be adequate for discussion of the temperature-dependent low-frequency spectra and have an error of approximately 1%–2%.

C. Appendix to Chapter 3

Table C.1. Water Contents for Ionic Liquids

samples	water content (ppm)
$[C_4MIm][PF_6]$	46
$[C_4MIm][BF_4]$	62
$[C_4MIm]I$	71
$[C_4MIm][OTf]$	54
$[C_4MIm][SCN]$	78
$[C_4MIm][DCA]$	93
$[C_4MIm][NCyF]$	27
$[C_4MIm][NF_2]$	33
$[C_4MIm][NTf_2]$	32
$[C_4MIm][NPf_2]$	15
$[C_6MIm][PF_6]$	46
$[C_7MIm][PF_6]$	40

C.2. Temperature-Dependent Viscosities for Ionic Liquids.

Table C.2.1. Spherical Top Anions

Temperature (K)	Viscosity (cP)				
	$[C_4MIm][PF_6]$	$[C_4MIm][BF_4]$	$[C_4MIm]I$	$[C_6MIm][PF_6]$	$[C_7MIm][PF_6]$
278	1192	375	8824	2782	3454
283	780	260	4936	1779	2210
288	541	189	2873	1184	1443
293	371	139	1753	713	945
298	269	104	1109	488	591
303	198	79.8	852	347	422
308	149	62.7	582	256	303
313	111	51.0	400	192	226
318	86.6	40.4	284	146	172
323	69.3	32.9	209	112	132
328	57.9	27.4	154	88.0	102
333	46.8	23.0	119	69.5	81.2
338	38.2	19.4	92.9	56.6	64.8
343	31.6	16.3	70.4	46.0	52.8
348	26.6	13.8	56.2	37.9	42.9
353	22.5	11.8	45.3	31.8	35.5

Table C.2.2. Lower Symmetric Anions.

Temperature (K)	Viscosity (cP)			
	[C_4MIm][OTf]	[C_4MIm][SCN]	[C_4MIm][DCA]	[C_4MIm][NCyF]
278	276	238	71.7	-
283	201	169	54.3	485
288	150	123	42.1	331
293	113	91.6	33.5	239
298	86.7	71.2	27.6	178
303	69.0	56.1	22.8	134
308	55.1	44.4	19.1	102
313	44.4	35.7	16.3	79.7
318	36.0	29.6	13.9	63.6
323	30.2	24.7	12.0	51.6
328	25.6	21.0	10.5	41.7
333	21.8	17.8	9.26	34.5
338	18.8	15.1	8.25	29.1
343	16.1	12.8	7.56	24.9
348	14.0	11.0	7.00	21.3
353	12.2	9.08	6.59	18.3

Table C.2.3. Anions Having Conformers

Temperature (K)	Viscosity (cP)		
	$[C_4MIm][NF_2]$	$[C_4MIm][NTf_2]$	$[C_4MIm][NPf_2]$
278	75.3	134	382
283	58.5	98.5	265
288	46.6	76.6	191
293	37.5	62.3	140
298	31.0	48.4	104
303	26.0	38.7	79.5
308	22.1	32.0	62.9
313	19.0	26.7	50.4
318	16.4	22.6	40.4
323	14.3	19.2	33.1
328	12.5	16.5	27.9
333	11.1	14.3	23.8
338	9.86	12.4	20.3
343	8.86	11.0	17.6
348	8.08	9.59	15.3
353	7.51	8.58	13.4

C.3. Kerr Transients, Fourier Transform Spectra, and Difference Spectra for Imidazolium-Based Ionic Liquids and Molecular Liquids

Figure C.3.1. 1-Butyl-3-methylimidazolium hexafluorophosphate ([C_4MIm][PF_6]).

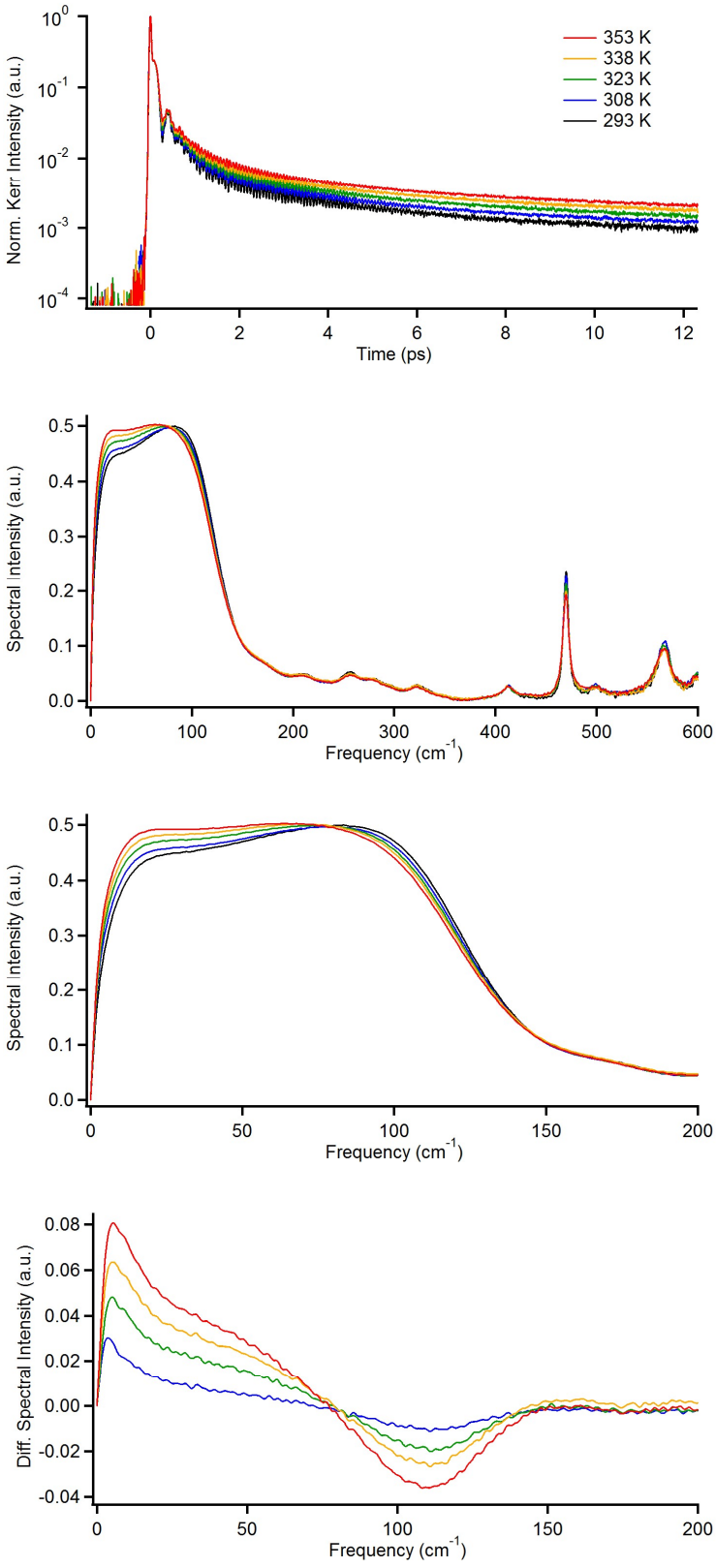

Figure C.3.2. 1-Butyl-3-methylimidazolium tetrafluoroborate ([C_4MIm][BF_4]).

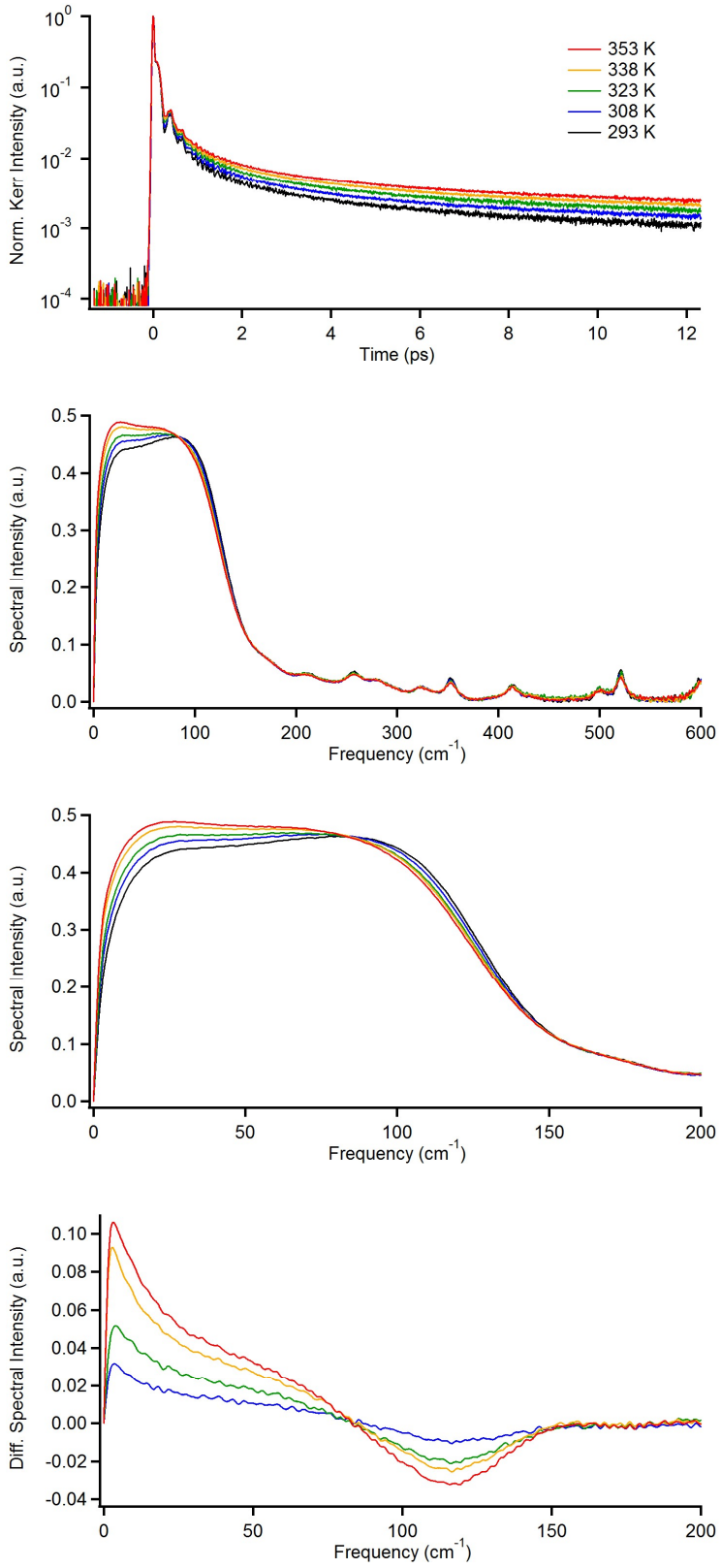

Figure C.3.3. 1-Butyl-3-methylimidazolium iodide ([C_4MIm]I).

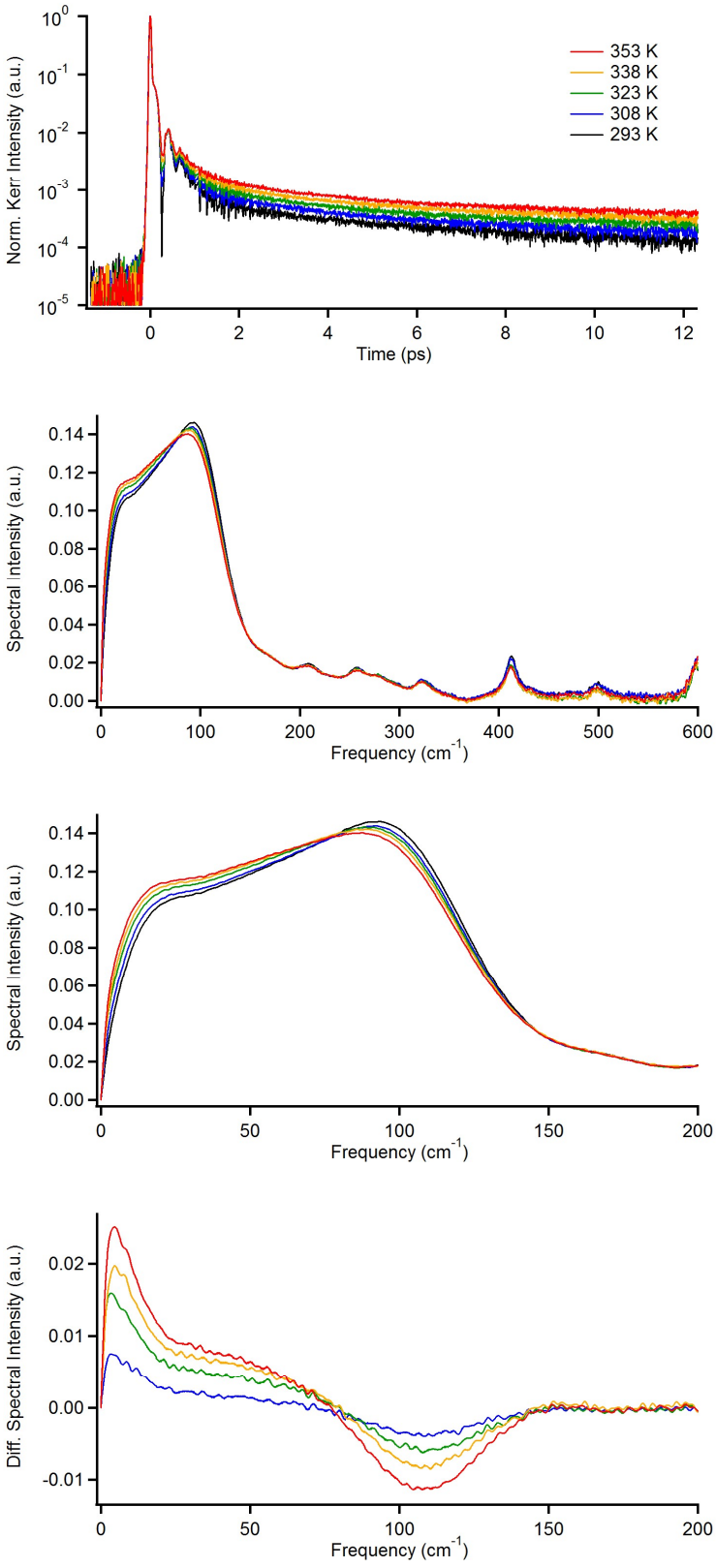

Figure C.3.4. 1-Butyl-3-methylimidazolium trifluoromethanesulfonate ([C_4MIm][OTf]).

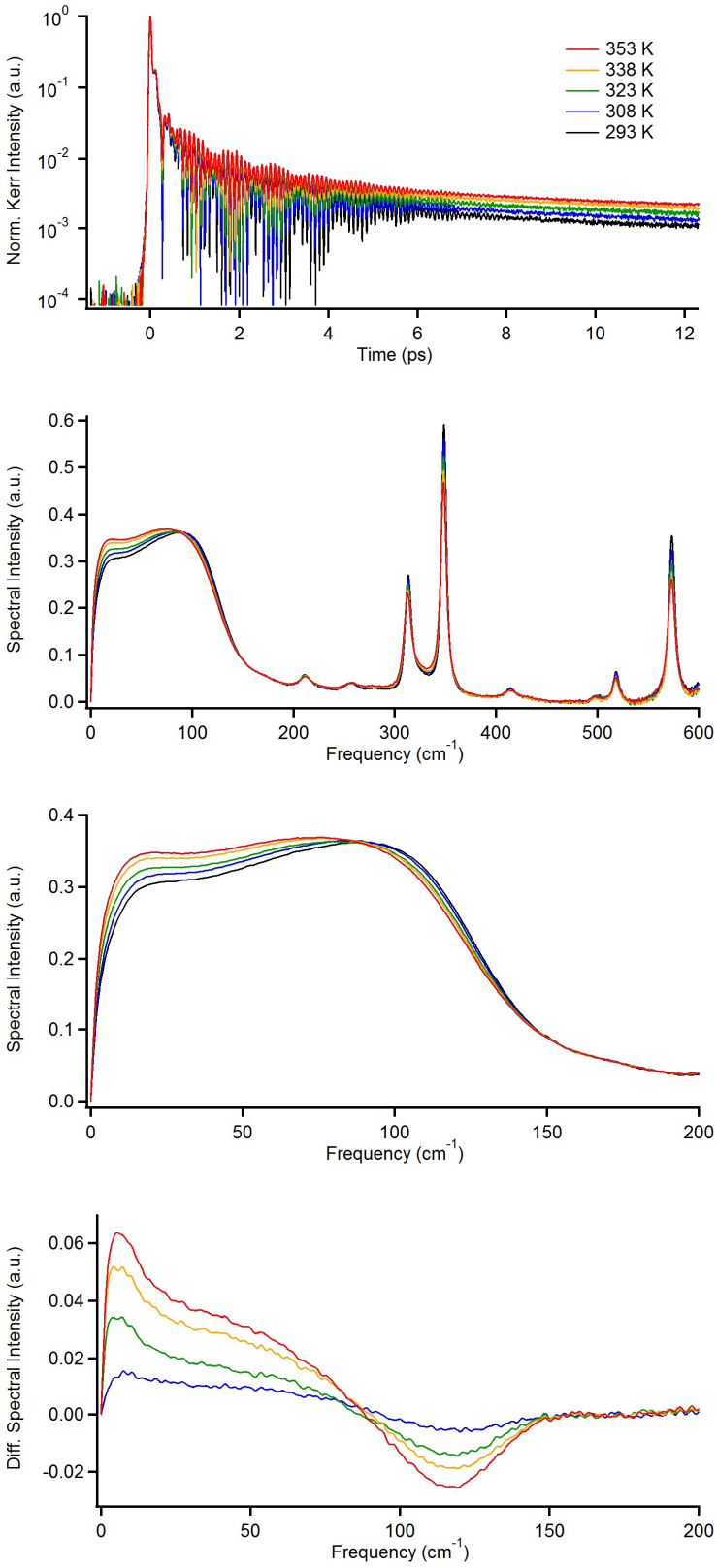

Figure C.3.5. 1-Butyl-3-methylimidazolium thiocyanate ([C_4MIm][SCN]).

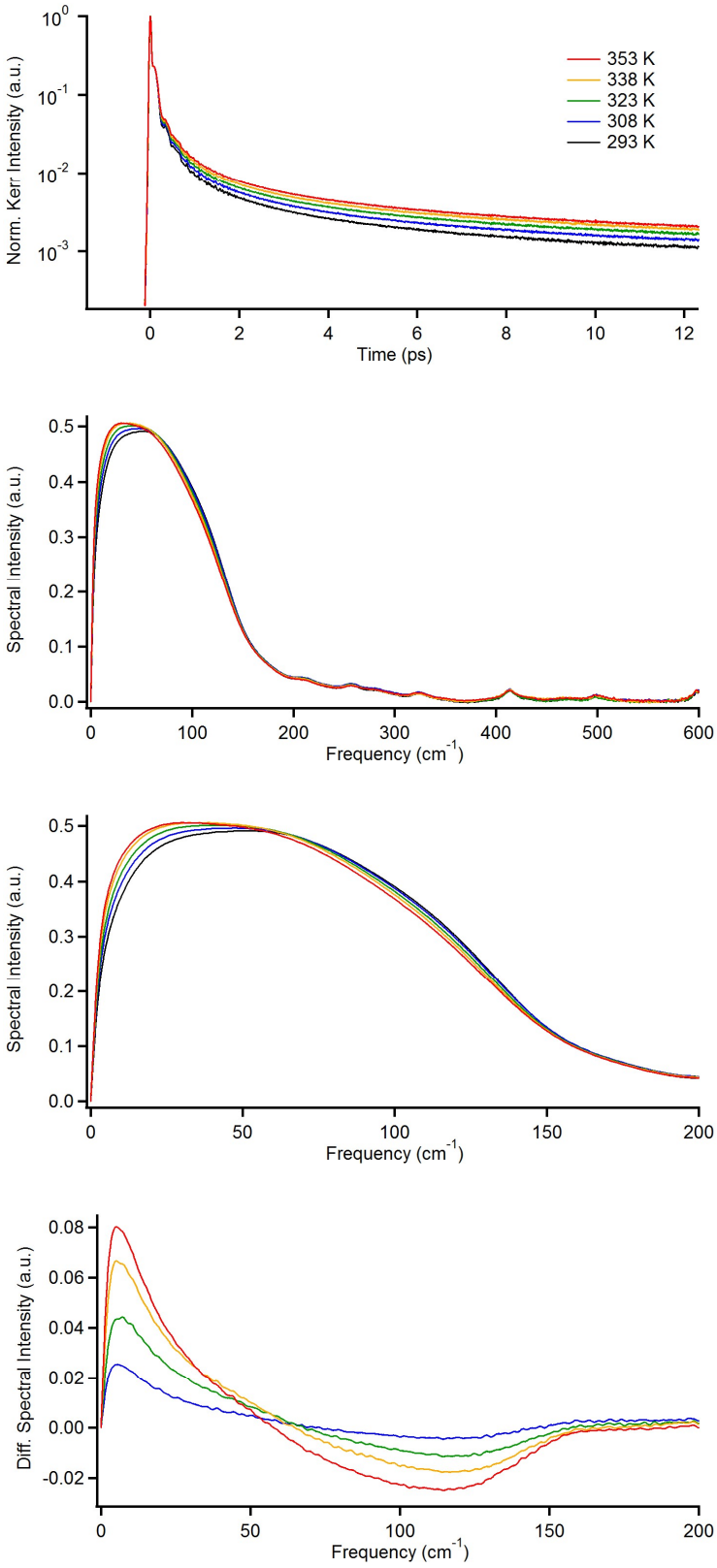

Figure C.3.6. 1-Butyl-3-methylimidazolium dicyanamide ([C_4MIm][DCA]).

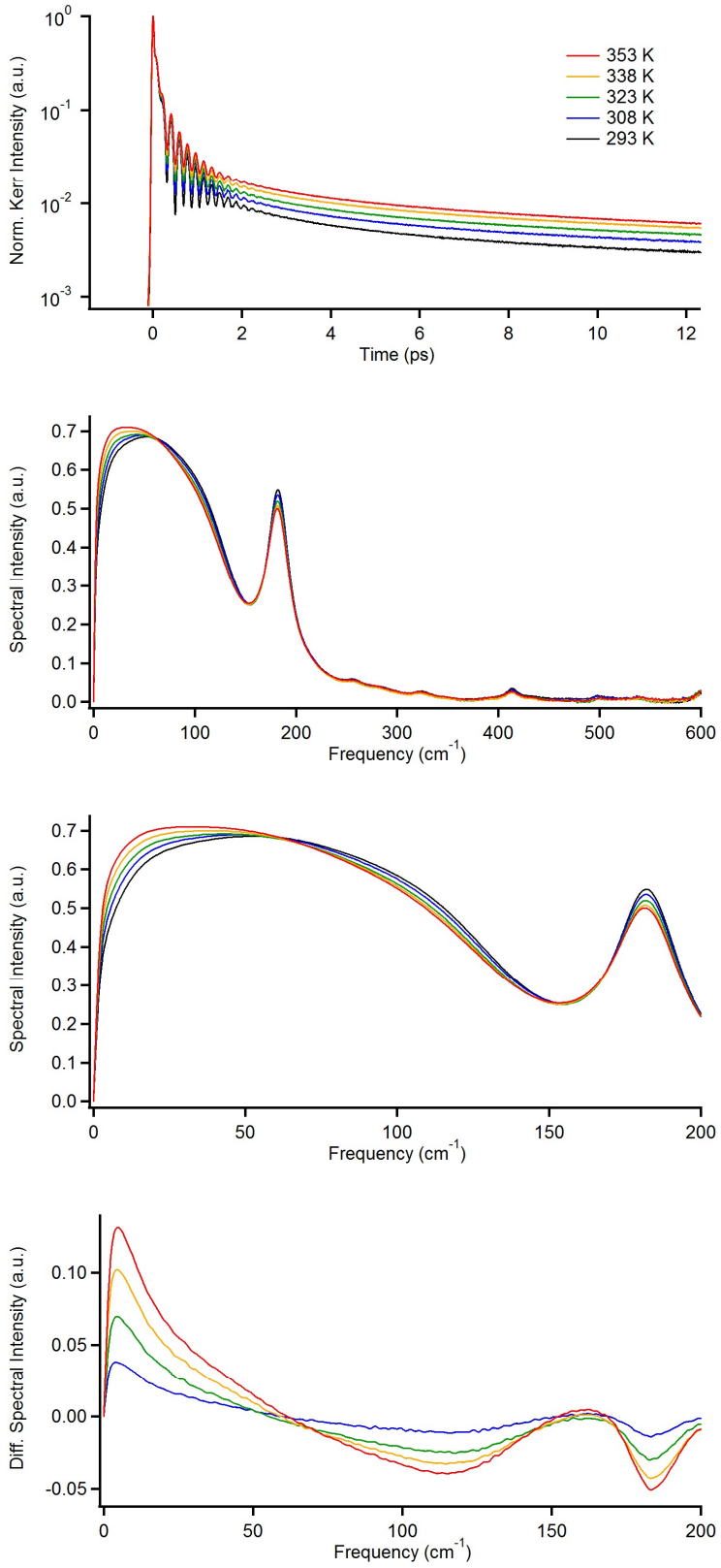

Figure C.3.7. 1-Butyl-3-methylimidazolium cyclohexafluoropropane-1,3-bis(sulfonyl)amide ([C4MIm][NCyF]).

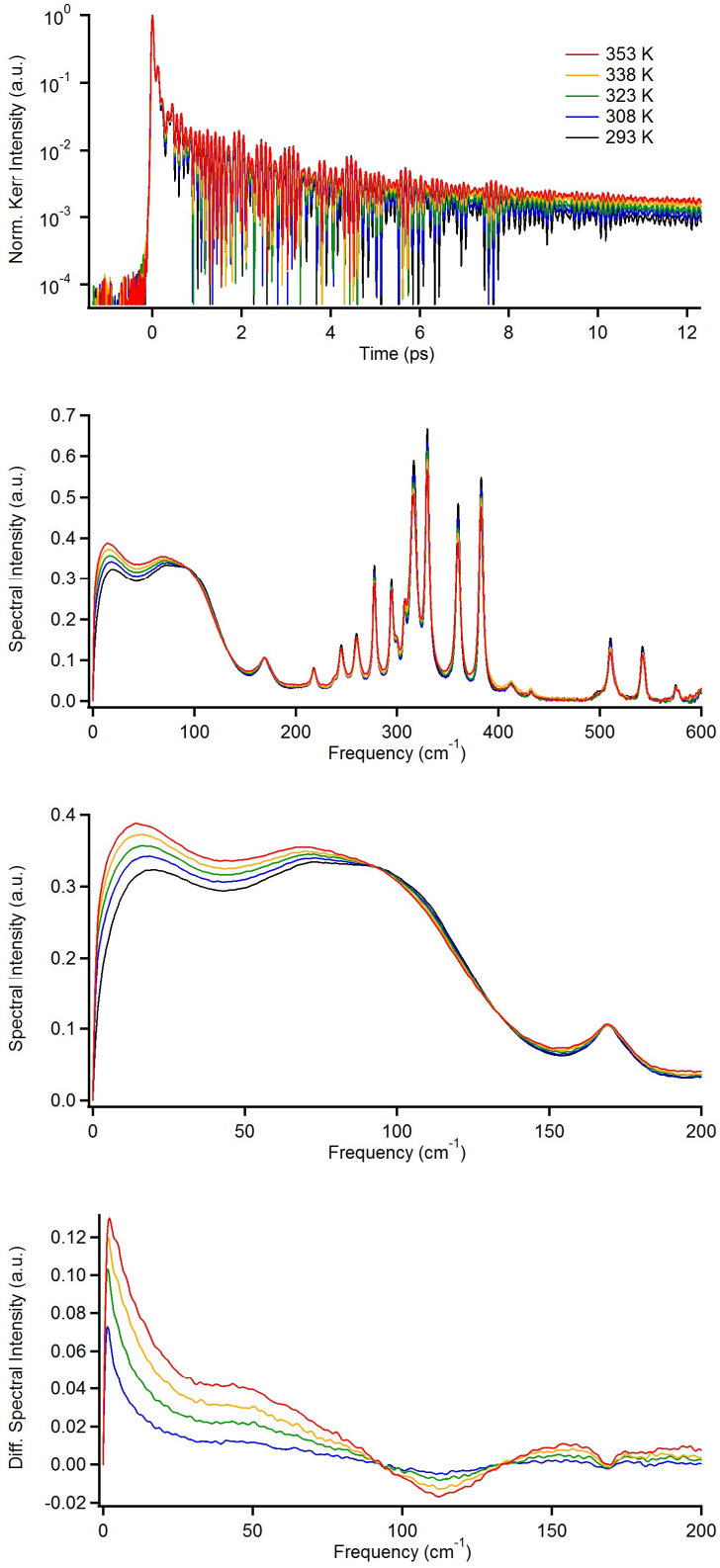

Figure C.3.8. 1-Butyl-3-methylimidazolium bis(fluorosulfonyl)amide ([C_4MIm][NF_2]).

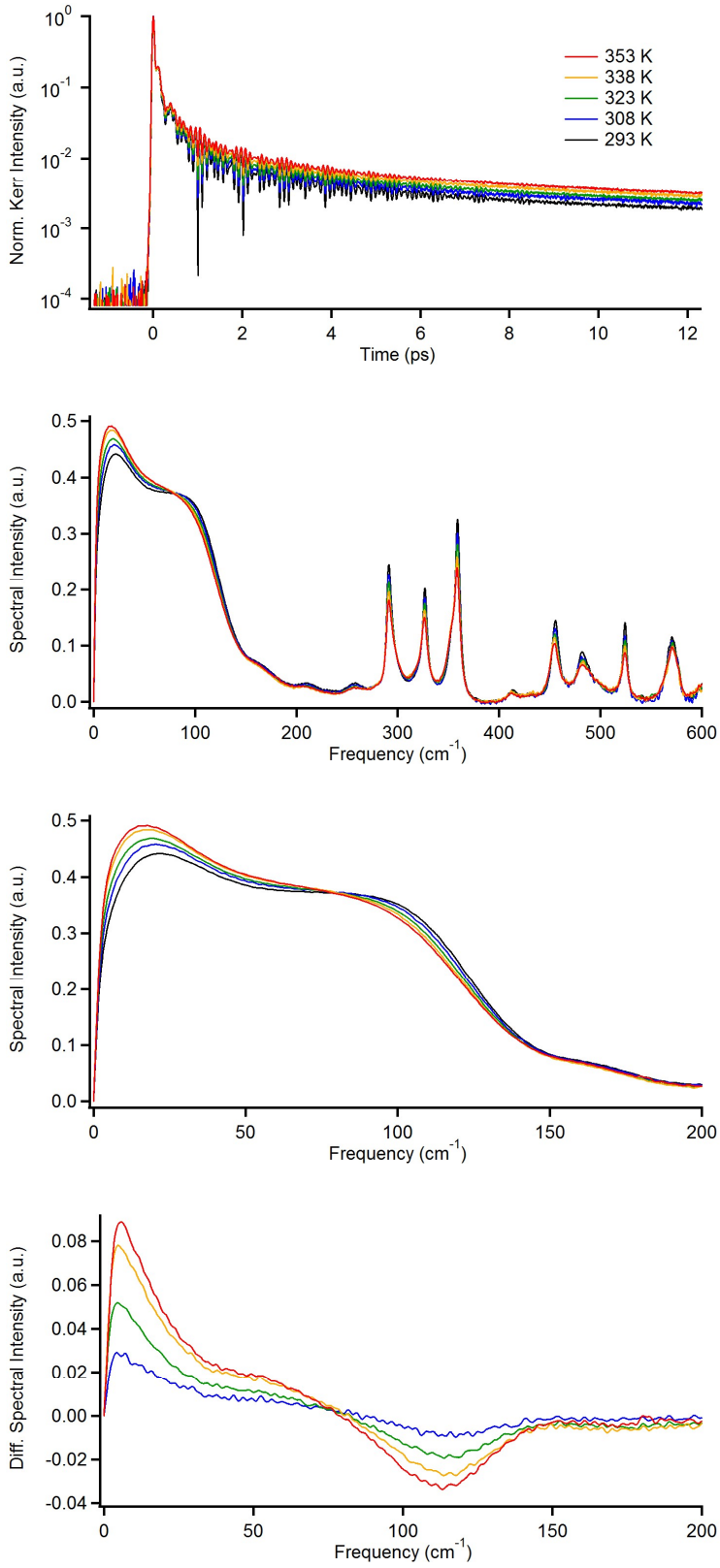

Figure C.3.9. 1-Butyl-3-methylimidazolium bis(trifluoromethylsulfonyl)amide ([C_4MIm][NTf_2]).

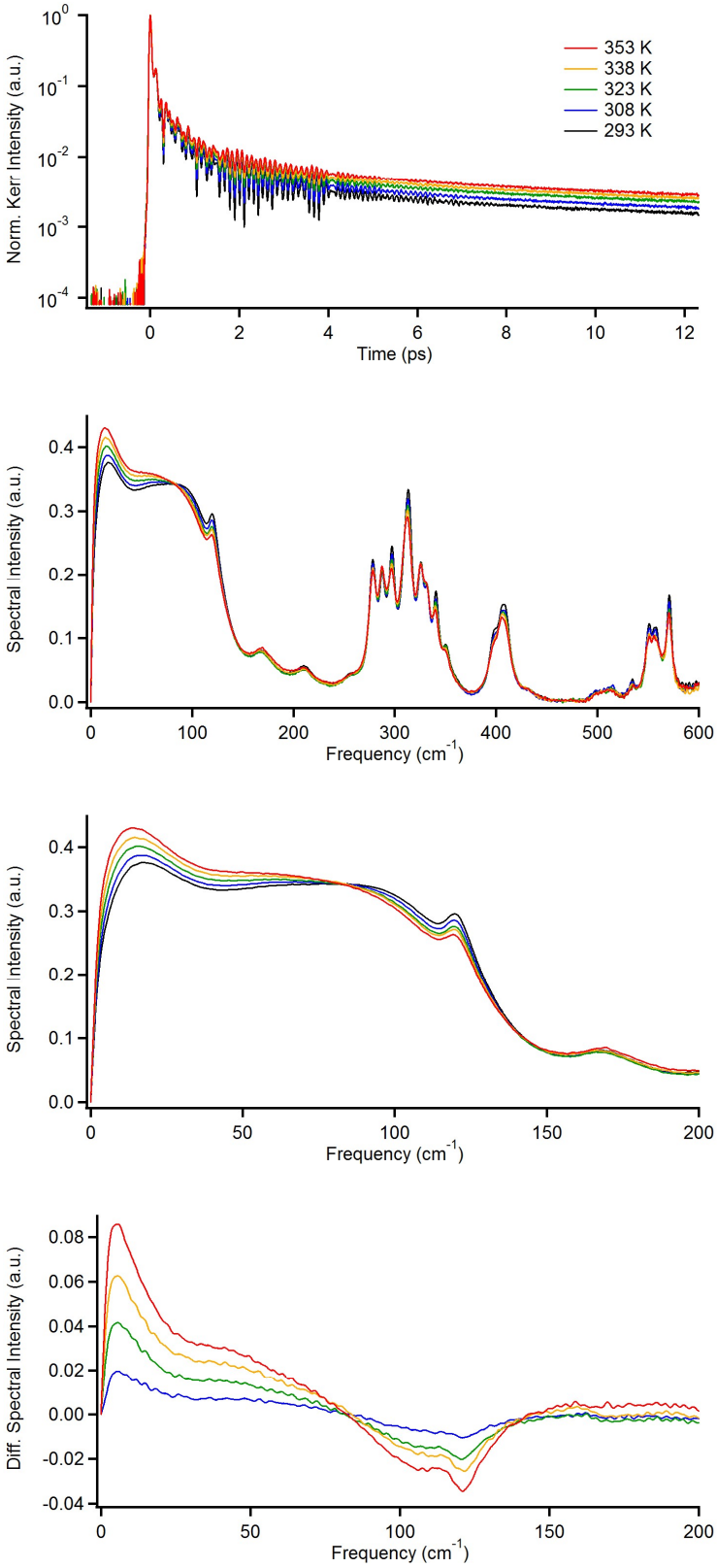

Figure C.3.10. 1-Butyl-3-methylimidazolium bis(pentafluoroethylsulfonyl)amide ([C_4MIm][NPf_2]).

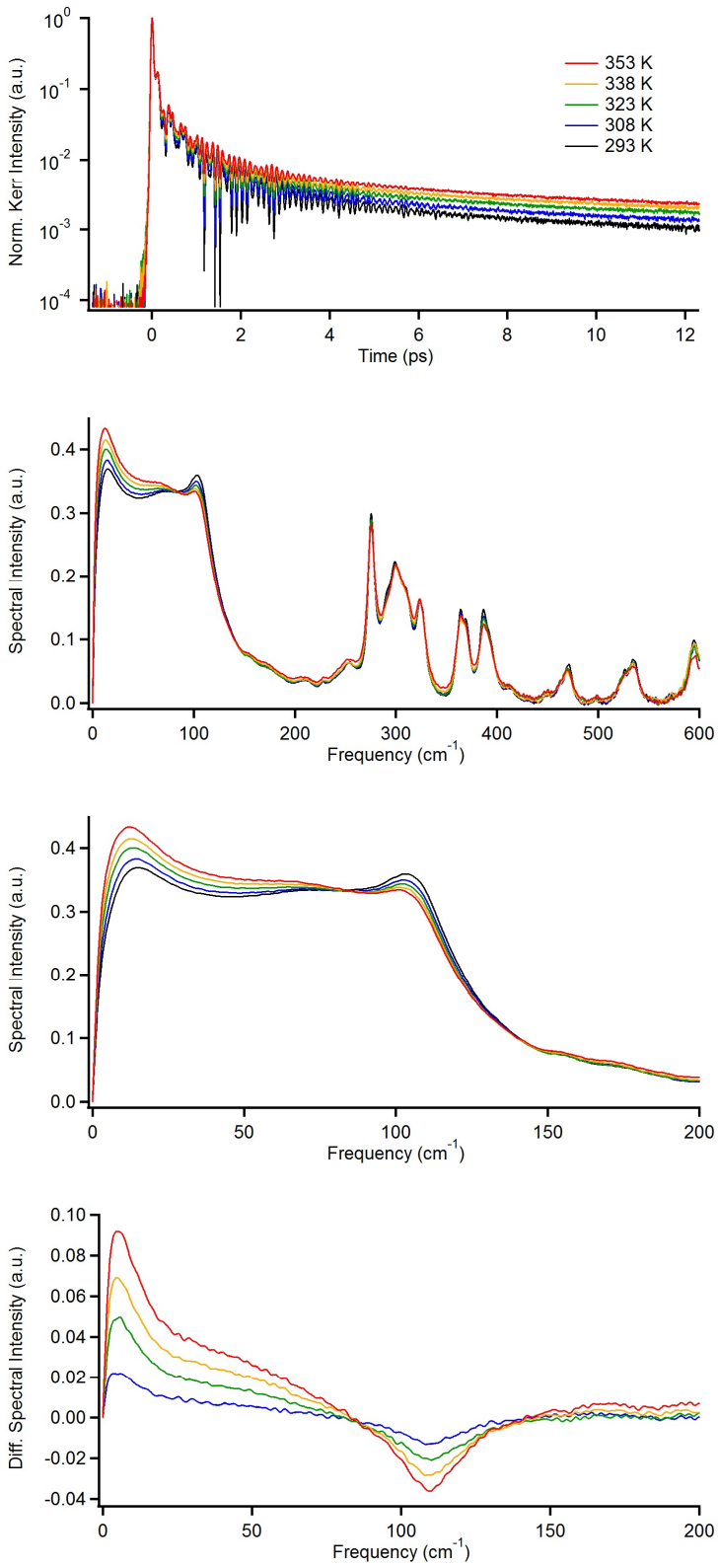

Figure C.3.11. 1-Hexyl-3-methylimidazolium hexafluorophosphate ([C_6MIm][PF_6]).

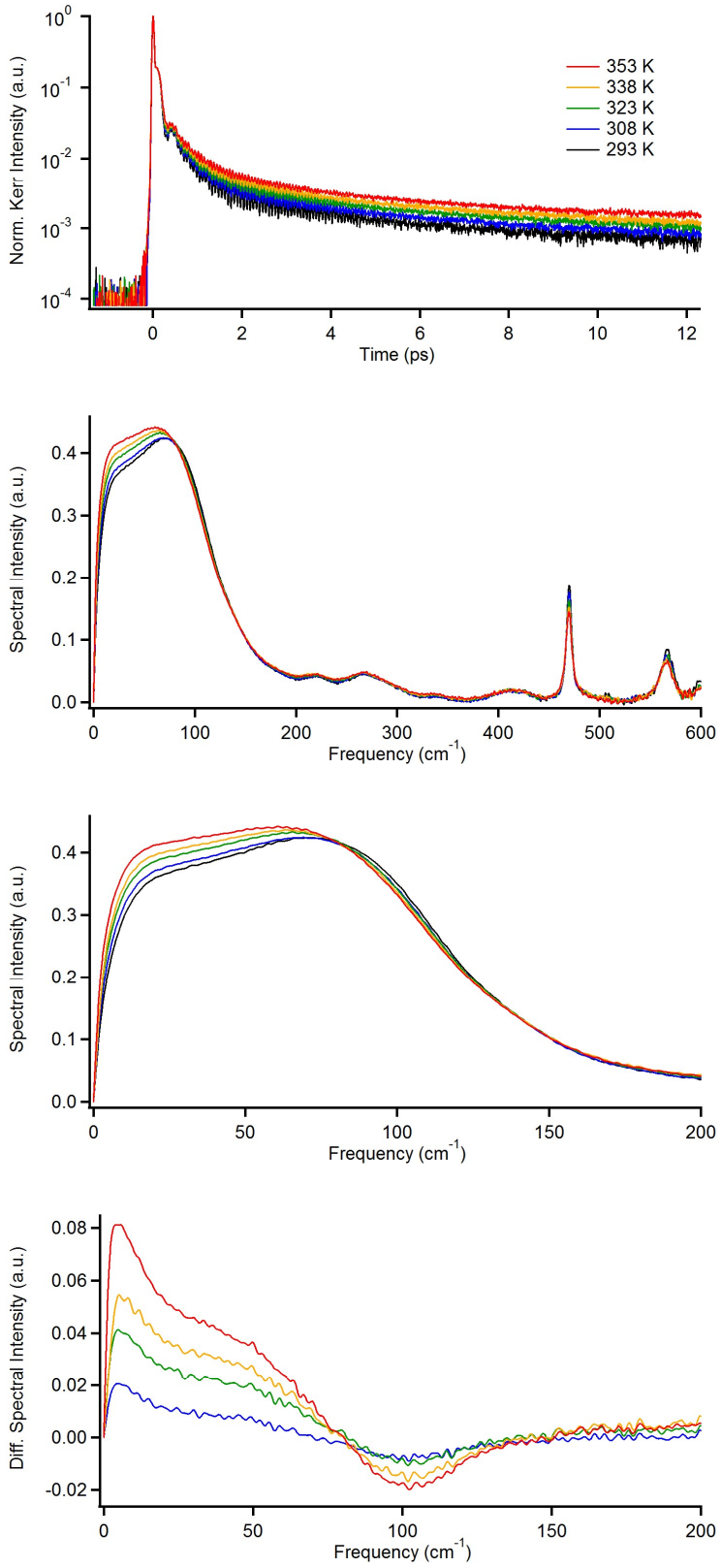

Figure C.3.12. 1-Heptyl-3-methylimidazolium hexafluorophosphate ([C_7MIm][PF_6]).

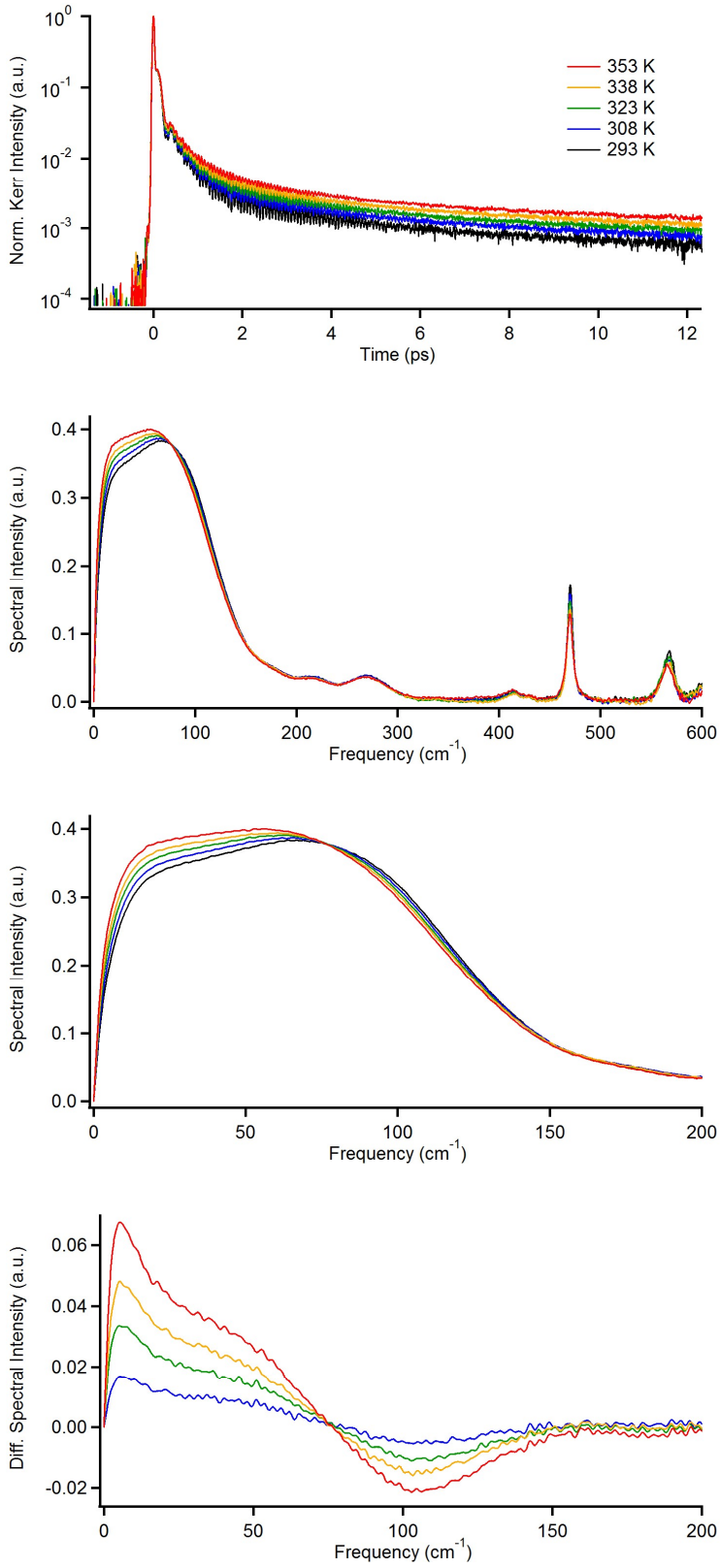

Figure C.3.13. 1-Methylimidazole.

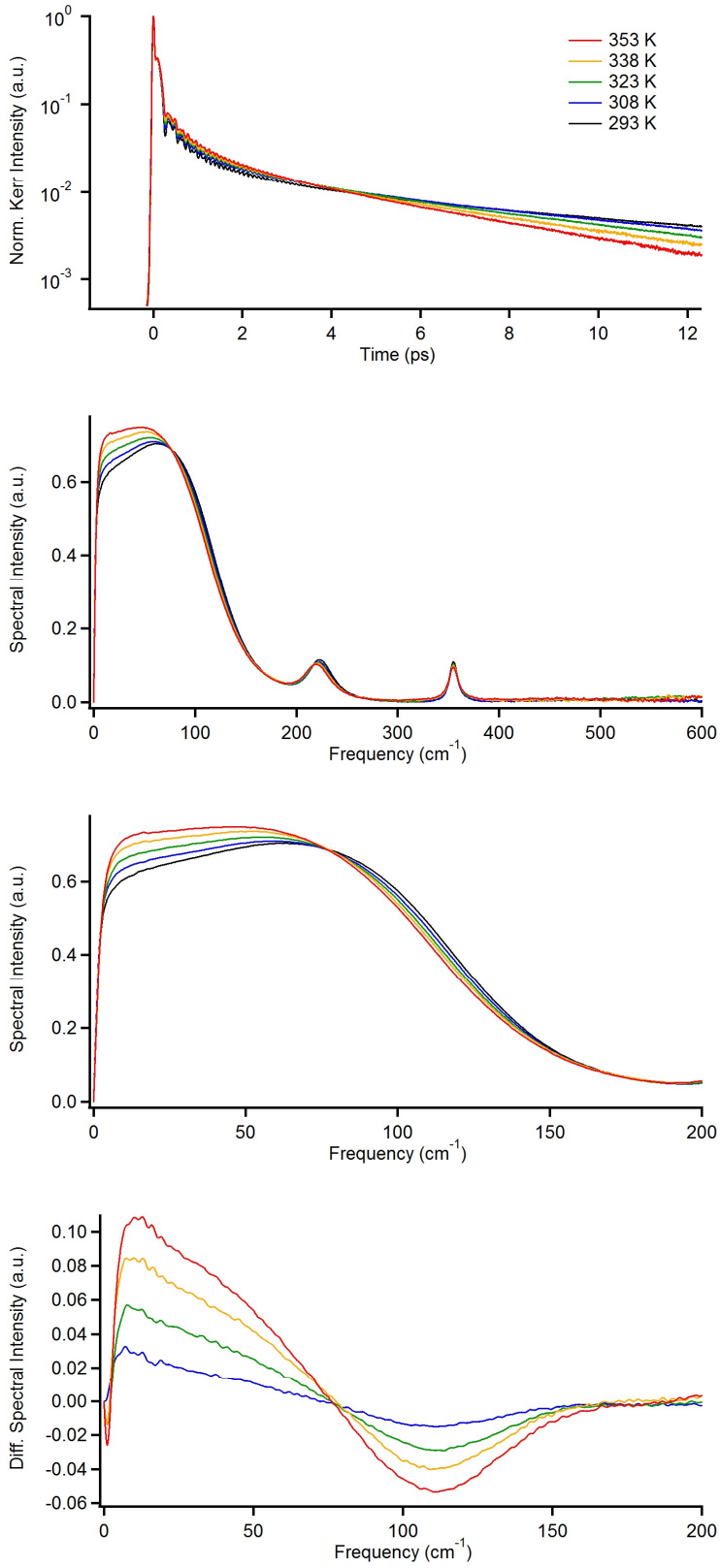

Figure C.3.14. Propionitrile.

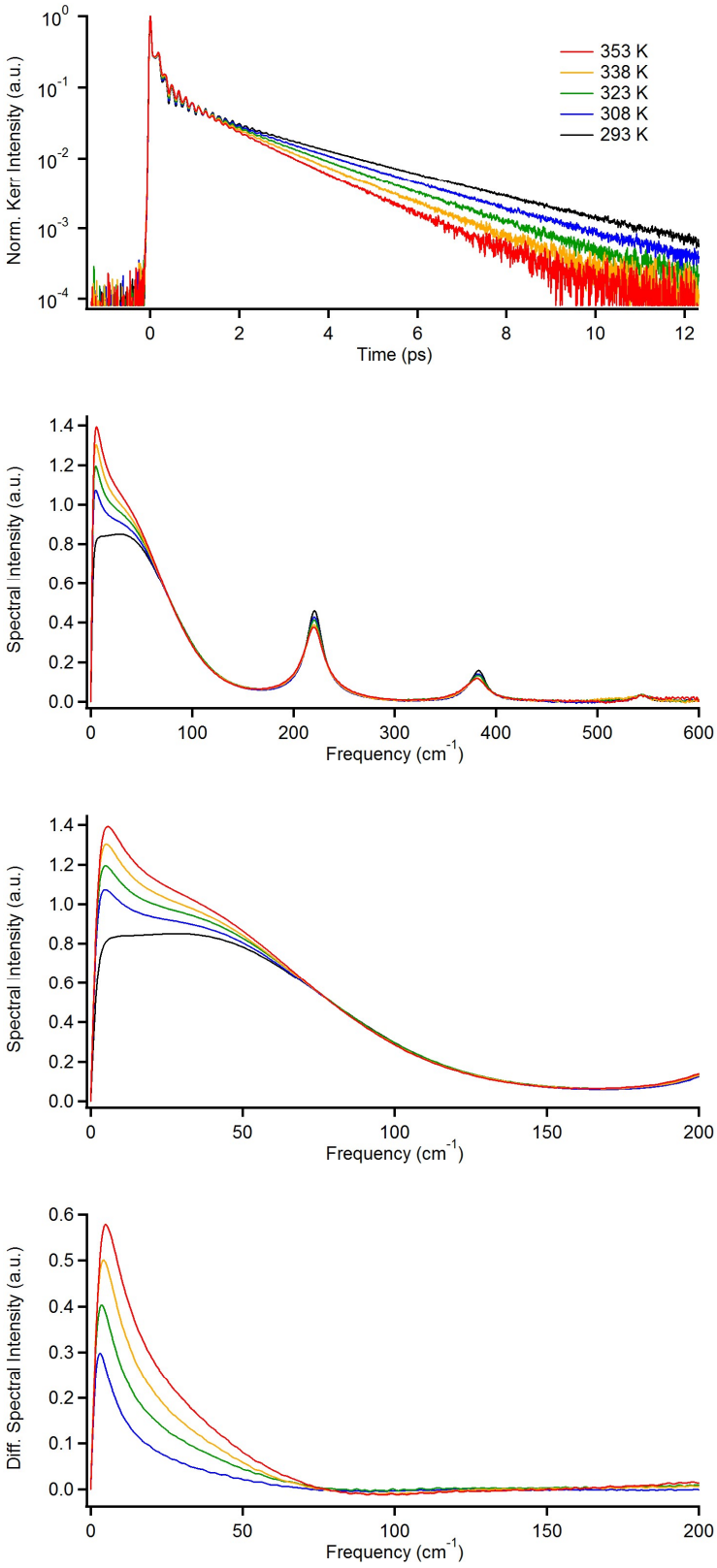

Figure C.3.15. Carbon tetrachloride.

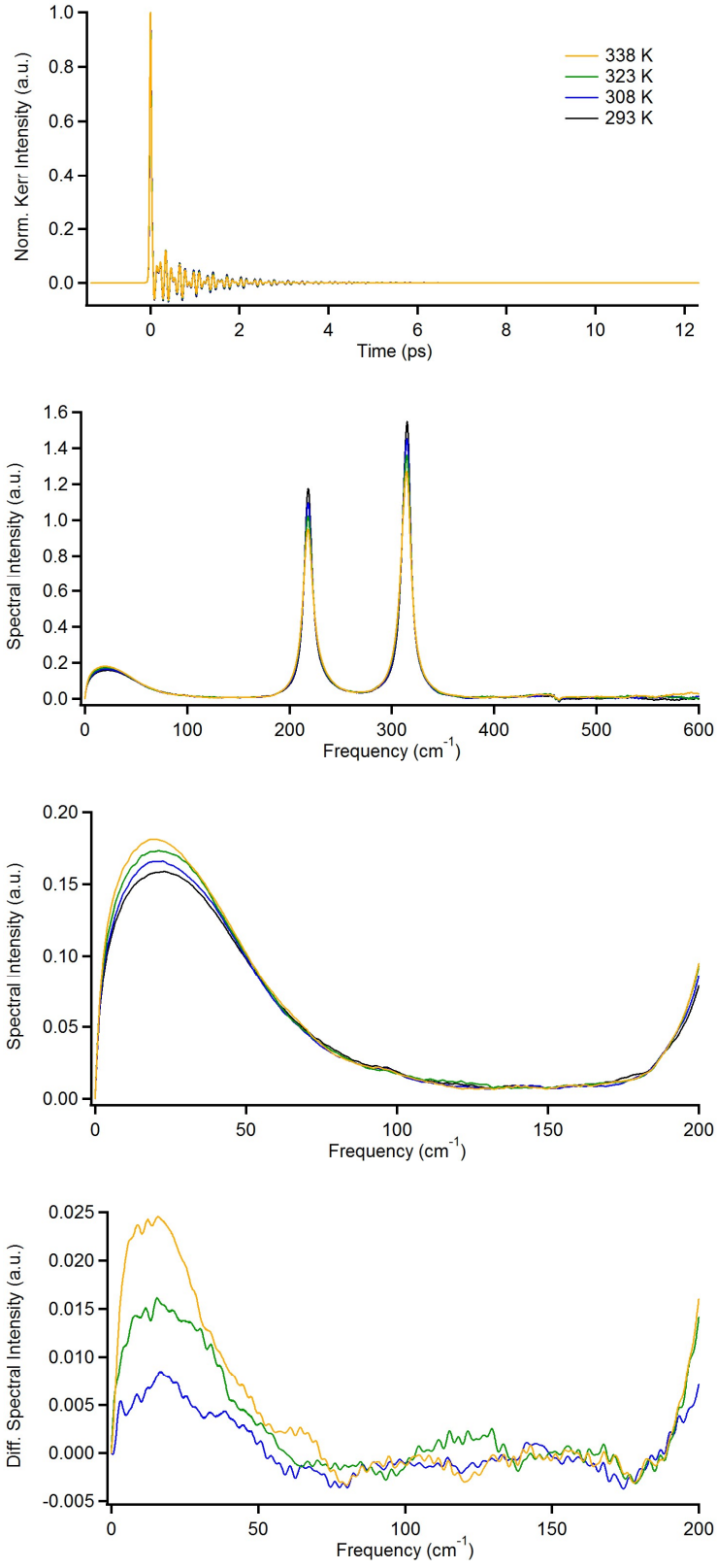

C.4. Biexponential Fit Parameter for Kerr Transients in Imidazolium-Based Ionic Liquids and Molecular Liquids at Various Temperatures.

Table C.4.1. Spherical Top Anions

Temperature (K)	a_0	a_1	τ_1 (ps)	a_2	τ_2 (ps)
		[C_4MIm][PF_6]			
293	0.00076	0.00472	1.66	0.00251	5.11
308	0.00082	0.00792	1.50	0.00268	6.41
323	0.00096	0.00896	1.40	0.00347	6.47
338	0.00120	0.01010	1.38	0.00404	6.35
353	0.00143	0.01049	1.37	0.00463	6.28
		[C_4MIm][BF_4]			
293	0.00048	0.00797	1.43	0.00244	8.29
308	0.00072	0.00795	1.54	0.00284	8.21
323	0.00093	0.00960	1.50	0.00345	8.32
338	0.00111	0.01051	1.50	0.00401	8.33
353	0.00122	0.01182	1.48	0.00478	8.33
		[C_4MIm]I			
293	0.00006	0.00060	1.52	0.00034	7.73
308	0.00011	0.00115	1.49	0.00038	7.73
323	0.00018	0.00118	1.80	0.00036	7.48
338	0.00019	0.00134	1.56	0.00059	7.95
353	0.00025	0.00169	1.60	0.00066	7.82
		[C_6MIm][PF_6]			
293	0.00046	0.00356	1.48	0.00169	6.03
308	0.00056	0.00468	1.45	0.00206	6.19
323	0.00070	0.00638	1.36	0.00245	6.30
338	0.00074	0.01228	1.05	0.00317	6.40
353	0.00111	0.00610	1.70	0.00290	6.38
		[C_7MIm][PF_6]			
293	0.00039	0.00340	1.42	0.00145	6.26
308	0.00052	0.00452	1.36	0.00185	6.30
323	0.00064	0.00473	1.44	0.00215	6.24
338	0.00077	0.00543	1.41	0.00259	6.28
353	0.00098	0.00678	1.40	0.00283	6.36

Table C.4.2. Lower Symmetric Anions

Temperature (K)	a_0	a_1	τ_1 (ps)	a_2	τ_2 (ps)
		[C_4MIm][OTf]			
293	0.00077	0.00341	1.76	0.00216	6.34
308	0.00093	0.00355	1.77	0.00274	6.30
323	0.00118	0.00464	1.84	0.00300	6.34
338	0.00147	0.00532	1.81	0.00342	6.25
353	0.00162	0.00560	1.75	0.00403	6.19
		[C_4MIm][SCN]			
293	0.00078	0.00810	1.30	0.00297	5.63
308	0.00095	0.00918	1.32	0.00346	5.91
323	0.00118	0.01053	1.28	0.00410	5.69
338	0.00128	0.01228	1.27	0.00446	6.23
353	0.00139	0.01203	1.33	0.00487	6.22
		[C_4MIm][DCA]			
293	0.00167	0.01114	1.70	0.00467	9.63
308	0.00222	0.01243	1.73	0.00577	9.65
323	0.00269	0.01427	1.68	0.00692	9.55
338	0.00302	0.01548	1.70	0.00850	9.74
353	0.00324	0.01739	1.64	0.01002	9.65
		[C_4MIm][NCyF]			
293	0.00043	0.00149	3.23	0.00185	8.11
308	0.00071	0.00318	3.27	0.00111	8.64
323	0.00091	0.00375	3.63	0.00118	7.69
338	0.00107	0.00409	3.49	0.00150	8.33
353	0.00118	0.00490	3.02	0.00206	8.29

Table C.4.3. Anions Having Conformers

Temperature (K)	a_0	a_1	τ_1 (ps)	a_2	τ_2 (ps)
		$[C_4MIm][NF_2]$			
293	0.00128	0.00729	1.73	0.00363	7.03
308	0.00149	0.00887	1.66	0.00432	7.24
323	0.00156	0.00937	1.70	0.00511	7.33
338	0.00179	0.01210	1.55	0.00602	7.18
353	0.00187	0.01441	1.42	0.00725	7.13
		$[C_4MIm][NTf_2]$			
293	0.00087	0.01030	1.30	0.00298	8.24
308	0.00100	0.01344	1.20	0.00385	8.17
323	0.00125	0.01206	1.32	0.00447	8.23
338	0.00139	0.01205	1.36	0.00509	8.23
353	0.00150	0.01443	1.33	0.00579	8.29
		$[C_4MIm][NPf_2]$			
293	0.00048	0.00797	1.43	0.00244	8.29
308	0.00072	0.00795	1.54	0.00284	8.21
323	0.00093	0.00960	1.50	0.00345	8.32
338	0.00111	0.01051	1.50	0.00401	8.33
353	0.00122	0.01182	1.48	0.00478	8.33

Table C.4.4. Molecular Liquids

Temperature (K)	a_0	a_1	τ_1 (ps)	a_2	τ_2 (ps)
		1-Methylimidazole			
293	-	0.01765	1.82	0.01237	10.84
308	-	0.01982	1.72	0.01450	8.87
323	-	0.02050	1.59	0.01664	7.21
338	-	0.02324	1.47	0.01812	6.14
353	-	0.02703	1.34	0.02091	5.10
		Propionitrile			
293	-	0.03144	1.52	0.04029	2.97
308	-	0.04586	1.62	0.02941	2.76
323	-	0.05519	1.52	0.02618	2.42
338	-	0.06758	1.39	0.02157	2.20
353	-	0.08387	1.23	0.01779	2.07

C.5. Fit Parameters and First Moments M_1 for Low-Frequency Kerr Spectra of Imidazolium-Based Ionic Liquids and Molecular Liquids at Various Temperatures.

Table C.5.1. Spherical Top Anions.

Intermolecular Vibrations

	T (K)	M_1 (cm^{-1})	$a_{O,1}$	$\omega_{O,1}$ (cm^{-1})	$a_{G,1}$	$\omega_{G,1}$ (cm^{-1})	$\Delta\omega_{G,1}$ (cm^{-1})	$a_{G,2}$	$\omega_{G,2}$ (cm^{-1})	$\Delta\omega_{G,2}$ (cm^{-1})	$a_{G,3}$	$\omega_{G,3}$ (cm^{-1})	$\Delta\omega_{G,3}$ (cm^{-1})
$[C_4MIm][PF_6]$	293	69.2	0.073	5.4	0.286	7.9	32.1	0.481	49.5	86.5	0.226	104.8	45.0
	308	68.2	0.091	4.7	0.295	7.8	30.2	0.517	40.7	87.0	0.255	103.4	47.8
	323	67.3	0.095	5.1	0.284	8.0	31.0	0.538	39.3	87.9	0.243	103.0	48.1
	338	66.4	0.102	5.0	0.284	8.0	30.3	0.526	38.7	82.9	0.265	102.1	49.9
	353	65.7	0.109	5.1	0.281	8.0	30.1	0.516	37.8	78.5	0.284	100.9	51.6
$[C_4MIm][BF_4]$	293	70.8	0.075	5.3	0.272	9.2	34.5	0.441	52.0	83.5	0.226	109.5	48.1
	308	69.7	0.095	4.7	0.297	8.2	32.5	0.480	43.1	85.9	0.245	107.6	50.6
	323	68.7	0.105	4.6	0.306	7.8	31.6	0.502	38.5	84.2	0.259	106.1	52.6
	338	68.1	0.141	3.8	0.334	7.1	28.9	0.486	34.2	73.2	0.327	102.0	57.2
	353	67.4	0.147	3.9	0.340	7.0	28.8	0.508	31.5	73.3	0.328	100.8	58.3
$[C_4MIm]I$	293	72.6	0.007	6.3	0.089	7.9	32.4	0.093	46.9	48.0	0.131	97.8	50.7
	308	71.7	0.011	4.5	0.072	8.1	28.7	0.100	44.3	54.4	0.123	98.1	50.9
	323	70.6	0.017	3.7	0.068	7.9	26.7	0.107	42.1	60.9	0.115	98.5	51.2
	338	70.2	0.017	4.6	0.070	8.0	28.1	0.101	41.7	54.4	0.122	96.4	52.9
	353	69.4	0.021	4.1	0.069	7.9	26.8	0.103	39.7	56.0	0.119	95.7	53.8

Intramolecular Vibrations

	T (K)	$a_{L,1}$	$\omega_{L,1}$ (cm^{-1})	$\Delta\omega_{L,1}$ (cm^{-1})	$a_{L,2}$	$\omega_{L,2}$ (cm^{-1})	$\Delta\omega_{L,2}$ (cm^{-1})
$[C_4MIm][PF_6]$	293	40.0	167.1	27.6	20.1	215.5	24.3
	308	38.1	166.2	27.0	20.9	215.0	25.9
	323	42.1	165.3	28.3	22.6	215.6	27.0
	338	48.8	164.6	29.5	25.7	215.4	28.3
	353	47.5	164.7	29.7	24.9	216.1	29.0
$[C_4MIm][BF_4]$	293	33.2	169.3	24.9	20.6	215.2	24.1
	308	30.7	169.2	24.6	23.2	214.9	25.9
	323	29.0	168.3	24.6	35.5	214.5	31.0
	338	27.2	169.0	24.1	34.2	214.4	30.8
	353	27.8	168.7	24.7	37.1	214.5	32.6
$[C_4MIm]I$	293	16.0	164.6	29.0	6.9	212.5	22.5
	308	15.8	164.6[a]	29.0[a]	6.8	212.5[a]	22.5[a]
	323	15.8	164.6[a]	29.0[a]	6.7	212.5[a]	22.5[a]
	338	16.0	164.6[a]	29.0[a]	6.7	212.5[a]	22.5[a]
	353	15.7	164.6[a]	29.0[a]	6.6	212.5[a]	22.5[a]

[a] Fixed to achieve reasonable fit parameters.

Intermolecular Vibrations

	T (K)	M_1 (cm^{-1})	$a_{O,1}$	$\omega_{O,1}$ (cm^{-1})	$a_{G,1}$	$\omega_{G,1}$ (cm^{-1})	$\Delta\omega_{G,1}$ (cm^{-1})	$a_{G,2}$	$\omega_{G,2}$ (cm^{-1})	$\Delta\omega_{G,2}$ (cm^{-1})	$a_{G,3}$	$\omega_{G,3}$ (cm^{-1})	$\Delta\omega_{G,3}$ (cm^{-1})
$[C_6MIm][PF_6]$	293	73.4	0.048	6.4	0.223	7.8	34.3	0.745	29.7	121.7	0.045	93.1	32.7
	308	72.4	0.058	6.1	0.215	8.6	34.4	0.716	31.3	120.5	0.036	92.5	30.8
	323	71.7	0.067	6.0	0.238	8.3	34.8	0.747	30.6	120.4	0.028	91.6	28.1
	338	71.0	0.069	6.4	0.226	8.4	36.2	0.812	28.1	120.7	0.022	90.1	26.9
	353	69.9	0.091	5.9	0.292	8.0	34.8	0.850	27.2	120.0	0.015	90.4	22.7
$[C_7MIm][PF_6]$	293	71.4	0.043	6.9	0.158	9.6	34.4	0.754	25.0	117.7	0.056	100.7	42.3
	308	70.6	0.050	6.7	0.166	9.6	35.1	0.760	25.2	117.5	0.047	100.6	41.3
	323	69.7	0.058	6.2	0.180	9.8	34.7	0.766	25.4	117.1	0.039	101.0	39.7
	338	69.2	0.064	6.2	0.191	9.7	35.3	0.771	25.6	117.1	0.032	101.3	37.6
	353	68.0	0.073	5.8	0.209	9.6	35.3	0.775	25.7	116.0	0.026	102.2	36.4

Intramolecular Vibrations

	T (K)	$a_{L,1}$	$\omega_{L,1}$ (cm^{-1})	$\Delta\omega_{L,1}$ (cm^{-1})	$a_{L,2}$	$\omega_{L,2}$ (cm^{-1})	$\Delta\omega_{L,2}$ (cm^{-1})
$[C_6MIm][PF_6]$	293	28.1	215.9	33.4	26.8	272.4	27.1
	308	29.8	215.9[a]	33.4[a]	27.0	272.4[a]	27.1[a]
	323	32.3	215.9[a]	33.4[a]	27.4	272.4[a]	27.1[a]
	338	36.4	215.9[a]	33.4[a]	27.4	272.4[a]	27.1[a]
	353	35.6	215.9[a]	33.4[a]	27.9	272.4[a]	27.1[a]
$[C_7MIm][PF_6]$	293	86.7	205.9	55.4	9.4	272.3	18.6
	308	89.7	205.9[a]	55.4[a]	9.2	272.3[a]	18.6[a]
	323	85.6	205.9[a]	55.4[a]	8.7	272.3[a]	18.6[a]
	338	86.3	205.9[a]	55.4[a]	8.8	272.3[a]	18.6[a]
	353	83.0	205.9[a]	55.4[a]	9.0	272.3[a]	18.6[a]

[a] Fixed to achieve reasonable fit parameters.

Table C.5.2. Lower Symmetric Anions

Intermolecular Vibrations

	T (K)	M_1 (cm^{-1})	$a_{O,1}$	$\omega_{O,1}$ (cm^{-1})	$a_{O,2}$	$\omega_{O,2}$ (cm^{-1})	$a_{G,1}$	$\omega_{G,1}$ (cm^{-1})	$\Delta\omega_{G,1}$ (cm^{-1})	$a_{G,2}$	$\omega_{G,2}$ (cm^{-1})	$\Delta\omega_{G,2}$ (cm^{-1})	$a_{G,3}$	$\omega_{G,3}$ (cm^{-1})	$\Delta\omega_{G,3}$ (cm^{-1})
[C_4MIm][OTf]	293	71.6	0.057	5.1			0.221	8.3	32.4	0.325	57.6	79.3	0.180	109.2	44.8
	308	70.7	0.062	5.1			0.226	8.1	32.2	0.333	56.0	79.8	0.177	108.6	45.4
	323	69.6	0.078	4.5			0.234	8.0	30.6	0.342	51.9	82.4	0.176	107.4	46.5
	338	68.7	0.087	4.4			0.249	7.4	29.7	0.356	46.5	82.1	0.192	105.9	48.8
	353	67.9	0.090	4.5			0.254	7.2	30.0	0.363	44.7	82.2	0.191	105.2	49.6
[C_4MIm][SCN]	293	70.7	0.076	5.3			0.281	8.8	35.0	0.483	49.6	81.8	0.187	115.6	58.0
	308	70.0	0.088	5.2			0.293	8.4	34.3	0.487	46.0	80.7	0.204	113.3	60.8
	323	69.3	0.095	5.2			0.301	8.2	34.1	0.493	435.	80.1	0.211	111.6	62.3
	338	68.6	0.106	5.1			0.299	8.2	33.2	0.489	39.7	77.3	0.235	108.1	65.4
	353	68.3	0.115	4.9			0.308	7.9	32.6	0.478	37.0	75.0	0.251	105.2	68.2
[C_4MIm][DCA]	293	71.7	0.167	3.8			0.316	8.9	27.4	0.684	30.6	72.1	0.465	102.2	67.9
	308	71.1	0.191	3.7			0.336	8.5	27.0	0.572	31.2	63.1	0.511	96.6	72.8
	323	70.4	0.208	3.7			0.368	7.9	27.0	0.507	30.5	58.6	0.529	92.3	76.8
	338	69.9	0.228	3.7			0.338	8.5	25.8	0.538	25.5	59.7	0.537	89.6	80.0
	353	69.5	0.241	3.7			0.367	8.0	26.1	0.477	25.8	56.6	0.550	86.1	84.0
[C_4MIm][NCyF]	293	67.6	0.060	2.0	0.050	11.4	0.172	31.3	36.8	0.106	59.4	28.3	0.307	95.8	53.2
	308	66.1	0.170	1.4	0.064	7.6	0.259	24.0	38.9	0.121	56.8	29.2	0.306	94.8	54.4
	323	65.1	0.210	1.3	0.075	6.7	0.287	21.5	38.7	0.131	55.7	29.8	0.306	93.9	55.3
	338	64.4	0.217	1.4	0.083	6.8	0.287	22.0	38.5	0.121	55.6	29.4	0.308	92.3	57.2
	353	63.6	0.193	1.6	0.081	7.5	0.288	22.6	43.2	0.092	56.9	28.3	0.309	91.2	58.0

Intramolecular Vibrations

	T (K)	$a_{L,1}$	$\omega_{L,1}$ (cm^{-1})	$\Delta\omega_{L,1}$ (cm^{-1})	$a_{L,2}$	$\omega_{L,2}$ (cm^{-1})	$\Delta\omega_{L,2}$ (cm^{-1})
[C_4MIm][OTf]	293	34.5	168.0	27.7	6.7	213.3	12.7
	308	33.5	167.5	27.5	8.1	213.5	14.1
	323	39.0	167.2	29.8	8.2	214.0	14.3
	338	37.8	166.8	29.2	9.0	213.9	15.3
	353	39.5	166.2	29.9	9.9	214.2	16.2
[C_4MIm][SCN]	293	13.3	174.6	21.4	26.2	212.6	28.5
	308	11.9	174.1	21.0	36.5	2112.4	32.0
	323	11.4	173.6	21.1	37.2	212.0	32.7
	338	9.3	173.4	20.7	43.2	211.3	35.3
	353	8.1	173.2	20.4	41.4	210.9	35.5
[C_4MIm][DCA]	293	99.9	182.4	14.0	21.6	218.5	23.3
	308	100.2	182.3	14.3	21.0	218.3	23.2
	323	98.6	182.2	14.5	23.0	218.2	24.8
	338	98.7	182.1	14.7	20.9	218.0	24.0
	353	99.3	182.0	14.9	24.5	218.9	25.7
[C_4MIm][NCyF]	293	7.5	72.9	14.7	11.4	169.6	11.1
	308	8.6	72.9[a]	14.7[a]	12.9	169.9	11.9
	323	8.1	72.9[a]	14.7[a]	15.2	170.1	12.9
	338	7.0	72.9[a]	14.7[a]	16.8	170.1	13.6
	353	6.5	72.9[a]	14.7[a]	19.8	170.3	14.7

[a] Fixed to achieve reasonable fit parameters.

Table C.5.3. Anions Having Conformers

Intermolecular Vibrations

	T (K)	M_1 (cm^{-1})	$a_{O,1}$	$\omega_{O,1}$ (cm^{-1})	$a_{G,1}$	$\omega_{G,1}$ (cm^{-1})	$\Delta\omega_{G,1}$ (cm^{-1})	$a_{G,2}$	$\omega_{G,2}$ (cm^{-1})	$\Delta\omega_{G,2}$ (cm^{-1})	$a_{G,3}$	$\omega_{G,3}$ (cm^{-1})	$\Delta\omega_{G,3}$ (cm^{-1})
$[C_4MIm][NF_2]$	293	64.6	0.110	4.3	0.382	7.9	32.9	0.386	43.9	78.8	0.213	105.6	46.1
	308	63.5	0.125	4.2	0.407	7.4	32.0	0.401	40.5	76.7	0.225	104.0	47.7
	323	62.8	0.139	4.1	0.436	6.5	30.9	0.405	36.6	71.3	0.251	101.4	50.9
	338	61.9	0.150	4.1	0.413	6.9	30.3	0.409	35.1	69.0	0.259	99.8	52.4
	353	61.3	0.148	4.4	0.393	7.4	30.7	0.428	33.6	72.3	0.242	100.0	52.3
$[C_4MIm][NTf_2]$	293	66.3	0.083	4.5	0.309	7.9	29.2	0.273	41.7	54.3	0.287	97.1	55.9
	308	65.4	0.091	4.6	0.291	8.0	28.6	0.290	40.2	59.0	0.271	97.5	56.0
	323	64.6	0.104	4.4	0.282	8.0	27.5	0.302	36.4	61.0	0.270	96.0	57.7
	338	64.0	0.115	4.4	0.277	8.1	27.1	0.304	33.3	60.2	0.279	93.7	60.1
	353	63.3	0.129	4.2	0.287	7.9	26.5	0.285	31.0	55.6	0.294	89.8	63.8
$[C_4MIm][NPf_2]$	293	63.1	0.079	4.0	0.185	7.0	21.2	0.185	17.4	39.7	0.311	70.8	79.6
	308	62.5	0.093	3.8	0.195	6.8	20.9	0.192	16.6	39.3	0.314	69.4	80.8
	323	61.3	0.107	3.9	0.206	6.8	21.4	0.191	17.5	39.5	0.316	68.9	79.9
	338	60.6	0.118	3.9	0.214	6.6	21.2	0.199	17.2	39.7	0.320	68.2	80.0
	353	60.4	0.130	3.9	0.207	6.9	20.8	0.195	17.1	38.3	0.328	65.9	83.3

Intramolecular Vibrations

	T (K)	$a_{L,1}$	$\omega_{L,1}$ (cm^{-1})	$\Delta\omega_{L,1}$ (cm^{-1})	$a_{L,2}$	$\omega_{L,2}$ (cm^{-1})	$\Delta\omega_{L,2}$ (cm^{-1})	$a_{L,3}$	$\omega_{L,3}$ (cm^{-1})	$\Delta\omega_{L,3}$ (cm^{-1})	$a_{L,4}$	$\omega_{L,4}$ (cm^{-1})	$\Delta\omega_{L,4}$ (cm^{-1})
$[C_4MIm][NF_2]$	293	28.7	164.7	6.2	7.8	213.3	18.9						
	308	29.7	164.3	6.2	7.2	213.1	19.2						
	323	25.4	164.3	6.4	6.9	212.9	19.4						
	338	25.3	164.1	6.5	6.4	212.0	19.8						
	353	31.2	164.0	6.7	7.2	212.6	21.6						
$[C_4MIm][NTf_2]$	293	3.2	121.8	6.2	15.7	170.4	16.1	17.4	211.2	19.5			
	308	3.0	121.8	6.2	16.5	170.3	16.6	15.4	211.0	19.2			
	323	3.0	121.9	6.4	16.3	170.2	16.8	15.6	211.1	19.9			
	338	2.9	121.8	6.5	16.8	170.1	17.0	18.7	210.8	21.5			
	353	2.9	121.7	6.7	15.8	170.5	16.4	23.4	210.4	23.3			
$[C_4MIm][NPf_2]$	293	25.2	106.6	13.3	0.22	155.7	4.8	20.4	174.2	23.9	3.4	212.4	11.8
	308	23.4	106.3	13.4	0.25	155.6	5.3	20.9	173.2	23.8	3.4	212.3	12.3
	323	21.9	106.2	13.2	0.07	155.5	3.6	28.0	171.9	27.3	3.7	212.4	13.0
	338	21.2	105.9	13.4	0.08	155.6	3.7	32.4	171.3	28.2	3.9	212.9	13.6
	353	20.0	105.6	13.4	0.11	155.0	4.4	28.2	171.6	26.2	6.8	212.6	16.3

Table C.5.4. Molecular Liquids

Intermolecular Vibrations & Intramolecular Vibrations

	T (K)	M_1 (cm^{-1})	$a_{O,1}$	$\omega_{O,1}$ (cm^{-1})	$a_{O,2}$	$\omega_{O,2}$ (cm^{-1})	$a_{G,1}$	$\omega_{G,1}$ (cm^{-1})	$\Delta\omega_{G,1}$ (cm^{-1})	$a_{G,2}$	$\omega_{G,2}$ (cm^{-1})	$\Delta\omega_{G,2}$ (cm^{-1})	$a_{L,1}$	$\omega_{L,1}$ (cm^{-1})	$\Delta\omega_{L,1}$ (cm^{-1})
1-Methylimidazole	293	69.0	0.230	2.4	0.111	8.1	0.251	19.5	45.6	0.683	73.4	86.9	33.7	222.2	17.4
	308	68.1	0.222	2.5	0.116	8.2	0.214	21.1	42.4	0.691	70.3	89.2	30.5	221.6	17.0
	323	67.3	0.197	2.8	0.113	9.1	0.138	26.3	36.1	0.707	66.6	91.9	31.1	220.8	17.4
	338	66.5	0.197	3.0	0.113	9.6	0.106	27.1	34.0	0.727	62.6	95.0	34.3	220.0	18.4
	353	65.6	0.169	3.2	0.118	9.2	0.126	25.1	34.7	0.746	59.2	96.8	33.2	219.0	18.4
Propionitrile	293	56.8	0.326	3.2	0.107	11.5	1.194	21.1	87.2	0.365	17.2	172.2			
	308	52.3	0.550	2.9	0.145	10.5	1.120	19.5	81.6	0.656	15.1	137.9			
	323	51.8	0.586	3.1	0.150	11.0	1.145	19.6	81.3	0.655	15.1	142.5			
	338	51.2	0.598	3.4	0.150	11.6	1.245	18.8	82.9	0.602	13.8	153.1			
	353	49.3	0.575	3.7	0.148	12.3	1.072	20.5	80.2	0.652	14.8	139.6			
CCl_4	293	39.4	0.033	5.7			0.224	12.0	49.9	0.039	45.7	81.8	27.3	218.3	4.8
	308	37.9	0.034	5.8			0.251	11.2	49.8	0.036	46.5	77.4	29.9	218.2	5.2
	323	37.9	0.037	5.6			0.271	10.7	49.1	0.039	43.5	81.0	32.9	218.2	5.7
	338	36.6	0.039	5.9			0.261	10.4	47.9	0.046	43.8	71.3	35.1	218.1	6.1

D Appendix to Chapter 4.

D.1. Examples of Line Shape Analysis Results for Low-Frequency Spectra of Ionic Liquids.

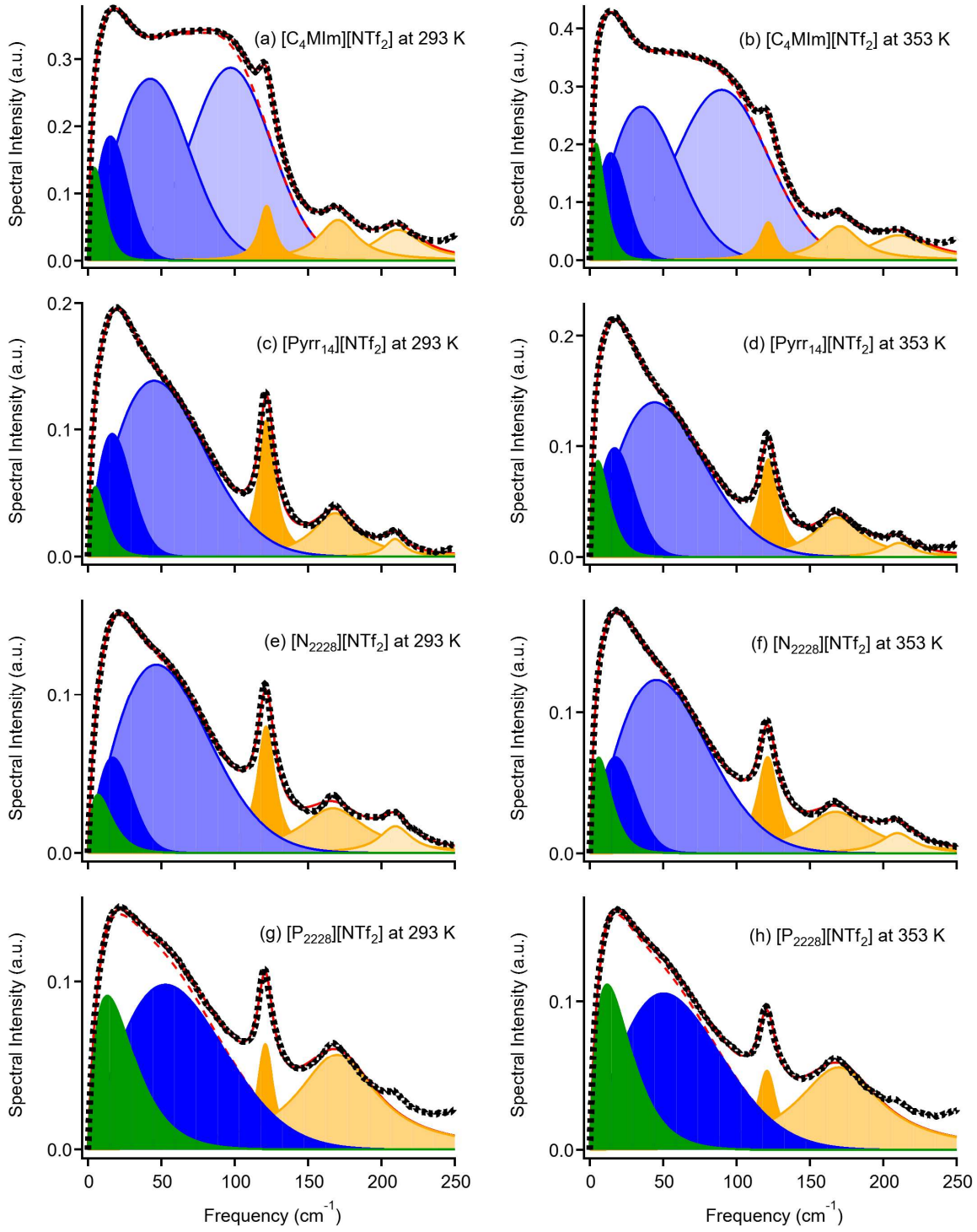

Figure D.1. Line shape analysis results of the low-frequency spectra of (a)(b) $[C_4MIm][NTf_2]$, (c)(d) $[Pyrr_{14}][NTf_2]$, (e)(f) $[N_{2228}][NTf_2]$, and (g)(h) $[P_{2228}][NTf_2]$ at each temperature. Black

dots denote the experimentally obtained data. Green, blue, and orange areas denote Ohmic, antisymmetrized Gaussian, and Lorentzian functions, respectively. Red lines denote the entire fit. Dashed red lines denote the sum of the Ohmic and the antisymmetrized Gaussian functions.

D.2. Kerr Transients of Molecular Liquids.

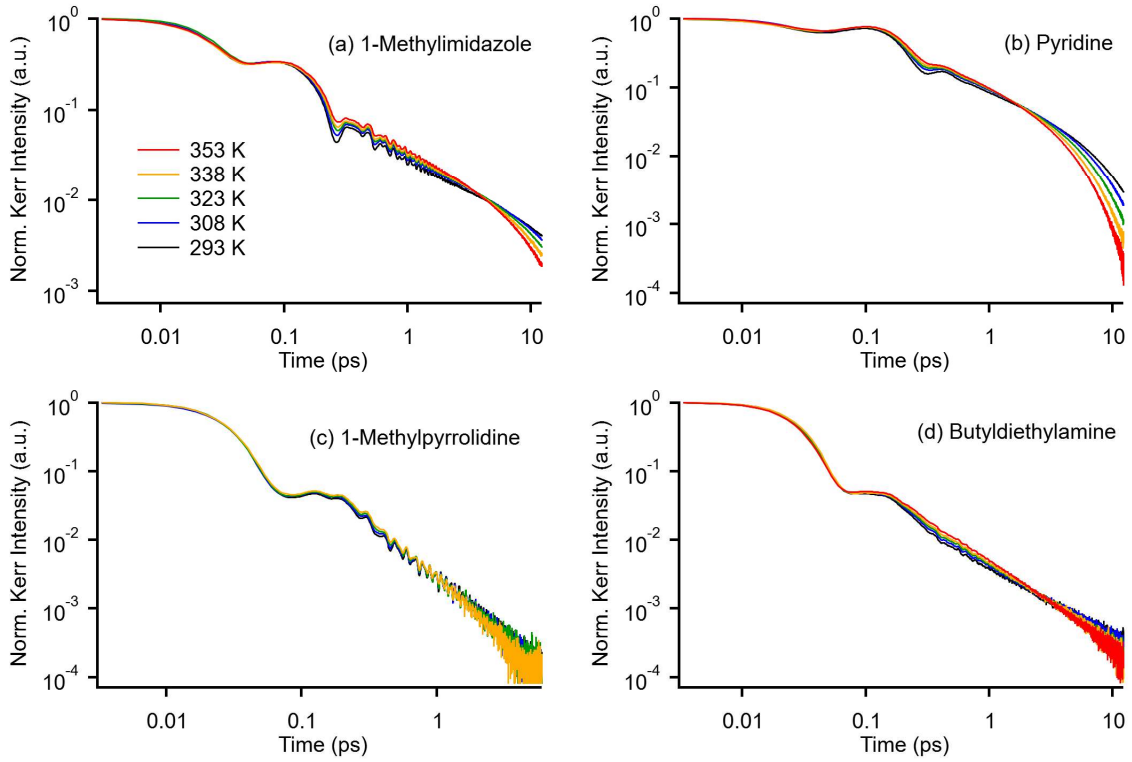

Figure D.2. Log–log plots of Kerr transients for (a) 1-methylimidazole, (b) pyridine, (c) 1-methylpyrrolidine, and (d) butyldiethylamine at 293 K (black), 308 K (blue), 323 K (green), 338 K (yellow), and 353 K (red).

Table D.3. Biexponential Fit Parameters for Kerr Transients of Molecular Liquids at Various Temperatures

temperature (K)	a_1	τ_1 (ps)	a_2	τ_2 (ps)
	1-methylimidazole			
293	0.0176	1.82	0.0124	10.84
308	0.0198	1.72	0.0145	8.87
323	0.0205	1.59	0.0166	7.21
338	0.0232	1.47	0.0181	6.14
353	0.0270	1.33	0.0209	5.10
	pyridine			
293	0.0605	1.36	0.0506	4.32
308	0.0661	1.23	0.0616	3.55
323	0.0822	0.999	0.0736	2.94
338	0.0832	0.968	0.0826	2.49
353	0.104	0.758	0.0985	2.12
	1-methylpyrrolidine			
293	0.0021	2.10		
308	0.0020	1.95		
323	0.0019	2.00		
338	0.0017	1.85		
353	-	-		
	butyldiethylamine			
293	0.0032	1.62	0.0011	8.78
308	0.0033	1.55	0.0013	7.90
323	0.0036	1.60	0.0012	7.01
338	0.0033	1.64	0.0016	6.51
353	0.0059	1.24	0.0013	6.21

D.4. Fit Parameters and First Moments M_1 for Low-Frequency Kerr Spectra

Table D.4.1. Fit Parameters and First Moments M_1 for Low-Frequency Kerr Spectra of Ionic Liquids

Intermolecular Vibrations

	T (K)	M_1 (cm^{-1})	$a_{O,1}$	$\omega_{O,1}$ (cm^{-1})	$a_{G,1}$	$\omega_{G,1}$ (cm^{-1})	$\Delta\omega_{G,1}$ (cm^{-1})	$a_{G,2}$	$\omega_{G,2}$ (cm^{-1})	$\Delta\omega_{G,2}$ (cm^{-1})	$a_{G,3}$	$\omega_{G,3}$ (cm^{-1})	$\Delta\omega_{G,3}$ (cm^{-1})
$[C_4MIm][NTf_2]$	293	66.3	0.083	4.5	0.309	7.9	29.2	0.273	41.7	54.3	0.287	97.1	55.9
	308	65.4	0.091	4.6	0.291	8.0	28.6	0.290	40.2	59.0	0.271	97.5	56.0
	323	64.6	0.104	4.4	0.282	8.0	27.5	0.302	36.4	61.0	0.270	96.0	57.7
	338	64.0	0.115	4.4	0.277	8.1	27.1	0.304	33.3	60.2	0.279	93.7	60.1
	353	63.3	0.129	4.2	0.287	7.9	26.5	0.285	31.0	55.6	0.294	89.8	63.8
$[Pyrr_{14}][NTf_2]$	293	68.1	0.030	5.0	0.152	9.1	31.2	0.180	31.0	81.4			
	308	67.3	0.033	5.1	0.161	8.7	31.5	0.192	28.6	81.9			
	323	66.5	0.036	5.4	0.165	8.5	31.9	0.195	28.0	81.9			
	338	65.8	0.043	5.0	0.179	8.3	31.7	0.198	27.6	81.5			
	353	65.1	0.043	5.5	0.178	8.0	32.5	0.202	26.8	81.8			
$[C_4Py][NTf_2]$	293	46.6	0.112	5.0	0.488	10.6	32.2	0.295	43.8	36.6	0.577	91.0	55.5
	308	45.9	0.128	4.8	0.473	10.3	31.0	0.300	41.9	37.2	0.573	89.9	56.9
	323	45.4	0.149	4.5	0.421	9.5	28.6	0.328	38.2	40.0	0.563	89.0	58.2
	338	44.7	0.158	4.6	0.432	9.9	29.1	0.312	38.4	38.8	0.559	87.9	59.3
	353	44.4	0.178	4.4	0.379	9.2	27.0	0.339	34.4	41.6	0.551	86.8	60.8
$[N_{1224}][NTf_2]$	293	49.9	0.022	5.2	0.126	9.8	29.7	0.193	29.6	86.9			
	308	48.9	0.029	4.8	0.137	9.5	29.6	0.192	29.9	85.6			
	323	48.6	0.030	5.6	0.132	9.4	30.8	0.199	28.5	86.4			
	338	48.1	0.033	5.6	0.138	9.3	30.9	0.194	29.6	85.6			
	353	47.1	0.040	5.4	0.149	8.9	31.4	0.200	28.5	85.1			

Intramolecular Vibrations

	T (K)	$a_{L,1}$	$\omega_{L,1}$ (cm^{-1})	$\Delta\omega_{L,1}$ (cm^{-1})	$a_{L,2}$	$\omega_{L,2}$ (cm^{-1})	$\Delta\omega_{L,2}$ (cm^{-1})	$a_{L,3}$	$\omega_{L,3}$ (cm^{-1})	$\Delta\omega_{L,3}$ (cm^{-1})
$[C_4MIm][NTf_2]$	293	3.2	121.8	6.2	15.7	170.4	16.1	17.4	211.2	19.5
	308	3.0	121.8	6.2	16.5	170.3	16.6	15.4	211.0	19.2
	323	3.0	121.9	6.4	16.3	170.2	16.8	15.6	211.1	19.9
	338	2.9	121.8	6.5	16.8	170.1	17.0	18.7	210.8	21.5
	353	2.9	121.7	6.7	15.8	170.5	16.4	23.4	210.4	23.3
$[Pyrr_{14}][NTf_2]$	293	4.9	121.7	6.8	12.0	168.4	18.7	0.9	209.3	8.1
	308	5.1	121.7	7.0	11.2	168.2	18.1	1.1	209.7	9.0
	323	5.0	121.7	7.2	13.5	168.1	19.8	0.9	209.5	8.6
	338	5.3	121.7	7.5	12.6	169.0	19.2	0.7	209.7	8.0
	353	5.5	121.7	7.9	14.8	168.7	20.4	1.9	210.9	12.1
$[C_4Py][NTf_2]$	293	1.6	122.5	5.0	23.2	171.8	17.0	9.9	215.0	15.8
	308	1.5	122.5	5.0	23.4	171.6	17.1	8.3	214.8	15.2
	323	1.4	122.4	5.0	24.1	171.3	17.4	11.5	214.6	17.6
	338	1.6	122.5	5.3	24.2	171.0	17.7	8.6	214.1	16.3
	353	1.4	122.4	5.2	26.3	171.1	18.3	12.2	214.3	18.5
$[N_{1224}][NTf_2]$	293	5.5	121.7	7.0	14.8	166.7	20.4	1.7	210.9	10.6
	308	5.7	121.7	7.3	16.8	166.7	21.4	2.0	211.4	11.5
	323	5.7	121.6	7.5	19.3	166.6	22.8	1.8	211.2	11.6
	338	5.9	121.6	7.8	17.4	166.6	22.0	1.8	211.8	11.7
	353	6.3	121.6	8.1	20.5	166.7	23.2	1.6	211.6	11.3

Table D.4.2. Fit Parameters and First Moments M_1 for Low-Frequency Kerr Spectra of Ionic Liquids Intermolecular Vibrations and Intramolecular Vibrations

	T (K)	M_1 (cm^{-1})	$a_{O,1}$	$\omega_{O,1}$ (cm^{-1})	$a_{G,1}$	$\omega_{G,1}$ (cm^{-1})	$\Delta\omega_{G,1}$ (cm^{-1})	$a_{G,2}$	$\omega_{G,2}$ (cm^{-1})	$\Delta\omega_{G,2}$ (cm^{-1})
$[N_{2228}][NTf_2]$	293	49.9	0.015	6.8	0.085	10.4	31.3	0.159	31.2	84.7
	308	49.0	0.018	6.7	0.091	10.0	31.6	0.164	30.4	84.2
	323	48.2	0.024	6.2	0.084	11.8	31.2	0.157	32.2	82.5
	338	47.7	0.027	6.2	0.109	9.0	32.9	0.185	26.6	85.3
	353	47.1	0.031	6.0	0.117	8.7	33.3	0.190	25.7	85.3
$[P_{2228}][NTf_2]$	293	54.3	0.019	13.1	0.120	39.1	93.0			
	308	53.7	0.021	12.6	0.133	35.6	94.4			
	323	52.8	0.023	12.3	0.137	34.2	93.8			
	338	51.9	0.024	12.1	0.144	31.9	93.6			
	353	51.3	0.026	11.8	0.157	29.5	93.8			

	T (K)	$a_{L,1}$	$\omega_{L,1}$ (cm^{-1})	$\Delta\omega_{L,1}$ (cm^{-1})	$a_{L,2}$	$\omega_{L,2}$ (cm^{-1})	$\Delta\omega_{L,2}$ (cm^{-1})	$a_{L,3}$	$\omega_{L,3}$ (cm^{-1})	$\Delta\omega_{L,3}$ (cm^{-1})
$[N_{2228}][NTf_2]$	293	4.3	121.4	7.3	20.2	166.9	26.8	3.0	209.5	13.2
	308	4.4	121.4	7.6	21.3	167.0	27.0	2.7	209.7	13.3
	323	4.6	121.3	7.9	21.8	167.1	27.4	2.4	209.6	12.9
	338	5.1	121.3	8.5	19.9	167.4	26.0	3.2	209.7	14.2
	353	5.0	121.2	8.6	21.7	167.5	27.2	2.9	209.6	14.2
$[P_{2228}][NTf_2]$	293	2.6	120.9	6.5	60.3	169.7	32.7			
	308	2.8	120.8	6.8	62.4	169.7	33.6			
	323	2.9	120.7	7.1	66.8	169.9	34.3			
	338	3.1	120.7	7.5	66.5	169.8	34.4			
	353	3.2	120.7	7.8	65.3	169.6	34.4			

Table D.4.3. Fit Parameters and First Moments M_1 for Low-Frequency Kerr Spectra of Molecular Liquids

	T (K)	M_1 (cm^{-1})	$a_{O,1}$	$\omega_{O,1}$ (cm^{-1})	$a_{O,2}$	$\omega_{O,2}$ (cm^{-1})	$a_{G,1}$	$\omega_{G,1}$ (cm^{-1})	$\Delta\omega_{G,1}$ (cm^{-1})	$a_{G,2}$	$\omega_{G,2}$ (cm^{-1})	$\Delta\omega_{G,2}$ (cm^{-1})	$a_{L,1}$	$\omega_{L,1}$ (cm^{-1})	$\Delta\omega_{L,1}$ (cm^{-1})
1-Methylimidazole	293	69.0	0.230	2.4	0.111	8.1	0.251	19.5	45.6	0.683	73.4	86.9	33.7	222.2	17.4
	308	68.1	0.222	2.5	0.116	8.2	0.214	21.1	42.4	0.691	70.3	89.2	30.5	221.6	17.0
	323	67.3	0.197	2.8	0.113	9.1	0.138	26.3	36.1	0.707	66.6	91.9	31.1	220.8	17.4
	338	66.5	0.197	3.0	0.113	9.6	0.106	27.1	34.0	0.727	62.6	95.0	34.3	220.0	18.4
	353	65.6	0.169	3.2	0.118	9.2	0.126	25.1	34.7	0.746	59.2	96.8	33.2	219.0	18.4
Pyridine	293	61.0	0.328	3.2	0.262	8.3	0.364	22.7	34.4	1.378	64.1	81.1			
	308	60.8	0.260	3.6	0.252	8.3	0.339	21.6	32.3	1.415	59.4	86.0			
	323	60.4	0.385	6.4			0.456	19.6	31.6	1.456	55.2	88.8			
	338	60.0	0.363	6.6			0.443	19.8	32.1	1.472	52.6	90.6			
	353	59.7	0.306	8.5			0.200	26.1	27.4	1.609	45.2	95.4			
1-Methylpyrrolidine	293	51.1	0.010	10.6	0.005	28.3	0.090	29.2	76.9	0.039	45.7	81.8			
	308	50.7	0.009	9.3	0.008	26.5	0.084	26.1	79.5	0.036	46.5	77.4			
	323	50.2	0.011	11.8	0.006	28.6	0.096	24.9	75.9	0.039	43.5	81.0			
	338	49.2	0.010	9.5	0.010	26.2	0.073	26.6	73.6	0.046	43.8	71.3			
Butyldiethylamine	293	58.8	0.033	3.1	0.014	13.1	0.102	40.2	78.2	0.021	106.7	78.9			
	308	58.1	0.030	3.4	0.015	13.1	0.093	39.3	72.2	0.030	95.3	85.0			
	323	57.0	0.035	3.1	0.018	12.4	0.103	37.9	74.1	0.027	99.0	83.8			
	338	55.7	0.035	3.2	0.020	12.6	0.106	36.3	75.7	0.026	98.6	84.6			
	353	55.5	0.034	4.0	0.019	14.5	0.070	42.5	66.1	0.038	82.5	96.0			

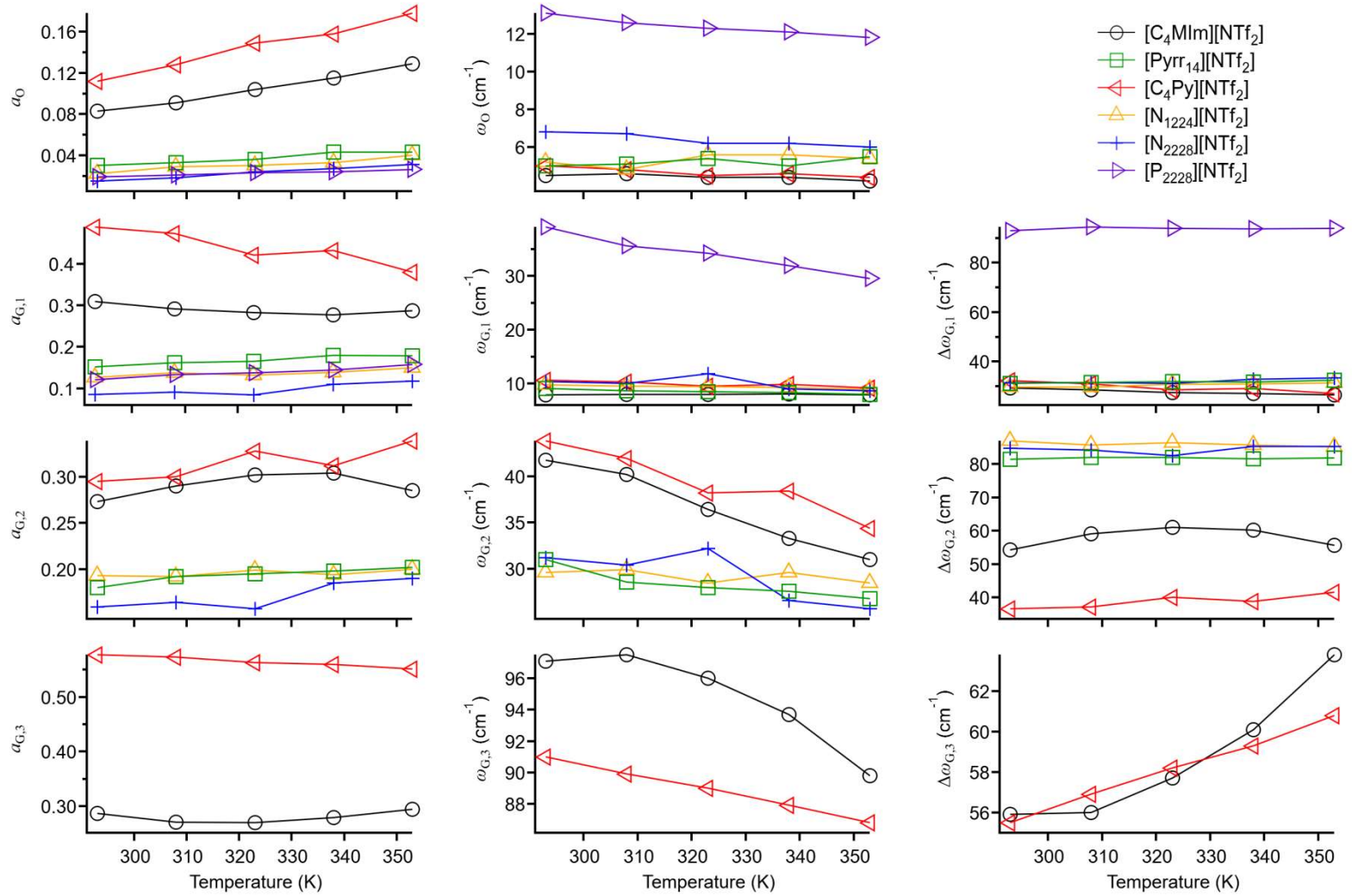

Figure D.5. Plots of Fit Parameters for Low-Frequency Kerr Spectra of Ionic Liquids vs Temperature.

D.6. Temperature-Dependent Viscosities for Ionic Liquids.

Table D.6.1. Measured Viscosities of Ionic Liquids at Various Temperatures

temp. (K)	viscosity (cP)					
	$[C_4MIm][NTf_2]$	$[Pyrr_{14}][NTf_2]$	$[C_4Py][NTf_2]$	$[N_{1224}][NTf_2]$	$[N_{2228}][NTf_2]$	$[P_{2228}][NTf_2]$
278	134	234	177	469	1055	384
283	98.5	171	129	313	686	270
288	76.6	127	96.0	225	465	197
293	62.3	97.1	73.4	161	313	146
298	48.4	75.4	57.8	119	227	110
303	38.7	56.0	45.7	87.1	168	83.8
308	32.0	48.2	37.0	69.1	126	67.7
313	26.7	39.3	30.3	54.5	95.5	54.0
318	22.6	32.6	25.5	43.4	73.9	43.0
323	19.2	27.5	21.6	35.1	58.0	35.0
328	16.5	23.4	18.5	29.2	47.0	29.3
333	14.3	20.0	15.9	24.6	38.0	24.6
338	12.4	17.4	13.8	20.7	31.3	20.9
343	11.0	15.0	12.1	17.8	26.4	17.9
348	9.59	13.2	10.6	15.3	22.3	15.4
353	8.58	11.7	9.50	13.2	18.9	13.3

E. Appendix to Chapter 5

Table E.1. Water Contents of Ionic Liquids

ILs	Water Content (ppm)
$[Pyrr_{1(1O2)}][PF_6]$	69
$[Pyrr_{1(1O2)}][BF_4]$	90
$[Pyrr_{14}][OTf]$	84
$[Pyrr_{14}][DCA]$	93
$[Pyrr_{14}][TCM]$	81
$[Pyrr_{14}][FAP]$	58
$[Pyrr_{14}][NTf_2]$	51
$[Pyrr_{14}][NF_2]$	81
$[Pyrr_{14}][NPf_2]$	76
$[Pyrr_{14}][NCyF]$	55
$[Pyrr_{1(1O2)}][NTf_2]$	80
$[Pyrr_{1(1O2)}][NF_2]$	84
$[Pyrr_{1(1O2)}][NCyF]$	68

Table E.2. Temperature-Dependent Viscosities of Ionic Liquids

Temperature (K)	Viscosity (cP)		
	$[Pyrr_{1(1O2)}][PF_6]$	$[Pyrr_{1(1O2)}][BF_4]$	$[Pyrr_{14}][OTf]$
278	-	608	623
283	-	428	427
288	-	305	306
293	753	232	227
298	546	186	171
303	422	141	132
308	321	112	102
313	250	88.2	81.6
318	195	71.6	64.6
323	156	58.8	53.0
328	124	48.6	43.5
333	100	40.1	36.0
338	78.3	33.9	30.7
343	65.2	29.1	26.4
348	54.8	25.2	22.7
353	46.1	21.8	19.7

Table E.2. Continued.

Temperature (K)	Viscosity (cP)		
	[$Pyrr_{14}$][DCA]	[$Pyrr_{14}$][TCM]	[$Pyrr_{14}$][FAP]
278	73.2	65.2	914
283	58.3	51.0	606
288	47.0	40.6	408
293	38.8	33.0	288
298	32.5	27.5	210
303	27.3	23.2	157
308	23.4	19.7	119
313	20.3	17.0	92.0
318	17.7	14.7	71.6
323	15.4	12.7	57.3
328	13.6	11.1	46.4
333	12.0	9.79	37.9
338	10.7	8.81	31.9
343	9.67	7.91	26.9
348	8.81	7.35	23.0
353	8.07	6.76	19.7

Table E.2. Continued.

Temperature (K)	Viscosity (cP)			
	$[Pyrr_{14}][NTf_2]$	$[Pyrr_{14}][NF_2]$	$[Pyrr_{14}][NPf_2]$	$[Pyrr_{14}][NCyF]$
278	234	117	1100	1557
283	171	93.1	736.0	1027
288	127	71.2	493.5	688
293	97.1	61.4	341.0	486
298	75.4	53.0	249.8	340
303	60.0	42.5	184.6	258
308	48.2	35.7	138.4	195
313	39.4	30.7	106.7	150
318	32.6	26.6	78.93	118
323	27.5	23.3	63.27	92.8
328	23.4	20.4	50.53	72.7
333	20.0	18.0	41.18	59.4
338	17.4	15.9	33.86	49.3
343	15.0	14.2	28.61	40.8
348	13.2	12.8	24.20	34.2
353	11.7	11.4	20.69	29.5

Table E.2. Continued

Temperature (K)	Viscosity (cP)		
	$[Pyrr_{1(1O2)}][NTf_2]$	$[Pyrr_{1(1O2)}][NF_2]$	$[Pyrr_{1(1O2)}][NCyF]$
278	153	89.7	895
283	110	72.2	617
288	82.6	58.9	429
293	64.0	47.9	308
298	51.5	39.5	228.
303	41.8	33.2	175
308	34.2	28.0	135
313	28.4	24.5	106
318	24.1	21.3	81.8
323	20.6	18.5	66.8
328	17.9	16.2	54.6
333	15.5	14.4	45.0
338	13.5	12.9	37.4
343	11.9	11.5	31.9
348	10.5	10.3	27.9
353	9.41	9.36	24.0

E.3. Atom Coordinates for 1-butyl-1-methylpyrrolidinium $[Pyrr_{14}]^+$ and 1-butyl-1(2-methoxy)ethylpyrrolidinium $[Pyrr_{1(1O2)}]^+$ cations calculated at the B3LYP/6-311+G(d,p) level of theory.

Table E.3.1. Atom Coordinates for $[Pyrr_{14}]^+$.

Center Number	Atomic Number	Coordinates (Angstroms) X	Y	Z
1	6	2.083636	0.358266	-0.931052
2	6	2.496172	-1.096625	-0.665244
3	6	1.951606	-1.428740	0.753102
4	6	1.320775	-0.128544	1.258029
5	7	0.907660	0.629518	0.003221
6	1	1.779738	0.572816	-1.954610
7	1	2.082217	-1.771555	-1.414448
8	1	2.739053	-1.751430	1.433694
9	1	2.052586	0.502543	1.764070
10	1	2.870140	1.057419	-0.645746
11	1	3.580596	-1.188216	-0.720041
12	1	1.217377	-2.234179	0.713674
13	1	0.459435	-0.251809	1.909502
14	6	-0.368701	0.058583	-0.624986
15	6	-1.643715	0.172513	0.204940
16	1	-0.154905	-0.985391	-0.853633
17	1	-0.482008	0.589585	-1.572275
18	6	-2.829331	-0.458471	-0.548693
19	1	-1.531243	-0.334443	1.168303
20	1	-1.878470	1.219824	0.415137
21	6	-4.139282	-0.356774	0.236638
22	1	-2.944978	0.034574	-1.520368
23	1	-2.607568	-1.510719	-0.759092
24	1	-4.959769	-0.811050	-0.321906
25	1	-4.068927	-0.871411	1.199077
26	1	-4.407949	0.685338	0.430667
27	6	0.752766	2.096720	0.269011
28	1	0.466559	2.597850	-0.655030
29	1	-0.012323	2.250865	1.025853
30	1	1.703269	2.491193	0.624154

Rotational constants (GHz): 2.2706254 0.6692996 0.6171179

Table E.3.2 Atom Coordinates for $[Pyrr_{1(1O2)}]^+$

Center Number	Atomic Number	Coordinates (Angstroms) X	Y	Z
1	6	-2.125883	0.753058	0.285819
2	6	-2.619422	-0.661842	0.599011
3	6	-1.746483	-1.600714	-0.281736
4	6	-0.754642	-0.686559	-1.011754
5	7	-0.676080	0.586024	-0.161487
6	1	-2.169733	1.457382	1.115453
7	1	-2.504514	-0.896092	1.657926
8	1	-2.342825	-2.152643	-1.007970
9	1	-1.139364	-0.368791	-1.981677
10	1	-2.656856	1.180326	-0.565437
11	1	-3.681302	-0.745244	0.369076
12	1	-1.226898	-2.340262	0.328025
13	1	0.249057	-1.084304	-1.128119
14	6	0.209119	0.383797	1.067785
15	6	1.712304	0.455822	0.839992
16	1	-0.056973	-0.584821	1.487432
17	1	-0.070811	1.160087	1.781876
18	1	2.026433	1.459535	0.521731
19	1	2.173626	0.276355	1.822392
20	6	3.530190	-0.636912	-0.228419
21	1	3.712729	-1.408939	-0.973241
22	1	3.971908	0.307553	-0.565252
23	1	3.983781	-0.933570	0.723143
24	6	-0.216935	1.761102	-0.969710
25	1	-0.165594	2.641683	-0.329899
26	1	0.760448	1.543040	-1.393547
27	1	-0.933365	1.931304	-1.771177
28	8	2.109166	-0.518910	-0.095782
Rotational constants (GHz):		2.2924049	0.8153283	0.7429142

E.4. Kerr Transients, Fourier Transform Spectra, and Differential Spectra for Purrolidinium-Based Ionic Liquids.

Figure E.4.1. 1-(2-Methoxyethyl)-1-methylpyrrolidinium hexafluorophosphate ([$Pyrr_{1(1O2)}$][PF_6]).

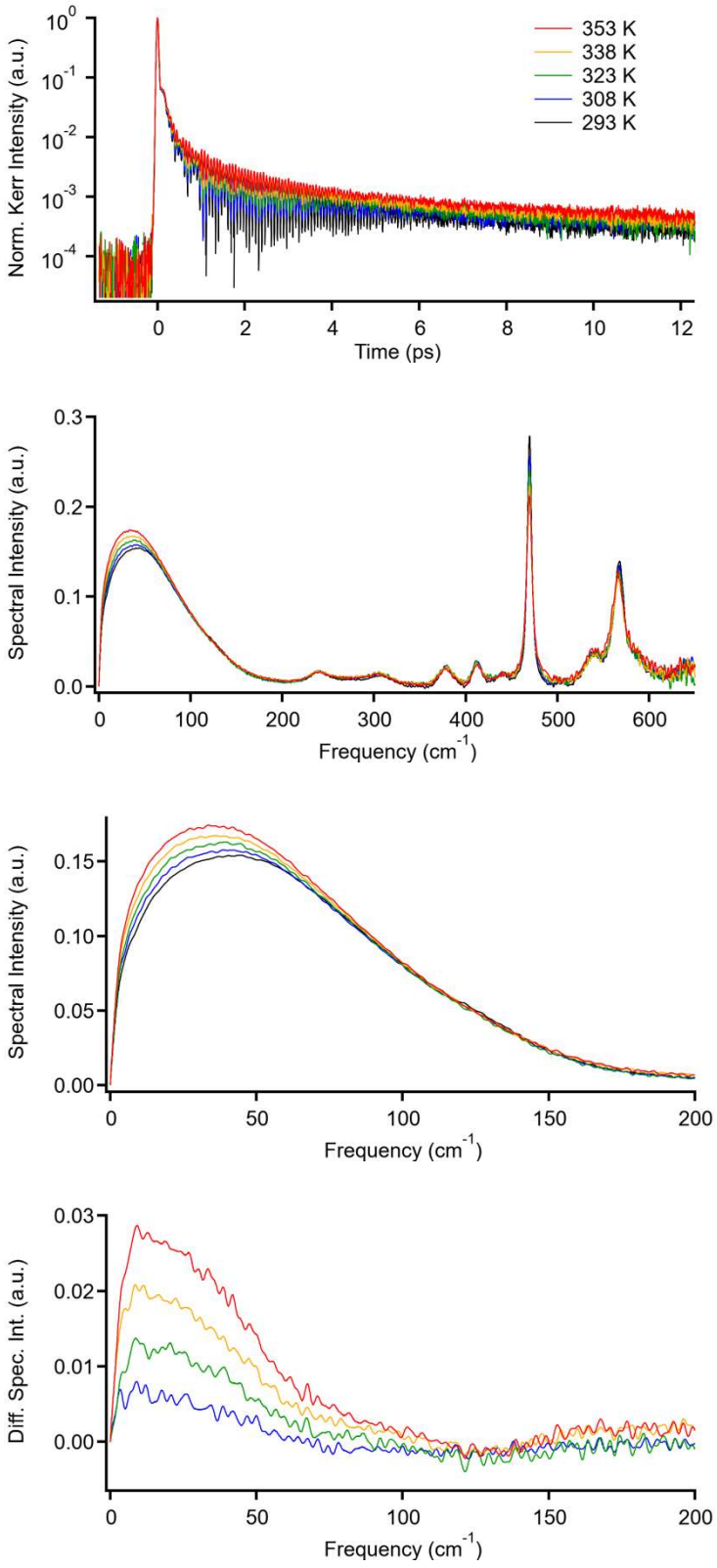

Figure E.4.2. 1-(2-Methoxyethyl)-1-methylpyrrolidinium tetrafluoroborate ([$Pyrr_{1(1O2)}$][BF_4]).

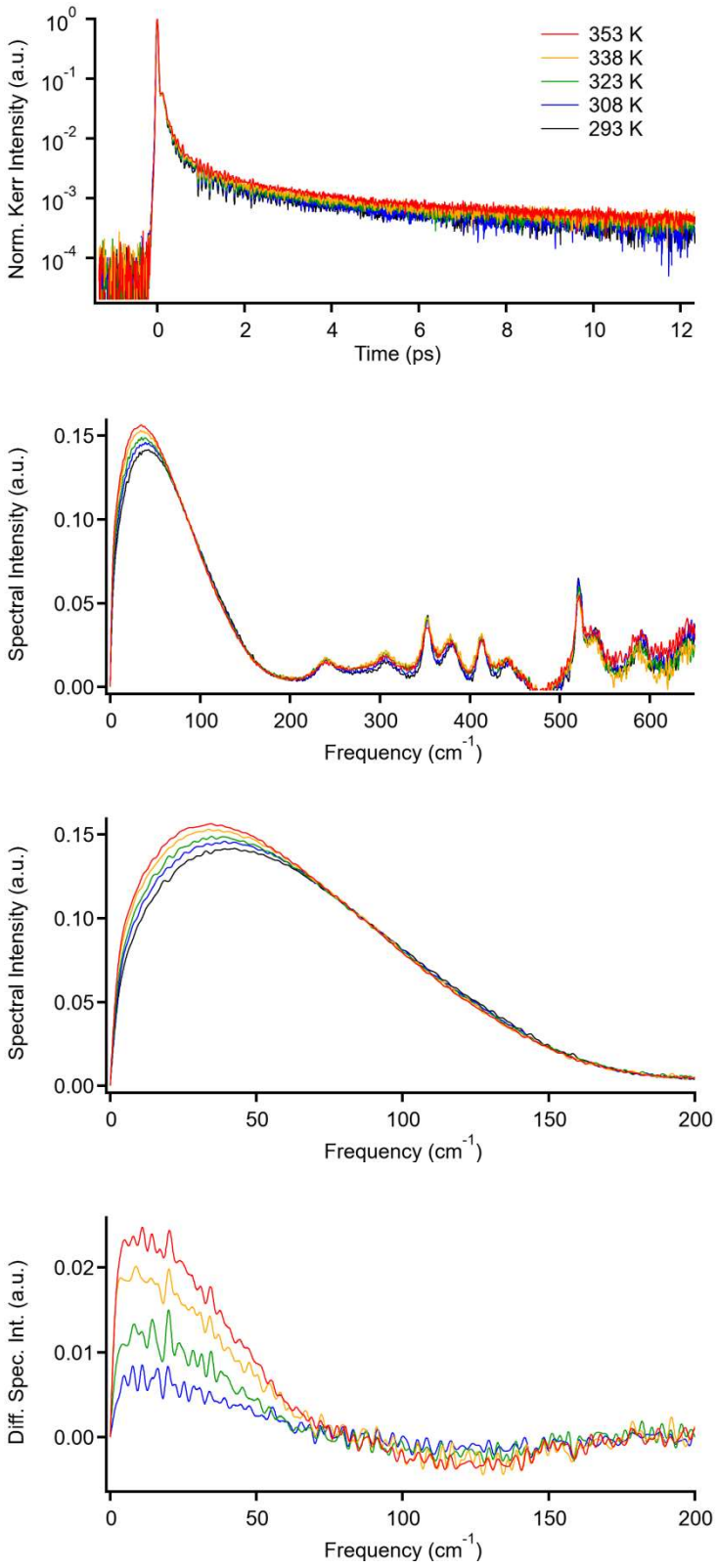

Figure E.4.3. 1-Butyl-1-methylpyrrolidinium trifluoromethanesulfonate ([$Pyrr_{14}$][OTf]).

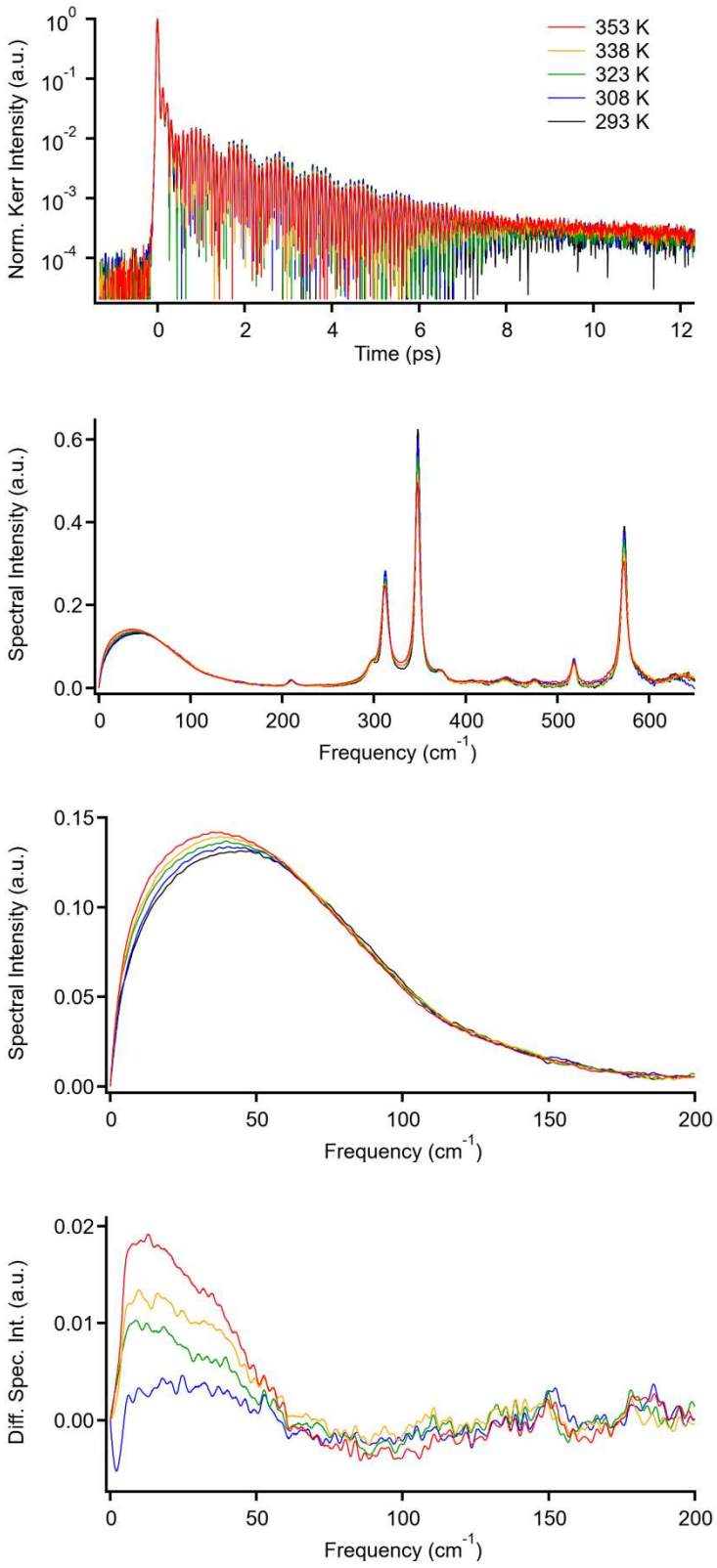

Figure E.4.4. 1-Butyl-1-methylpyrrolidinium dicyanamide ([Pyrr$_{14}$][DCA]).

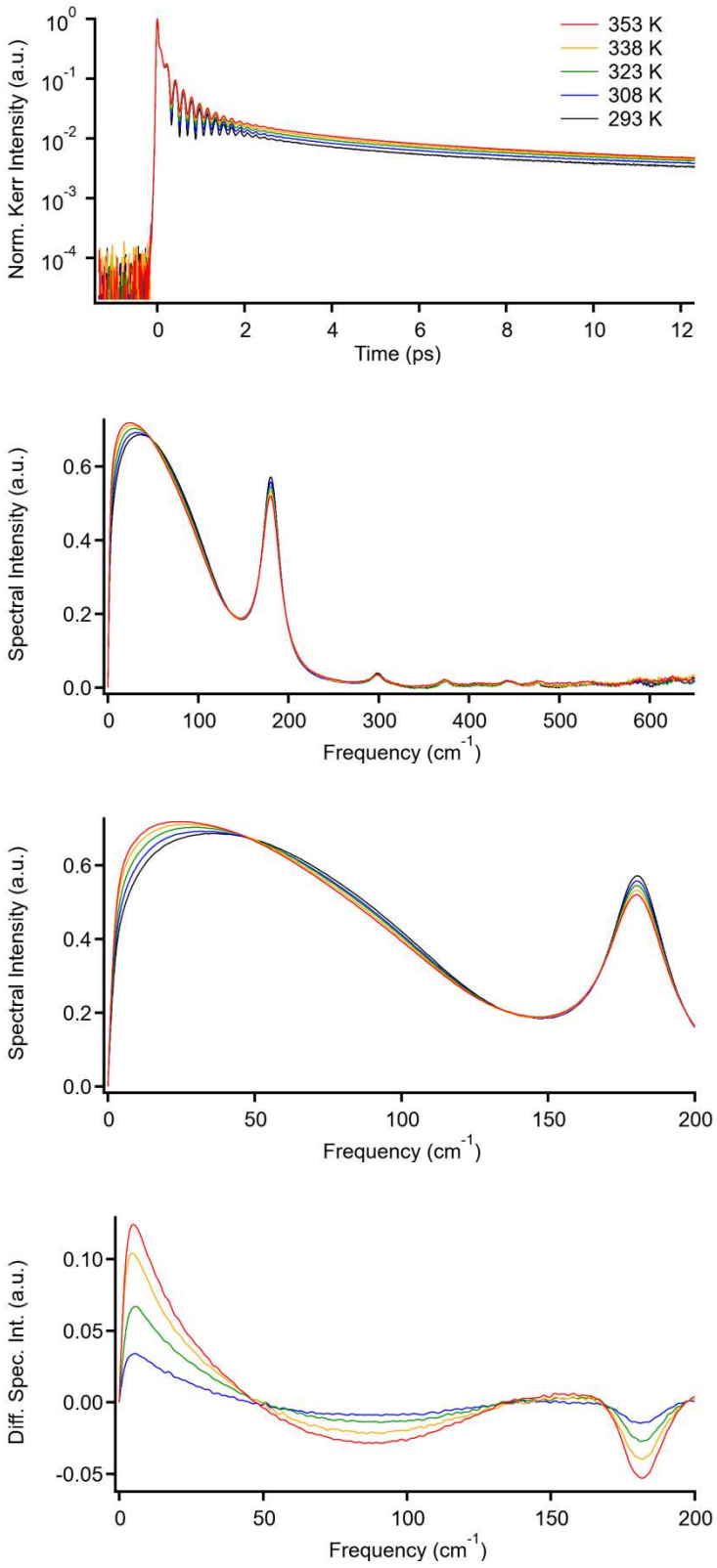

Figure E.4.5. 1-Butyl-1-methylpyrrolidinium tricyanomethide ([Pyrr$_{14}$][TCM]).

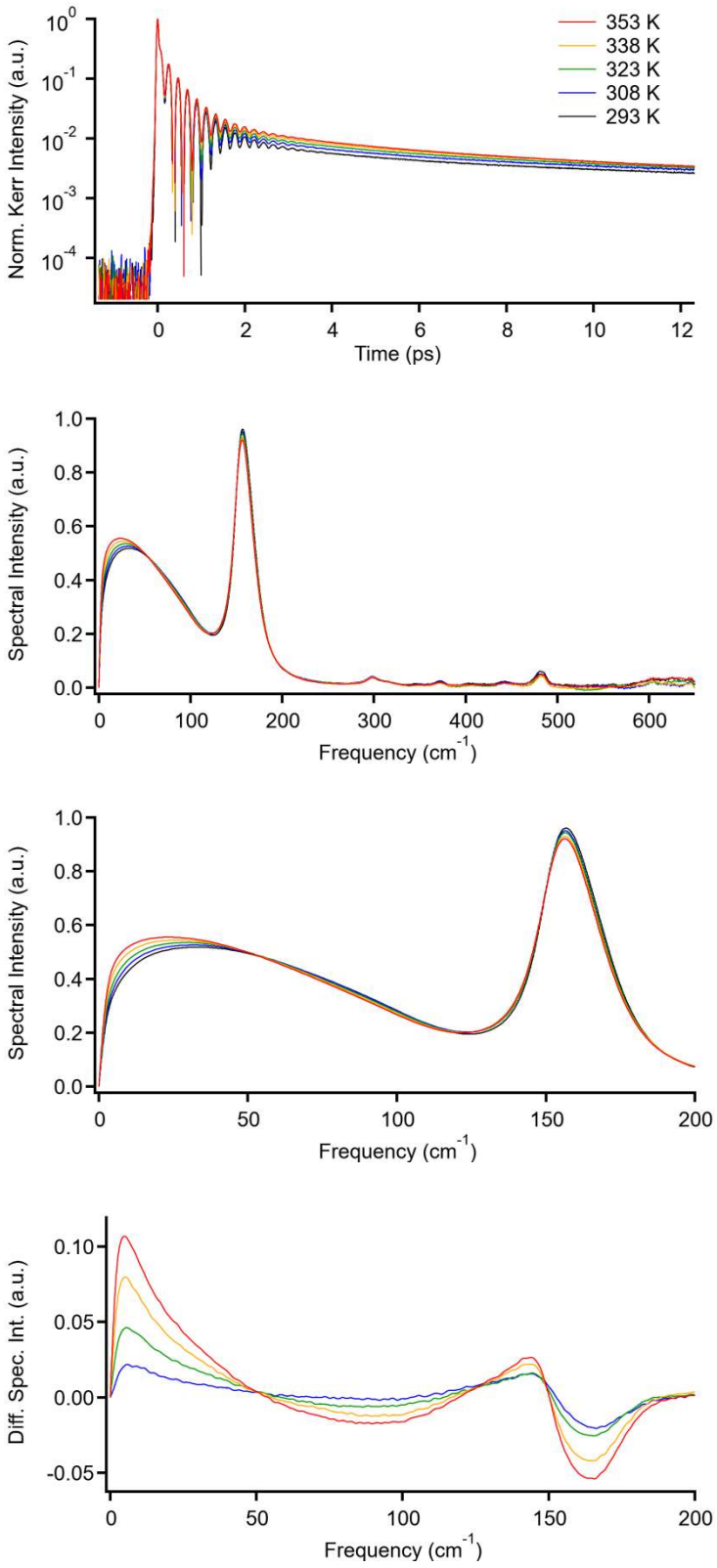

Figure E.4.6. 1-Butyl-1-methylpyrrolidinium tris(pentafluoroethyl)trifluorophosphate ([Pyrr$_{14}$][FAP]).

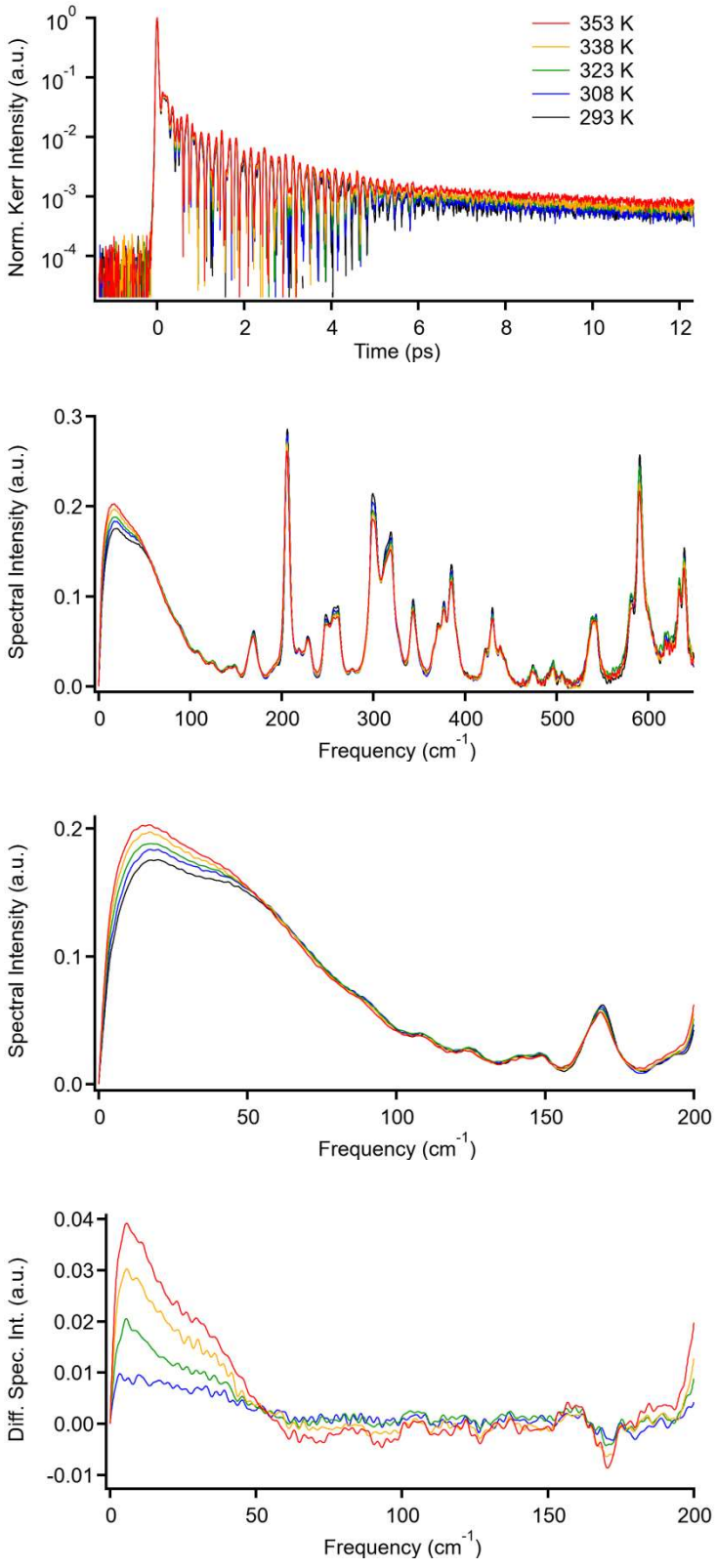

Figure E.4.7. 1-Butyl-1-methylpyrrolidinium bis(trifluoromethylsulfonyl)amide ([$Pyrr_{14}$][NTf_2]).

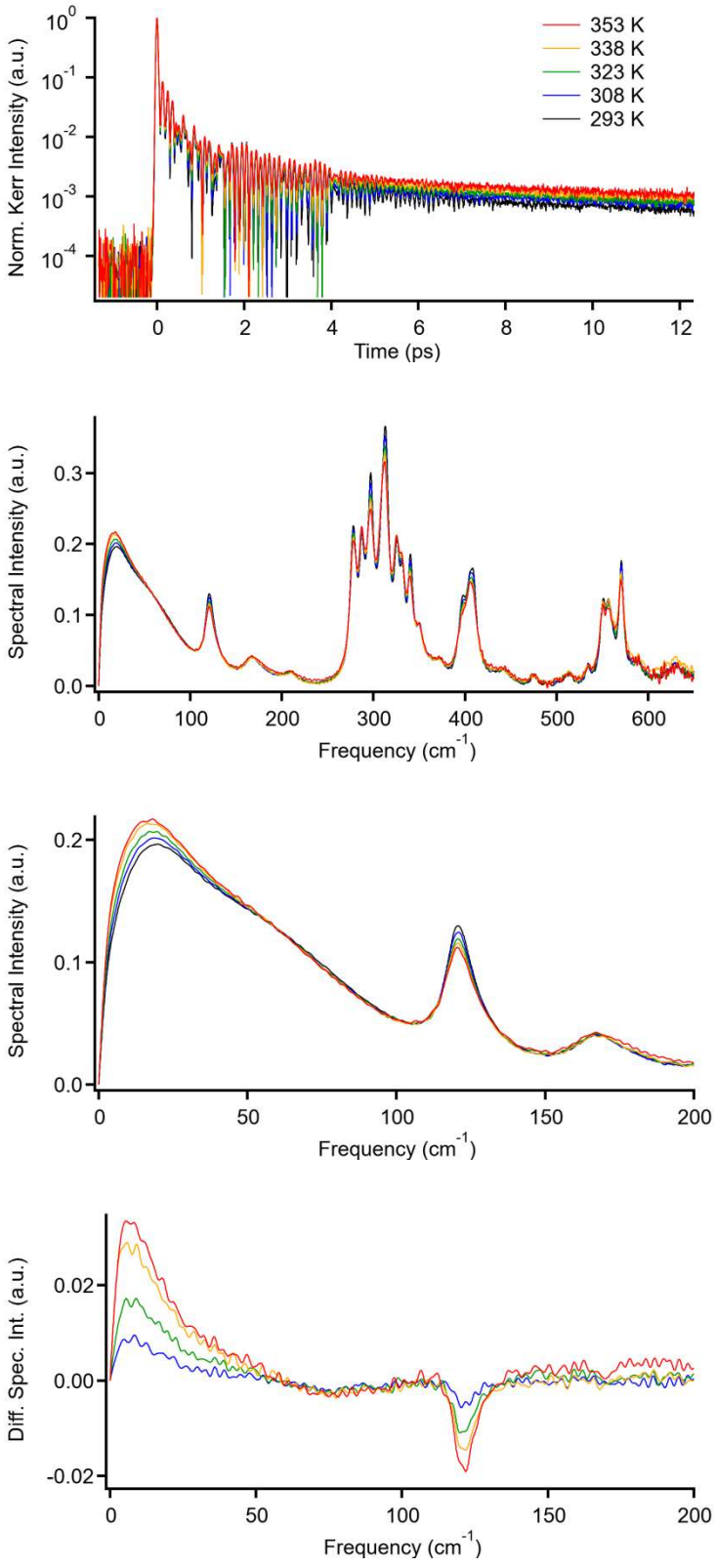

Figure E.4.8. 1-(2-Methoxyethyl)-1-methylpyrrolidnium bis(trifluoromethylsulfonyl)amide ([$Pyrr_{1(1O2)}$][NTf_2]).

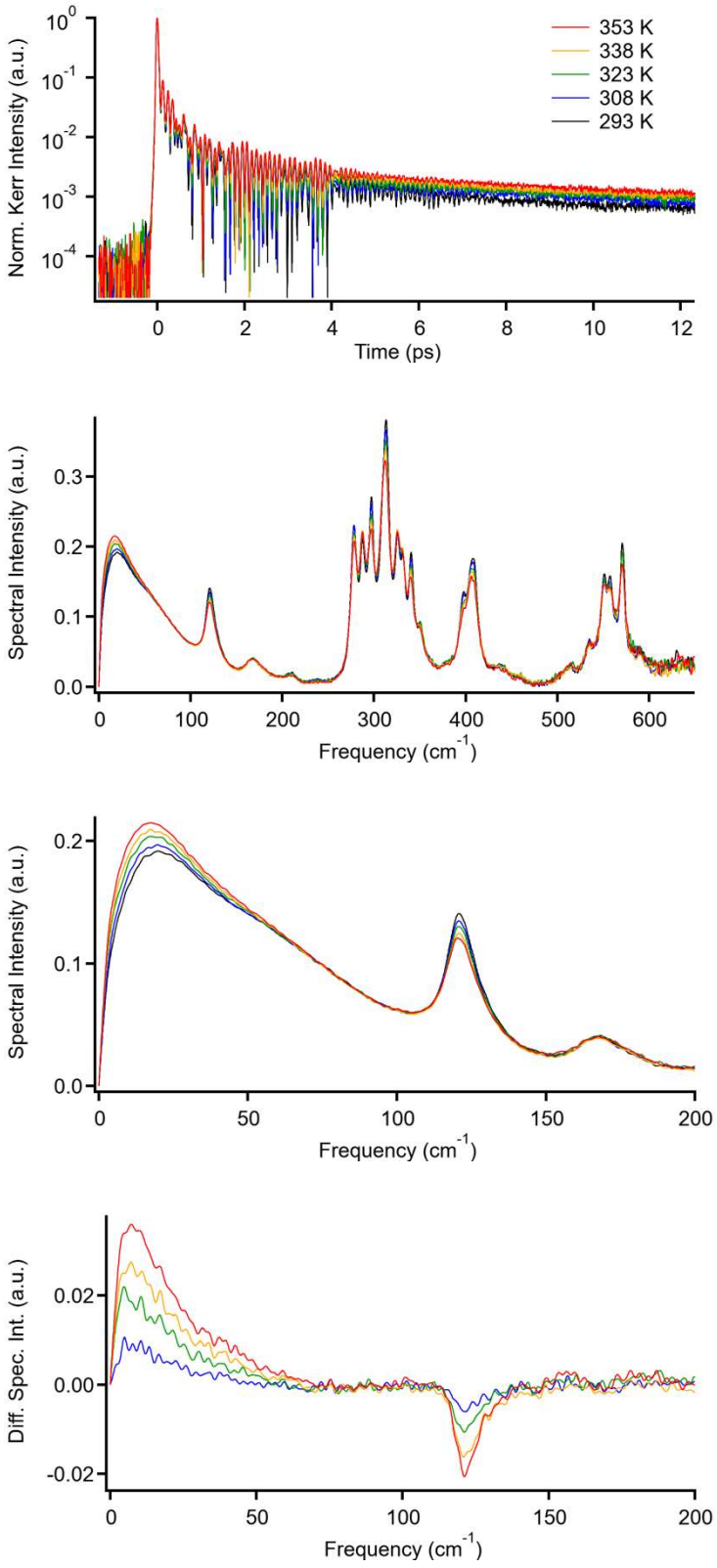

Figure E.4.9. 1-Butyl-1-methylpyrrolidnium bis(fluorosulfonyl)amide ([Pyrr$_{14}$][NF_2]).

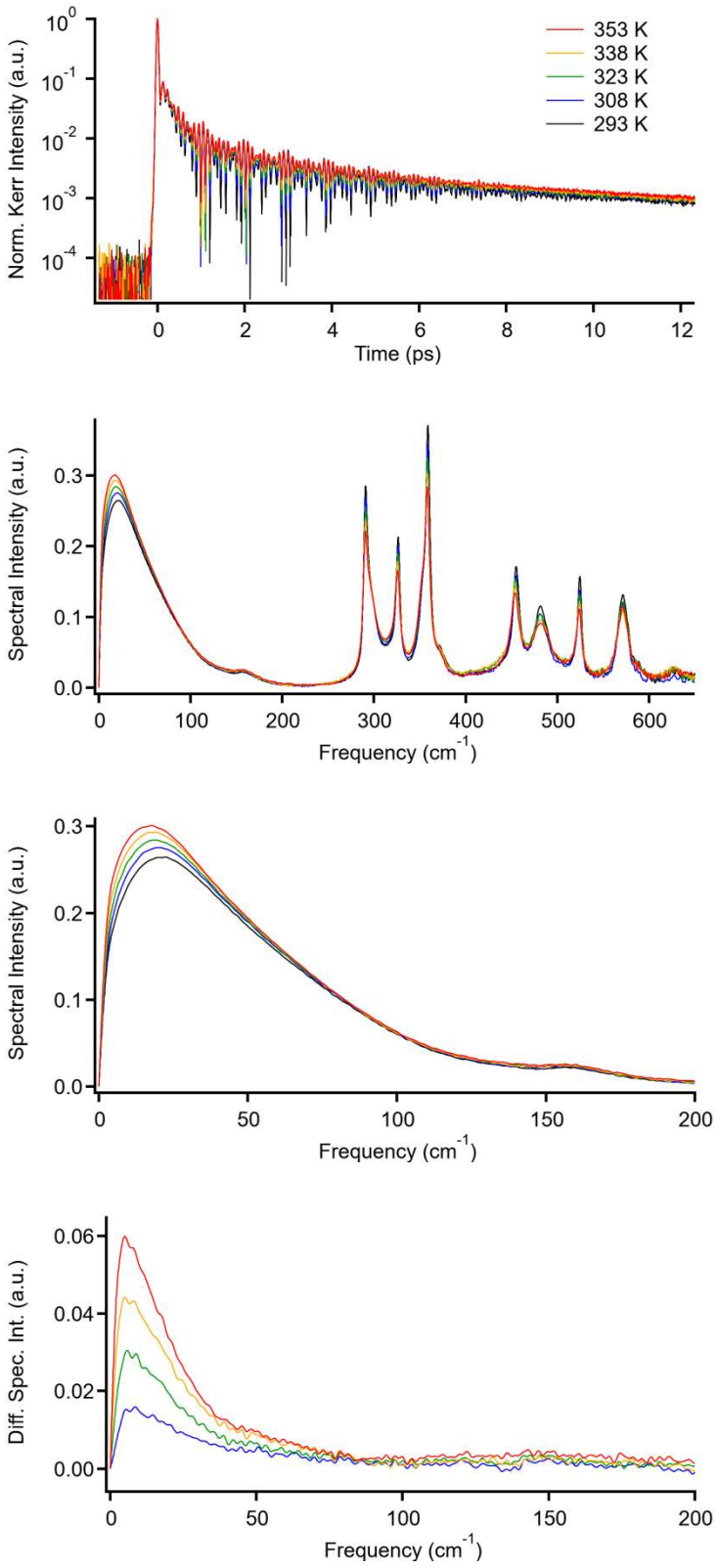

Figure E.4.10. 1-(2-Methoxyethyl)-1-methylpyrrolidnium bis(fluorosulfonyl)amide ([$Pyrr_{1(1O2)}$][NF_2]).

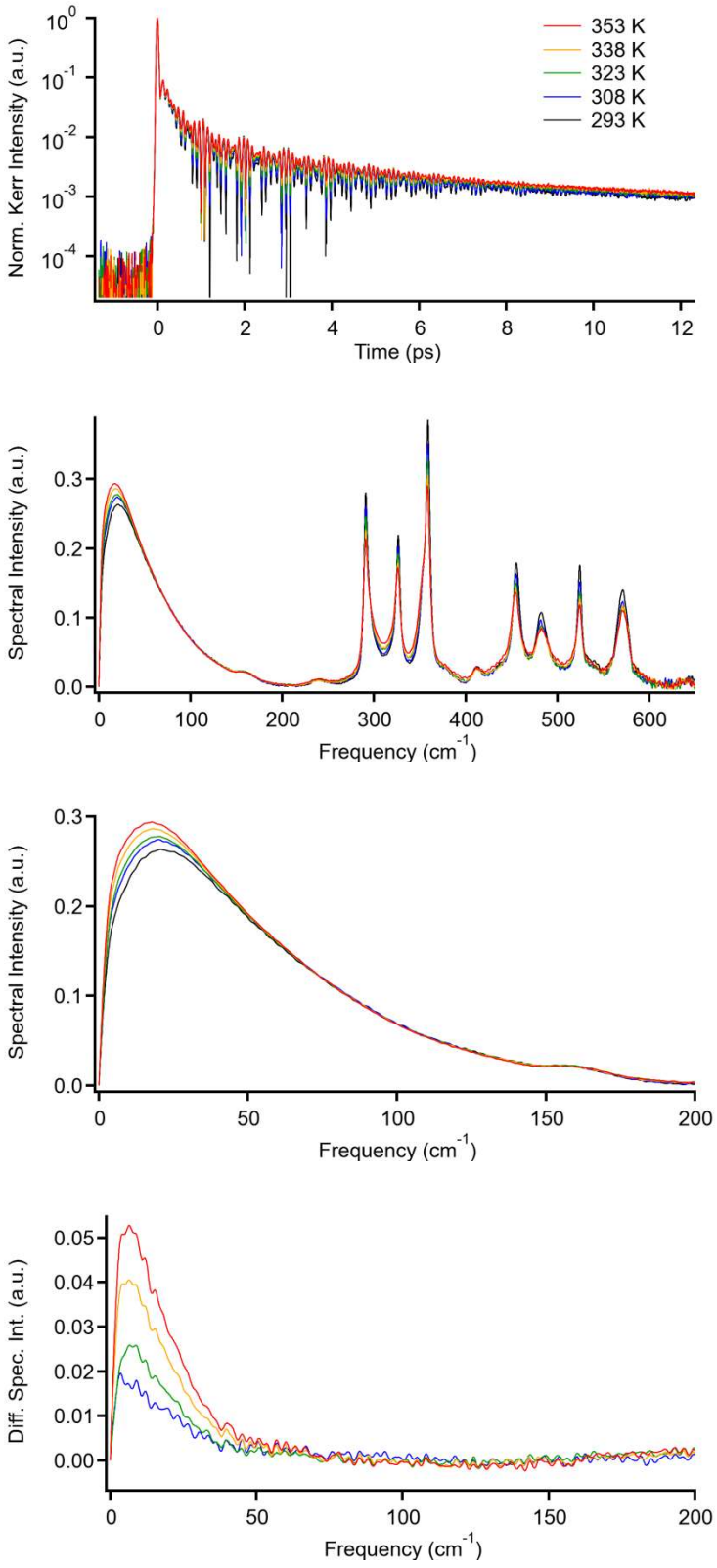

Figure E.4.11. 1-Butyl-1-methylpyrrolidinium bis(pentafluoroethylsulfonyl)amide ([$Pyrr_{14}$][NPf_2]).

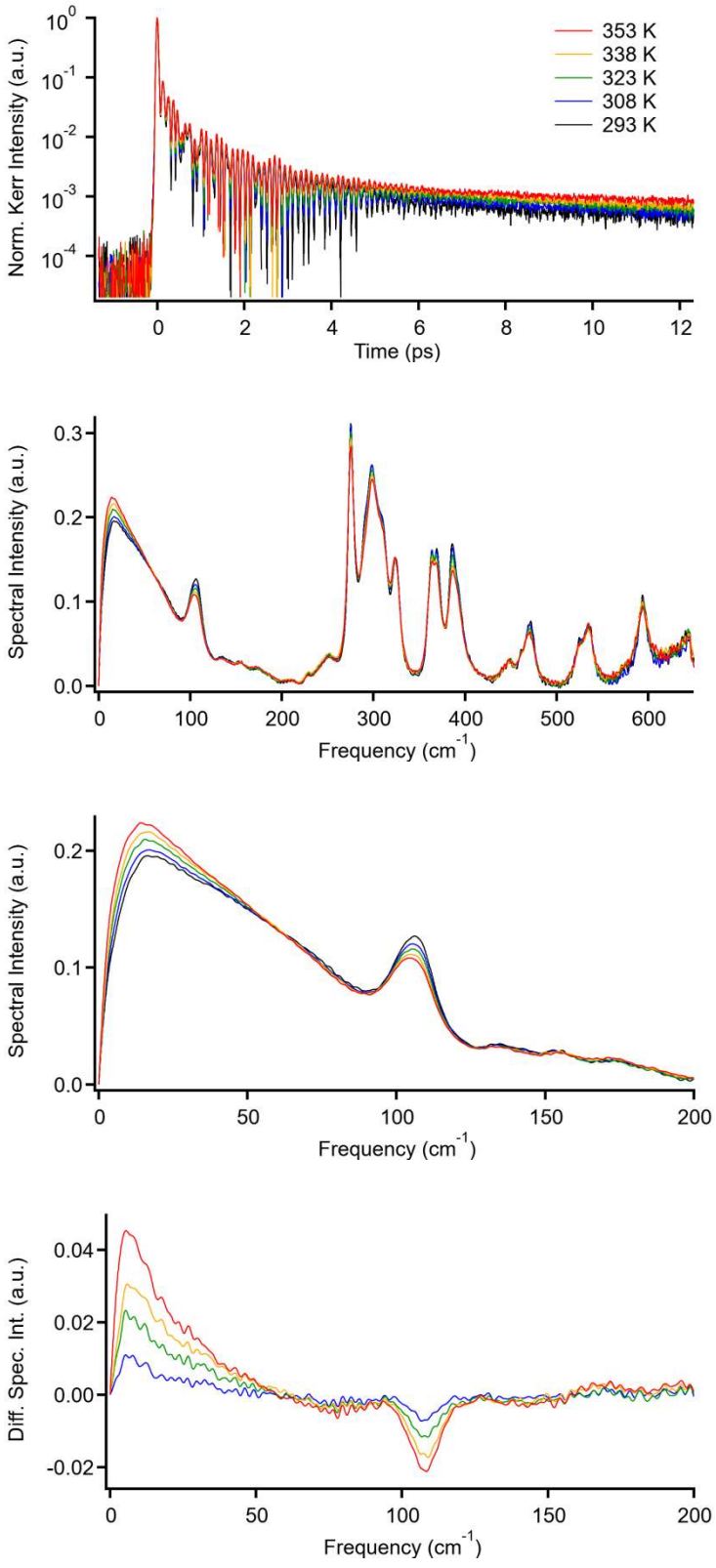

Figure E.4.12. 1-Butyl-1-methylpyrrolidinium cyclohexafluoropropane-1,3-bis(sulfonyl)amide ([Pyrr$_{14}$][NCyF]).

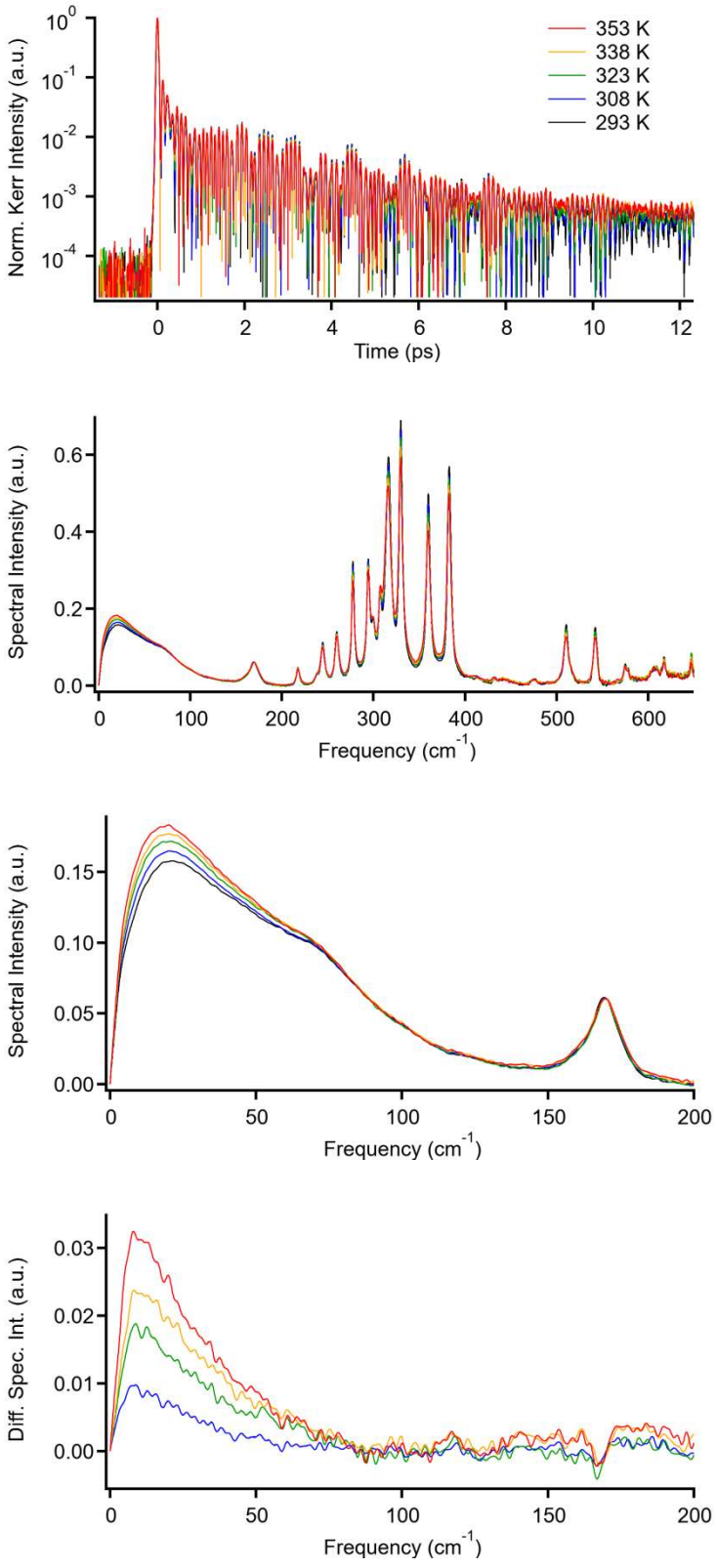

Figure E.4.13. 1-(2-Methoxyethyl)-1-methylpyrrolidinium cyclohexafluoropropane-1,3-bis(sulfonyl)amide ([Pyrr$_{1(1O2)}$][NCyF]).

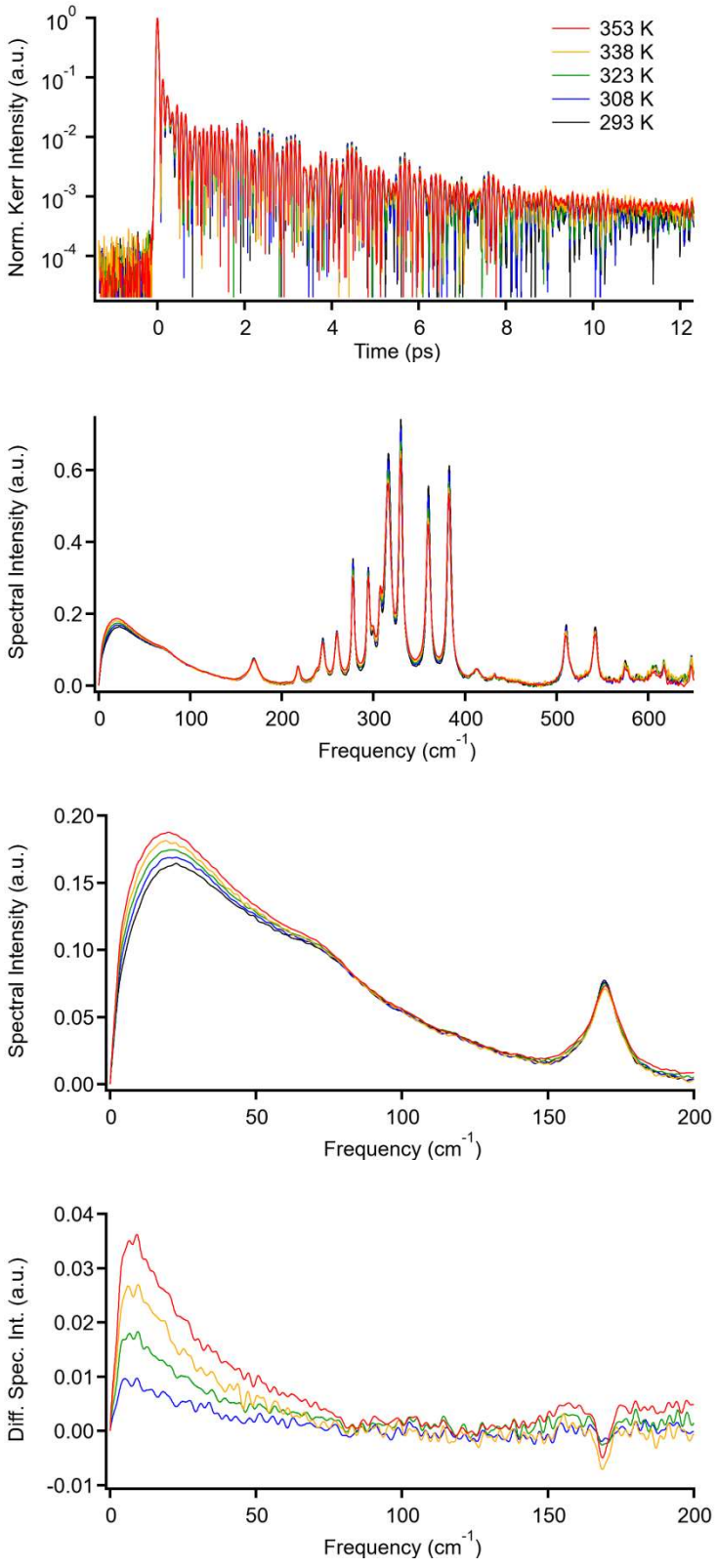

Table E.5. Biexponential Fit Parameter for Kerr Transients of Pyrrolidinium-Based Ionic Liquids at Various Temperatures.

Temperature (K)	a_0	a_1	τ_1 (ps)	a_2	τ_2 (ps)
		[$Pyrr_{1(1O2)}$][PF_6]			
293	0.00014	0.00491	1.09	0.00069	7.24
308	0.00019	0.00548	1.11	0.00080	7.17
323	0.00013	0.00571	1.04	0.00118	7.15
338	0.00016	0.00636	1.08	0.00122	7.10
353	0.00019	0.00806	0.97	0.00148	7.12
		[$Pyrr_{1(1O2)}$][BF_4]			
293	0.00010	0.00291	1.13	0.00085	7.60
308	0.00013	0.00319	1.13	0.00092	6.94
323	0.00020	0.00276	1.28	0.00092	7.15
338	0.00029	0.00271	1.46	0.00084	6.64
353	0.00021	0.00499	1.15	0.00119	7.42
		[$Pyrr_{14}$][OTf]			
293	0.00016	0.001706	1.34	0.00061	4.64
308	0.00018	0.001435	1.02	0.00094	4.32
323	0.00017	0.001622	1.36	0.00086	4.30
338	0.00018	0.001518	1.23	0.00113	4.33
353	0.00019	0.001409	1.25	0.00124	4.24
		[$Pyrr_{14}$][DCA]			
293	0.00222	0.01610	1.38	0.00760	6.42
308	0.00257	0.01682	1.40	0.00893	6.26
323	0.00273	0.01951	1.35	0.01036	6.35
338	0.00281	0.02047	1.42	0.01123	6.45
353	0.00287	0.02332	1.35	0.01275	6.32
		[$Pyrr_{14}$][TCM]			
293	0.00179	0.01092	1.34	0.00619	6.16
308	0.00204	0.01374	1.25	0.00774	5.85
323	0.00212	0.01416	1.29	0.00897	5.87
338	0.00193	0.01681	1.28	0.01014	6.29
353	0.00198	0.01712	1.34	0.01120	5.96

Table E.5. Continued.

Temperature (K)	a_0	a_1	τ_1 (ps)	a_2	τ_2 (ps)
		[$Pyrr_{14}$][NTf_2]			
293	0.00035	0.01010	0.93	0.00138	7.01
308	0.00043	0.01019	0.95	0.00172	6.91
323	0.00044	0.01088	0.94	0.00201	6.98
338	0.00058	0.01163	1.00	0.00211	6.84
353	0.00067	0.01258	0.94	0.00253	6.47
		[$Pyrr_{14}$][NF_2]			
293	0.00044	0.00736	1.22	0.00287	6.22
308	0.00044	0.01055	1.11	0.00342	6.20
323	0.00042	0.01026	1.14	0.00375	6.13
338	0.00043	0.01062	1.20	0.00395	6.07
353	0.00046	0.01134	1.25	0.00403	6.20
		[$Pyrr_{14}$][NPf_2]			
293	0.00033	0.00319	1.27	0.00118	5.69
308	0.00031	0.00394	1.20	0.00169	5.76
323	0.00040	0.00475	1.10	0.00181	5.88
338	0.00038	0.00509	1.06	0.00225	5.91
353	0.00058	0.00712	1.11	0.00200	5.81
		[$Pyrr_{14}$][NCyF]			
293	0.000094	0.00132	6.86	-	-
308	0.000152	0.00156	6.42	-	-
323	0.000275	0.00198	5.06	-	-
338	0.000420	0.00244	4.26	-	-
353	0.000347	0.00267	4.78	-	-
		[$Pyrr_{14}$][FAP]			
293	0.00025	0.00151	0.97	0.00143	6.07
308	0.00020	0.00251	1.08	0.00191	6.01
323	0.00031	0.00224	1.15	0.00198	5.98
338	0.00031	0.00330	1.11	0.00214	6.04
353	0.00042	0.00437	1.14	0.00244	6.02

Table E.5. Continued.

Temperature (K)	a_0	a_1	τ_1 (ps)	a_2	τ_2 (ps)
		$[Pyrr_{1(1O2)}][NTf_2]$			
293	0.000341	0.01769	0.81	0.00176	6.70
308	0.000442	0.02543	0.74	0.00211	6.87
323	0.000521	0.02555	0.79	0.00225	7.22
338	0.000536	0.01828	0.85	0.00288	6.69
353	0.000535	0.02744	0.78	0.00326	7.14
		$[Pyrr_{1(1O2)}][NF_2]$			
293	0.000415	0.00943	1.11	0.00294	6.94
308	0.000435	0.01182	1.09	0.00326	6.76
323	0.000430	0.01160	1.06	0.00387	6.55
338	0.000463	0.01296	1.10	0.00401	6.53
353	0.000465	0.01562	1.06	0.00435	6.39
		$[Pyrr_{1(1O2)}][NCyF]$			
293	0.000206	0.00059	0.99	0.00146	6.22
308	0.000223	0.00074	1.10	0.00171	6.20
323	0.000209	0.00076	1.14	0.00202	6.21
338	0.000255	0.00109	1.09	0.00228	6.20
353	0.000222	0.00123	1.06	0.00264	6.20

Table E.6. Fit Parameters and First Moments M_1 for Low-Frequency Kerr Spectra of Ionic Liquids at Various Temperatures.

Intermolecular Vibrations

	T (K)	M_1 (cm^{-1})	$a_{O,1}$	$\omega_{O,1}$ (cm^{-1})	$a_{O,2}$	$\omega_{O,2}$ (cm^{-1})	$a_{G,1}$	$\omega_{G,1}$ (cm^{-1})	$\Delta\omega_{G,1}$ (cm^{-1})	$a_{G,2}$	$\omega_{G,2}$ (cm^{-1})	$\Delta\omega_{G,2}$ (cm^{-1})	$a_{G,3}$	$\omega_{G,3}$ (cm^{-1})	$\Delta\omega_{G,3}$ (cm^{-1})
$[Pyrr_{1(1O2)}][PF_6]$	293	65.6	0.024	4.3			0.056	9.8	29.1	0.085	35.8	58.1	0.088	70.8	99.3
	308	64.4	0.027	4.3			0.051	10.5	27.4	0.099	30.8	61.7	0.087	70.2	99.4
	323	63.4	0.026	4.8			0.057	9.6	29.7	0.103	29.8	62.6	0.088	70.2	97.4
	338	63.4	0.030	4.6			0.064	9.2	29.8	0.113	27.4	64.6	0.088	69.4	100.2
	353	62.6	0.030	5.2			0.060	10.1	31.3	0.122	27.6	64.9	0.085	72.0	97.8
$[Pyrr_{1(1O2)}][BF_4]$	293	67.0	0.019	5.0			0.039	10.6	31.1	0.077	27.8	61.5	0.093	70.1	97.9
	308	65.9	0.021	5.0			0.044	9.8	30.7	0.064	28.2	56.0	0.108	59.8	103.4
	323	65.5	0.024	4.7			0.048	8.9	29.9	0.060	25.5	52.7	0.172	34.3	117.6
	338	64.3	0.030	4.3			0.054	9.5	29.4	0.059	27.5	51.3	0.148	40.8	113.4
	353	63.8	0.030	4.5			0.058	9.2	30.2	0.064	26.6	52.4	0.150	39.7	114.2
$[Pyrr_{14}][OTf]$	293	65.1	0.011	4.72	0.009	33.15	0.031	65.0	51.7						
	308	64.5	0.008	6.06	0.009	33.27	0.031	61.1	53.0						
	323	63.8	0.013	5.15	0.010	32.70	0.025	63.5	48.6						
	338	63.5	0.012	5.61	0.010	32.69	0.027	61.6	53.8						
	353	61.9	0.013	5.77	0.011	31.85	0.025	61.6	51.8						

Intermolecular and Intramolecular Vibrations

	T (K)	M_1 (cm^{-1})	$a_{O,1}$	$\omega_{O,1}$ (cm^{-1})	$a_{G,1}$	$\omega_{G,1}$ (cm^{-1})	$\Delta\omega_{G,1}$ (cm^{-1})	$a_{G,2}$	$\omega_{G,2}$ (cm^{-1})	$\Delta\omega_{G,2}$ (cm^{-1})	$a_{G,3}$	$\omega_{G,3}$ (cm^{-1})	$\Delta\omega_{G,3}$ (cm^{-1})
[$Pyrr_{14}$][DCA]	293	64.8	0.156	4.1	0.201	11.2	23.1	0.201	26.0	38.6	0.810	39.0	110.6
	308	64.1	0.174	4.1	0.213	10.6	23.6	0.229	24.0	41.5	0.830	36.9	111.9
	323	63.5	0.187	4.3	0.225	10.5	24.7	0.242	23.5	43.4	0.832	36.3	112.5
	338	62.8	0.215	4.0	0.263	9.1	24.6	0.273	22.2	44.7	0.799	37.2	112.3
	353	62.5	0.219	4.2	0.273	9.3	25.8	0.298	20.8	48.2	0.767	37.9	112.9
[$Pyrr_{14}$][TCM]	293	56.8	0.096	6.5	0.365	18.3	48.3	0.376	67.2	71.5			
	308	57.1	0.105	6.2	0.298	16.2	44.0	0.415	58.8	80.6			
	323	56.4	0.118	6.0	0.309	15.6	43.2	0.420	56.8	82.2			
	338	55.9	0.137	5.5	0.305	13.6	40.0	0.474	47.1	89.9			
	353	55.3	0.152	5.3	0.327	13.0	39.6	0.507	42.2	93.2			

	T (K)	$a_{L,1}$	$\omega_{L,1}$ (cm^{-1})	$\Delta\omega_{L,1}$ (cm^{-1})	$a_{L,2}$	$\omega_{L,2}$ (cm^{-1})	$\Delta\omega_{L,2}$ (cm^{-1})
[$Pyrr_{14}$][DCA]	293	80.7	180.5	12.2			
	308	81.7	180.4	12.5			
	323	84.4	180.3	12.8			
	338	85.6	180.3	13.1			
	353	88.0	180.2	13.5			
[$Pyrr_{14}$][TCM]	293	41.7	154.6	8.4	79.8	163.6	12.4
	308	42.4	154.4	8.6	80.0	163.2	12.6
	323	41.4	154.4	8.6	82.6	163.0	12.8
	338	40.2	154.2	8.7	85.2	162.6	13.0
	353	43.3	154.2	9.0	81.1	162.6	13.0

Intermolecular Vibrations

	T (K)	M_1 (cm^{-1})	$a_{O,1}$	$\omega_{O,1}$ (cm^{-1})	$a_{O,2}$	$\omega_{O,2}$ (cm^{-1})	$a_{G,1}$	$\omega_{G,1}$ (cm^{-1})	$\Delta\omega_{G,1}$ (cm^{-1})	$a_{G,2}$	$\omega_{G,2}$ (cm^{-1})	$\Delta\omega_{G,2}$ (cm^{-1})	$a_{G,3}$	$\omega_{G,3}$ (cm^{-1})	$\Delta\omega_{G,3}$ (cm^{-1})
$[Pyrr_{14}][NTf_2]$	293	46.6	0.030	5.2			0.115	12.6	29.7	0.165	34.8	78.8			
	308	45.9	0.033	5.4			0.120	12.1	30.2	0.165	34.5	78.2			
	323	45.4	0.036	5.6			0.122	12.0	30.7	0.166	34.2	78.1			
	338	44.7	0.043	5.2			0.136	11.3	30.6	0.170	33.3	78.2			
	353	44.4	0.043	5.7			0.127	11.6	32.4	0.173	32.4	78.7			
$[Pyrr_{14}][NF_2]$	293	47.2	0.045	3.1	0.033	17.5	0.092	52.5	82.3						
	308	46.7	0.046	3.3	0.036	17.0	0.100	50.8	83.4						
	323	46.1	0.052	3.4	0.038	16.6	0.103	51.1	82.3						
	338	45.7	0.059	3.2	0.040	15.5	0.132	40.4	89.0						
	353	45.0	0.068	3.3	0.042	15.7	0.110	49.8	81.7						
$[Pyrr_{14}][NPf_2]$	293	42.9	0.024	4.1			0.084	11.2	20.3	0.151	29.2	41.0	0.087	68.7	40.0
	308	42.3	0.027	5.2			0.066	11.4	19.9	0.154	26.6	41.9	0.089	66.8	41.3
	323	41.6	0.034	6.4			0.040	13.8	17.3	0.158	26.1	42.7	0.087	66.7	41.5
	338	41.4	0.039	8.2			0.012	15.9	12.0	0.155	25.5	46.9	0.080	67.5	42.0
	353	40.4	0.043	5.4			0.062	12.3	19.6	0.168	26.2	43.6	0.082	67.4	40.7
$[Pyrr_{14}][NCyF]$	293	51.1	0.020	7.2			0.118	18.0	37.5	0.063	60.2	45.1	0.038	63.6	92.5
	308	50.7	0.022	7.4			0.124	18.0	38.4	0.062	61.3	44.4	0.038[a]	60.3	97.5
	323	49.7	0.024	7.9			0.134	17.9	40.4	0.061	61.7	41.2	0.038[a]	69.9	84.8
	338	50.1	0.024	8.4			0.131	17.7	40.8	0.062	61.8	42.4	0.038[a]	67.2	91.8
	353	49.6	0.028	8.6			0.123	20.1	41.2	0.058	63.5	41.0	0.038[a]	64.2	96.0

[a] Fixed to achieve reasonable fit parameters.

Intramolecular Vibrations

	T (K)	$a_{L,1}$	$\omega_{L,1}$ (cm^{-1})	$\Delta\omega_{L,1}$ (cm^{-1})	$a_{L,2}$	$\omega_{L,2}$ (cm^{-1})	$\Delta\omega_{L,2}$ (cm^{-1})	$a_{L,3}$	$\omega_{L,3}$ (cm^{-1})	$\Delta\omega_{L,3}$ (cm^{-1})	$a_{L,4}$	$\omega_{L,4}$ (cm^{-1})	$\Delta\omega_{L,4}$ (cm^{-1})
[$Pyrr_{14}$][NTf_2]	293	4.9	121.7	6.8	12.0	168.4	18.7	0.92	209.3	8.1			
	308	5.1	121.7	7.0	11.2	168.2	18.1	1.10	209.7	9.0			
	323	5.0	121.7	7.2	13.5	168.1	19.8	0.93	209.5	8.6			
	338	5.3	121.7	7.5	12.6	169.0	19.2	0.71	209.7	8.0			
	353	5.5	121.7	7.9	14.8	168.7	20.4	1.88	210.9	12.1			
[$Pyrr_{14}$][NF_2]	293	9.5	157.7	23.6									
	308	9.7	157.3	22.9									
	323	12.2	156.2	25.0									
	338	11.8	157.0	24.9									
	353	17.1	155.5	28.7									
[$Pyrr_{14}$][NPf_2]	293	9.6	106.1	9.3	1.6	136.3	9.1	1.6	153.7	9.6	2.4	175.8	13.5
	308	9.9	105.9	9.7	1.6	136.4	9.3	1.3	153.6	9.1	2.9	175.0	14.1
	323	9.8	105.7	9.9	1.5	136.1	9.0	1.2	153.7	9.1	3.0	174.0	14.4
	338	9.6	105.5	10.1	1.5	136.1	9.4	1.4	153.8	9.7	3.5	174.2	15.0
	353	10.1	105.3	10.5	1.4	135.6	9.2	1.4	153.9	10.2	4.0	174.1	15.9
[$Pyrr_{14}$][NCyF]	293	2.0	169.1	5.8									
	308	2.0	169.4	5.9									
	323	2.1	169.5	6.0									
	338	2.4	169.3	6.5									
	353	2.4	169.4	6.4									

Intermolecular Vibrations

	T (K)	M_1 (cm^{-1})	$a_{O,1}$	$\omega_{O,1}$ (cm^{-1})	$a_{G,1}$	$\omega_{G,1}$ (cm^{-1})	$\Delta\omega_{G,1}$ (cm^{-1})	$a_{G,2}$	$\omega_{G,2}$ (cm^{-1})	$\Delta\omega_{G,2}$ (cm^{-1})	$a_{G,3}$	$\omega_{G,3}$ (cm^{-1})	$\Delta\omega_{G,3}$ (cm^{-1})
$[Pyrr_{14}][FAP]$	293	44.8	0.028	8.5	0.021	17.5	16.2	0.158	39.2	66.8			
	308	44.6	0.033	8.3	0.016	18.7	13.7	0.176	34.1	71.1			
	323	44.0	0.037	8.3	0.012	19.5	13.0	0.185	31.5	72.3			
	338	42.8	0.036	5.8	0.083	9.8	26.6	0.195	30.0	71.1			
	353	41.6	0.040	6.0	0.079	9.7	27.8	0.187	31.6	68.2			
$[Pyrr_{1(1O2)}][NTf_2]$	293	48.2	0.027	5.7	0.143	10.0	33.7	0.160	34.6	83.9			
	308	47.8	0.030	6.0	0.145	10.0	34.5	0.160	34.4	84.2			
	323	47.0	0.036	5.5	0.157	10.0	33.9	0.164	33.5	84.0			
	338	46.6	0.038	5.9	0.158	9.8	34.7	0.163	33.9	83.8			
	353	46.2	0.040	6.2	0.155	9.9	35.3	0.163	34.0	83.7			
$[Pyrr_{1(1O2)}][NF_2]$	293	51.7	0.055	4.8	0.183	9.4	33.8	0.183	25.5	63.6	0.065	77.9	86.6
	308	50.8	0.066	4.4	0.161	10.3	31.3	0.146	25.4	56.1	0.099	56.6	96.8
	323	50.9	0.064	4.8	0.188	9.2	32.9	0.159	22.6	60.6	0.103	48.6	106.5
	338	50.0	0.074	4.6	0.204	8.4	32.0	0.164	21.3	59.0	0.112	45.9	105.4
	353	49.5	0.079	4.6	0.205	8.6	31.7	0.158	22.2	58.0	0.124	40.9	107.6
$[Pyrr_{1(1O2)}][NCyF]$	293	54.8	0.020	6.4	0.174	14.8	41.3	0.091	62.2	46.2	0.031	110.2	55.6
	308	53.7	0.024	6.1	0.184	15.0	41.4	0.084	61.2	43.5	0.036	102.6	59.7
	323	54.1	0.027	6.2	0.207	13.0	42.1	0.077	60.2	42.9	0.040	97.0	67.5
	338	52.7	0.029	6.5	0.203	12.9	41.8	0.089	60.0	46.3	0.033	104.2	60.8
	353	53.4	0.032	6.5	0.194	14.1	41.9	0.059	60.4	40.7	0.050	82.5	81.5

Intramolecular Vibrations

	T (K)	$a_{L,1}$	$\omega_{L,1}$ (cm^{-1})	$\Delta\omega_{L,1}$ (cm^{-1})	$a_{L,2}$	$\omega_{L,2}$ (cm^{-1})	$\Delta\omega_{L,2}$ (cm^{-1})	$a_{L,3}$	$\omega_{L,3}$ (cm^{-1})	$\Delta\omega_{L,3}$ (cm^{-1})	$a_{L,4}$	$\omega_{L,4}$ (cm^{-1})	$\Delta\omega_{L,4}$ (cm^{-1})
[$Pyrr_{14}$][FAP]	293	1.0	91.4	8.4	0.71	110.5	6.7	0.452	125.1	5.4	1.9	146.1	9.7
	308	0.9	90.8	8.3	0.70	110.0	6.9	0.416	124.8	5.4	2.1	146.0	10.1
	323	1.3	90.2	10.0	0.89	110.0	7.7	0.376	124.7	5.3	2.4	146.1	10.8
	338	1.5	90.1	10.4	0.93	110.4	7.8	0.301	124.6	4.8	2.2	145.8	10.8
	353	1.5[a]	88.5	9.8	1.24	109.0	8.7	0.400	124.4	5.7	2.5	146.3	11.4
[$Pyrr_{1(1O2)}$][NTf_2]	293	6.5	122.0	7.6	8.9	168.5	16.3	0.92	209.4	8.0			
	308	6.3	121.9	7.6	8.8	168.5	16.4	1.08	209.4	8.9			
	323	6.5	121.9	7.9	10.0	168.9	17.2	1.08	209.9	9.0			
	338	6.4	121.9	8.0	8.6	168.8	16.2	0.81	209.4	8.6			
	353	6.7	121.8	8.4	10.6	168.8	17.7	0.76	210.0	8.9			
[$Pyrr_{1(1O2)}$][NF_2]	293	1.4	160.4	11.5									
	308	1.8	160.4	12.8									
	323	1.7	161.1	12.9									
	338	1.9	160.7	13.6									
	353	2.0	162.1	13.7									
[$Pyrr_{1(1O2)}$][NCyF]	293	2.4	169.5	5.8									
	308	2.6	169.5	6.1									
	323	2.8	169.5	6.4									
	338	2.6	169.5	6.3									
	353	3.1	169.6	6.9									

[a] Fixed to achieve reasonable fit parameters.

E.7. Temperature Dependence of Bose-Einstein Thermal Occupation Factors.

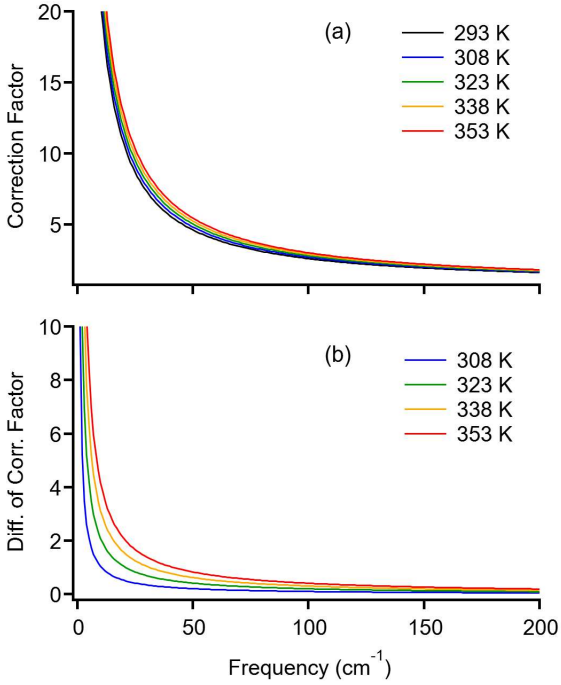

Figure E.7. (a) Temperature dependence of Bose-Einstein thermal occupation factors $[1-\exp(-\hbar\omega/k_{\mathrm{B}}T)]^{-1}$[1–3] at 293 K (black), 308 K (blue), 323 K (green), 338 K (yellow) and 353 K (red) and (b) difference intensities of the factor at each temperature (308 K: blue, 323 K: green, 338 K: yellow, and 353 K: red) relative to that at 293 K in the frequency range of 0–200 cm^{-1}.

Reference

(1) Cho, M.; Du, M.; Scherer, N. F.; Fleming, G. R.; Mukamel, S. *J. Chem. Phys.* **1993**, *99*, 2410–2428.

(2) Chang, Y. J.; Castner, E. W. Jr. *J. Chem. Phys.* **1993**, *99*, 7289.

(3) Lotshaw, W. T., McMorrow, D.; Thantu, N.; Melinger, J. S.; Kitchenham, R. *J. Raman Spectrosc.* **1995**, *26*, 571.

F. Appendix to Chapter 6

Table F.1. First Moments M_1 of Low-Frequency Kerr Spectra in ILs at 293, 308, 323, 338, and 353 K

temperature (K)	$[C_3MIm][NTf_2]$ (cm^{-1})	$[C_6MIm][NTf_2]$ (cm^{-1})	$[C_6(MIm)_2][NTf_2]_2$ (cm^{-1})	$[C_{12}(MIm)_2][NTf_2]_2$ (cm^{-1})
293	69.5	68.7	69.6	68.8
308	68.7	67.7	69.2	67.8
323	68.1	67.6	68.0	67.3
338	66.9	66.3	67.3	66.6
353	66.7	65.4	66.6	65.8

Table F.2. Fit Parameters for Fourier Transform Kerr Spectra of Ionic Liquids at Various Temperatures

Intermolecular Vibrations

	T (K)	$a_{O,1}$	$\omega_{O,1}$ (cm^{-1})	$a_{G,1}$	$\omega_{G,1}$ (cm^{-1})	$\Delta\omega_{G,1}$ (cm^{-1})	$a_{G,2}$	$\omega_{G,2}$ (cm^{-1})	$\Delta\omega_{G,2}$ (cm^{-1})	$a_{G,3}$	$\omega_{G,3}$ (cm^{-1})	$\Delta\omega_{G,3}$ (cm^{-1})
$[C_3MIm][NTf_2]$	293	0.095	4.6	0.200	12.6	24.9	0.149	31.4	45.0	0.329	80.7	87.7
	308	0.114	4.4	0.221	11.7	24.6	0.135	30.4	41.6	0.343	75.8	92.5
	323	0.128	4.3	0.226	11.5	24.5	0.137	29.8	42.0	0.343	74.2	94.3
	338	0.145	4.2	0.220	11.1	23.8	0.154	26.0	43.8	0.347	71.7	94.9
	353	0.161	4.0	0.308	7.5	25.5	0.224	17.7	51.9	0340	71.4	98.2
$[C_6MIm][NTf_2]$	293	0.056	5.4	0.150	14.1	22.6	0.057	31.6	27.4	0.310	69.1	91.3
	308	0.068	5.1	0.159	13.5	23.2	0.054	31.4	271.	0.318	65.5	94.4
	323	0.077	4.9	0.169	13.4	22.9	0.046	31.6	24.3	0.335	60.1	100.3
	338	0.099	4.3	0.192	12.2	22.6	0.052	30.6	24.0	0.353	54.4	103.9
	353	0.122	3.6	0.219	10.0	21.6	0.072	27.8	24.8	0.379	49.0	107.1
$[C_6(MIm)_2][NTf_2]_2$	293	0.051	4.6	0.163	12.5	25.1	0.116	25.8	42.3	0.328	79.6	78.4
	308	0.062	4.4	0.182	12.3	24.7	0.093	27.9	36.8	0.337	76.5	82.3
	323	0.082	4.1	0.193	12.1	24.1	0.090	28.2	35.1	0.341	74.4	83.7
	338	0.091	4.0	0.204	10.9	24.1	0.092	26.8	34.3	0.344	72.2	85.9
	353	0.105	3.9	0.216	10.9	24.0	0.091	26.9	33.6	0.350	70.5	87.1
$[C_{12}(MIm)_2][NTf_2]_2$	293	0.039	4.7	0.222	12.0	28.8	0.066	40.2	33.7	0.268	79.6	78.3
	308	0.058	4.0	0.201	11.2	26.3	0.082	33.3	38.1	0.270	77.5	80.5
	323	0.059	4.7	0.164	13.6	24.6	0.079	32.9	38.4	0.271	75.8	82.6
	338	0.073	4.0	0.164	11.0	23.7	0.099	25.0	39.9	0.279	72.4	86.2
	353	0.079	4.1	0.173	10.8	23.5	0.095	26.2	37.8	0.284	70.8	87.1

Intramolecular Vibrations

	T (K)	$a_{G,1}$	$\omega_{G,1}$ (cm^{-1})	$\Delta\omega_{G,1}$ (cm^{-1})	$a_{G,2}$	$\omega_{G,2}$ (cm^{-1})	$\Delta\omega_{G,2}$ (cm^{-1})	$a_{G,3}$	$\omega_{G,3}$ (cm^{-1})	$\Delta\omega_{G,3}$ (cm^{-1})
$[C_3MIm][NTf_2]$	293	4.96	122.5	7.2	1.66	170.7	8.3	19.72	220.6	23.5
	308	5.21	122.5	7.5	1.93	170.9	8.9	26.56	220.6	25.8
	323	4.80	122.4	7.4	2.22	170.9	9.5	23.54	219.8	24.7
	338	5.27	122.4	7.9	2.78	170.7	10.0	44.18	219.7	31.0
	353	4.08	122.3	7.4	3.07	169.3	11.5	19.92	218.7	24.7
$[C_6MIm][NTf_2]$	293	1.69	121.9	5.3	5.70	172.1	13.6	16.69	214.7	22.2
	308	1.85	122.0	5.7	6.37	172.2	14.5	15.92	214.8	21.8
	323	1.72	122.0	5.7	6.22	171.6	14.2	23.49	215.2	25.2
	338	1.88	122.1	6.0	6.72	171.7	14.9	19.87	213.8	24.8
	353	2.06	122.2	6.4	9.46	172.4	16.7	17.16	214.2	21.3
$[C_6(MIm)_2][NTf_2]_2$	293	4.16	123.1	6.9	7.61	172.6	13.1	28.5	208.6	28.7
	308	3.97	123.0	6.9	8.88	172.5	13.8	32.2	209.3	28.7
	323	4.12	123.1	7.2	9.28	172.1	14.3	35.5	209.2	30.5
	338	4.05	123.0	7.3	10.34	172.4	14.8	26.5	209.7	26.8
	353	4.23	123.1	7.5	13.47	172.4	16.4	29.3	210.5	26.9
$[C_{12}(MIm)_2][NTf_2]_2$	293	2.54	122.1	6.2	9.65	171.6	15.6	16.5	211.6	22.9
	308	2.52	122.2	6.3	10.56	171.6	16.3	15.5	211.1	22.3
	323	2.29	122.2	6.2	10.19	171.5	16.0	20.5	211.4	25.4
	338	2.21	122.1	6.2	7.94	171.3	14.8	25.9	212.0	28.6
	353	2.35	122.0	6.5	11.95	171.7	17.3	19.7	211.5	25.3

G. Appendix to Chapter 7

Table G.1. Biexponential Fit Parameter for Kerr Transients of Ionic Liquids at Various Temperatures.

temperature (K)	a_0	a_1	τ_1 (ps)	a_2	τ_2 (ps)
		[CHxmMPyrr][NTf_2]			
293	0.00028	0.01698	0.82	0.00120	6.72
308	0.00033	0.01566	0.85	0.00137	7.14
323	0.00037	0.01654	0.85	0.00172	6.53
338	0.00044	0.01535	0.87	0.00215	6.00
353	0.00047	0.01227	0.92	0.00219	6.18
		[CHxmMIm][NTf_2]			
293	0.00028	0.01537	0.88	0.00152	7.38
308	0.00044	0.01183	1.01	0.00186	7.36
323	0.00066	0.00855	1.22	0.00203	7.32
338	0.00076	0.01169	1.10	0.00261	7.41
353	0.00092	0.01006	1.20	0.00299	7.31
		[CHxmPy][NTf_2]			
293	-	-	-	-	-
308	0.00059	0.00872	1.26	0.00238	7.50
323	0.00071	0.00927	1.25	0.00304	7.32
338	0.00102	0.01103	1.26	0.00343	7.41
353	0.00121	0.01041	1.32	0.00408	7.20

(Continued)

Temperature (K)	a_0	a_1	τ_1 (ps)	a_2	τ_2 (ps)
		[BzMPyrr][NTf_2]			
293	0.00057	0.01071	1.12	0.00259	6.44
308	0.00070	0.01259	1.09	0.00343	6.47
323	0.00110	0.01259	1.14	0.00393	6.25
338	0.00126	0.01637	1.07	0.00470	6.26
353	0.00155	0.01878	1.06	0.00537	6.22
		[BzMIm][NTf_2]			
293	0.00053	0.01185	1.31	0.00320	7.95
308	0.00071	0.01166	1.42	0.00391	8.05
323	0.00096	0.01352	1.45	0.00447	7.99
338	0.00108	0.01559	1.40	0.00542	8.07
353	0.00126	0.01709	1.41	0.00614	8.07
		[BzPy][NTf_2]			
293	0.00063	0.00934	1.47	0.00360	7.18
308	0.00095	0.01206	1.50	0.00388	7.30
323	0.00108	0.01266	1.52	0.00460	7.27
338	0.00124	0.01464	1.47	0.00577	7.54
353	0.00144	0.01585	1.49	0.00616	7.44

G.2. Examples of Line Shape Analysis Results for Low-Frequency Spectra.

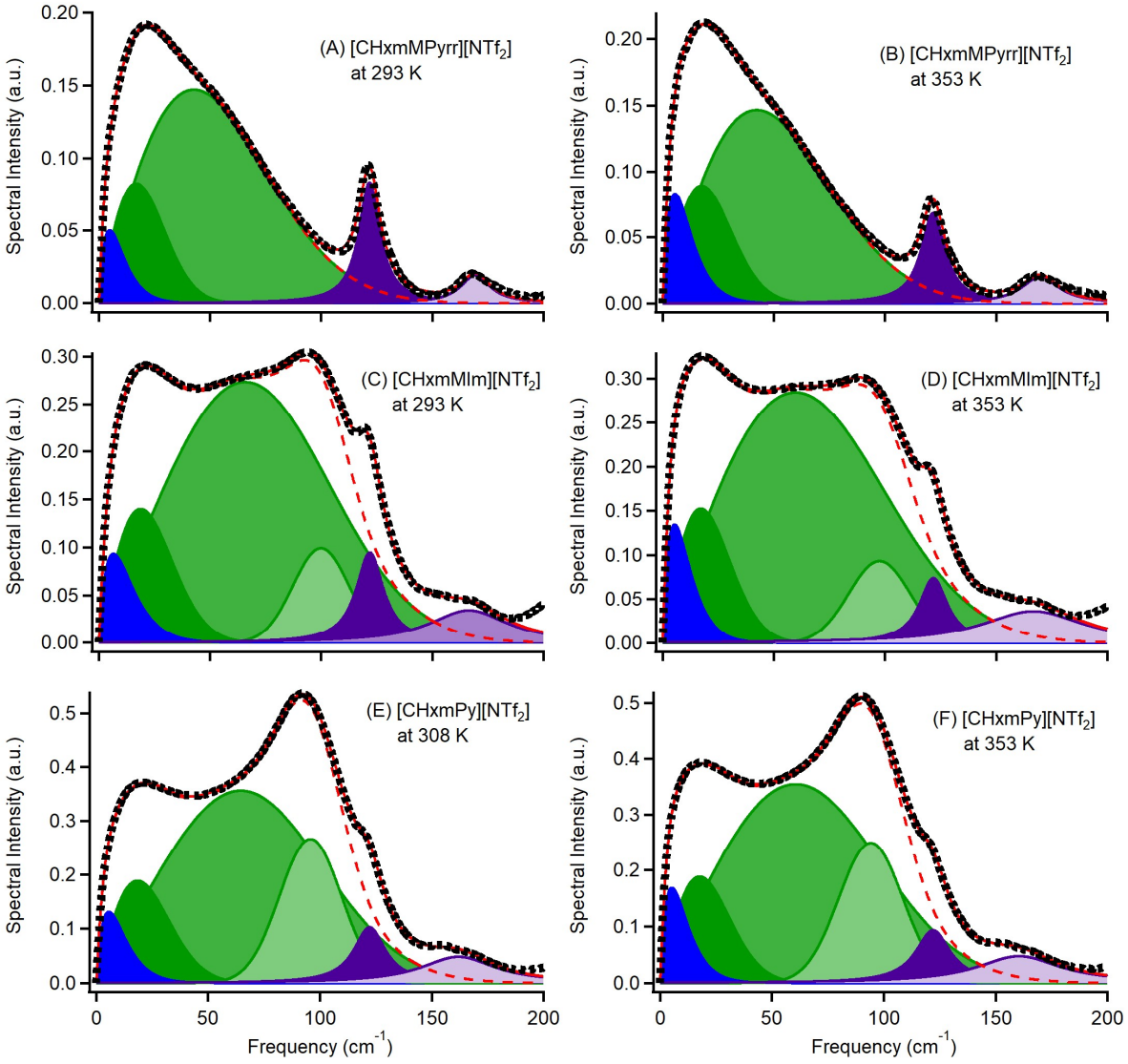

Figure G.2.1. Line shape analysis results obtained for the low-frequency Kerr spectra in the frequency range of 0–200 cm^{-1} for [CHxmMPyrr][NTf_2] at (A) 293 K and (B) 353 K, [CHxmMIm][NTf_2] at (C) 293 K and (D) 353 K, and [CHxmPy][NTf_2] at (E) 308 K and (F) 353 K. Dots denote the experimentally obtained spectra, red lines denote the entire fits, blue areas denote the Ohmic components, green areas denote the antisymmetrized Gaussian components, purple areas denote the Lorentzian component, and red broken lines denote the sums of Ohmic and antisymmetrized Gaussian components.

(Continued)

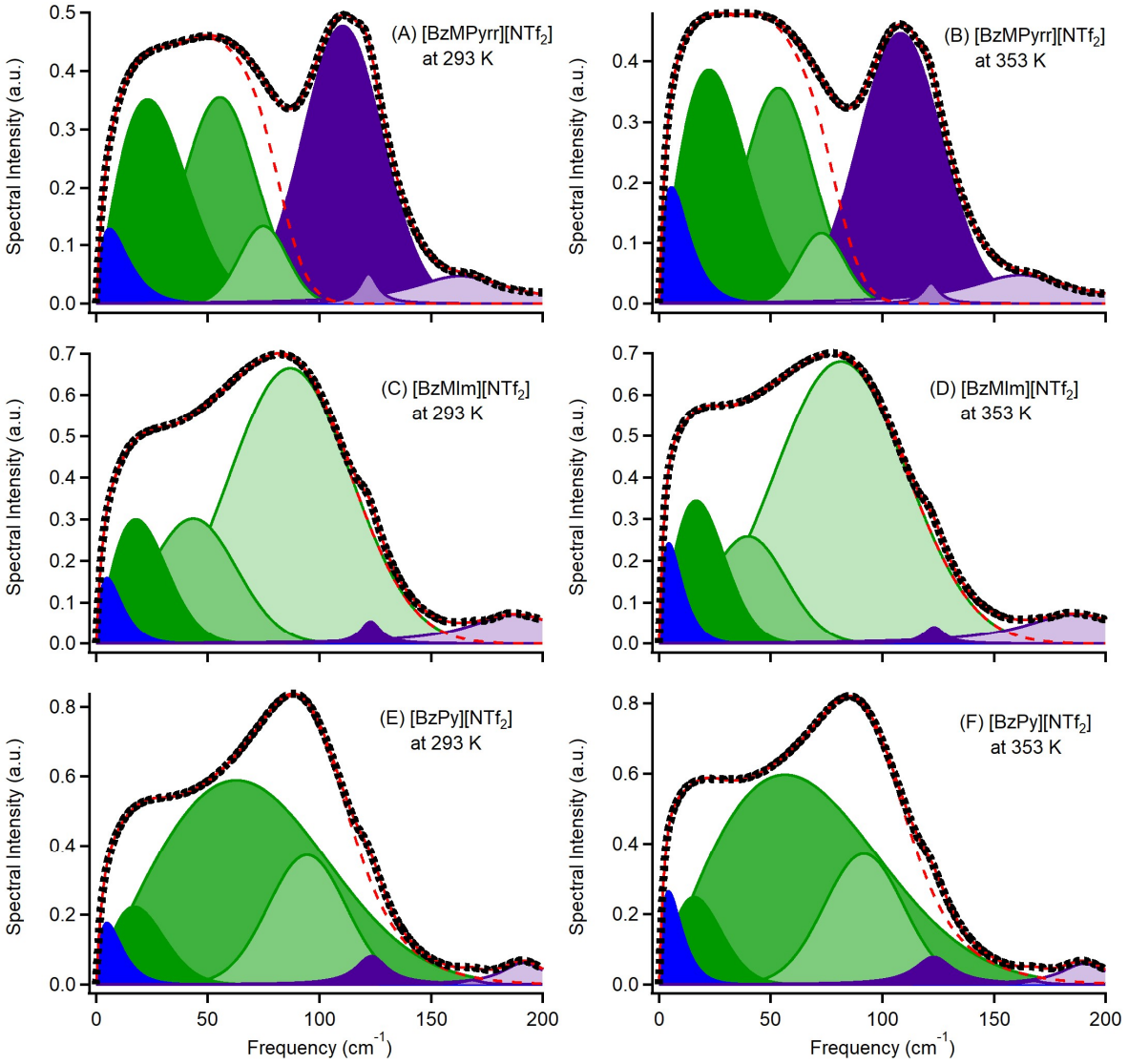

Figure G.2.2. Line shape analysis results obtained for the low-frequency Kerr spectra in the frequency range of 0–200 cm^{-1} for [BzMPyrr][NTf_2] at (A) 293 K and (B) 353 K, [BzMIm][NTf_2] at (C) 293 K and (D) 353 K, and [BzPy][NTf_2] at (E) 293 K and (F) 353 K. Dots denote the experimentally obtained spectra, red lines denote the entire fits, blue areas denote the Ohmic components, green areas denote the antisymmetrized Gaussian components, purple areas denote the Lorentzian component, and red broken lines denote the sums of Ohmic and antisymmetrized Gaussian components.

Table G.3. Fit Parameters and First Moments for Low-Frequency Kerr Spectra of Ionic Liquids at Various Temperatures Intermolecular Vibrations

	T (K)	M_1 (cm^{-1})	$a_{O,1}$	$\omega_{O,1}$ (cm^{-1})	$a_{G,1}$	$\omega_{G,1}$ (cm^{-1})	$\Delta\omega_{G,1}$ (cm^{-1})	$a_{G,2}$	$\omega_{G,2}$ (cm^{-1})	$\Delta\omega_{G,2}$ (cm^{-1})	$a_{G,3}$	$\omega_{G,3}$ (cm^{-1})	$\Delta\omega_{G,3}$ (cm^{-1})
[CHxmMPyrr][NTf_2]	293	45.4	0.028	4.84	0.095	13.5	28.5	0.194	29.0	77.5			
	308	44.6	0.031	5.21	0.093	13.7	28.9	0.183	30.9	75.4			
	323	44.1	0.034	5.16	0.110	12.0	30.3	0.185	30.0	76.0			
	338	43.7	0.035	5.64	0.110	12.0	31.3	0.186	29.7	76.2			
	353	43.0	0.041	5.47	0.123	11.2	31.9	0.186	30.0	75.6			
[CHxmMIm][NTf_2]	293	65.1	0.039	6.52	0.170	14.1	32.9	0.274	65.4	76.3	0.099	99.9	25.2
	308	64.3	0.047	5.92	0.178	13.2	31.9	0.276	62.7	78.4	0.099	99.2	26.3
	323	63.6	0.058	5.23	0.207	11.5	31.5	0.282	60.6	80.4	0.098	98.6	26.8
	338	62.9	0.062	5.44	0.198	11.8	31.4	0.286	59.6	80.9	0.095	98.1	27.1
	353	62.4	0.069	5.28	0.202	11.5	31.0	0.290	57.5	82.6	0.093	97.5	27.6
[CHxmPy][NTf_2]	293	-	-	-	-	-	-	-	-	-	-	-	-
	308	66.7	0.064	5.58	0.240	13.0	33.0	0.357	64.3	73.1	0.266	95.7	27.6
	323	66.0	0.071	5.51	0.233	13.1	32.2	0.358	62.6	74.3	0.260	95.2	28.0
	338	65.0	0.081	5.19	0.240	12.4	31.5	0.355	60.4	75.4	0.257	94.6	28.5
	353	64.4	0.088	5.22	0.241	12.4	31.5	0.357	59.8	75.8	0.249	94.2	28.6

Intramolecular Vibrations

	T (K)	$a_{L,1}$	$\omega_{L,1}$ (cm^{-1})	$\Delta\omega_{L,1}$ (cm^{-1})	$a_{L,2}$	$\omega_{L,2}$ (cm^{-1})	$\Delta\omega_{L,2}$ (cm^{-1})
[CHxmMPyrr][NTf_2]	293	2.85	121.7	5.84	1.28	169.3	8.12
	308	3.02	121.7	6.19	1.37	169.3	8.41
	323	2.95	121.6	6.29	1.66	169.2	9.10
	338	2.89	121.6	6.40	1.82	169.6	9.54
	353	2.98	121.6	6.60	2.15	169.8	10.3
[CHxmMIm][NTf_2]	293	5.41	121.8	7.56	15.8	166.4	21.5
	308	5.00	121.9	7.55	18.7	166.5	23.4
	323	4.82	121.8	7.62	20.7	166.5	24.3
	338	4.69	121.8	7.73	23.0	166.2	25.5
	353	4.47	121.7	7.78	28.2	166.7	27.8
[CHxmPy][NTf_2]	293	-	-	-	-	-	-
	308	7.57	122.2	8.59	20.2	161.9	20.4
	323	7.72	122.2	8.84	21.6	161.2	21.3
	338	8.37	122.1	9.27	24.1	160.6	22.3
	353	8.34	122.0	9.45	25.0	160.5	22.9

(Continued)

Intermolecular Vibrations

	T (K)	M_1 (cm^{-1})	$a_{O,1}$	$\omega_{O,1}$ (cm^{-1})	$a_{G,1}$	$\omega_{G,1}$ (cm^{-1})	$\Delta\omega_{G,1}$ (cm^{-1})	$a_{G,2}$	$\omega_{G,2}$ (cm^{-1})	$\Delta\omega_{G,2}$ (cm^{-1})	$a_{G,3}$	$\omega_{G,3}$ (cm^{-1})	$\Delta\omega_{G,3}$ (cm^{-1})
[BzMPyrr][NTf_2]	293	44.2	0.058	6.01	0.406	18.4	39.3	0.355	55.4	32.8	0.133	74.9	21.5
	308	43.3	0.067	5.92	0.413	18.3	39.2	0.354	55.1	32.7	0.123	74.4	21.2
	323	42.4	0.077	5.73	0.427	18.0	38.6	0.357	54.4	32.4	0.120	73.7	21.1
	338	41.6	0.086	5.62	0.430	18.4	38.1	0.353	53.8	31.8	0.122	73.2	21.2
	353	40.9	0.095	5.52	0.440	18.2	37.8	0.356	53.4	31.6	0.116	72.7	20.9
[BzMIm][NTf_2]	293	68.1	0.090	4.83	0.421	11.2	32.9	0.302	43.4	38.8	0.665	86.9	54.8
	308	67.3	0.108	4.59	0.439	10.8	32.0	0.291	42.0	37.3	0.670	85.3	56.1
	323	66.4	0.128	4.32	0.456	9.57	30.8	0.301	39.8	37.7	0.672	84.1	57.0
	338	65.7	0.138	4.36	0.502	9.58	31.2	0.272	40.1	35.4	0.679	82.5	58.2
	353	65.1	0.153	4.30	0.515	9.67	30.9	0.259	39.8	34.2	0.680	81.4	59.2
[BzPy][NTf_2]	293	70.3	0.099	4.82	0.372	8.82	32.4	0.596	61.3	83.1	0.373	94.5	34.8
	308	69.6	0.129	4.31	0.409	7.84	31.0	0.606	55.7	88.4	0.385	93.6	35.4
	323	69.0	0.144	4.24	0.447	7.16	30.6	0.628	52.0	91.6	0.382	93.0	35.5
	338	68.1	0.153	4.33	0.457	7.13	30.7	0.637	51.5	91.2	0.370	92.3	35.2
	353	67.1	0.169	4.23	0.490	6.73	30.3	0.659	48.1	92.4	0.372	91.7	35.3

(Continued)

Intramolecular Vibrations

	T (K)	$a_{G,4}$	$\omega_{G,4}$ (cm^{-1})	$\Delta\omega_{G,4}$ (cm^{-1})	$a_{L,1}$	$\omega_{L,1}$ (cm^{-1})	$\Delta\omega_{L,1}$ (cm^{-1})	$a_{L,2}$	$\omega_{L,2}$ (cm^{-1})	$\Delta\omega_{L,2}$ (cm^{-1})	$a_{L,3}$	$\omega_{L,3}$ (cm^{-1})	$\Delta\omega_{L,3}$ (cm^{-1})
[BzMPyrr][NTf_2]	293	0.477	110.4	35.8	1.24	122.0	4.93	33.3	163.0	26.5			
	308	0.466	109.8	36.2	1.02	121.9	4.72	34.5	162.6	27.0			
	323	0.461	109.3	36.8	0.881	121.9	4.63	32.2	162.5	26.5			
	338	0.451	108.6	37.1	0.704	121.8	4.38	37.8	162.2	28.4			
	353	0.446	108.1	37.6	0.674	121.8	4.46	36.7	161.7	28.0			
[BzMIm][NTf_2]	293				1.62	122.9	5.47	46.7	188.0	25.6			
	308				1.57	123.0	5.58	47.4	187.7	25.9			
	323				1.32	122.9	5.37	50.4	187.0	26.6			
	338				1.30	123.0	5.49	52.3	186.3	27.4			
	353				1.27	123.2	5.64	58.3	186.5	28.5			
[BzPy][NTf_2]	293				5.80	123.3	8.47	0.325	168.3	5.15	8.67	191.5	11.8
	308				5.90	123.3	8.69	0.314	168.4	5.16	9.14	191.4	12.1
	323				6.47	123.3	9.18	0.311	168.3	5.25	9.20	191.0	12.2
	338				6.56	123.1	9.41	0.301	167.9	5.34	10.0	190.7	12.8
	353				8.24	123.0	10.3	0.258	167.7	5.18	9.45	190.3	12.7

Figure G.4. Plots for Fit Parameters for Low-Frequency Kerr Spectra of Ionic Liquids vs Temperatures.

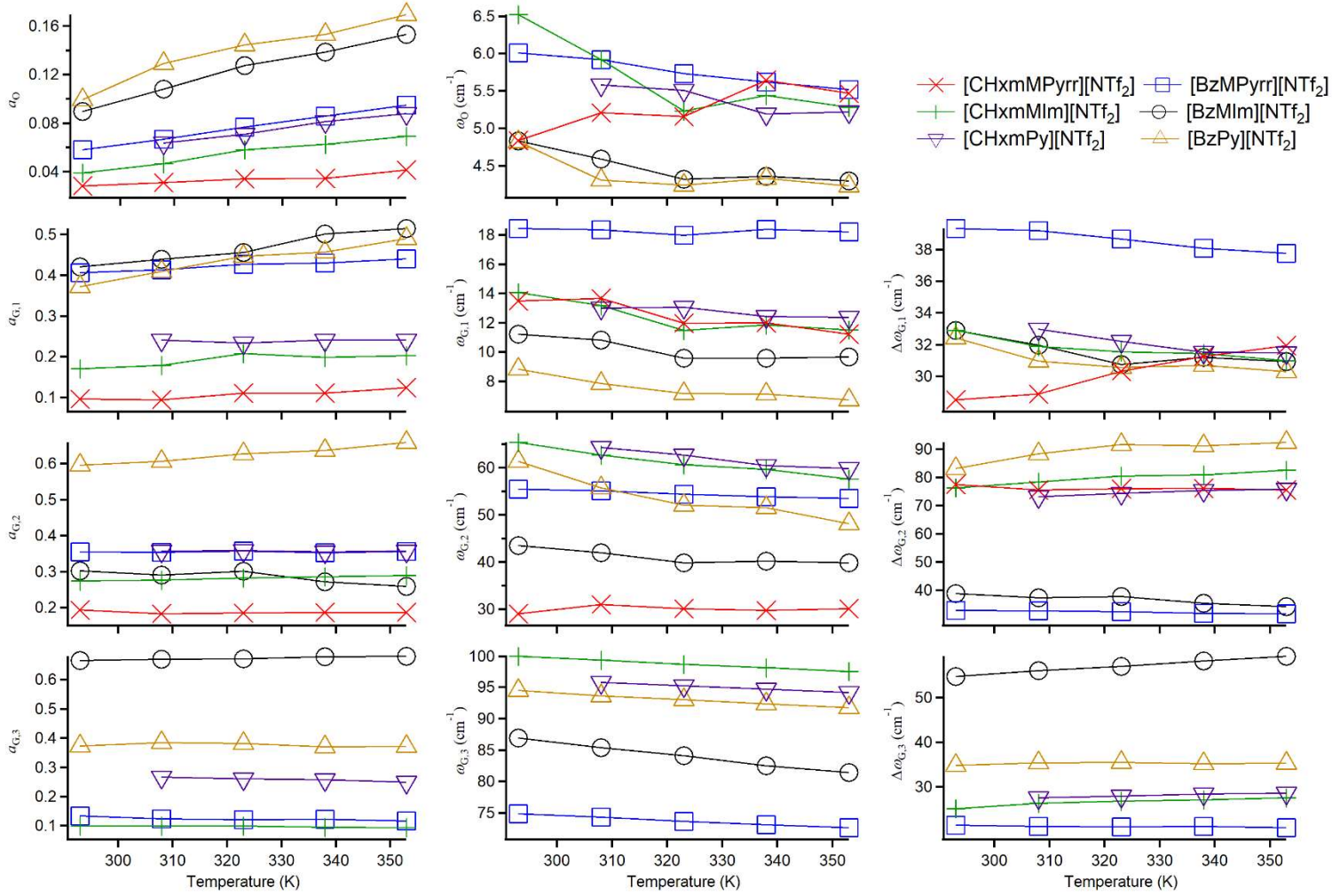

H. Appendix to Chapter 8

Table H.1. Fit Parameters for Fourier Transform Kerr Spectra of Six-Membered-Ring Molecular Liquids

liquid	M_1 (cm^{-1})	$a_{O,1}$	$\omega_{O,1}$ (cm^{-1})	$a_{O,2}$	$\omega_{O,2}$ (cm^{-1})	$a_{G,1}$	$\omega_{G,1}$ (cm^{-1})	$\Delta\omega_{G,1}$ (cm^{-1})	$a_{G,2}$	$\omega_{G,2}$ (cm^{-1})	$\Delta\omega_{G,2}$ (cm^{-1})	a_L	ω_L (cm^{-1})	$\Delta\omega_L$ (cm^{-1})
benzene	59.0	0.390	5.81			0.520	14.68	32.46	1.587	50.02	88.49			
		±0.001	±0.06			±0.058	±1.86	±1.34	±0.007	±0.31	±0.26			
1,3-cyclohexadiene	51.0	0.188	5.54			0.376	8.88	34.49	1.375	17.73	92.98	44.797	200.03	26.02
		±0.000	±0.02			±0.218	±5.56	±2.09	±0.474	±6.41	±1.66	±0.474	±0.08	±0.16
1,4-cyclohexadiene	50.6	0.641	3.52	0.178	13.42	0.657	45.64	69.32	0.264	41.75	137.21			
		±0.001	±0.01	±0.001	±0.16	±0.042	±0.76	±1.41	±0.529	±90.2	±34.4			
cyclohexene	42.9	0.242	3.90	0.088	15.12	0.661	22.53	86.03				13.856	173.6	18.32
		±0.000	±0.01	±0.000	±0.11	±0.125	±4.55	±1.60				±0.208	±0.087	±0.16
cyclohexane	46.7	0.024	5.92	0.016	24.00	0.094	40.91	60.09						
		±0.000	±0.02	±0.000	±0.02	±0.001	±0.19	±0.18						

Table H.2. Polarizability tensor elements α_{ij}, mean polarizability volume α_0, and polarizability anisotropy α_{anis} estimated by quantum chemistry calculations based on the B3LYP/6-311++G(d,p) level of theory. Unit is Å^3, except for the relative values

molecule	α_{xx}	α_{xy}	α_{yy}	α_{xz}	α_{yz}	α_{zz}	α_0 (α_0/α_0(benzene))	α_{anis} ($\alpha_{anis}/\alpha_{anis}$(benzene))
benzene	11.639	0.000	11.638	0.000	0.000	6.180	9.819	5.459
							(1.00)	(1.00)
1,3-cyclohexadiene	7.679	-0.146	11.674	0.000	0.000	11.514	10.289	3.926
							(1.05)	(0.72)
1,4-cyclohexadiene	13.048	0.000	9.662	0.000	0.000	7.278	9.996	5.022
							(1.02)	(0.92)
cyclohexene	11.980	-0.002	10.371	-0.224	-0.008	8.450	10.267	3.086
							(1.05)	(0.565)
cyclohexane	10.817	0.000	10.816	0.000	0.000	9.493	10.375	1.324
							(1.06)	(0.243)

H.3. Atom coordinates for benzene, 1,3-cyclohexadiene, 1,4-cyclohexadiene, cyclohexene, and cyclohexane calculated at the B3LYP/6-311+G(d,p) level of theory.

H.3.1. benzene.

Center Number	Atomic Number	Coordinates (Angstroms) X	Y	Z
1	6	0.993961	−0.977837	−0.000002
2	6	−0.350003	−1.349567	−0.000057
3	6	−1.343873	−0.371850	0.000052
4	6	−0.993876	0.977926	−0.000006
5	6	0.349886	1.349595	−0.000054
6	6	1.343906	0.371735	0.000047
7	1	1.766732	−1.738428	0.000076
8	1	−0.621964	−2.399218	−0.000095
9	1	−2.388907	−0.660907	0.000123
10	1	−1.766837	1.738316	−0.000019
11	1	0.622096	2.399177	0.000000
12	1	2.388875	0.661049	0.000034
Rotational constants (GHz):		5.7069749	5.7061296	2.8532761

H.3.2. 1,3-cyclohexadiene.

Center Number	Atomic Number	Coordinates (Angstroms) X	Y	Z
1	6	−0.049461	1.423428	0.112512
2	1	−0.014223	2.508214	0.115955
3	6	0.049461	0.731227	1.257209
4	1	0.182875	1.244330	2.203997
5	6	−0.049461	−0.731227	1.257209
6	1	−0.182875	−1.244330	2.203997
7	6	0.049461	−1.423428	0.112512
8	1	0.014223	−2.508214	0.115955
9	6	0.302045	−0.706942	−1.192698
10	1	−0.090303	−1.283418	−2.035044
11	1	1.390799	−0.643324	−1.347050
12	6	−0.302045	0.706942	−1.192698
13	1	0.090303	1.283418	−2.035044
14	1	−1.390799	0.643324	−1.347050
Rotational constants (GHz):		5.0689611	5.0610373	2.6862375

H.3.3. 1,4-cyclohexadiene.

Center Number	Atomic Number	Coordinates (Angstroms) X		Z
1	6	0.666212	1.254398	−0.000014
2	1	1.202607	2.199517	−0.000074
3	6	−0.666208	1.254434	−0.000125
4	1	−1.202587	2.199580	−0.000079
5	6	1.497756	0.000000	0.000055
6	1	2.172272	0.000000	−0.869141
7	1	2.171706	0.000000	0.869620
8	6	0.666212	−1.254398	−0.000014
9	1	1.202607	−2.199517	−0.000073
10	6	−0.666208	−1.254434	−0.000125
11	1	−1.202587	−2.199580	−0.000079
12	6	−1.497832	0.000000	0.000126
13	1	−2.171858	0.000000	−0.869300
14	1	−2.171755	0.000000	0.869709
Rotational constants (GHz):		5.1526318	4.9047248	2.5913394

H.3.4. cyclohexene.

Center Number	Atomic Number	Coordinates (Angstroms) X	Y	Z
1	6	−0.665345	1.305058	0.057043
2	1	−1.195842	2.252380	0.113356
3	6	0.664562	1.305414	−0.057102
4	1	1.194521	2.253043	−0.113536
5	6	1.496957	0.048600	−0.110316
6	1	1.886940	−0.085789	−1.129315
7	1	2.380800	0.166924	0.527180
8	6	0.698889	−1.192271	0.317115
9	1	1.244211	−2.102654	0.049871
10	1	0.596088	−1.195424	1.409097
11	6	−0.698184	−1.192583	−0.317236
12	1	−0.595562	−1.195560	−1.409229
13	1	−1.242951	−2.103345	−0.050050
14	6	−1.496973	0.047748	0.110472
15	1	−2.381061	0.165618	−0.526781
16	1	−1.886583	−0.086997	1.129555
Rotational constants (GHz):		4.7201969	4.5379220	2.5455130

H.3.5. cyclohexane.

Center Number	Atomic Number	Coordinates (Angstroms) X	Y	Z
1	6	0.560712	1.356511	−0.225301
2	6	−0.894650	1.163630	0.225674
3	6	−1.455283	−0.192718	−0.226065
4	6	−0.560859	−1.356257	0.225962
5	6	0.894406	−1.163884	−0.225475
6	6	1.455535	0.192652	0.225215
7	1	−2.472137	−0.327284	0.157704
8	1	−0.943795	1.226792	1.321106
9	1	−1.519496	1.976975	−0.158298
10	1	0.591508	1.431572	−1.320629
11	1	0.952167	2.304044	0.159848
12	1	−0.591526	−1.429618	1.321410
13	1	−0.952479	−2.304278	−0.157794
14	1	1.519227	−1.977062	0.158893
15	1	0.943246	−1.227854	−1.320874
16	1	1.536565	0.203252	1.320523
17	1	2.471708	0.327130	−0.160416
18	1	−1.534150	−0.203269	−1.321534
Rotational constants (GHz):		4.284332	4.2825969	2.4387628

Acknowledgments

I would like to express my deep gratitude to Professor Hideaki Shirota. His kind instruction and advice have been most instrumental in my research through the course of this work.

I am indebted to Dr. Tateki Ishida at the Institute for Molecular Science for providing the valuable data of temperature-dependent DOS spectra for ILs. This data corroborated the discussion on the temperature-dependent features of the low-frequency spectra for aromatic ILs.

I am grateful to Dr. James F. Wishart and Ms. Sharon Ramati for providing the six sample ILs in Chapter 7. This series of ILs enabled the insightful discussion about the difference of the contributions on the temperature-dependent low-frequency spectra between charged and neutral aromatic rings.

I am grateful to Mr. Motoyasu Fujiwara at the Institute for Molecular Science for his kind help with the DSC measurements at the Institute for Molecular Science.

I would like to thank Professor Takehisa Konishi, Professor Hiroyuki, Yoshida, Professor Shoichi Katsuta, and Professor Yoshifumi Kimura for critical discussions and insightful comments as the examiners of the degree.

Part of the works in this thesis was supported by JSPS Research Fellowship for Young Scientist (18J12979).

Finally, I would like to thank my family for supporting my life. Their kind support enabled my study in doctoral course.

Publication List

Original papers

(1) Dynamic Kerr Effect Study on Six-Membered-Ring Molecular Liquids: Benzene, 1,3-Cyclohexadiene, 1,4-Cyclohexadiene, Cyclohexene, and Cyclohexane.
Shohei Kakinuma and Hideaki Shirota.
J. Phys. Chem. B, **2015**, *119*, 4713–4724.

(2) Temperature Dependence of Low-Frequency Spectra in Molten Bis(trifluoromethylsulfonyl)amide Salts of Imidazolium Cations Studied by Femtosecond Raman-Induced Kerr Effect Spectroscopy.
Hideaki Shirota and **Shohei Kakinuma**.
J. Phys. Chem. B, **2015**, *119*, 9835–9846.

(3) Femtosecond Raman-Induced Kerr Effect Study of Temperature-Dependent Intermolecular Dynamics in Imidazolium-Based Ionic Liquids: Effects of Anion Species and Cation Alkyl Groups.
Shohei Kakinuma, Tateki Ishida, and Hideaki Shirota.
J. Phys. Chem. B, **2017**, *121*, 250–264.

(4) Effects of aromaticity in cations and their functional groups on the temperature dependence of low-frequency spectrum.
Shohei Kakinuma, Sharon Ramati, James F. Wishart, and Hideaki Shirota.
J. Chem. Phys. **2018**, *148*, 193805/1–10. (Special topic on "Chemical Physics of Ionic Liquids")

(5) Femtosecond Raman-Induced Kerr Effect Study of Temperature-Dependent Intermolecular Dynamics in Molten Bis(trifluoromethylsulfonyl)amide Salts: Effects of Cation Species.
Shohei Kakinuma and Hideaki Shirota.
J. Phys. Chem. B, **2018**, *122*, 6033–6047.

(6) Femtosecond Raman-Induced Kerr Effects Study of Temperature-Dependent Intermolecular Dynamics in Pyrrolidinium-Based Ionic Liquids: Effects of Anion Species.
Shohei Kakinuma and Hideaki Shirota.
J. Phys. Chem. B, **2019**, *123*, 1307–1323. (Selected as Supplementary Cover Article)

Other works

(1) Effects of Tetrafluoroborate and Bis(trifluoromethylsulfonyl)amide Anions on the Microscopic Structures of 1-Methyl-3-octylimidazolium-Based Ionic Liquids and Benzene Mixtures: A Multiple Approach by ATR-IR, NMR, and Femtosecond Raman-Induced Kerr Effect Spectroscopy.
Hideaki Shirota, **Shohei Kakinuma**, Yu Itoyama, Tatsuya Umecky, and Toshiyuki Takamuku.
J. Phys. Chem. B, **2016**, *120*, 513–526.

(2) Ultrafast Dynamics in Aromatic Cation Based Ionic Liquids: A Femtosecond Raman-Induced Kerr Effect Spectroscopic Study.
Hideaki Shirota, **Shohei Kakinuma**, Kotaro Takahashi, Akito Tago, Hocheon Jeong, and Tomotsumi Fujisawa.
Bull. Chem. Soc. Jpn, **2016**, *89*, 1106−1128.

(3) Liquid Properties of Ionic Liquids Based on Phosphonium Cations with (Alkylthio)alkyl Groups
Hideaki Shirota, Kotaro Takahashi, Masatoshi Ando, and **Shohei Kakinuma**.
Submitted.